DOCTORAL THESIS

CHARACTERIZATION OF THE KIIRUNAVAARA IRON ORE DEPOSIT FOR MINERAL PROCESSING WITH A FOCUS ON THE HIGH SILICA ORE TYPE B2

Kari Niiranen, M.Sc.

Chair of Mineral Processing

Department Mineral Resources and Petroleum Engineering

Montanuniversitaet Leoben, Austria

Affidavit:

I declare in lieu of oath, that I wrote this thesis and performed the associated research myself, using only literature cited in this volume.

Leoben, 20 October 2015

_____

Kari Niiranen, M.Sc.

ACKNOWLEDGEMENT

This thesis would not have been possible without support, supervision and encouragement from many friends and colleagues at LKAB in Sweden and at the Institute of Mineral Processing, Montanuniversitaet Leoben in Austria throughout the years. A huge amount work has been done during this study and many people have performed their best at LKAB to get new information about the Kiirunavaara iron ore deposit.

First of all, my sincerest thanks go to Dr. Andreas Böhm at the Institute of Mineral Processing, Montanuniversitaet Leoben, for your support. I'm deeply grateful for your time and interest in this study. Your excellence in mineral processing and guidance, your encouragement and immense knowledge during the research work made it possible for me to reach the target. Working with you was a true pleasure and I hope for a good cooperation also in the future.

Furthermore, I would like to thank Professor Dr. Helmut Flachberger and the staff, my colleagues, and friends at the Institute of Mineral Processing, Montanuniversitaet Leoben, for encouragement and for a nice time working together. During this study many international contacts, especially in Austria, could be established and they provided valuable input to various aspects of this work. I have encountered a very open mind which is much appreciated.

I especially acknowledge Dr. Andreas Fredriksson for you encouragement and support during this work and for reading and valuable comments on this thesis. I also want to thank Susanne Rostmark for interest and for allowing me the time to write this thesis. I would like to thank my colleagues Therése Lindberg, Charlotte Mattsby, David Alldén, and Dr. Henrikki Rutanen for your interest and the staff at LKAB's mineral processing laboratory in Malmberget to name but a few. Thanks also to all my colleagues at LKAB R&D who have always encouraged me during this work. Furthermore, I acknowledge Christopher Gordon for language checking and comments.

Last but not least I would like to thank Dr. Heinrich Mali at the Institute of Geology and Economic Geology, Montanuniversitaet Leoben, for interesting discussions, Sandra Haslinger for your help at the laboratory work in summer of 2010, and all my dear friends in Finland, Sweden, Austria and Germany for encouragement during these years.

KURZFASSUNG

Die Eisenerzlagerstätte am Kiirunavaara zeigt derzeit einen eher niedrigen SiO2-Gehalt (ca. 2,3 bis 3,3% SiO_2), aber es wird erwartet, dass er in den tieferen Teilen der Lagerstätte ansteigen wird. Im Jahr 2007 wurde ein Projekt „Silica in the Mine“ mit dem Ziel gestartet, ein vereinfachtes Verfahren im Labormaßstab in Bezug auf Aufbereitungseigenschaften zu entwickeln, um den Energieverbrauch und den SiO_2 Gehalt der Magnetit-Konzentrate und weitere aufbereitungstechnische Eigenschaften des Roherzes vorherzusagen.

Das erste Ziel dieser Studie war es, die Zerkleinerungs- und Aufbereitungstests, die im Ramen des Projekts „Silica in the Mine“ im Aufbereitungslabor von LKAB durchgeführt wurden, mit den Zerkleinerungs- und Aufbereitungstests im Labor des Lehrstuhls für Aufbereitung und Veredlung, Montanuniversität Leoben, zu vergleichen und zu ergänzen. Für diesen Zweck wurden drei ausgewählte Proben, die die Haupterztypen (B1, B2 und D) der Lagerstätte repräsentieren, nach der Methode der „Optimierten Zerkleinerungskette“ (OZK) zerkleinert. Daraus kann geschlossen werden, dass diese drei Erztypen einen Unterschied in ihrer Bruchcharakteristik aufweisen, was durch die Unterschiede in der Korngrößenverteilung der Zerkleinerungsprodukte sowie unterschiedlichen in dem maßspezifischen Energieverbrauch angezeigt wird. Eine wichtige Erkenntnis aus der Zerkleinerungstests im Labor des Lehrstuhls für Aufbereitung und Veredlung ist das untypische, korngrößenabhängige Zerkleinerungsverhalten. Dieses könnte mit der Textur des Magnetiterzes erklärt werden.

Da offensichtlich der Anteil des SiO_2-reichen Erztyps B2 in Zukunft zunehmen wird, wurden detaillierte Aufbereitungstests wurden für die prozessmineralogische Charakterisierung dieses Erztyps im Labor des Lehrstuhls für Aufbereitung und Veredlung im Sommer 2010 durchgeführt. Diese Tests kombinierten geologische, mineralogische und geochemische Daten mit aufbereitungstechnischen Eigenschaften wie Energieverbrauch, Korngrößenverteilung, Aufschlussgrad und Verwachsungen. Ein wesentlicher Teil dieser Studie waren die mineralogischen Untersuchungen mittels automatisierter Mineralogie (QEMSCAN®), um die modale Mineralogie, die Verteilung der Silikaten in den verschiedenen Korngrößenklassen nach der Zerkleinerung, die Verteilung von Silizium (Si) zwischen verschiedenen Silikaten sowie Aufschlussgrad und Verwachsungen von Magnetit und Silikaten zu untersuchen. Ein wichtiges Ergebnis dieser Studie war die Entdeckung von zwei Subtypen im Erztyp B2, die sich durch das Auftreten von Aktinolith im Subtyp B2-a unterscheiden. Das wird als Ursache für die unterschiedliche Mahlbarkeit (d.h. Bruchcharakteristik) dieser beiden Subtypen angesehen.

SCLAGWORTE: Aufbereitung, Aufschlussgrad, Davis Rohrscheider, QEMSCAN, automatisierte Mineralogie, Magnetit, Aktinolith, LKAB, Kiirunavaara

ABSTRACT

The Kiirunavaara iron ore deposit shows a rather low content of silica (ca. 2.3 to 3.3% SiO_2) but the silica grade is expected to increase in the deeper parts of the deposit. A project called "Silica in the Mine" was started in 2007 with the target to develop a simplified method in laboratory scale to predict the energy consumption and SiO2 grade in the magnetite concentrate at the industrial scale and further predict the physical properties of the crude ore with respect to mineral processing characteristics.

The first target of this study was to control and compare the comminution and mineral processing tests in relation to the "Silica in the Mine" project carried out at LKAB's mineral processing laboratory to the comminution and mineral processing tests at the laboratory of the Institute of Mineral Processing, Montanuniversitatet Leoben. For the purpose of this study, three samples were selected representing three main ore types (B1, B2, D) of the Kiirunavaara iron ore deposit. They were first were first ground according to the "Optimized Comminution Sequence" (OCS) method. It can be concluded that these three samples, representing different ore types, show a difference in their breakage behavior based on the ore characterization data defined by the differences in the particle size distribution within comminution products, as well as in differences in the mass-specific energy consumption. It is significant to note based on the information from the comminution test that there might be a deviant breakage characteristic in relation to the iron ore from the Kiirunavaara deposit, which can be explained can be explained with the crystal structure of magnetite. Furthermore, a separation with Davis magnetic tube was a crucial part of the mineral processing test to study the liberation of magnetite and silicates.

As it was evident that the amount of the high-SiO_2 ore type B2 increases, detailed mineral processing tests were carried out for process mineralogical characterization of this ore type at the laboratory of the Institute of Mineral Processing in summer of 2010. These tests combined geological, mineralogical, and geochemical information with mineralogical processing characteristics such as energy consumption, particle size distribution, and liberation and intergrowths. The essential part of this study was the mineralogical investigations using automated mineralogy (QEMSCAN®) to study the modal mineralogy, the distribution of silicates in the different particle size classes after comminution, the deportment of silicon (Si) between various silicates and degree of liberation and intergrowth of magnetite and silicates. An important result of this study was the discovery of two separate subtypes within ore type B2 based on the occur of actinolite in the subtype B2-a. This can be considered as the cause of the difference in grindability (i.e., characteristic) of these two subtypes.

KEYWORDS: mineral processing, liberation analysis, Davis magnetic tube, QEMSCAN, automated mineralogy, magnetite, actinolite, LKAB, Kiirunavaara.

ACKNOWLEDGEMENT

KURZFASSUNG

ABSTRACT

1. INTRODUCTION ... 1

1.1 Background ... 1

1.2 Previous studies ... 2

1.2.1 Mineral processing model for the Leveäniemi open pit ... 2

1.2.2 Comparing the comminution at laboratory scale to pilot and large scale ... 4

2. OBJECTIVES ... 4

3. THE KIIRUNAVAARA IRON ORE DEPOSIT ... 6

3.1 Geology and mineralogy ... 6

3.2 Ore types ... 8

3.2.1 Preface ... 8

3.2.2 Ore type B1 ... 8

3.2.3 Ore type B2 ... 9

3.2.5 Ore types D1, D3 and D5 ... 10

3.3 SiO_2-bearing minerals ... 11

3.3.1 Preface ... 11

3.3.2 Actinolite $Ca_2(Mg,Fe)_5SiO_8O_{22}(OH,F,Cl)_2$ ... 12

3.3.3 Phlogopite $KMg_3(Si_3Al)O_{10}(F,OH)_2$ ... 13

3.3.4 Chlorite $(Mg,Al,Fe)_{12}[(Si,Al)_8O_{22}](OH)_{16}$ ... 15

3.3.5 Titanite $CaTiSiO_5$ ... 16

3.3.6 Quartz SiO_2 ... 16

3.3.7 Alkali Feldspar (Albit $Na[AlSi_3O_8]$ and K-Feldspar $K[AlSi_3O_8]$) ... 17

3.3.8 Talc $Mg_6[Si_6O_{20}](OH)_4$ ... 18

4. COMMINUTION TESTS ... 18

4.1 Sampling ... 18

4.2 Optimized Comminution Sequence (OCS) ... 20

4.2.1 Samples ... 20

4.2.2 Optimized Comminution Sequence (OCS) ... 20

4.2.3 Comminution tests ... 21

4.2.3.1 Laboratory rod mill ... 21

4.2.3.2 Laboratory ball mill ... 23

4.3. Comminution in an open circuit ... 24

4.3.1 Samples ... 24

4.3.2 Comminution tests for characterization of ore type B2 ... 24

4.3.2.1 Laboratory rod mill ... 24

4.3.2.2 Laboratory ball mill 25
4.4 Comminution tests related to the "Silica in the Mine" project 25
5. MINERAL PROCESSING TESTS 27
5.1 Separation with Davis magnetic tube 27
5.1.1 Preface 27
5.1.2 Davis magnetic tube tests at the laboratory of the Institute of Mineral Processing 29
5.1.3 Davis magnetic tube tests for characterization of ore type B2 30
5.1.4 "Silica in the Mine" project 30
5.2 Specific gravity 31
5.2.1 Determination of specific gravity with He-gas Pycnometer 31
5.2.3 Determination of specific gravity at the laboratory of the Institute of Mineral Processing 33
5.2.4 "Silica in the Mine" project 33
5.3 Specific surface area 34
5.3.1 Preface 34
5.3.2 Determination of specific surface area with Blaine method and Permaran 34
5.3.3 Svensson's method related to the "Silica in the Mine" project 36
5.4 Chemical analysis 36
5.5 Additional mineral processing tests 38
5.5.1 Laser diffraction 38
5.5.2 Satmagan test 38
6. DETERMINATION OF THE DISPERSITY OF THE COMMINUTION PRODUCTS 40
6.1 Particle size distribution 40
6.1.1 Preface 40
6.1.2 Screen analysis 40
6.1.3 Comparative comminution tests at the laboratory of the Institute of Mineral Processing ... 41
6.1.4 Particle size distribution of ore type B2 43
6.1.3 Particle size distribution related to "Silica in the Mine" project 44
6.2 Particle size distribution below 125 μm 47
6.3 Specific surface area, shape factor and P_{80} values 48
6.3.1 Specific surface area 48
6.3.1.1 Comparative tests at the laboratory of the Institute of Mineral Processing 48
6.3.1.2 Specific surface of samples for characterization of ore type B2 49
6.3.2 Shape factor 50
6.3.3 P_{80} values 51
6.3.3.1 P_{80} values for comminution products at the laboratory of the Institute of Mineral Processing 51
6.3.3.2 P_{80} values related to characterization of ore type B2 52
6.3.3.3 P_{80} values related to the "Silica in the Mine" project 53

7. ENERGY CONSUMPTION 54
7.1 Optimized Comminution Sequence (OCS) 54
7.1.1 Preface 54
7.1.2 Energy consumption (laboratory rod mill) 56
7.1.3 Energy consumption (laboratory ball mill) 59
7.1.4 Mass specific energy consumption 60
7.1.5 Rittinger coefficient 61
7.1.6 Energy register diagrams 61
7.2 Energy consumption in open comminution circuit used for characterization of ore type B2 63
7.2.1 Energy consumption (laboratory rod mill) 63
7.2.2 Energy consumption (laboratory ball mill) 64
7.2.4 Correlation between mass specific energy consumption and P_{80} 67
7.3 Energy consumption related to the "Silica in the Mine" project 69
7.3.1 Preface 69
7.3.2 Principle of the estimation of the energy consumption 70
7.3.3 Estimation of the energy consumption for selected samples 72
8. MINERALOGICAL CHARACTERIZATION OF ORE TYPE B2 75
8.1 Automated mineralogy 75
8.1.1 Optical microscopy versus automated mineralogy 75
8.1.2. Principle of the automated systems for mineralogical characterization 76
8.1.3 QEMSCAN® Analysis 77
8.1.4 Mineralogical investigations at LKAB's metallurgical laboratory 78
8.1.5 EMPA analysis on SiO_2-bearing minerals 80
8.1.6 Assay reconciliation 81
8.1.7 Identification of magnetite and hematite 83
8.2 Modal mineralogy 84
8.3 Modal mineralogy of silicates 85
8.4 Distribution of SiO_2-bearing minerals 86
8.5 Deportment of silicon (Si) 90
9. LIBERATION ANALYSIS 93
9.1 Preface 93
9.2 Intergrowths of magnetite 94
9.2.1 intergrowths of magnetite and gangue mineral 94
9.2.2 Intergrowth of magnetite with silicate minerals 98
9.3 Liberation analysis based on the Henry-Reinhardt charts 100
9.3.1 Principle of the Henry-Reinhardt charts 100
9.3.2. Construction of the Henry-Reinhardt chart 102

9.3.3 Henry-Reinhardt charts for samples 6382 (B1), 6365 (B2), and 6354 (D3) 103
9.3.4 Henry-Reinhardt charts for ore type B2 107
9.4 Liberation analysis with QEMSCAN 110
9.5 Separation of magnetite and silicates 114
10. PREDICTION OF SiO_2 GRADE FROM LABORATY SCALE TO INDUSTRIAL SCALE 117
10.1 Estimation of SiO_2 at P_{80} = 45 μm at the laboratory scale 117
10.2 Comparison of SiO_2 grade between laboratory scale and industrial scale 119
10.3 Function for estimation of SiO_2 grade from the laboratory scale to industrial scale 120
10.4 SiO_2 grade at industrial scale 122
11. DISCUSSION AND CONCLUSIONS 127
REFERENCES
LIST OF FIGURES
LIST OF TABLES
APPENDICES

1. INTRODUCTION

1.1 Background

LKAB (Luossavaara-Kiirunavaara AB) is operating an underground iron ore mine, three beneficiation plants (KA1, KA2 and KA3) and three pelletizing plants (KK2, KK3 and KK4) in Kiruna, Sweden. Methods of mineral processing at LKAB are comprised of a sequence of two-stage comminution, WLIMS (*Wet Low Intensity Magnetic Separation*) and reversed apatite flotation, in which magnetic separation is regarded as the crucial part of silicate mineral separation from the ore. The aim of this process is to liberate and free the ore of phosphorous (apatite) and silica (silicate minerals) as far as possible (Adolfsson 2008, Adolfsson & Fredriksson 2011).

In the spring of 2007, the variations were observed in SiO_2 grade in the crude ore. The increasing silica grade in the crude ore might be demanding, especially with respect to production of direct reduction pellets (LKAB DR Oxide Pellets, LKAB 2014), which is one of the main products of LKAB in Kiruna. DR Pellets show an average silica grade under 0.75% SiO_2 (Fe grade 67.9% and P grade 0.025%). The high-grade iron ore deposit of Kiirunavaara has today a rather low grade of silica *in situ*, -approximately 2.3 to 3.3% SiO_2 (estimated from the geological block model, LKAB). However, the silica grade is expected to increase and the phosphorous level to decrease in incoming material to the cobbing plant in Kiruna in the future based on information from the 3D resource model generated from exploration and grade control drilling (Fig. 1).

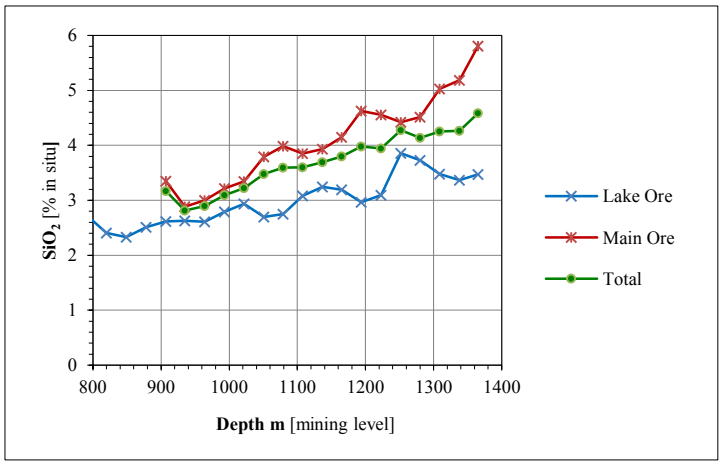

Figure 1. SiO_2 (in situ) estimated from the resource block model for the Kiirunavaara mine (LKAB). x-axis corresponds the mining level (z) in the coordinate system used in the mine.

The silicates are only SiO_2-bearing minerals in the Kiirunavaara iron ore deposit. It can be assumed that the mineralogy of silicates and the SiO_2 grade in the crude ore undoubtedly impact the SiO_2 grade in the final product; i.e., the iron ore pellets and/or the iron ore fines. In addition, mineral processing parameters, such as the breakage characteristics, the specific energy consumption and the liberation of magnetite and silicate minerals, are essential for understanding the processes at the beneficiation plants

in Kiruna. This is especially pertinent to the high-silica ore type B2. The whole production chain from the mine to mill and to product is being observed in several projects during an ongoing study "Silica in the Mine", which is an important area of the research and development at LKAB (Adolfsson 2008, Quinteiro 2008, Drugge 2009, Adolfsson & Fredriksson 2011). The ongoing "Silica in the Mine" project in the Kiirunavaara mine is an essential part of this study (Niiranen & Fredriksson 2012, Niiranen & Böhm 2013).

As additional information can be noted that the present mining levels (Fig.1) are at 820 m and 849 m in the northern part of the ore body (known as Lake Ore, located north of Y1400 in the local coordinate system used in the mine) and on the level of 993 m and 1022 m in the middle and southern part of the ore body (known as Main Ore, located south of Y1400). The local coordinate system, used in the mine, has Y-values increasing to the south, X-values increasing to the east and the Z-values increasing to the depth from a reference level of 0 m located on the former top of the Kiirunavaara Mountain.

1.2 Previous studies

1.2.1 Mineral processing model for the Leveäniemi open pit

It should be noted, in fact, that the ideas of "mine to mill" and "minerals to product" are nothing entirely new at LKAB (Fagerberg & Ornstein 1962, Bergström & Anttila 1973, Niiranen & Fredriksson 2014). In this context, it is worth highlighting two early projects, which have been carried out to create a connection between test results from the laboratory scale to the larger-scale beneficiation process. As an early example, from 1962, a systematic macroscopic examination of drill cores was made in order to produce a rough, preliminary forecast for the product outcome of beneficiation of the Leveäniemi iron ore deposit (Fagerberg & Ornstein 1962). The Leveäniemi mine ran from 1964 until 1983, when operations were discontinued due to an economic downturn. The Leveäniemi open pit has been reactivated as one of three new mines that are planned to open in Svappavaara in 2015 (Fig. 2).

Figure 2. Former Leveäniemi open pit after it has been emptied of water in 2014 (Photo: LKAB).

The background for the idea was to create a 3D model for ore recovery in the process at the beneficiation plant in Svappavaara as a part of the feasibility study on the Leveäniemi deposit. The model was planned to be based on data from systematically core logging for processing parameters and the preliminary beneficiation tests. Each drill core had previously been prepared by an inventory protocol, which included identification data, chemical assays, and section boundaries for the proposed mining pallets (Fig. 3).

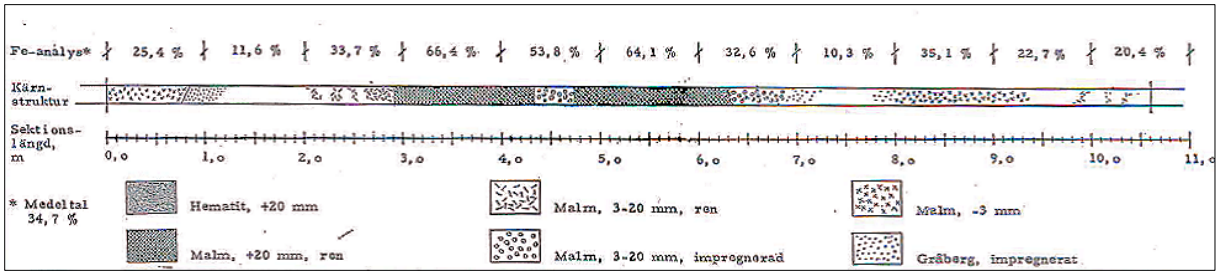

Figure 3. Identification protocol on a drill core containing chemical assays of iron (Fe-analys), ore type and structure (Kärnstruktur) and section boundaries for the proposed mining pallets (Sektionslängd). Hematit = hematite; Malm = ore; Gråberg = waste (Fagerberg & Ornstein 1962).

Each core section was examined on the mineralogy and texture for the mineral processing properties, whereupon the probable product outcome for a concentrator flow sheet was estimated and recorded. The particular interest of the study was the possible variations in ore texture and/or the relationship between different ore qualities in the horizontal or vertical direction, which could lead to the changing of the product outcome from year to year. In addition, a mining block (10 x 10 x 10 m^3) will be placed around each drill hole per mining level and the mineral processing properties based on the information from drill cores should apply to the entire block (Fig. 4). Then, the product outcome could has been easily calculated through summation of benches and profiles, respectively, and the variation in different parts of the ore body could easily be examined. From this model, it would have conceivably been possible to estimate the average recovery and to study its variation in different parts of the deposit (Fagerberg & Ornstein 1962). But it is obvious that more objective and analytical data is required to build a predictive model for processing parameters.

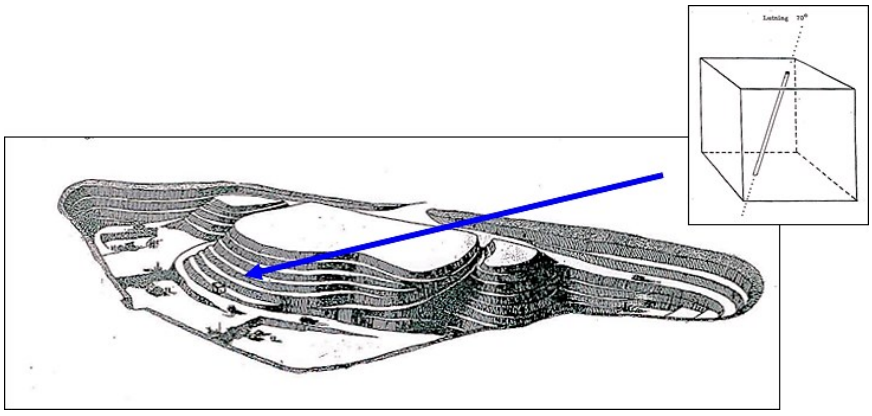

Figure 4. Schematic picture combing of the mining lay out and a mining block containing mineral processing parameters for the Leveäniemi open pit (Fagerberg & Ornstein 1962).

1.2.2 Comparing the comminution at laboratory scale to pilot and large scale

Bergström and Anttila (1973) carried out comminution tests in an open comminution system to compare the results of grinding with rod mill, ball mill, and pebble mill with waste pebbles. Further, their target was to determine the efficiency of the mills, the energy consumption and conversion ratio at the laboratory scale, and pilot scale and industrial scale (beneficiation plant) based on these tests. Their work included experiments in three different methods to determine the grinding capacity of mills, which was divided into three subsections: estimation according to empirically developed formula, braking test, and comminution experiment. Furthermore, their work is basis to estimate the energy consumption from the laboratory scale to the industrial scale and will be describe in detail in Chapter 7.3.

2. OBJECTIVES

The understanding the Kiirunavaara iron ore deposit from both a mineralogical and geochemical perspective, and not least, from a mineral processing perspective is increasingly important as the production in the mine is advancing toward deeper levels with higher concentrations of silica-rich ore. This will result in new challenges and requirements for production at LKAB. The reliable, sufficient and enough detailed information about the mineralogy, modal mineralogy, geological context and texture of an ore and further the entire deposit is a fundamental key to understanding its potential amenability to the beneficiation process. Equally important are the mineral processing parameters such as particle size distribution, composition of particles, liberation analysis (liberation, middlings, locked), and flotation behavior of particles as they pass through a circuit from mine to mill and further into concentrate consisting one or more of following stages blasting, crushing, grinding and flotation (Henley 1983, Butcher 2010).

To overcome the problem with the periods of high SiO_2 grade and fluctuations on SiO_2 grade in the crude ore as described in Chapter 1, the “Silica in the Mine” project was started in the autumn of 2007. Furthermore, it can be regarded as a pilot project to create and test a simplified methodology for similar projects related to exploiting of new iron ore deposits in the future. In the past, there have been several projects at LKAB, which have examined the impact of mineralogical and chemical characteristic of the crude ore, and, in particular, the effect of mineral composition on mineralogy and chemistry on magnetite concentrate after the beneficiation process. These investigations have had a focus, above all, on phosphorous and alkali grade in the magnetite concentrate, but there have also been some investigations that focused on silica (Adolfsson 1995, Adolfsson 1996, Andréasson 1997, Knights 2001, Moen 2007, Adolfsson 2008, Ståhlström 2008). However, the “Silica in the Mine” project, in which a systematic sampling from drill cores covers the entire deposit and the number of samples is significant, is the first project with a main focus on silica (SiO_2).

The first issue of the "Silica in the Mine" project involved the characterization and identification of the problem related to SiO_2 and to find out, if possible, the reason for the fluctuation of SiO_2 grade and especially periods of high SiO_2 grade in the crude ore. The second issue of this project was development of a comprehensive sampling methodology and a simplified methodology for mineral processing tests at the laboratory scale (Appendix 1) for predicting the physical and chemical properties of the ore (Adolfsson 1996, Adolfsson 2008, Drugge 2009, Drugge 2010, Niiranen & Böhm 2012). Further, both raw data from the tests and estimated processing parameters for characterization of the ore and different ore types will be stored in the ORACLE database to be implemented into the geological 3D model (resource model). However, the model has to be modified based on test results from process mineralogical investigations.

The first target of this study is to complete and compare the mineral processing tests, which were carried out in relation to the "Silica in the Mine" project carried out at LKAB's mineral processing laboratory to the mineral processing tests at the laboratory of the Institute of Mineral Processing, Montanuniversitaet Leoben under the guidance of Dr Andreas Böhm. After the completed comminution tests according to the "Optimized Comminution Sequence" (OCS) method, the screen analysis and the determination of specific surface were carried out on the resulting comminution products. The net energy consumption and the specific surface area of selected particle size classes of the comminution product were measured at each stage as well as the particle size distribution of the feed and the comminution product to provide the data to construct the energy-register diagram. The results of these comparative mineral processing tests are presented in this study

Furthermore, the liberation analysis and the magnetic separation with the Davis magnetic tube were an essential part of this study. The results will be presented as Henry-Reinhardt charts, which can be regarded as a graphic combination of the mineralogical or chemical information and separability or physical parameters. The Henry-Reinhardt chart also provides information on the best possible separation result at a given physical property setting, as well as the intergrowth characteristics (liberation). In addition, the chemical analyses were also carried out on the feed and the comminution products..

As it was evident that the amount of the high-silica ore type B2 increases in the deeper part of the deposit and silicates are the most significant gangue minerals of this ore type, detailed mineral processing tests were carried out for process mineralogical characterization of the high-SiO_2 ore type B2 at the laboratory of the Institute of Mineral Processing in summer of 2010. A laboratory scale methodology was developed for the systematic characterization of ore type B2 for mineral processing (Appendix 2). This methodology is combining geological (ore type), mineralogical (mineralogy of silicates, modal mineralogy), geochemical (mineral chemistry, distribution of elements), and process mineralogical (energy consumption, liberation, intergrowths, simulation of SiO_2 grade in concentrate) characteristics. The crucial part of the characterization of ore type B2 for mineral processing was the investigations on

the intergrowths and liberation of magnetite and silicates. For the liberation analysis, not only the magnetic separation with the Davis magnetic tube was used, but also automated mineralogy (*QEMSCAN*®) was used to analyze the degree of liberation and intergrowth of magnetite and silicates. The focus of these investigation, which were carried out at LKAB's metallurgical laboratory in Luleå, was on the modal mineralogy, the distribution of silicates in the different particle size classes after comminution, and the deportment of silicon (Si) between various silicates.

3. THE KIIRUNAVAARA IRON ORE DEPOSIT

3.1 Geology and mineralogy

Kiruna is the type area for the iron ore deposits with iron oxide (magnetite and hematite) and apatite as the main minerals first named the style of mineralization as "Kiruna type" by Geijer (1910, 1931). Approximately 40 iron ore deposits of this type are known in Northern Sweden and individual deposits show an average grade of iron and phosphorous varying between 30 and 70% Fe, and 0.05 and 5% P respectively (Bergman et al. 2001). The Kiirunavaara deposit is the largest and the best known example of this type. The deposit is a high grade iron ore deposit consisting mainly of magnetite and apatite with an average grade of 63.8% Fe, and 0.4% P (estimated from the 3D resource model, LKAB) and with varying, but mostly small amounts of gangue minerals. The Kiruna-type iron ore deposits have geochemically been distinguished from magmatic and sedimentary types of iron ores by their generally low content of titanium (0.04–0.31% Ti) and their high content of vanadium (317–2310 ppm V) (Loberg & Horndahl 1983). Hematite is only locally encountered and is mainly developed as a secondary product along grain boundaries and fractures in magnetite ore. Meanwhile there is a larger body of hematite-magnetite ore (martite) reported in the northern most part of the ore body containing about 2.4 M tons martite ore, which is so far without any economic value (Hansson 2001, Rutanen 2012, Wartbichler 2014).

The Kiirunavaara iron ore deposit is a sheet like body, north to south striking and approximately 4 km to 4.5 km long and 50 to 100 m thick with a maximum thickness of over 200 m in the northern part (Fig. 5). The ore body is well known down to a depth of -1365 m below the surface, but it extends at least down to the depth of -1800 m level below the surface in the northern part of the deposit.

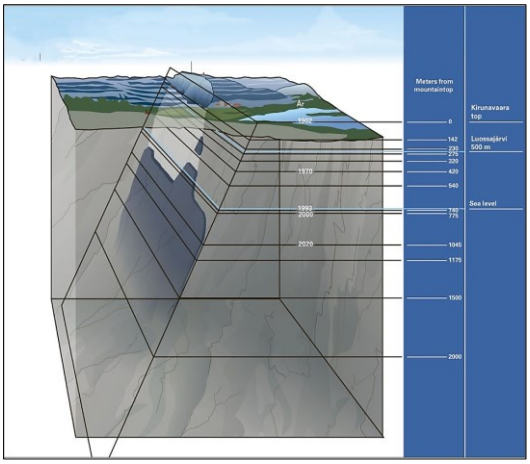

Figure 5. Schematic picture of the Kiirunavaara orebody, seen from north (Picture: LKAB).

This high grade iron ore deposit was probably formed as an intrusive sill (Pehrdal 1994; Martinsson 2004) and the geochronologic data for the Kiirunavaara and the Luossavaara deposits indicates the emplacement at the period between ca. 1880 Ma and 1900 Ma (Cliff et al. 1990, Romer et al. 1994). Younger ages of 1624 ± 39 Ma (Westhues et al. 2013) and 1638 ± 39 Ma (Aupers 2014) probably represent a secondary hydrothermal overprint.

Magnetite (Fe_3O_4) is as of today the only ore mineral of economic value in the Kiirunavaara deposit. The composition of the most important minerals in the deposit, magnetite and apatite, has been studied in several occasions from the economic point of view. Apatite might be economically interesting as a possible source for phosphorous in the future (Pålsson & Fredriksson 2012), but also because it consists REEs (Frietsch & Pehrdahl 1995, Martinsson et al. 2012). A body of martite (hematite-magnetite) ore has recently been discovered in the northern part of the deposit as mentioned above but so far, the martite mineralization is not considered to be economic.

In this context, only a few previous studies have been carried out to characterize the gangue mineralogy of the Kiiirunavaara iron ore deposit in recent years (Jarousseau & Pålsson 2000, Andréasson 1997, Knights 2001). Most of these mineralogical investigations are focused on REE and apatite (Smith et al. 2009, Martinsson 2011, Pålsson & Fredriksson 2012, Martinsson et al. 2012). Besides apatite, green minerals of the amphibole group, mostly actinolite, are the most common gangue minerals described in the deposit. Phlogopite, titanite, ilmenite, rutile, quartz, talc, albite and Ca-sulphates (mostly anhydrite and occasionally gypsum) may occur, but commonly in lesser quantities as well as carbonates (calcite, Fe-dolomite and ankerite) and sulfide minerals (mostly pyrite and chalcopyrite) (Niiranen 2012 b, Nordstrand 2012, Aupers 2014).

3.2 Ore types

3.2.1 Preface

The apatite-magnetite ore in the Kiirunavaara deposit is divided into two main types (low phosphorous ore and high phosphorous ore) from the practical and also the historical point of view (Geijer 1931). The low phosphorous ore is further divided into two subtypes: ore type B1 (low phosphorous, low silica,) and ore type B2 (low phosphorous, high silica). The high phosphorous ore, ore type D, is divided into three different subtypes based on phosphorous grade (Table 1).

Table 1. Limit values, % Fe and % P, for different ore types of the Kiirunavaara deposit (Niiranen 2006, Niiranen & Fredriksson 2012) and mean values for SiO_2 estimated from the Oracle database (LKAB).

ORE TYPE	Fe%	P%	$\overline{X}$ SiO_2%
B1 (low P, low SiO_2)	> 66	< 0.1	1.8
B2 (low P, high SiO_2)	> 50	< 0.1	5.6
D1 (high P)	> 50	0.1 – 0.8	4.3
D3 (high P)	> 50	0.8 – 2.2	1.2
D5 (high P)	> 50	> 2.2	1.0

However, SiO_2 grade is not taken into account in this classification. Also displayed in the Table 1, the mean values for SiO_2 grade in the different ore types are estimated from the assays on drill cores stored in the Oracle database by LKAB. These limit values are used when the drill core data with analysed sections is visualized in MicroStation using a software (GeoCad) developed by Propak AB. But by the reporting of drill cores from exploration and grade control drilling and mapping of geology underground, these different ore types are used based on the macroscopic mineralogy of the ore. The difference between ore types based on the mineralogy will also be described in more detail in this chapter.

Until 2009, the these different ore types were mined separately in the Kiirunavaara mine using a mining method called large-scale sublevel caving (Wimmer & Niiranen 2005, Wimmer 2012, Niiranen 2012 a). However, because of the increasing production of the crude ore from 22.3 M tons (in 2000) to 28.4 M tons (in 2014), different ore types are now mixed together by mining and only one type of crude ore is hauled (Niiranen 2012 a).

3.2.2 Ore type B1

The typical appearance of this ore type is massive, dark greyish, and very homogeneous, most often containing ca. 95 area-% of magnetite. Because of the high grade of magnetite, the density is also high (ca. 5 g/cm^3). The grain size of magnetite seems to be significantly less than 1 mm. Usually, gangue minerals show a grain size larger than the fine-grained magnetite (Fig. 6). The most common gangue mineral of the ore type B1 that closely associated with magnetite is mica (phlogopite), which sometimes shows retrograde reaction to chlorite (Nordstrand 2012, Aupers 2014). Other gangue minerals associated with magnetite are titanite, quartz, minerals of the amphibole group (mostly actinolite), ilmenite, rutile,

carbonates and, locally, Ca-sulphates. Hematite is a minor component and occurs most often as needle-shaped crystals forming in fracture-related veinlets (Nordstrand 2012, Aupers 2014).

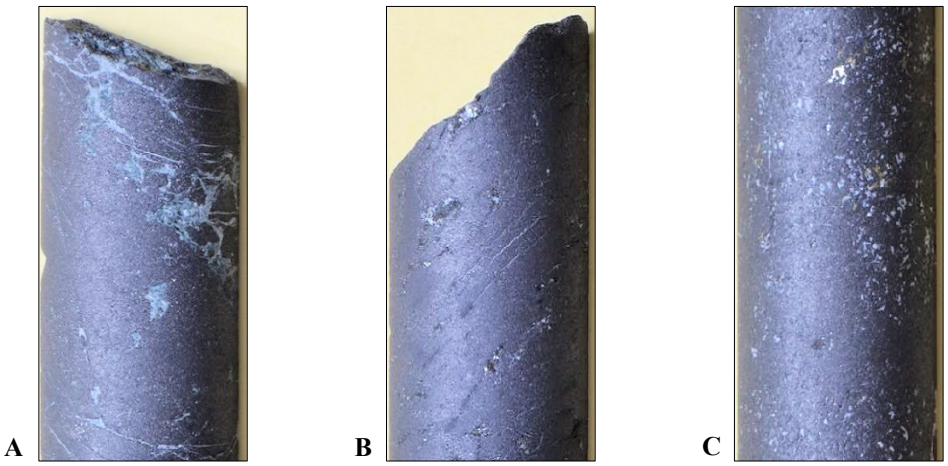

Figure 6. Ore type B1 (drill core ø ca. 29 mm). (A) Sample 6127: some veinlets of gangue minerals (actinolite, talc) cutting the ore; (B) Sample 6524: some very fine cracks filled by carbonate minerals cutting the ore; (C) Sample 6139: fine-grained calcite, phlogopite, titanite and sulphides between magnetite crystals (Photo: K. Aupers).

Actinolite is typically coarse-grained (> 500 µm), and phlogopite , talc and quartz are closely associated with it (Fig. 6 A). The intergrowth of titanite and magnetite is characteristic for this ore type, and titanite often grows along the edges of magnetite. Another Ti-bearing mineral typical for this ore type is ilmenite which often occurs as fine inclusions in magnetite (Niiranen 2012 a, Nordstrand 2012, Aupers 2014).

3.2.3 Ore type B2

This problem with silicates in the crude ore and also with high SiO_2 grade appears to be linked, above all, to ore type B2 (high-silica ore) (Niiranen 2012 a, Niiranen & Böhm 2013, Aupers 2014). The ore type B2 is characterized by magnetite associated with green-coloured amphibole minerals, mostly actinolite (Fig. 7). The appearance of the ore type B2 is more heterogeneous, and its density is generally lower compared to the ore type B1. This is highly dependent on the amount and distribution of silicate minerals. Locally, gangue minerals have a grain size of ca. 1 mm, while magnetite does not differ in grain size compared to the ore type B1 (Niiranen 2012 a, Aupers 2014).

The most significant SiO_2-bearing minerals in the ore type B2 are actinolite, phlogopite, chlorite, titanite and in some cases also quartz. In some cases, talc and feldspar, mostly albite but also K-feldspar, can be of importance. Zircon, allanite and thorite, which were identified in only a few cases, are uncommon. In particular, actinolite, phlogopite and titanite, and in some cases also quartz, chlorite and albite are of importance because they are the main sources of SiO_2 in the crude ore. Besides ilmenite, titanite is also an important source of TiO_2, especially in the ore type B2 (Niiranen 2012 b, Niiranen 2014, Aupers 2014). The mineralogy of ore type B2 will be described in detail in Chapter 8 based on information obtained by automated mineralogy.

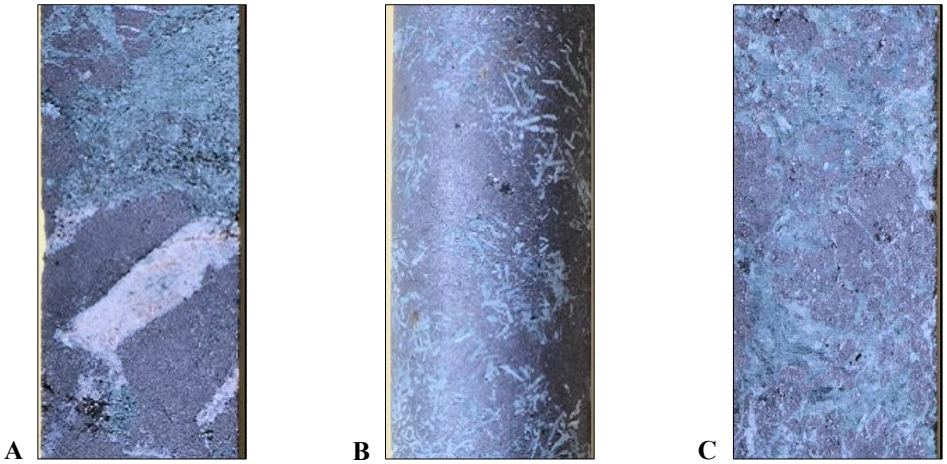

Figure 7. Ore type B2 (drill core ø ca. 29 mm). (A) Sample 6200: coarse-grained, green actinolite brecciates magnetite. (B) Sample 6196: euhedral actinolite as finely disseminated in the magnetite ore. (C) 6245: stockwork-like appearance of silicate minerals, mostly green actinolite (Photo: K. Aupers).

3.2.5 Ore types D1, D3 and D5

High phoshorous ore type D is divided into three subtypes, D1, D3, and D5 (Fig. 8), based on their phosphorous grade (Table 1), of which subtype D3 can be regarded as the most common. In the deeper parts of the ore body, ore type D occurs only in the northern-most part (Lake Ore), and the amount of this ore type decrases as the depth increases (Niiranen & Fredriksson 2012, Niiranen & Böhm 2012).

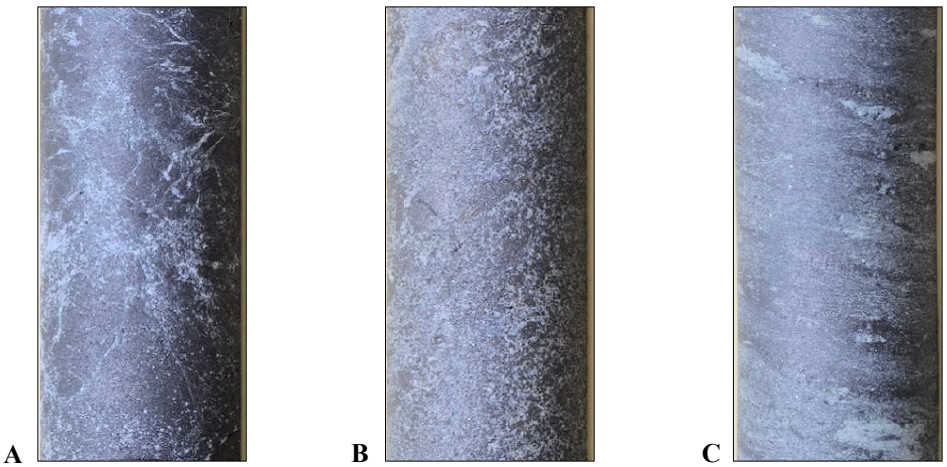

Figure 8. Ore type D (drill core ø ca. 29 mm). (A) Sample 6287: subtype D1, fine veinlets of apatite associated with calcite in magnetite, creating a network-like structure. (B) Sample 6453: subtype D3, high amounts of apatite associated with magnetite. (C) Sample 6138: subtype D5, "schlieren"-like structure of apatite-rich layers and greenish minerals (actinolite?) described by Geijer (1910) (Photo: K. Aupers).

The ore type D usually contains large amount of apatite with a grain size most often similar to magnetite. Structures and textures (e.g., brecciated magnetite, gangue mineralogy) observed in the ore type D, are locally similar to those in the low phosphorous ore types B1 and B2. Apatite is a characteristic gangue, with varying amounts dependent on the subtype. For example, apatite content varies between 12 and 20 wt.% in the samples presenting the subtype D3. Apatite is often euhedral and grain size varies between

a tenth to a hundredth microns. “Ghost structure” is one very characteristic structure in ore type D in the Kiirunavaara deposit. It is defined as thin, whitish bands that consist of a tight intergrowth of magnetite and apatite (Aupers 2014). Besides apatite, monazite is other P-bearing mineral in this ore type (Martinsson 2011, Pålsson & Fredriksson 2012, Martinsson et al. 2012). Gangue minerals like amphibole, phlogopite, talc and carbonates are also common in various amounts. In general, the mineralogy is similar to the subtypes of ore type D.

3.3 SiO_2-bearing minerals

3.3.1 Preface

Recently, even the silicates in the Kiirunavaara iron ore deposit have been a target of mineralogical investigations (Niiranen 2012 b, Nordstrand 2012, Aupers 2014). Not least because of their increasing importance for mineral processing, when the SiO_2 grade *in situ* increases in the deeper part of the deposit, which has a direct connection to the amount of silicates in the crude ore (Adolfsson 2008, Adolfsson & Fredriksson 2011, Niiranen & Böhm 2013).

For this study 24 polished thin sections were produced from the provided drill core samples (6252, 6351, 6363, 6367, 6370, 6387) at the laboratory of GeoPräp in Austria. The polished thin sections were investigated with a regular petrographic polarizing microscope (*Nikon Eclipse E600*) using both reflected and transmitted light sources, in both unpolarized and polarized states at LKAB’s mineral processing laboratory. Special attention was paid on the identification of different minerals and especially the identification of silicates. As support for mineral identification several volumes of Rock Forming Minerals by Deer, Zussman & Howie (edit.) were used.

The most significant SiO_2-bearing minerals, especially in ore type B2, are actinolite, phlogopite, chlorite, titanite and quartz. Besides ilmenite, titanite is also an important source of TiO_2, especially in ore type B2 (Niiranen 2014, Aupers 2014). In some cases, talc and feldspar, mostly albite but also K-feldspar, can be of importance. Zircon, allanite and thorite, which were identified in only a few cases, are uncommon. Besides the minerals mentioned above, some clay minerals, andradite (Fe-Garnet) and stilbite have been described, but they occur very rarely. In this chapter the mineralogy of the essential silicate minerals and quartz will be described in detail. In particular, actinolite, phlogopite and titanite will be looked on in detail, because they are the main source of SiO_2 in the crude ore, in some cases also quartz, chlorite and albite are of significance. Furthermore, talc can also be an important source of SiO_2 in the crude ore. Other minerals containing SiO_2 such as potassium feldspar, allanite, thorite and zircon, are uncommon and occur very sporadically.

3.3.2 Actinolite $Ca_2(Mg,Fe)_5SiO_8O_{22}(OH,F,Cl)_2$

The minerals of the amphibole group are by far the most abundant silicate minerals in the Kiirunavaara deposit (Geijer 1910, Knights 2007, Niiranen 2012 b, Nordstrand 2012, Aupers 2014) and characteristic for ore type B2 (low-P, high-SiO_2 ore), but they can be found in a wide range of mineral associations in different ore types (Nordstrand 2012, Aupers 2014). However, the minerals of the amphibole group seem to be less abundant in the most iron-rich parts of the deposit (Aupers 2014).

Actinolite can occur at least in two different textural forms. A part of it occurs as large coarse crystals which are partly euhedral, partly subhedral. They are often arranged in a flow-like patterns in brecciated magnetite ore (Fig. 9 A), but it can also occur as large needle-like crystals in the magnetite matrix (Fig. 9 B). The second type is probably a pseudomorph of pyroxene (clinopyroxene) resulting from metamorphism and alteration of the ore (Deer et al. 1997). Most actinolite of the latter type contains magnetite as fine inclusions (Fig. 4 B), which is expected to be an important texture when considering the liberation of magnetite and the magnetic separation with LIMS (*Low Intensity Magnetic Separation*) at the beneficiation plants in Kiruna. It can also be noted that very fine-grained titanite can sometimes be found at the edges of actinolite crystals at contacts with magnetite.

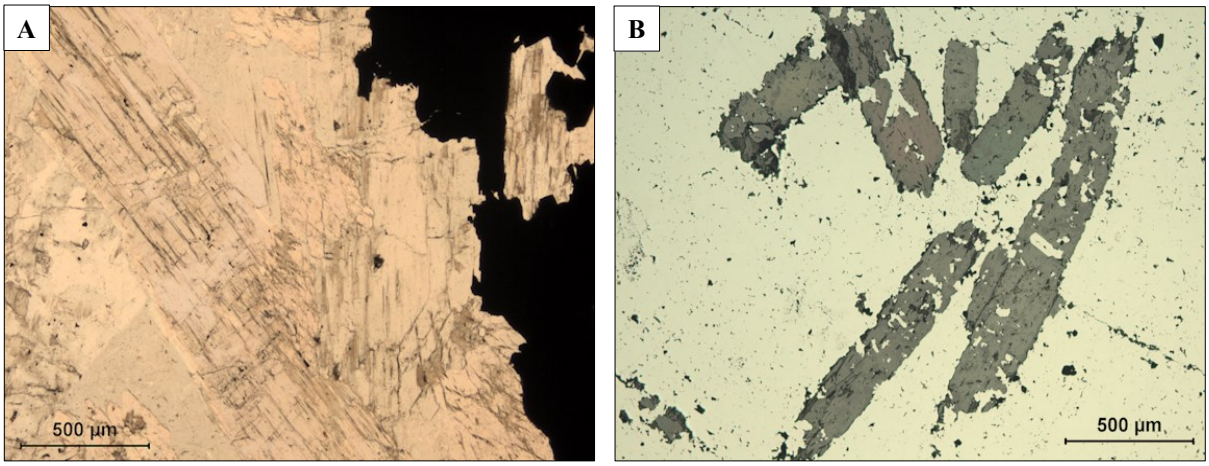

Figure 9. (A) Coarse-grained, subhedral, almost colorless actinolite in brecciated magnetite ore (Sample 6387.3; transmitted light); (B) large needle-like subhedral/euhedral actinolite crystals with fine-grained magnetite inclusions (Sample 6252.4, reflected light).

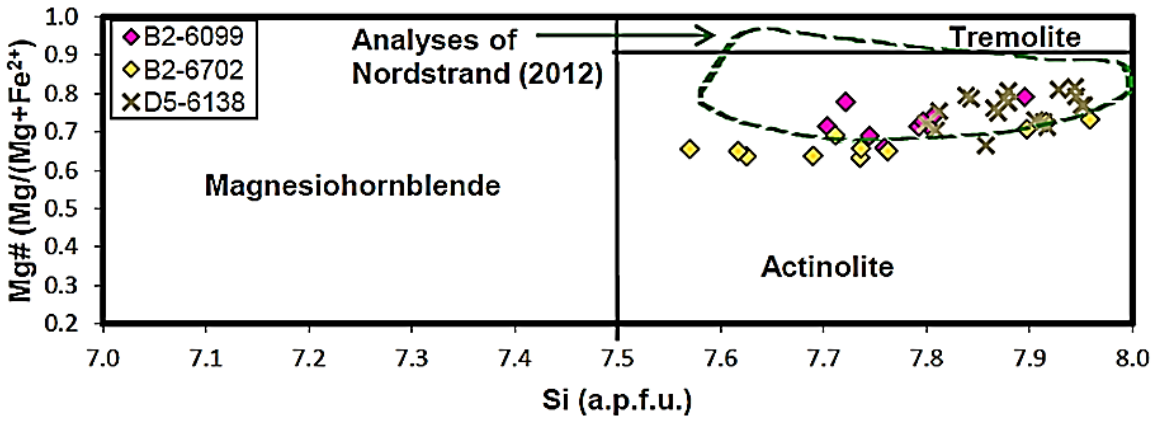

Figure 10. Chemical classification scheme of amphibole group minerals (after Leake et al. 1997). All the analyzed samples fall into the actinolite group (Aupers 2014). The green dotted line marks the EPMA analyses carried out by Nordstrand (2012).

According to the chemical classification by Leake et al. (1997) based on the Mg-number and Si (atoms per formula unit), most of the amphibole group minerals in the Kiirunavaara deposit (Fig. 10) falls within the boundaries of actinolite (Nordstrand 2012, Aupers 2014). According to Nordstrand (2012) and Aupers (2014), the rims of actinolite crystals often show a slightly elevated content of Mg compared to the core of the crystals. Si content in actinolite also varies over a wide range, especially in ore type B2 relative to actinolite in ore type D5. In some cases, a core of actinolite grains/crystals can also contain secondary gypsum and/or mica (Nordstrand 2012).

3.3.3 Phlogopite $KMg_3(Si_3Al)O_{10}(F,OH)_2$

The minerals of the biotite group (mica) are the second most abundant silicate minerals in the Kiirunavaara deposit and can be classified as phlogopite. Phlogopite belongs to the class of tri-octahedral micas with six (octahedral) ions, in which Ti can substitute for Al (Fleet 2003). Phlogopite can be present in a variety of textural positions within all parts of the deposit. The crystals are most commonly subhedral to euhedral crystals or aggregates. They are most often colorless (Fig. 11 A) or dark brown (Fig. 11 B) (Knights 2001, Niiranen 2012 b, Nordstrand 2012, Aupers 2014). Phlogopite occurs often enclosed within the magnetite, as bundles of grains in contact with magnetite breccia fragments, and in some cases, as parallel-oriented flow-like textures, very similar to those of actinolite. Deformation features in phlogopite can be locally observed. Phlogopite sometimes displays alteration towards chlorite, which is usually one of the common alteration products of micas (Fleet 2003).

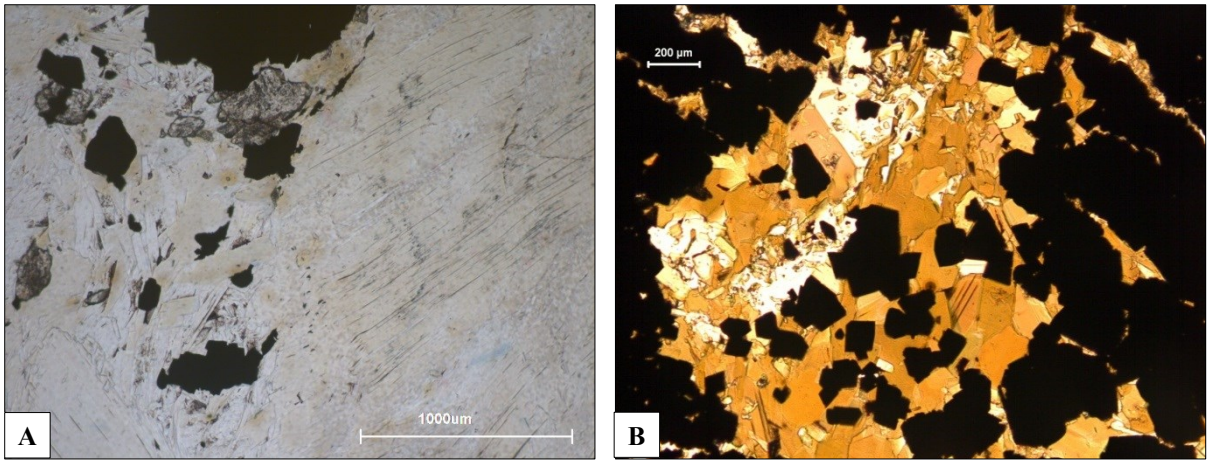

Figure 11. (A) Coarse-grained, colorless Mg-rich phlogopite (Sample B2-6172; transmitted light; Photo: K. Aupers); (B) Dark brown Fe-rich phlogopite (transmitted light; Photo: J. Nordstrand).

According to Nordstrand (2012) phlogopite might also be an important source of potassium (K) in the crude ore. The content of K seems to be constant at 9.91 wt.% throughout the samples analyzed by Aupers (2014). According to Aupers (2014), Ti content varies significantly between different samples (0.08 wt.% to 1.54 wt.%) and there seems to be a negative correlation in concentration of SiO_2 and TiO_2 (Fig. 12) depending on the ore type. However, this trend seems to be limited mainly to the low-phosphorous ore types (B1 and B2).

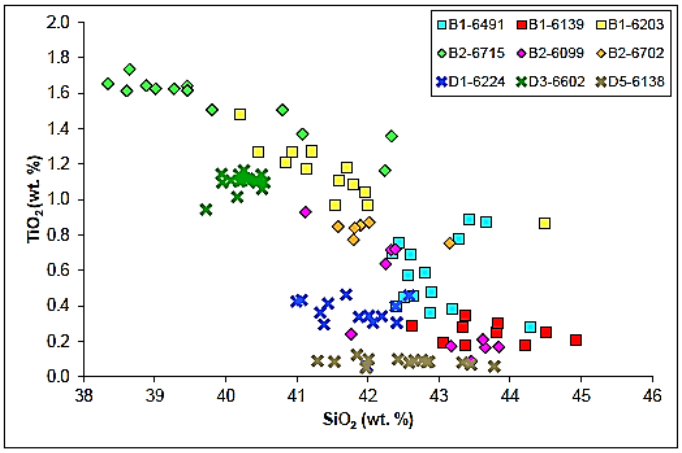

Figure 12. Oxide concentration (SiO_2 and TiO_2) in phlogopite in different ore types based on EPMA analysis (Aupers 2014). Oxide concentrations in ore types B1 and B2 (squares) show variations in TiO_2 concentrations within a sample, while D-type ores (crosses) display constant TiO_2 values.

A negative correlation between SiO_2 and TiO_2 in phlogopite might be an important characteristics to take into consideration in the next few years, when a new or modified beneficiation process will be designed at LKAB in Kiruna and which will take into account the observation both SiO_2 and TiO_2 grades are increasing rapidly while the P grade is decreasing in the deeper part of the ore body. This applies in particular to flotation, which currently consists of only reverse apatite flotation. Furthermore, fluorine (F) content in phlogopite seems be constant within one sample but varies between different samples

from 0.70–3.99 wt.%, but it incorporate not more than 0.04 atoms of chlorine per formula unit (Nordstrand 2012, Aupers 2014). Outside of apatite phlogopite can also be an important source of Cl and F in the beneficiation process.

3.3.4 Chlorite $(Mg,Al,Fe)_{12}[(Si,Al)_8O_{22}](OH)_{16}$

Chlorites are a group of phyllosilicates with a general formula, which can be summarized as $A_{5\text{-}6}T_4Z_{18}$, where A = Al, Fe^{2+}, Fe^{3+}, Li, Mg, Mn or Ni, while T = Al or Si or a combination of them and Z = O and/or OH (Deer et al. 2009). Chlorite is generally a less common silicate compared to actinolite and phlogopite. However, in sample 6351, chlorite is the most common SiO_2-bearing mineral. Most of chlorite seems to be an alteration product of phlogopite and it often occurs as alteration lamellae within phlogopite grains (Fig. 13 A). According to Aupers (2014) most chlorites in ore type B2 have a composition of brunsvigite $(Fe^{2+},Mg,Al)_6(Si,Al)_4O_{10}(OH)_8$. Both chlorite and phlogopite are not uncommon minerals in the ore, but they are very seldom reported macroscopically by core logging, because they normally are very fine-grained. The possible impact of chlorite on SiO_2 grade in the crude ore and magnetite concentrate will be discussed in Chapter 8 in the same context as other minerals showing the same sheet-like structure, such as phlogopite and talc.

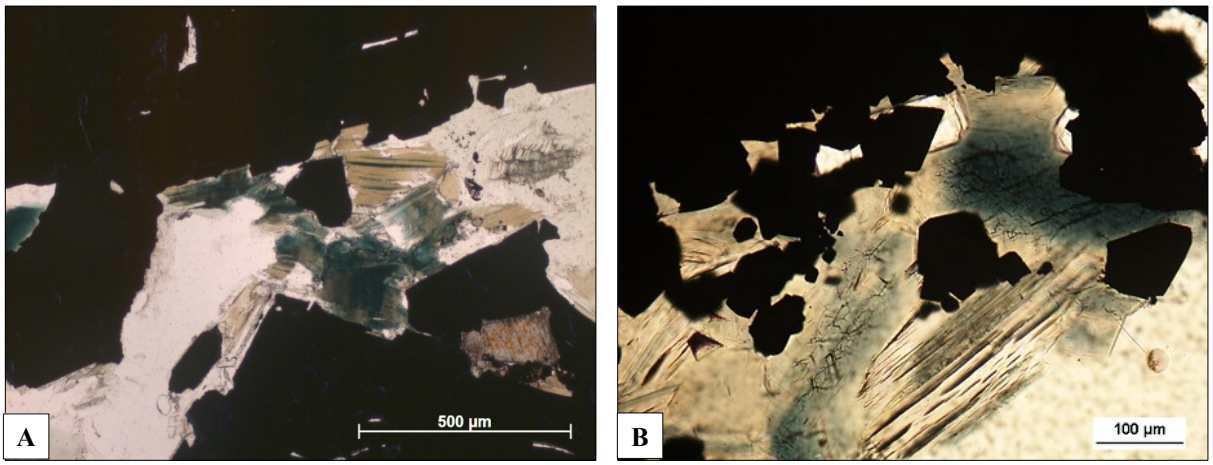

Figure 13. Chlorite as an alteration product of phlogopite in transmitted light. (Photo: K. Aupers (A) and J. Nordstrand (B)).

Compositionally, chlorite shows a wide range in Fe, Mg and Al content (Nordstrand 2012). The average element concentration in chlorite for Fe, Mg and Al is12.2 wt.% (FeO), 25.4 wt.% (MgO) and 18.1 wt.% (Al_2O_3) respectively (Aupers 2014). In Figure 13 B, tiny needles of rutile (TiO_2), called sagenite, can been seen in the chlorite. The presence of sagenite especially in chlorite is apparently related to the alteration of phlogopite to chlorite. Phlogopite can contain more than 15 wt.% TiO_2. Chlorite, however, normally contains less than 0.8 wt.% TiO_2 (Fleet 2003). During the alteration of phlogopite to chlorite most of Ti precipitates and crystallizes as fine rutile needles and grains (Höfig 2014).

3.3.5 Titanite $CaTiSiO_5$

Titanite (sphene) seems to be a common mineral in small quantities, although being fine-grained it is seldom reported macroscopically during core logging. Mineralogical studies indicate that two different generations of titanite occur in the ore (Niiranen 2012 b, Nordstrand 2012). This is the same conclusion was made by Smith et al. (2009) and Storey et al. (2007), based on data from samples of the associated rocks of the porphyry group in the Kiruna area, which are same units both in the foot and hanging wall of the Kiirunavaara deposit.

Titanite occurs mainly as bundles of fine-grained crystals along the edges of magnetite crystals and grains, but it also shows a tendency to occur as disseminated interstitial grains (Fig. 14 A) in granular magnetite (Niiranen 2012 b). This type is normally Fe-rich and Ti-poor (Knights 2001) and may represent the first (older) generation of titanite. It should be noted that part of this fine-grained mineral might be ilmenite or rutile. Titanite also occurs as coarse-grained subhedral or euhedral crystals as the second generation (Fig. 14 B) in relation to the alteration. Titanite containing the least amount of Fe, is transparent in color, while those that containing the highest proportion of Fe, usually occur at some distance from the magnetite and has a more reddish color (Nordstrand 2012).

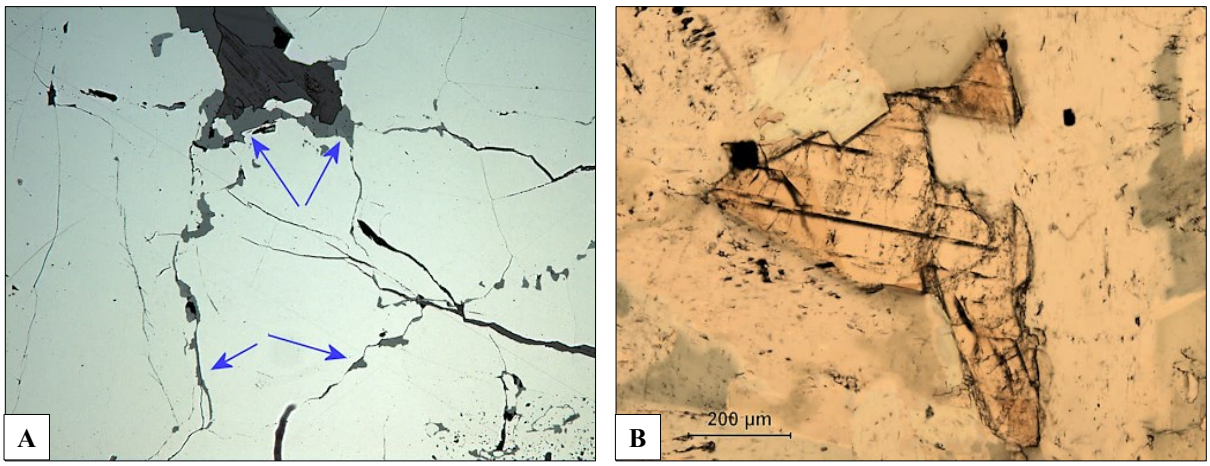

Figure 14. (A) Fine-grained titanite as interstitial to granular magnetite and between magnetite and silicates (reflected light; see blue arrows); (B) Coarse-grained titanite as subhedral to euhedral crystals (transmitted light).

3.3.6 Quartz SiO_2

Quartz seems to be a relatively uncommon mineral based on these samples. It occurs in a somewhat larger amount only in sample 6370. According to the modal mineralogy, the quartz grade falls between 0 and 0.29 wt.% (except sample 6370). It usually occurs as anhedral grains along with carbonates in narrow veins and veinlets and is typically fresh and unaltered (Fig. 15 A). Quartz in sample 6370.2 shows a distinct undulose extinction (Fig. 15 B), which can be regarded as evidence of a moderate grade of metamorphism (Deer et al. 2001).

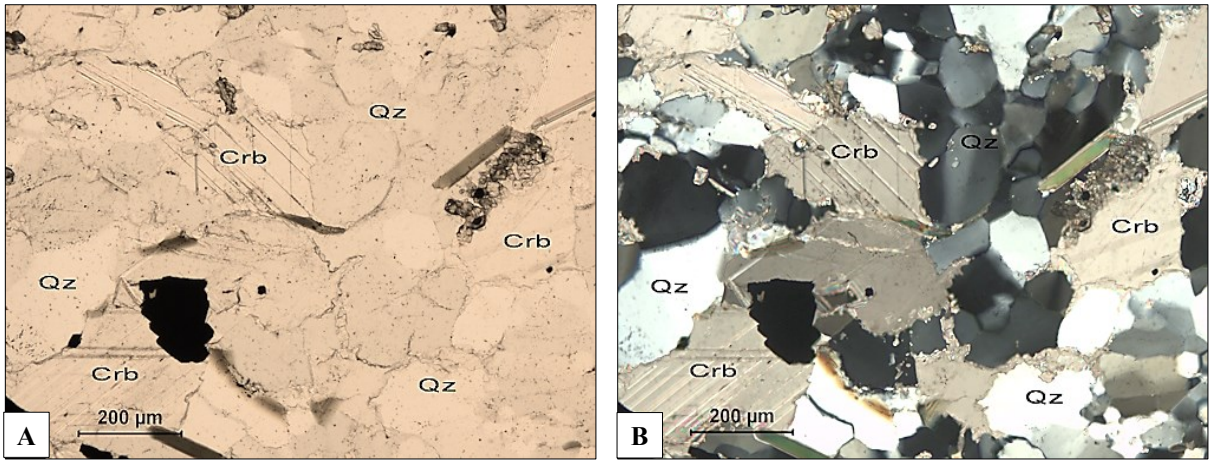

Figure 15. (A) Quartz grains (Qz) with carbonate (Crb) in sample 6370.2 (transmitted light); (B) Undulose extinction of quartz grains (transmitted light; polarized state).

*3.3.7 **Alkali Feldspar** (**Albit** $Na[AlSi_3O_8]$ and **K-Feldspar** $K[AlSi_3O_8]$)*

There are two phases of alkali feldspars described in the Kiirunvaara deposit: K-feldspar (orthoclase) and Na-feldspar (albite) (Jarousseau & Pålsson 2000, Knights 2001, Niiranen 2012 b, Aupers 2014) (Fig. 16). In this study, only some uncertain grains of K-feldspar were identified in one thin section by optical mineralogy.

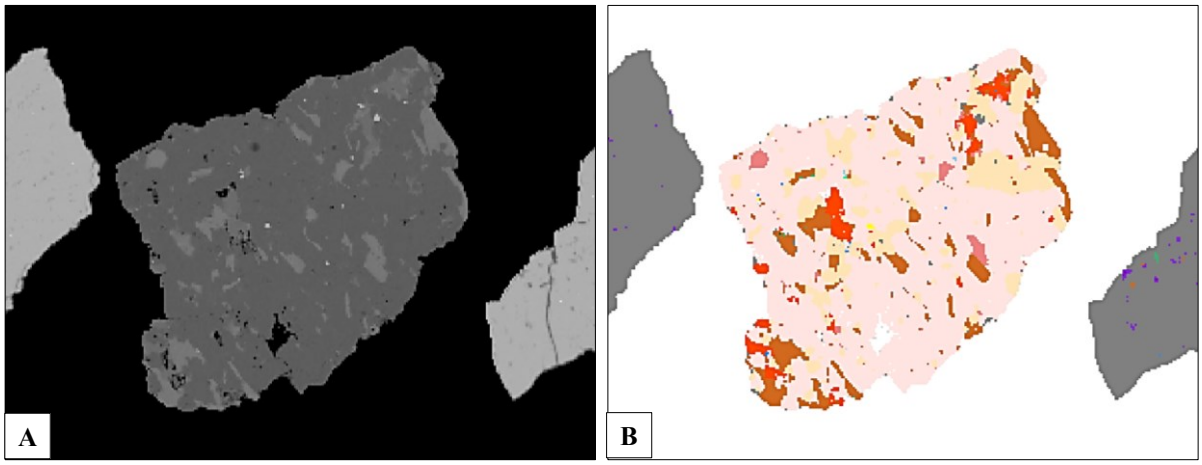

Figure 16. Albite (light brown) and K-Feldspar (red) in a particle together with phlogopite and quartz; (A) BSE image; (B) Processed with a secondary SIP List presented in Figure 58 B. Sample 6370, Fraction 1.0/0.5 mm.

Albite seems to occur more frequently among subtypes of ore type B2 according to QEMSCAN analysis (Chapter 8). K-feldspar occurs most frequently with albite and phlogopite (Fig. 16 B). Alkali feldspars is commonly found in the brecciated ore at the contacts of the orebody and can end up in the beneficiation process. This type of ore is not so common except in a zone in the middle and the contact zones of the ore body. However, alkali feldspars are common constituents of the acidic and alkaline plutonic and volcanic rocks (Deer et al. 2001). Both the rocks in the foot wall (volcanic rocks of trachytic and trachy-andesitic composition) and in the hanging wall (volcanic rocks of rhyolitic and rhyodacitic

composition) are dominated by alkali feldspars (microcline and albite) (Ekström & Ekström 1997, Bergman et al. 2001).

3.3.8 Talc $Mg_6[Si_6O_{20}](OH)_4$

Talc is may also have an impact on the SiO_2 grade in the magnetite concentrate at the beneficiation plants. However, talc is not as common as actinolite, phlogopite or even titanite. It is a metamorphic mineral and its occurrence is largely dependent on the availability of sufficient magnesium (Mg) (Deer et al. 2009). Only minor amounts of talc were encountered in these samples, even though it might be a more common mineral in the ore according to core logging reports.

Talc shows a small variation in chemical composition with silicon (Si) and magnesium (Mg) and a fairly high amount of Fe (3.65–5.22 wt.% FeO, respectively, 2.74–4.89 wt.%) (Nordstrand 2012, Aupers 2014). Talc occurs mainly with actinolite (Fig. 17 A) and in pores and narrow veinlets in the magnetite matrix along with carbonate minerals and phlogopite (Fig. 17 B).

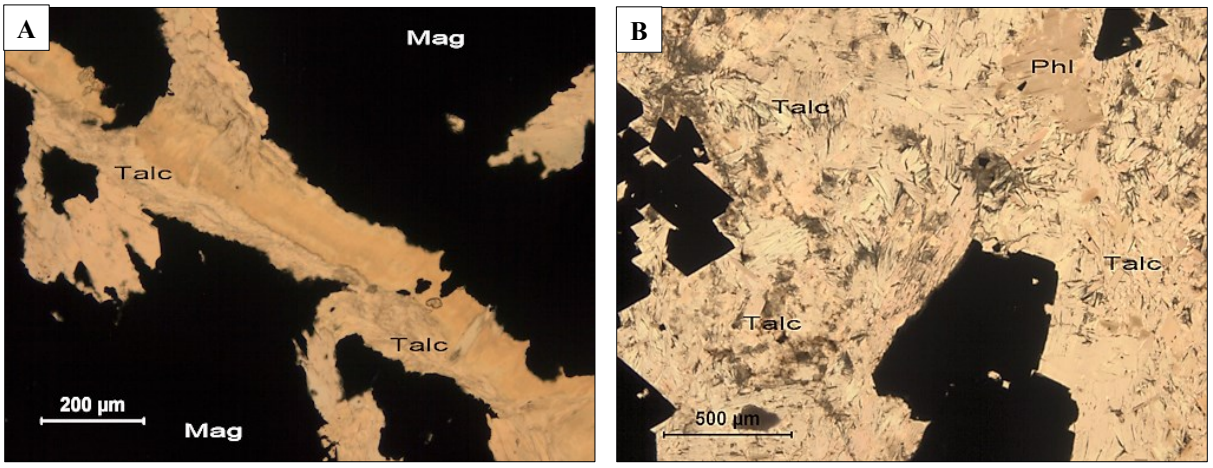

Figure 17. (A) Fine-grained talc (Talc) with colorless actinolite between magnetite (Mag) grains (transmitted light); (B) massive, fine-grained talc (Talc) as an aggregate with phlogopite (Phl) (transmitted light).

Together with talc, Nordstrand (2012) has also analyzed probable clay minerals showing a composition in the range of 48–59 wt.% SiO_2, 11–15 wt.% Al_2O_3 and 9–12 wt.% FeO which are dominant elements.

4. COMMINUTION TESTS

4.1 Sampling

The samples selected for the mineral processing tests at LKAB's mineral processing laboratory related to the "Silica in the Mine" project were derived from drill cores from the exploration drilling and grade control drilling underground in the Kiirunavaara mine. Besides the samples from the drill cores, there was also sampling (grab samples) during the development of the tunnels at the first stage of the project. This sampling included about 550 samples and started in the autumn of 2007 and ended at the end of

2009. The ore type of grab samples was defined based on the information from the geological maps of the mining blocks. In general, through the sampling, it was important to keep the different ore types separate, because it was expected that the physical properties and thus also process mineralogical characteristics are unequal for different ore types. The total amount of the samples from drill cores and tunneling is about 2950. For each sample, the coordinates (x, y, z in LKAB's coordinate system in the mine) were stored in the database to obtain spatial distribution in the ore body. Of this total amount of samples, 1815 samples are currently tested either in whole or in part to a minor extent until now. Each sample, aimed for mineral processing tests, was compounded of several subsamples after the crossing the drill cores (Ø approximately 29 mm) for chemical analysis according to the recommendation of the geologist based on the ore types after reporting drill cores.

Of these samples three samples, 6382 (B1), 6365 (B2), and 6354 (D3) representing the main ore types of the Kiirunavaara (Chapter 3.2) deposit, were selected as feed material for the comparative mineral processing tests at the laboratory of the Institute of Mineral Processing, Montanuniversitaet Leoben, based on the information from drill core logging and chemical analysis. Furthermore, six samples (6252, 6351, 6363, 6367, 6370, 6387) representing ore type B2 were selected as feed material for the process mineralogical tests at the laboratory of the Institute of Mineral Processing, Montanuniversitaet Leoben. They originated from the middle and southern part of the ore body and were composed of several sub-samples according to the recommendations of a geologist. There were two essential arguments for the selection of these samples for this study. First, they were classified by a geologist as ore type B2 in the drill core characterized by the green based on the green actinolite in the mineral association. The second important argument, was the relatively high SiO_2 grade in the crude ore and the strongly varying recovery of silica by the mineral processing tests carried out during the "Silica in the Mine" project at LKAB's mineral processing laboratory in Malmberget. For this study, further 18 samples representing different main ore types were selected for detailed investigations to illustrate the mineral processing test in relation to the "Silica in the Mine" project and evaluate its result. Smaller groups such as martite (hematite-magnetite) or ore breccia, which are represented by only some of the samples, are excluded from the focus of this investigation.

It should be noted that in many current mineral processing test practices, the predetermined geological, mineralogical, and/or grade characteristic is used as a control for sample selection and distribution of mineral processing indices. This was also the case for sampling in relation to the "Silica in the Mine" project. However, in several published cases, it has been demonstrated that this might be problematic. Using predefined boundaries or limits such as lithology and/or mineralogy and grade and/or cut off of the minerals and elements of interest to control the distribution of mineral processing performances indices and test work can represent uncertainty, specially without proper evaluation of the relationship between the definition of the ore types or domains and the mineral processing characteristic (Keeney & Walters 2011, Kittler et al. 2011). Walters (2009) has pointed out that there might be no guaranteed

direct relationship between the geological or mineralogical ore definition/characterization and the mineral processing performance.

4.2 Optimized Comminution Sequence (OCS)

4.2.1 Samples

The samples selected for the mineral processing tests at the laboratory of the Institute of Mineral Processing, were first crushed down to –3 mm in two stages using a jaw crusher and the MK 25 cone crusher in closed circuit at LKAB's mineral processing laboratory. The particle size distribution for the feed material is also shown in Figure 18 A, plotted on a Gates Gaudin Schuhmann grid (GGS grid), and in Figure 18 B on a half-logarithmic grid used at LKAB.

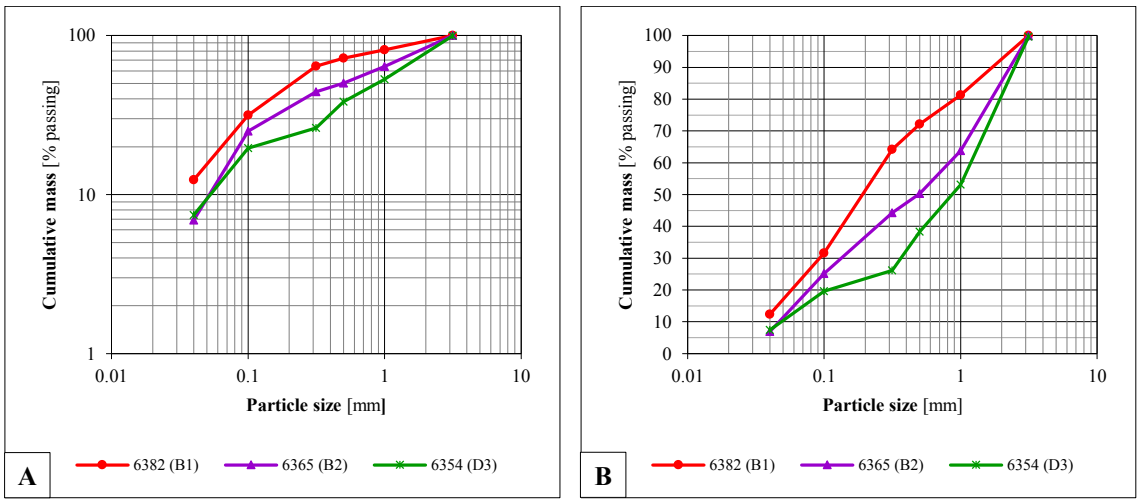

Figure 18. (A) Particle size distribution (PSD) for samples 6382 (B1), 6365 (B2), and 6354(D3) after crushing -3 mm at LKAB's mineral processing laboratory. (B) The same particle size distribution presented in Figure 18 A, but in the format of internal reports used at LKAB (cumulative mass, % passing is non-logarithmic). Numeric data available on CD.

4.2.2 Optimized Comminution Sequence (OCS)

A test procedure, named the "Optimized Comminution Sequence" (OCS), has been developed by Steiner (1990, 1996, 1998) at the Institute of Mineral Processing at Montanuniversitaet Leoben. The design of OCS calls for a characterization of the comminution properties of minerals and rocks with respect to their individual breakage characteristics and the specific energy consumption as a function of the product dispersity. The latter is described by the particle size distribution and the specific surface area of the products. The purpose OCS is to determine the "Natural (i.e., material inherent) breakage characteristics" (NBC) of brittle mineral matter. NBC can be defined as a size distribution with the lowest amount of fines at a given maximum particle size. Material ground at most energy efficient way by compressive stress and impact stress reveals the specific surface area/energy relationship,

culminating in the Rittinger coefficient (R), which relates the creation of new surface during the comminution to the net energy consumption (Steiner 1991, Boehm et al. 2002).

OCS obeys the principle of the energy-optimized comminution and consists of a succession of numerous comminution stages in closed circuit designed to guarantee a small size-reduction ratio. The settings of the apparatus of each stage are optimally adapted to the specific size-reduction step. The circuit design of "closed circuit with pre-screening" (Fig. 19) is estimated at the laboratory by cyclic comminution tests at high circulating load (at least 100%). High circulating load causes a short retention time of the particles within the comminution tool, resulting in a smaller number of stress events per particle and cycle. Pre-screening serves to separate the existing fines in the feed, thus directing the energy supplied by the comminution tool to the coarse particles. Each comminution cycle ends with intermediate classification at a defined screen aperture. The accurate intermediate screening after each comminution cycle removes the fine particles soon after their creation. Within each circuit, mechanical screening is completed by manual screening, which is still the most accurate laboratory method of particle-size separation in the particle size range from 0.04 to 100 mm (Boehm et al. 2002).

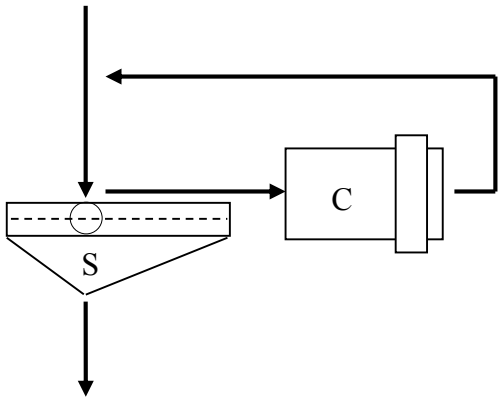

Figure 19. Scheme of the closed comminution circuit design with pre-screening (S = screening, C = Comminution tool) by Steiner (1990, 1996).

4.2.3 Comminution tests

4.2.3.1 Laboratory rod mill

The comparative comminution tests were carried out with the comminution tools belonging to the standard testing equipment at the laboratory of the Institute of Mineral Processing. The OCS was built up to analyse the three samples of the Kiirunavaara iron ore on its breakage behaviour abutted to the "Less Fines" project (Boehm et al. 2002) based on the principles of energy-optimized comminution. It consisted of two grinding stages, a laboratory rod mill and a laboratory ball mill, with pre-screening (Appendix 3). The laboratory rod mill is driven by a roller drive and powered by a frequency converter controlled electric motor and the number of revolutions was counted by a sensor (Fig. 20). The technical data for the used comminution tools is displayed in Table 2.

Table 2. Technical data for the laboratory rod mill (Fig. 22) and the laboratory ball mill used for the comminution tests at the laboratory of the Institute of Mineral Processing, Montanuniversitaet Leoben. For critical speed see Equation 1.

		Grinding by laboratory rod mill (1st stage)	**Grinding by laboratory ball mill** (2nd stage)
Mill diameter (inside)		154 mm	200 mm
Mill length (inside)		300 mm	200 mm
Grinding Media	*Material*	Steel rods	Steel balls
	Weight	7802 g	9188 g
	Degree of filling	--	40 vol-%
Rotation speed / % of Critical speed		~ 1 s^{-1} / 70%	1.1 s^{-1} / 70%

This data should be compared with the technical data for the comminution system used for the comminution tests related to the "Silica in the Mine" project at LKAB's mineral processing laboratory (Drugge 2009, Drugge 2010, Niiranen & Fredriksson 2012) described in next chapter.

Figure 20. The laboratory rod mill at the laboratory of the Institute of Mineral Processing, Montanuniversitaet Leoben (Photo: M. Wartbichler).

The revolution speed of the laboratory tumbling mill was adjusted 70% of the critical speed (n_c), which refers to the inside diameter of the mill as follows (Steiner 1996) (*Equation* 1*)*:

$$n_c = \sqrt{\frac{g}{2 \cdot \pi^2 \cdot D_i}} \qquad (Eq.\ 1)$$

n_c…… Critical speed

g…… Gravity acceleration [9.81 m/s^2]

D…… Inside diameter of a mill [m]

When grinding with a laboratory rod mill and with a laboratory ball mill, the bulk volume should always be the same. As reference material for volume, usually 500 g of quartz is used, with approximately the same particle size as the samples (Wartbichler 2014). The bulk density, yielded by a jolting volumeter, was used to estimate the required mass of the feed for each comminution stage. The required mass of

the feed varies between 500 g and 797 g for the laboratory rod mill and between 1114 g and 1214 g for the laboratory ball mill dependent on the different bulk density of the ore types. The output for the comminution tests (number of revolutions, feed, mass of fine and coarse material, circulating load, and specific fine material) are displayed in Appendix 4 and the flow sheet and mass balance in Appendix 5.

4.2.3.2 Laboratory ball mill

For the measurement of the total consumption of energy supplied to the ball mill, a torque sensor type Hottinger Baldwin T1 with a measuring and a recording unit was available at the laboratory of the Institute of Mineral Processing. With this equipment, the measuring shaft is bolted to the drive shaft between the electric drive and the mill over two rigid couplings. Four rotating gauges are placed in a Wheatstone bridge circuit onto the actual measuring body so that they are either stretched or compressed by measuring torque. The technical data for this laboratory ball mill is displayed in Table 2.

The ultimate goal of the power draw measurement is the determination of the net power draw of the mill, i.e., the power demand to tumbling the mill charge. To obtain reliable results, calibration procedure corrections are necessary (Steiner 1996). Also, for the comminution tests with the laboratory ball mill related to the comminution tests at the laboratory of the Institute of Mineral processing in summer of 2009, the ball mill was calibrated empty with various external loads to determine the mean of the torque both before and after every comminution sequence. After calibration, the measurement structure for the measurement data provided the conversion of the signals in a torsional and integral by recorder averaging of the time course of the torque over the measurement's period of time. The relationship between torsion and output voltage of the alleged bridge circuit was determined before each measurement and defined by torque load. The net torque during the comminution time is used for the estimation of the specific energy consumption of the ground material.

The calibration data for the mean torque is displayed as graphs in Appendix 6. The value of mean torque (ΔM_D) is estimated using *Equations* 2 and 3:

$$C = b \cdot B \qquad (Eq.\ 2)$$

$$\Delta M_D = C \cdot \Delta\left(\frac{IE}{t}\right) \qquad (Eq.\ 3)$$

b.....	Mean torque.
B……	1.25 (constant).
IE……	Integration units from recorder.
t……	Retention time of material in the mill.

4.3. Comminution in an open circuit

4.3.1 Samples

The samples selected for the characterization of the high-SiO_2 ore type B2 at the laboratory of the Institute of Mineral Processing, were first crushed down to –3 mm using the MK 25 cone crusher in closed circuit at LKAB's mineral processing laboratory. The particle size distribution of the feed material after crushing feed is presented in Figure 21 plotted on a GGS grid.

It is worth noting that the particle size distribution, based on a screen analysis after crushing (Fig. 21) differs for samples 6252 and 6387 compared to the rest of the samples. The finest particle size classes seem to be overrepresented. This can be interpreted as the result of a large amount of fine particles being generated at the first stage of the comminution sequence (crushing) in these two samples. There are also some indications that the iron ore in the Kiirunavaara deposit may have fragmentation characteristics, which differ from a normal hard rock (Wimmer 2012).

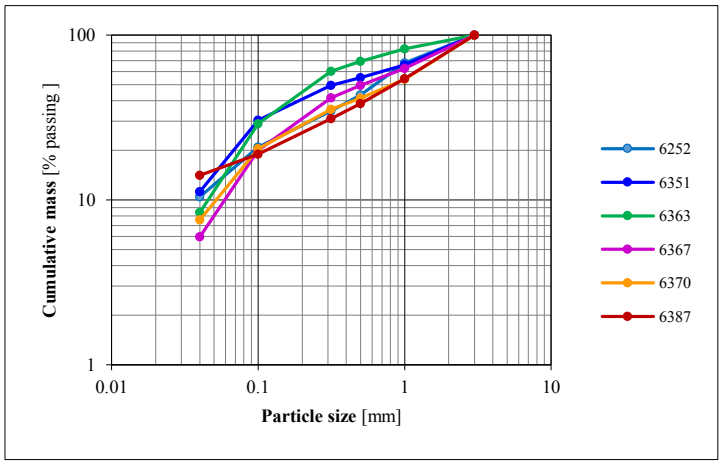

Figure 21. Particle size distribution of the samples selected for the mineral processing tests and mineralogical investigation representing ore type B2 after crushing to –3 mm at LKAB's mineral processing laboratory. Numeric data available on CD.

4.3.2 Comminution tests for characterization of ore type B2

4.3.2.1 Laboratory rod mill

The comminution tests for characterization of the high-SiO_2 ore type B2 were carried out with the comminution tools belonging to the standard testing equipment at the laboratory of the Institute of Mineral Processing. The test set up for the comminution sequence used is presented in Appendix 7, which was an open comminution circuit without pre-screening. In an open comminution circuit material passes through a comminution tool without a classification of product and a recycling of oversize particles. In contrast, an optimized comminution sequence (OCS) developed by Steiner (1990, 1996, 1998) at the Institute of Mineral Processing is a closed comminution circuit based on the principles of

energy optimized comminution. Because the equipment (Table 2) was somewhat different to that used for the comminution tests related to the project "Silica in the mine" at LKAB's mineral processing laboratory (Drugge 2009, 2010, Niiranen & Fredriksson 2012), the grade of the comminution in the laboratory rod mill was evaluated with the help of screening analyses to get approximately the equivalent particle size distribution (Fig. 22). The required comminution time varied between 5.8 and 12.5 minutes corresponding to 350 to 750 rounds. This likely reflects different breakage characteristics between the samples.

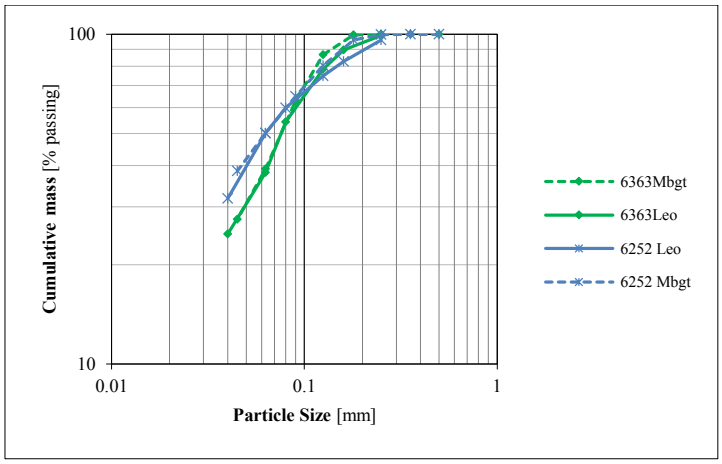

Figure 22. Comparison of the particle size distribution of samples 6252 and 6363 after comminution in the laboratory rod mill (10 minutes) at LKAB's mineral processing laboratory (Mbgt) and in the laboratory rod mill (550 and 750 rounds) at the laboratory of the Institute of Mineral Processing (Leo).

4.3.2.2 Laboratory ball mill

For the comminution and for the measurement of the total consumption of energy, the same ball mill was used as described in Chapter 4.2.3.2 with a torque sensor type Hottinger Baldwin T1 at the laboratory of the Institute of Mineral Processing. The technical data for this laboratory ball mill is displayed in Table 2. After calibration, the measurement structure the processing software for the measurement data provides the automatic conversion of the voltage signals in a torsional and integral averaging of the time course of the torque over the measurement's period of time. The calibration data for the laboratory ball mill is displayed in Appendix 8. The relationship between torsion and output voltage of the alleged bridge circuit is determined before each measurement and defined by moment load. The mean torque during the comminution time is used for the estimation of the specific energy consumption of the ground material. In addition, the energy consumption for open comminution circuit can be estimated.

4.4 Comminution tests related to the "Silica in the Mine" project

The samples selected (normally 15 to 20 kg) for the mineral processing tests at LKAB's mineral processing laboratory were first crushed down to –3 mm in two stages (Appendix 9). The first stage was

carried out using a jaw crusher in an open circuit and second stage with a cone crusher (MK 25 mortar crusher) in a closed circuit after which material, screened and coarser than + 3mm, was fed back into the crusher. By sampling, a geologist ensured, too, that large sections with waste rock have been excluded because there was no dry magnetic separation (Mörtzell) connected to the crushers. After crushing, the material was homogenized during the splitting and mixing in several steps. After homogenization and splitting, chemical analysis was carried out on feed (three samples 2 kg each) for the comminution tests and the rest of the crushed material was stored in the archives for conceivable control or complementary investigations.

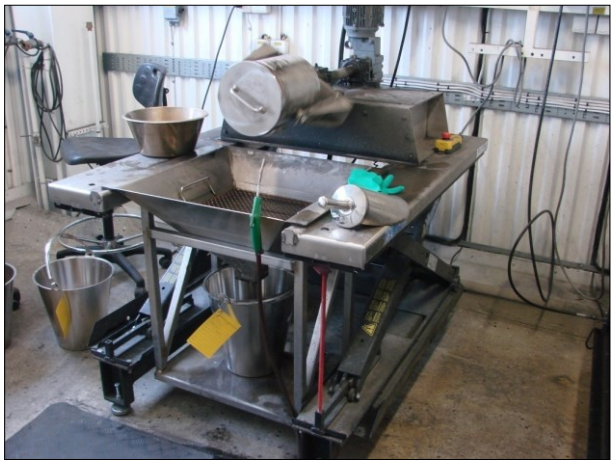

Figure 23. Laboratory tumbling mill used for the comminution tests with steel rods or steel balls as grinding media, at LKAB's mineral processing laboratory in Malmberget.

After crushing, the samples were grinded wet (2 kg material and 1 litre water) in open system in the laboratory rod mill for 10 minutes (Fig. 23). Technical data for the used comminution tools is displayed in Tables 3 and 4 and the comminution set up is displayed in Appendix 9. After grinding, the samples were placed in buckets and dried in the oven with a temperature of 105 ± 5 C^o for about two days. After drying, samples from two sub-samples were grinded in the laboratory ball mill for 25 minutes or for 35 minutes, respectively. After grinding, the samples was collected in 10 litres buckets then dried, homogenized, and split into sub-samples for the mineral processing test and chemical analysis (Drugge 2009, Niiranen & Fredriksson 2012, Niiranen & Böhm 2012).

Table 3. Technical data for the laboratory tumbling mill, with steel rods or balls, as grinding media used for the comminution tests related to the "Silica in the Mine" project at LKAB's mineral processing laboratory (Drugge 2009, Drugge 2010).

	Grinding by laboratory rod mill (1st stage)	**Grinding by laboratory ball mill (2nd stage)**
Mill diameter (*inside*)	200 mm	200 mm
Mill length (*inside*)	250 mm	250 mm
Grinding Media		
Material	Steel rods (LKAB)	Steel balls, Ø 15 mm (Maggotteaux)
Number	53*	--
Weight	ca. 14.2 kg ± 50 g	ca. 13.1 kg
Degree of filling	67 wt.%	67 wt.%
Rotation speed	65 rpm	65 rpm

Table 4. Detailed data for the steel rods used for comminution tests in the laboratory tumbling mill at LKAB's mineral processing laboratory.

Number of rods	**Diameter** [mm]	**Length** [mm]	**Number of rods**	**Diameter** [mm]	**Length** [mm]
3	25.4	240	6	12.5	240
4	22.0	240	8	10.0	240
4	19.0	240	10	8.0	240
5	16.0	240	13	6.0	240

Abrasion of grinding media over time can probably cause an error between comminution tests. This should be eliminated, if possible, because the error can also affect the estimation outcome of the mineral processing parameters. The elimination of this potential error follows the routine based on comminution tests and empirical observations that, after 100 grinding cycles, the grinding media should be completely replaced either with new steel rods or steel balls (Drugge 2010). Up grading of the steel rods within the 100 grinding cycles was made by adding a further 6 mm steel rod after approximately 50 grinding cycles or, alternatively, when rods have lost an equivalent 60 g in weight. Up grading of the steel balls was made by adding an additional steel ball (ø 15 mm) after approximately 20 grinding cycles or, alternatively, when balls have lost the equivalent in weight corresponding to a steel ball (Drugge 2010).

5. MINERAL PROCESSING TESTS

5.1 Separation with Davis magnetic tube

5.1.1 Preface

The magnetic separation of iron ores is based on the fact that magnetite, Fe_3O_4, is strongly attracted by a magnetic field, while the gangue minerals are not. Maghemite, γ-Fe_2O_3, which may occur in certain chemically processed ores, responds similarly to magnetite. The magnetic process is only applicable when the loss of iron in the form of relatively non-magnetic iron-bearing minerals, such as hematite Fe_2O_3 and goethite $Fe_2O_3 \cdot n\ H_2O$ or other iron minerals, can be tolerated (Schulz 1963).

The Davis magnetic tube test can be regarded as the most important of the mineral processing tests carried out at the laboratory of the Institute of Mineral Processing and at LKAB's mineral processing laboratory, especially with a focus on SiO_2 grade and liberation of magnetite and silicates. The Davis magnetic tube concentrator is a laboratory machine designed to separate small samples of pulverized magnetic ore into magnetic and non-magnetic fractions. It is a quite simple apparatus consisting of an inclined cylindrical glass tube supported adjacent to closely spaced pointed poles of a powerful C-magnet (Fig. 24).

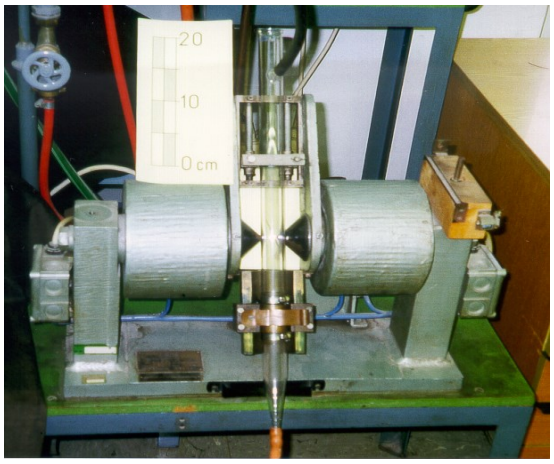

Figure 24. The apparatus for the Davis magnetic tube tests at the laboratory at the Institute of Mineral Processing, Montanuniversitaet Leoben (Photo: A. Böhm).

To conduct the Davis magnetic tube test, a sample of suitably prepared material is poured into the water-filled tube. With water flowing through, the tube is oscillated to gradually sort out the non-magnetic particles and magnetic (magnetically susceptible) particles, which are held in a magnetic field until the desired degree of separation is attained. Forces related to gravity, inertia and fluid-solid friction tend to remove the less susceptible particles from the field. The probability that a given middling particle will be rejected from the tube in a given period of time, is an inverse function of its magnetic content, with some modification related to particle size and mineral specific gravity. A sufficient washing time is required to allow the non-magnetic fraction to be washed out from the tube (Schulz 1963, 1964). Furthermore, the Davis magnetic tube has seven parameters that can be adjusted in order to correspond to the full-scale wet low magnetic separation at the beneficiation plant. It should be noted that the Davis magnetic tube parameters, such as stroke length, stroke frequency, angle of the tube, water flow rate and duration of the test, have to remain constant throughout the testing program (Farrell et al. 2011).

The net result is that ore particles tend to be rejected in their order of increasing magnetite content, while the retained portion of magnetic concentrate increases in the grade continuously during the process (Schulz 1964, Böhm 2009). Both magnetic fractions (concentrate) and non-magnetic fractions (tailings/waste) may be collected and recovered for mineralogical and chemical examination, but a routine analysis of the non-magnetic fraction is normally not conducted (Farrell et al. 2011).

5.1.2 Davis magnetic tube tests at the laboratory of the Institute of Mineral Processing

The samples selected for the Davies magnetic tube separation were screened in two different particle size classes (0.1/0.04 mm and < 0.04 mm) after the comminution in the laboratory ball mill. The mass of the samples (feed) was approximately 55 to 60 g. The water flow rate used was 0.6 litres per minute, and running time approximately 5 minutes. The stroke frequency varied somewhat and was between 1.28 s^{-1} and 1.51 s^{-1} (mean 1.42 s^{-1} and standard deviation 0.07). For the tests, different current intensities were used: 0.12 A, 0.18 A, 0.225 A and 1.78 A. At the first step, the lowest current intensity (0.12 A) was used. After sedimentation (at least 12 hours) and decantation, the magnetic part (retaining) was filtered, dried and weighed. The passed material was again separated to magnetic (retaining) and non-magnetic (passing) fractions using the next highest current intensity (0.18 A). After the whole test sequence, the particle size classes had been split into five samples of which four represent magnetic fraction (magnetite concentrate) and one non-magnetic fraction (waste). The input and output data and mass of the magnetic and the non-magnetic fractions after every test is displayed in Appendix 10. As an example, the result related to sample 6354 (D3) is presented as a cumulative distribution graph of the properties displayed in Figure 25. The numeric data is displayed in Table 5 (Böhm 2011).

Table 5. The mass fractions of property and Fe and SiO_2 grade for two particle size classes of sample 6354 for cumulative frequency curve from the Davis magnetic tube tests.

6354 (D3) 0.1 / 0.04 mm				
B [T]	**Mass** [g]	**Mass** [%]	**Fe** [%]	**SiO_2** [%]
0.12	2.72	8.76	56.70	1.73
0.18	21.59	69.51	65.47	1.47
0.225	2.64	8.50	53.70	3.06
1.78	1.78	5.73	8.54	28.67
> 1.78	2.33	7.50	3.13	11.08
Σ	31.06	100.00	55.76	3.91

6354 (D3) < 0.04 mm				
B [T]	**Mass** [g]	**Mass** [%]	**Fe** [%]	**SiO_2** [%]
0.12	0.82	2.76	58.00	1.01
0.18	18.92	63.68	68.27	0.54
0.225	4.51	15.18	57.60	1.28
1.78	0.26	0.88	48.20	7.87
> 1.78	5.2	17.50	2.60	11.53
Σ	29.71	100.00	54.69	2.65

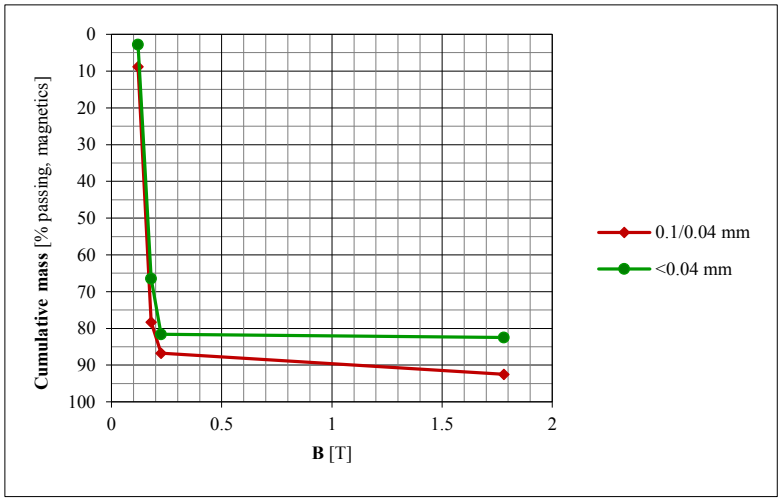

Figure 25. The cumulative frequency curve for sample 6354 (D3) based on data from the Davis magnetic tube tests. (two particle size classes after the comminution with the laboratory ball mill 0.1/0.04 mm and < 0.04 mm) displayed in Table 5.

5.1.3 Davis magnetic tube tests for characterization of ore type B2

For the Davis magnetic tube tests, 18 sub-samples were selected representing the three finest particle size classes (80/63 µm, 63/40 µm, and < 40 µm) after comminution in the laboratory ball mill for 35 minutes. Two replicate samples with mass of approximately 21 g were used for the tests. The water flow rate was set at 0.6 litres per minute and the stroke frequency at 1.45 s^{-1} (standard deviation 0.06). The voltage was set at 120 V and three different values for amperage were used (0.1 A, 0.2 A, and 1.8 A) to get a varying magnetic field intensity. The duration of the test (running time) was about 5 minutes. At the first step the current intensity was set at 0.1 A. The magnetic fraction (concentrate) was dried and weighed after sedimentation (at least 12 hours) and decantation. The passed fraction (waste) was further separated after sedimentation and decantation to magnetic and non-magnetic fractions while using the next current intensity of 0.2 A. At the last step, the highest current intensity of 1.8 A was used and both magnetic and non-magnetic fractions were dried and weighed. After the entire test sequence, there were 4 sub-samples, of which three were magnetic fractions (concentrate) and one was non-magnetic fraction (waste) for each sample (6252, 6351, 6363, 6367, 6370, 6387) and particle size class(80/63 µm, 63/40 µm, < 40 µm). Output data for the Davis magnetic tube tests on the magnetics (magnetic concentrate) and waste are given in Appendix 11.

5.1.4 "Silica in the Mine" project

Two samples (2 x 10 g) were weighted after every comminution stage, except crushing, for the DT tests related to the "Silica in the Mine" project at LKAB's mineral processing laboratory (Fig. 26). After the test, the magnetic fraction of the samples were collected, filtered, dried, weighed and prepared for chemical analysis. The following parameters were used by the test (Niiranen & Fredriksson 2012, Waara 2013):

Inside diameter of the tube (D)……	25 mm
→ $A_{cross} = D^2 \cdot \pi / 4$…..	491 mm^2
Diameter of drive pulley……	46 mm
Water flow……	0.6 liter / minute
Frequency……	1.33 s^{-1}
Voltage……	122 V
Amperage……	3.89 A
Maximum magnetic flux density (B)……	0.76 T
Running time……	2 minutes

Figure 26. Apparatus for the Davis magnetic tube tests at LKAB's mineral processing laboratory in Malmberget.

A test with the Davis magnetic tube serves as a practical basis for judging the amenability of an ore to magnetic separation and for controlling the magnetic separation (Schulz 1963, Schulz 1964). At the beneficiation plants within LKAB, the process with respect to the wet low intensity magnetic separation (WLIMS) is validated, thus comparing the actual silica levels in the process with the silica levels in the DT concentrate. The apparatus is regarded to give an optimal result that can be expected from LKAB's wet low intensity magnetic separators (Malm 2009, Adolfsson & Fredriksson 2011).

5.2 Specific gravity

5.2.1 Determination of specific gravity with He-gas Pycnometer

For the determination of the specific gravity (density) of the particle size fractions after comminution test, a He-gas Pycnometer (Type AccuPyc 1330) was used. The AccuPyc 1330 (Fig. 27) works by measuring the amount of displaced gas. The system is pressurized with high purity He gas.

Figure 27. He-gas Pycnometer (Type AccuPyc 1330) at the laboratory of the Institute of Mineral Processing (Photo: M. Wartbichler).

The working equations for the He-gas pycnometer follows from the equation of ideal gases at a strictly constant temperature (derivation according to the Operating Instruction AccuPyc 1330, modified by Wartbichler 2014) and are given in *Equations* 4 to 10. Furthermore, the cell volume has to be calibrated before the measurement by a standard of defined volume:

$$P_e \cdot (V_{Cell} - V_{Sample}) = n_c \cdot R \cdot T \qquad \textit{(Eq. 4)}$$

$$P_a \cdot V_{Exp} = n_e \cdot R \cdot T \qquad \textit{(Eq. 5)}$$

P_e……	Elevated pressure
V_{Cell}……	Volume of the sample cell
V_{Sample}……	Volume of the sample
n_c……	Number of moles of gas in the sample cell
R……	Gas constant
T……	Ambient temperature
P_a……	Ambient pressure (initial pressure in the expansion volume)
V_{Exp}……	Volume of the expansion cell
n_e……	Number of moles of gas in the expansion cell

When opening the valve, the pressure becomes an intermediate value (P_2) given in *Equation* 6:

$$P_2 \cdot (V_{Cell} - V_{Sample} + V_{Exp}) = n_c \cdot R \cdot T + n_e \cdot R \cdot T \qquad \textit{(Eq. 6)}$$

Substitution from *Equations 4* and 5 into *Equation* 6 results *Equations* 7 and 8:

$$(P_2 - P_e) \cdot (V_{Cell} - V_{Sample}) = (P_a - P_2) \cdot V_{Exp} \qquad \textit{(Eq. 7)}$$

$$V_{Cell} - V_{Sample} = \frac{P_a - P_2}{P_2 - P_e} \cdot V_{Exp} \qquad \textit{(Eq. 8)}$$

Adding and subtraction P_a in the denominator and dividing by (P_a – P_2) in both the numerator and denominator in *Equation* 9 ($P_e - P_a$) and ($P_2 - P_a$) are redefined as gauge pressure P_{eg} and P_{2g} in *Equation* 10:

$$V_{Sample} = V_{Cell} - \left[\frac{V_{Exp}}{\left(\frac{P_e - P_a}{P_2 - P_a}\right) - 1}\right] \quad \textit{(Eq .9)}$$

$$V_{Sample} = V_{Cell} - \left[\frac{V_{Exp}}{\left(\frac{P_{eg}}{P_{2g}}\right) - 1}\right] \quad \textit{(Eq. 10)}$$

5.2.3 Determination of specific gravity at the laboratory of the Institute of Mineral Processing

When considering the specific gravity (density) determined by a He-gas Pycnometer at the laboratory of the Institute of Mineral Processing given in Table 6, it also can be concluded that the values correspond well to previous information of specific gravity of the various ore types in the Kiirunavaara iron ore deposit. The specific gravity of ore type B1 is near the same as the specific density of magnetite, which varies between 5.10 and 5.20 g/cm^3, with a mean of approximately 5.15 g/cm^3 according to the literature. Gangue minerals reduce the specific gravity of ore types B2 and D, because the density of silicates (essential gangue minerals in ore type B2) and apatite, essential gangue mineral in ore type D, is significantly lower than magnetite. There also seems to be a correlation between the Fe grade and the specific gravity because most of the iron occurs in magnetite and only an insignificant part in hematite and other gangue minerals.

Table 6. Measurement results of the specific gravity determined with He-gas Pycnometer (type AccuPyc 1330) at the laboratory of the Institute of Mineral Processing.

	Fraction [mm]	**3.15/1** [g/cm^3]	**1/0.5** [g/cm^3]	**0.5/0.315** [g/cm^3]	**0.315/0.01** [g/cm^3]	**0.01/0.04** [g/cm^3]	**<0.04** [g/cm^3]
6382 (B1)	As received	5.06	5.03	5.06	5.10	5.12	4.95
	Rod mill	-	-	5.07	5.07	5.31	4.95
	Ball mill	-	-	-	-	5.11	4.99
6365 (B2)	As received	4.85	4.80	4.94	4.88	4.90	4.53
	Rod mill	-	-	4.77	4.86	4.95	4.58
	Ball mill	-	-	-	-	4.84	4.70
6354 (D3)	As received	4.71	4.68	4.66	4.56	4.28	4.38
	Rod mill	-	-	4.84	4.89	4.50	4.57
	Ball mill	-	-	-	-	4.71	4.62

5.2.4 "Silica in the Mine" project

Related to the "Silica in the Mine" project, the specific gravity (density) was also determined at LKAB's mineral processing laboratory for the samples by a He-gas Pycnometer. It can be concluded that the values correspond well to previous information of specific gravity of the various ore types.

5.3 Specific surface area

5.3.1 Preface

Besides the particle size distribution, particle density, and particle shape, the specific surface area is of particular importance for characterization of properties of the comminution product related to particle collectives or a dispersed systems. However, there is no direct method for determining the specific surface area of the irregularly shaped particles. All currently used methods are based on determination of one or more properties of the material, which are assumed to be dependent on the specific surface area in some way or other (Svensson 1949).

The specific surface area of a particle set can be estimated from the measured size distribution, when the shape factor is known. It also can be measured by the determination of the permeametry on the fluid flow (gas or liquid) through a particle bed based on the Kozeny equation (also known as Carman-Kozeny equation) (Boehm et al. 2002). In the permeability method, a discretely dispersed system is permeated by a fluid and counters this flow with certain resistance. This flow resistance is larger, thus, the finer the powder is, the larger is specific surface area. Specific surface area refers to total surface area of entire particles in a unit mass of material. It can be displayed as volume specific surface area S_v (cm^{-1}) or mass specific area S_m (cm^2/g). Specific surface area is always obtained through indirect measurement and it is essential to specify by which method it has been determined such as Blaine or Permaran (Teipel & Winter 2011).

5.3.2 Determination of specific surface area with Blaine method and Permaran

There are two quite simple apparatuses (Fig. 28) used to determine the specific surface area especially, of the newly created surface based on the Blaine method (constant volume) and the Permeran by Outokumpu (constant pressure). Both methods to determine the specific surface area for two finest fractions of 100/40 µm and < 40 µm were used in this study at the laboratory of the Institute of Mineral Processing.

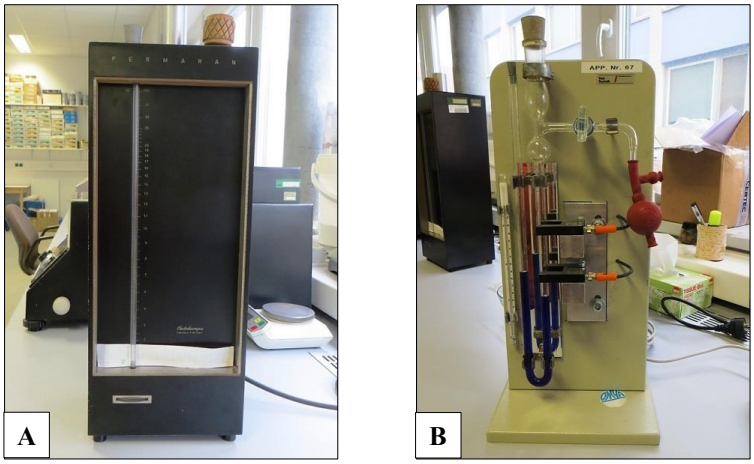

Figure 28. Permaran® (A) and Blaine (B) apparatuses used for the determination of the specific surface area at the laboratory of the Institute of Mineral Processing.

In *Equation* 11, the Darcy relationship of the pressure drop (D_p) along a particle bed of given height or length (L) is combined with the product of flow resistance, dynamic viscosity and the velocity of gas in the pores. The flow resistance is further resolved by the Kozeny equation, relating the resistance to flow of a particle bed to the square of the volume specific surface area of the pores of the bed. Back calculation to the volume specific surface area of the particles, including the empty pipe velocity, leads to the final formulation of *Equation* 11 as it is used to evaluate the results of Blaine´s apparatus based on the manual of Permeran:

$$\frac{\Delta p}{L} = c \cdot \frac{\varphi^2}{(1-\varphi)^3} \cdot a_v^2 \cdot \eta \cdot \frac{V}{A} \cdot \frac{1}{t} \qquad \textit{(Eq. 11)}$$

Δp……	Pressure drop [Pa]
L……	Total height of bed [cm]
c……	Kozeny constant [5]
φ……	Volume fraction of solids [-]
a_v……	Specific volume surface [1/cm^2]
η……	Viscosity of fluid [Pa·s]
V……	Volume of fluid [m^3]
A……	Cross section (area) of particle bed [m^2]
t……	Time of determination volume flow of fluid [s]

The volume specific surface area S_v is related to the mass specific surface area S_m according to *Equation* 12 based on the particle density ρ_p :

$$S_v = \rho_p \cdot S_m \qquad \textit{(Eq. 12)}$$

It should also be mentioned that owing to the permeation of the particle collective with air at room temperature and normal pressure, application of the Blaine apparatus is limited to volume specific

surface area (S_v) of around 3000 cm^{-1} to 12000 cm^{-1}. At volume specific surface area S_v > 12000 cm^{-1} the pores can't be regarded as large compared to the mean free path of the gas molecules. In this range, the Carman-Kozeny equation is no longer valid (Svensson 1949, Teipel & Winter 2011). The specific surface area will be discussed in detail in Chapter 6 together with state of dispersity, and in Chapter 7 together with energy consumption.

5.3.3 Svensson's method related to the "Silica in the Mine" project

The specific surface area is currently used by LKAB for controlling of the comminution at the beneficiation plants in Kiruna (Didic 2003). On the contrary, the screen analysis and, in some cases, laser diffraction (Malvern Mastersizer 2000) is used for controlling of the comminution at the beneficiation plants in Kiruna and Malmberget. An apparatus for Svensson's method is shown in Figure 29.

For the measurements, a known quantity of the granular material, whose specific surface is intended to be determined, is packed to a bed in a sample cell (Ø 3.5 cm; height 11 cm). It can be noted that, through the variations related to the bed dimensions, the pressure drop and the flow rate, the measuring range wide of Svensson's method is large. The specific surfaces varying from 10 cm^2/g up to 50 000 cm^2/g have been measured with it (Svensson 1949). For the principle of determination of the volume specific surface area (S_v) by Svensson's method see Svensson (1949).

Figure 29. Apparatus for the determination of specific surface area by Svensson's method at LKAB's mineral processing laboratory in Malmberget.

5.4 Chemical analysis

After the comminution tests and the separation with Davis magnetic tube at the laboratory of the Institute of Mineral Processing, the chemical analysis of the magnetic fraction (magnetite concentrate) and non-magnetic fraction (waste) from the Davis magnetic tube tests were carried out at the laboratory of

Labtium Oy, Finland. The used methods were XRF (Labtium method *179X*) and ICP-OES (*Inductively Coupled Plasma Optical Emission Spectrometry*, Labtium method *720p*). The analysis data on 11 essential elements is given in Appendix 12.

The chemical analysis on 11 essential elements the samples selected for characterization of the high-SiO_2 ore type B2 after crushing (as received) and comminution (10 minutes in a laboratory rod mill and 35 minutes in a laboratory ball mill) were carried out by XRF (*x-Ray Fluorescence*) for every particle size fraction at LKAB's chemical laboratory in Kiruna. The analysis data on 11 essential elements is given in Appendix 13.

Furthermore, chemical analysis on 27 elements of magnetic fractions (concentrate) and one non-magnetic fraction (waste) after DT tests was carried out by using ICP-OES (*Inductively Coupled Plasma Optical Emission Spectrometry*, Labtium's method 720p) at the laboratory of Labtium Oy. Assayed trace elements such as copper (Cu), cobalt (Co), nickel (Ni), zinc (Zn) and lithium (Li) will be ignored in this study. The data from the chemical analysis will be used to create the Henry-Reinhardt charts and to combine mineralogical data from automated mineralogy focusing on the liberation and intergrowth of magnetite and SiO_2-bearing minerals (silicates) called "middlings". The analysis data on 11 essential elements is given in Appendix 14.

Furthermore, the analysis data of these samples after crushing (as received) and comminution (10 minutes in a laboratory rod mill and 35 minutes in a laboratory ball mill) and from the DT testswas imported into iDiscover 5.3 (a software for the interpretation of the data measured by QEMSCAN). The data was used to investigate the content and distribution of silicon (Si) in different fractions and different mineral phases. In addition, the mass flow, the mass flow unit and the weight percentage for each fraction were also imported into iExplorer (Datastore). This information is essential, when data measured by QEMSCAN will be processed and certain type of reports are generated by iDiscover.

Chemical analyses related to the "Silica in the Mine" project were carried out on 11 essential elements the feed as well as the magnetic products after the DT tests using XRF (*x-ray fluorescence*) at LKAB's chemical laboratory in Kiruna. The chemical analysis includes the following elements: Fe, P, SiO_2, CaO, MgO, Al_2O_3, MnO, TiO_2, V_5O_2, K_2O and Na_2O, and also on S for some samples. The most important element, in relation to the "Silica in the Mine" project, is of course, silicon (Si) but there are indications that titanium (Ti) and vanadium (V) in the magnetic concentrate might be of importance in the near future. The amount of magnetic and non-magnetic fractions calculated in mass-% and the results of chemical analysis on the samples are stored in the database (ORACLE). Further, they will be used for estimation and determination for and the SiO_2 grade by P_{80} = 45 µm (80% passing) in the magnetite concentrate from the laboratory scale to the large-scale at the concentration plants (Chapter 10).

5.5 Additional mineral processing tests

5.5.1 Laser diffraction

By the process mineralogical tests at LKAB's, the laser diffraction was used to determine the particle size distribution below 125 µm. The Malvern Mastersizer 2000 uses the technique of laser diffraction to measure the size of particles. It does this by measuring the intensity of light scattered as a laser beam passes through a dispersed particulate sample. This data is then analysed to calculate the size of the particles that create the scattering pattern (Malvern 2015). At LKAB's mineral processing laboratory, the measurement with Malvern Mastersizer 2000 was carried out dry with compressed air (2.8 bar) as a dispersant, vibration of 50%, and Mie algorithm. Furthermore, the laser diffraction is routinely used for determination of the particle size distribution for comminution products within LKAB at the beneficiation plants in Kiruna and Malmberget (Didic & Norén 2003).

5.5.2 Satmagan test

Accurate analysis of ferro-magnetic compounds of iron, such as magnetite, is time consuming and expensive by the conventional chemical methods at the laboratory. This can be overcome by measuring the total magnetic balance of a sample in a high magnetic field, thereby measuring the magnetite content in a sample based on susceptibility of the material. Satmagan (*Saturation Magnetization Analyzer*) by Outokumpu is used for analyzing mixtures of a magnetic component (only one) and non-magnetic components (Fig. 30).

Figure 30. Satmagan by Outokumpu at the laboratory of the Institute of Mineral Processing (Photo: M. Wartbichler).

The Satmagan method is based on the magnetic balance, in which a sample containing ferromagnetic material, is weighed in gravitational and magnetic fields. If the magnetic field is strong enough (about 550 mT) to saturate the ferromagnetic material in the sample, the ratio of the two weigh-ins is linearly proportional to the amount of the ferromagnetic material (Rapiscan 2013). The Satmagan reading directly yields the desired weight fraction of the magnetic material. However, the Satmagan devices

only provide an estimation of the total magnetic content of a sample. Information about the recovery of the magnetic fraction of a sample cannot be estimated through this method (Farrell et al. 2011). The magnetite content was evaluated by Satmagan magnetic balance at the laboratory of the Institute of Mineral Processing. The results of the Satmagan test are presented as charts in Figure 31.

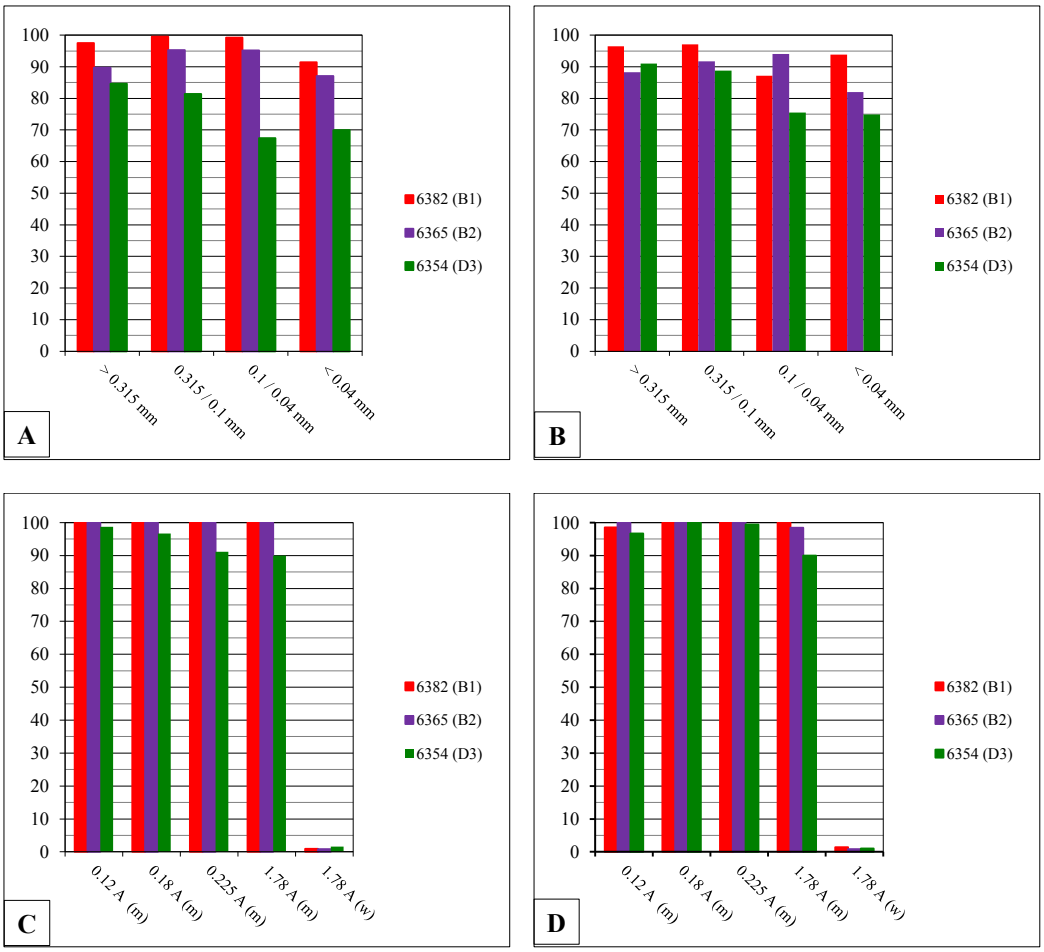

Figure 31. Results of the determination of magnetite content (wt.%) by Satmagan at the laboratory of the Institute of Mineral Processing. (A) The feed material classified into four particle size classes by screening; (B) Comminution products after grinding in the laboratory rod mill classified into four particle size classes by screening; (C) and (D) the Davis magnetic tube concentrate (m = magnetics) and waste (w = non-magnetics).

Wartbichler (2014) has studied the determination of magnetite and hematite content in the samples of martite ore from the Kiirunavaara deposit with both Satmagan (specific gravity) and the chemical analysis (total Fe vs. Fe^{+2}) in his Master's thesis. There seems to be a good correlation between these two methods and he recommended Satmagan as an alternative method to determine the magnetite content in samples of iron ore.

6. DETERMINATION OF THE DISPERSITY OF THE COMMINUTION PRODUCTS

6.1 Particle size distribution

6.1.1 Preface

Particle size distribution is by far the most important physical property of particulate samples. Particle size analysis of comminution products is a fundamental part of the laboratory testing procedure as well as in this study. It is of great importance when determining the result of the comminution and is also the first step towards establishing the degree of liberation. The primary function of the particle size analysis is, of course, to obtain quantitative information by size distribution. Screening can be regarded as one of the oldest methods of particle size analysis, in which the size is defined by a square of wire mesh. It continues to be used for many investigations because of its simplicity, low cost, and ease of interpretation. Using this method, the sample can be simply shaken on a screen until the amount of the retained particles becomes more or less constant. Alternatively, the sample can be blown with an air stream or washed with a non-reacting liquid, usually water, through the screen (Wills 2006). The latter method was also used for particle size analysis related to comminution tests carried out at LKAB's mineral processing laboratory in connection to the "Silica in Mine" project. There is also a wide range of instrumental and other methods available for particle size analysis or alternatively for the determining the result of the comminution.

6.1.2 Screen analysis

To determine the particle size distribution (PSD) in relation to the comminution tests based on the OCS carried out at the laboratory of the Institute of Mineral Processing, the comminution products were first screened with a laboratory sieve shaker and completed manually. The selected screen aperture of 3.15 mm, 1.0 mm, 500 µm, 315 µm, 100 µm, and 40 µm (DIN4188; wire mesh) were somewhat different than that used at LKAB's mineral processing laboratory. The respective results of the screen analyses is displayed in Appendix 15. The air jet screening of the particle size class 0.1/0.04 mm serves to purify the size class from < 0.04 mm material. It is necessary for the correct determination of the specific surface area thus correct evaluation of shape factor [*f*]. The data is displayed at the end of Appendix 15.

For characterization of the high-SiO_2 ore type, the particle size distribution (PSD) was, of course, determined by the screen analysis. Every comminution product was screened first mechanically with a laboratory test sieve shaker and completed manually after the comminution tests. The screen apertures used were 0.25 mm, 0.16 mm, 125 µm, 80 µm, 63 µm, and 40 µm (DIN4188; wire mesh) and somewhat different to that used at LKAB's mineral processing laboratory. The results of the screen analysis are displayed in Appendix 16.

In the relation to the "Silica in the Mine", an automated, manually controlled wet screen analysis on comminution products was carried out after each grinding stage at the LKAB's mineral processing

laboratory to obtain the particle size distribution (PSD) for estimation of the P_{80}. This value will further be used to estimate the grinding time for a laboratory ball mill to obtain P_{80} = 45 µm for the estimation of the total energy consumption. The selected screen aperture of (DIN4188, wire mesh) 5.6 mm, 4.0 mm, 2.8 mm, 2.0 mm, 1.4 mm, 1.0 mm, 710 µm, 500 µm, 355 µm, 250 µm, 180 µm, 125 µm, 90 µm, 63 µm, and 45 µm was used. Besides screening, there is also a wide range of instrumental and other methods of the particle size analysis available.

6.1.3 Comparative comminution tests at the laboratory of the Institute of Mineral Processing

According to the experience accumulated in mineral processing, "Optimized Comminution Sequence" (OCS) delivers a comminution product with a particle size distribution characterized by the smallest variation of particle sizes at a given maximum particle size independently from the used machinery. There is no technical process of mechanical multi-particle fragmentation known to produce a smaller amount of fines of a given material. Therefore this particle size distribution is regarded as a characteristic known as "Natural Breakage Characteristic" (NBC) (Boehm et al. 2002). The NBC concept originates from mechanical comminution studies carried out by Steiner (1990, 1998).

When the minerals/rock particles are broken in subsequent steps of small size reduction ratio known as OCS (Steiner1990, Steiner1998; described in Chapter 4.2.), the resulting fragmentation curve is the steepest possible. When the product stream of each circuit is classified, the resulting fragmentation curves plotted on a GGS-grid are shifted parallel vertically upwards as the comminution progresses indicating self-similarity. In Figures 32, 33, and 34, the particle size distributions are presented as plotted on a GGS grid for different ore types based on the comminution test carried out with the laboratory rod mill and the laboratory ball mill according to OCS. The numeric data of the screen analyses is displayed in Appendix 15. "As received" corresponds the feed material for comminution test crushed down to -3 mm.

It should be noted that the crushing of the sample material at LKAB's mineral processing laboratory was not done in OSC mode. This can be seen in the intersecting curve representing the feed (as received) and comminution product with the laboratory rod mill (Fig. 35), and in the particle size distribution of the feed material (As received) in Figures 32, 33, and 34. The expected PSD is presented as a dotted blue line, when the crushing had been carried out according to the OSC mode in a closed circuit of the comminution system.

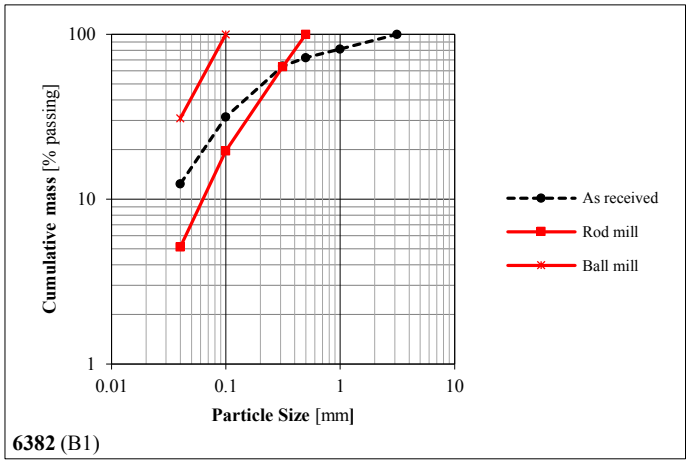

Figure 32. PSD of sample 6382 (B1) before pre-screening (as received), after the 3rd cycle in the laboratory rod mill and the 3rd and 4th cycles (combined) in the laboratory ball mill at the laboratory of the Institute of Mineral Processing.

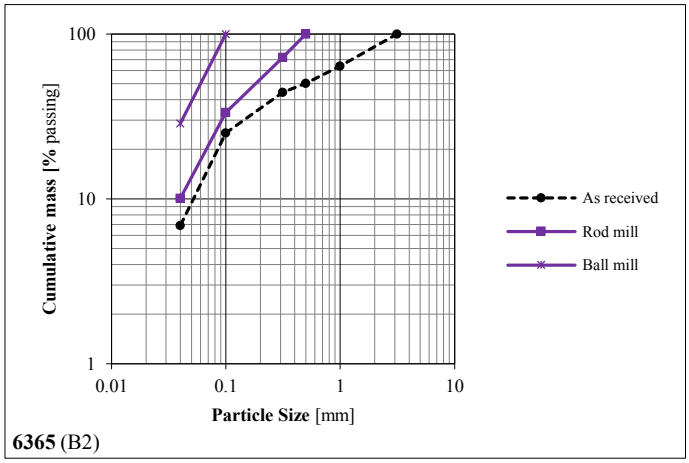

Figure 33. PSD of sample 6365 (B2) before pre-screening (as received), after the 3rd and 4th cycles (combined) in the laboratory rod mill and the 3rd and 4th cycles (combined) in the laboratory ball mill at the laboratory of the Institute of Mineral Processing.

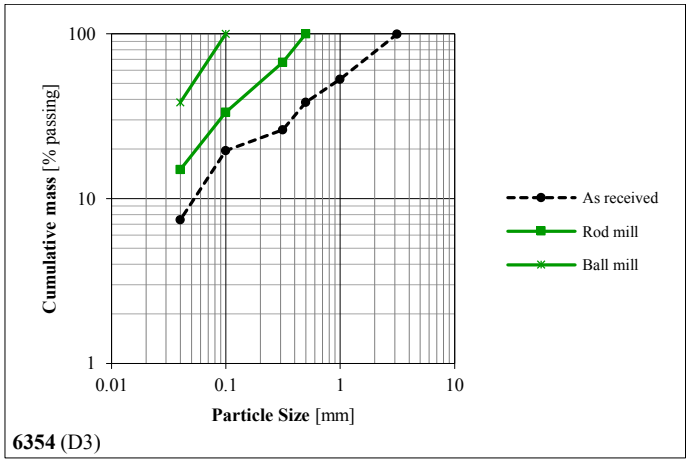

Figure 34. PSD of samples 6354 (D3) before pre-screening (as received), after the 4th and 5th cycles (combined) in the laboratory rod mill and the 3rd and 4th cycles (combined) in the laboratory ball mill at the laboratory of the Institute of Mineral Processing.

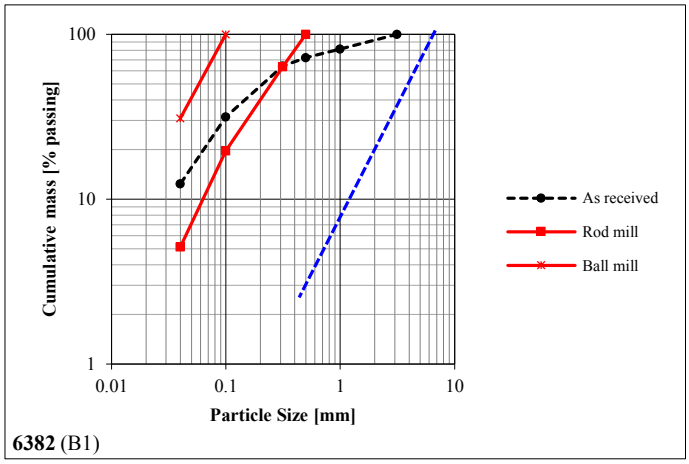

Figure 35. PSD of sample 6382 (B1, see Fig. 32). The blue dotted line presents the expected PSD for crushing according to OSC mode.

6.1.4 Particle size distribution of ore type B2

As an example, the particle size distribution is represented for the same samples, 6252 (B2) and 6351 (B2) in Figures 36 A and 36 B (Appendix 16). These results are from to comminution tests for characterization of ore type B2 carried out at the laboratory of the Institute of Mineral Processing, where cumulative undersize data are plotted against particle size on a log-log graph. In Figures 36 A and 36 B, the particle size distribution is represented after comminution for these same samples after comminution tests in the "Silica in the Mine" project to compare the particle size distribution.

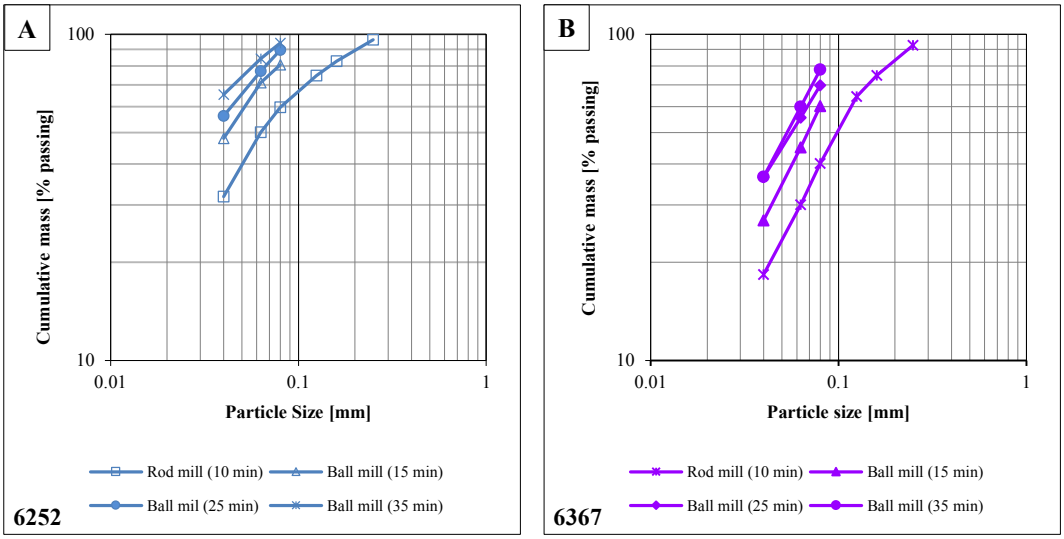

Figure 36. The particle size distribution for samples 6252 (A) and 6367 (B) after each comminution stage at the laboratory of the Institute of Mineral Processing.

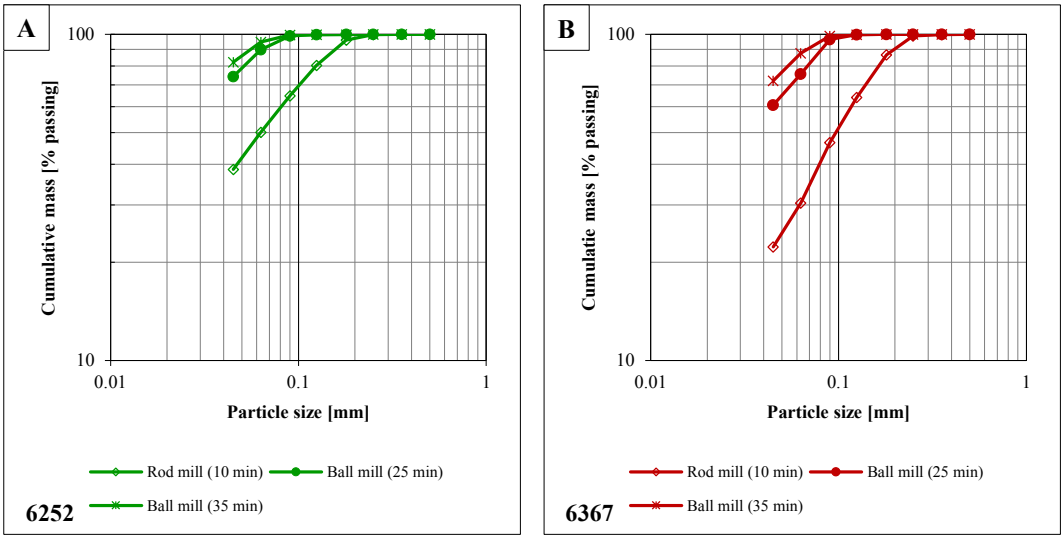

Figure 37. The particle size distribution for samples 6252 (A) and 6367 (B) after different comminution stages at LKAB's mineral processing laboratory related the "Silica in the Mine" project.

When comparing the particle size distribution of these two samples, it is obvious that the material was grinded finer at LKAB's mineral processing laboratory compared to the laboratory of the Institute of Mineral Processing despite the comminution time in laboratory rod mill and ball mill was equal. This depends most likely on the different test-sets used for comminution tests at LKAB's mineral processing laboratory (Drugge 2009), and at the laboratory of the Institute of Mineral Processing such as the mill diameter, the mass of the grinding media and the mass of material.

6.1.3 Particle size distribution related to "Silica in the Mine" project

The particle size distribution for the 18 selected samples is presented in Figure 38 for ore type B1, in Figure 39 for ore type B2, and in Figure 40 for ore type D based on the screen analysis carried out at LKAB's mineral processing laboratory, plotted on a log-log graph (GGS grid). This particle size distribution was also used to interpolated the P_{80} values for the estimation of the energy consumption and SiO_2 grade at the industrial scale (Chapters 7.3 and 10.1).

When looking at the differences between the main ore types of the Kiirunavaara deposit (B1, B2, and D) with regard to their behaviour during the different stages of the comminution, a few observations can be made. First, ore type B1 appears to be a homogenous group based on the particle size distribution presented in Figures 38 A, 39 A, and 40 A. This result was also expected. Regarding the high-SiO_2 ore type B2 in Figures 38 B, 39 B, and 40 B greater variation can be observed. This applies, in particular, to particle size distribution after comminution in the laboratory rod mill for 10 minutes. Samples 6385 and 6412 seem to have a higher comminution resistance than the other samples. The most inhomogeneous ore type to relation of the particle size distribution, is high-P ore type D presented in Figures 38 C, 39 C, and 40 C. Further, this result was expected based on the earlier information.

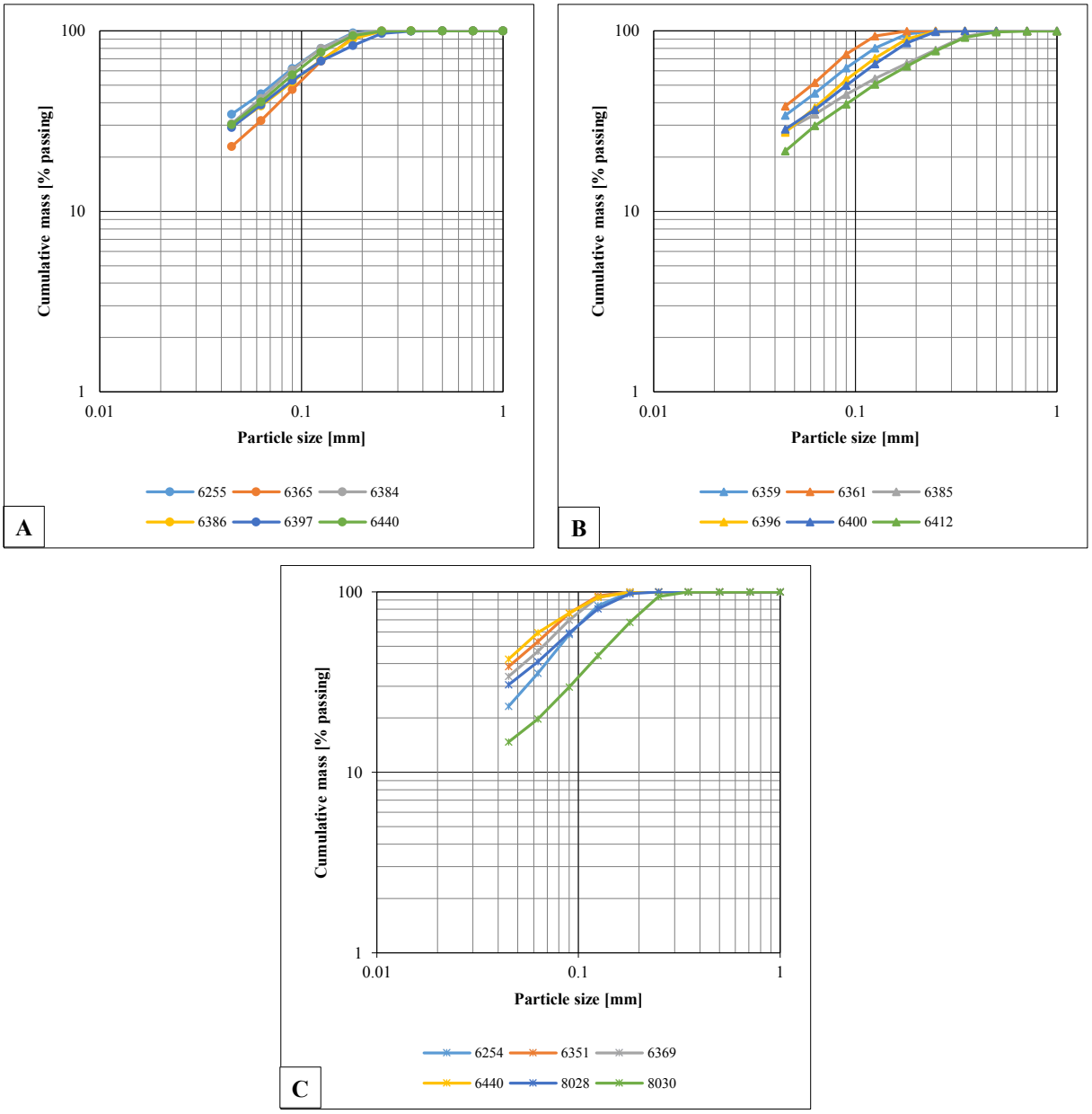

Figure 38. Particle size distribution for samples representing ore type B1 after (A), ore type B2 (B), and ore type (D) after comminution time of 10 minutes in the laboratory rod mill at LKAB's mineral processing laboratory related to the "Silica in the Mine" project. Numeric data available on CD.

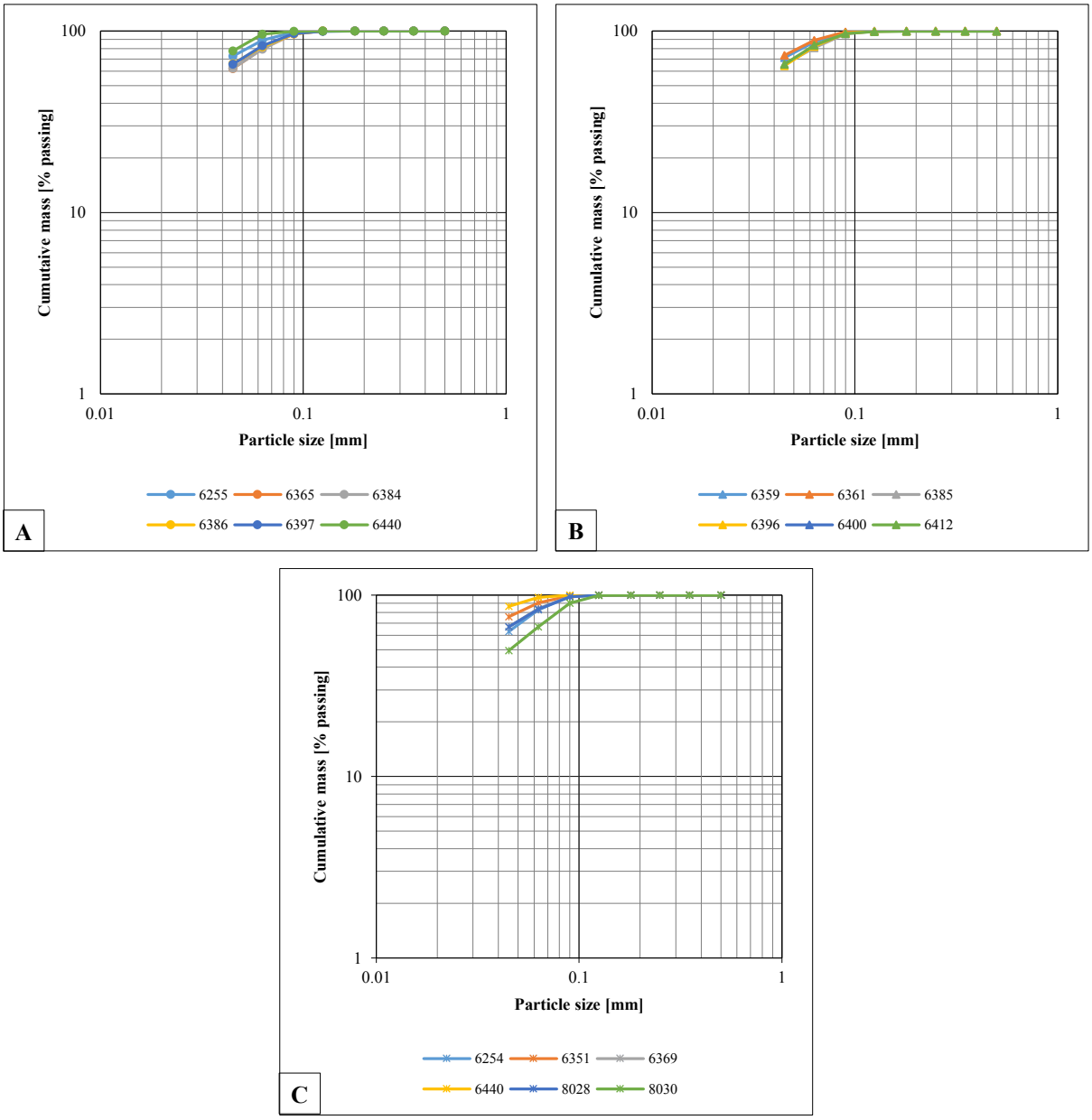

Figure 39. Particle size distribution for samples representing ore type B1 (A), ore type B2 (B), and ore type (D) after comminution time of 10 minutes in the laboratory rod mill and 25 minutes in the laboratory ball mill at LKAB's mineral processing laboratory related to the "Silica in the Mine" project. Numeric data available on CD.

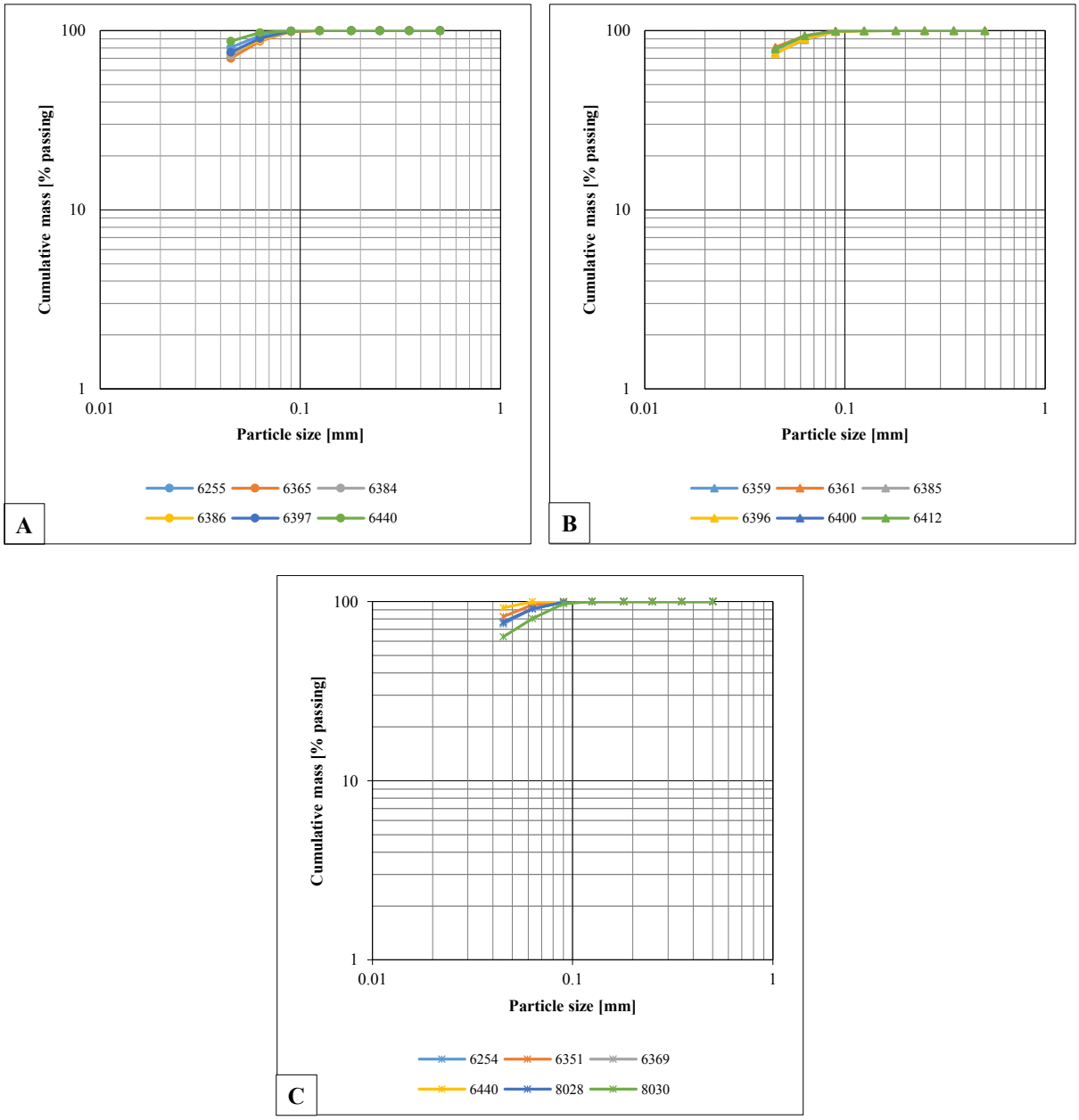

Figure 40. Particle size distribution for samples representing ore type B1 (A), ore type B2 (B), and ore type (D) after comminution time of 10 minutes in the laboratory rod mill and 35 minutes in the laboratory ball mill at LKAB's mineral processing laboratory related to the "Silica in the Mine" project. Numeric data available on CD.

6.2 Particle size distribution below 125 µm

To get some information about the particle size distribution below 45 µm a laser diffraction particle size analyser (Malvern Mastersizer 2000) was used on the comminution products from the "Silica in the Mine" project at LKAB's mineral processing laboratory because screen analysis is rarely carried out on a routine basis below 38 µm (Wills 2006).

In Figure 41, a comparison of particle size distribution determined by screen analysis and Malvern Mastersizer 2000 is shown as example for sample 6255. There are differences between particle size

distribution carried out by screening and Malvern with respect to the finer particle size classes. This is particularly evident when comparing the particle size class 45 µm.

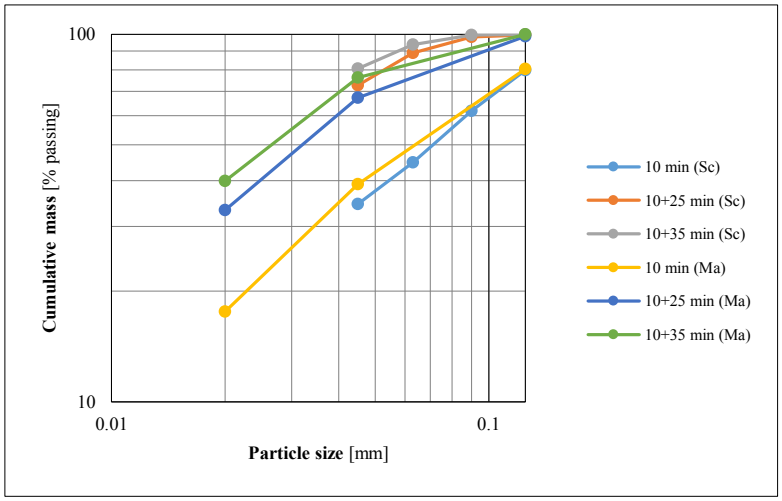

Figure 41. Comparison of particle size distribution for sample 6255 (ore type B1) determined by a screen analysis (Sc) and Malvern Mastersizer 2000 (Ma) at LKAB's mineral processing laboratory. Numeric data available on CD.

The difference seems to be increasing as more comminution steps are involved. However, no screen analysis has been carried out on the particle class < 45 µm. In any case, it is obvious that the amount of the finest fractions can be of importance when the impact of SiO_2 grade (crude ore) in the SiO_2 grade in the magnetite concentrate will be studied in an industrial scale. It should be noted that the particle size distribution on the comminution products was not determined by a laser diffraction particle size analyser after the comminution tests at the laboratory of the Institute of Mineral Processing.

6.3 Specific surface area, shape factor and P_{80} values

6.3.1 Specific surface area

6.3.1.1 Comparative tests at the laboratory of the Institute of Mineral Processing

The volume specific surface area (S_v) for samples 6382 (B1), 6365 (B2), and 6354 (D3) used is displayed in Table 7, and the mass specific surface area (S_m) in Table 8 for the particle size classes 100/40 µm and < 40 µm of the feed and the comminution products after the tests carried out at the laboratory of the Institute of Mineral Processing. Before the measurement, the samples that represented the fraction 100/40 µm was air jet sieved to remove the possible finest material remaining after the manual screening. Specific surface area is displayed as an arithmetic mean which includes three or two measurements of permeametry using the Blaine and Permaran® methods.

Table 7. Measurement results of the volume specific surface area (S_v) at the laboratory of the Institute of Mineral Processing, Montanuniversitaet Leoben. As received corresponds the feed material after crushing.

Sample	Particle Size Class [µm]	As received [cm^{-1}]	Rod mill. Cycle 3+4 [cm^{-1}]	Rod mill. Cycle 4+5 [cm^{-1}]	Ball mill. Cycle 3+4 [cm^{-1}]
6382 (B1)	100/40	1209	1473	-	1113
	< 40	8804	6893	-	9321
6365 (B2)	100/40	1134	1214	-	1180
	< 40	4484	6127	-	7983
6354 (D3)	100/40	1261	-	1244	1184
	< 40	6824	-	7876	7557

Table 8. Measurement results of the mass specific surface area (S_m) at the laboratory of the Institute of Mineral Processing, Montanuniversitaet Leoben. As received corresponds the feed material after crushing.

Sample	Particle Size Class [µm]	As received [cm^2/g]	Rod mill. Cycle 3+4 [cm^2/g]	Rod mill. Cycle 4+5 [cm^2/g]	Ball mill. Cycle 3+4 [cm^2/g]
6382 (B1)	100/40	236	278	-	218
	< 40	1779	1393	-	1868
6365 (B2)	100/40	231	245	-	244
	< 40	990	1338	-	1699
6354 (D3)	100/40	295	-	276	252
	< 40	1558	-	1724	1636

For comparison, the measurement results of the mass specific surface area (S_v) area are displayed in Table 9 for the comminution products without classification (screen analysis) after grinding tests using Svensson's method at LKAB's mineral processing laboratory.

Table 9. Measurement results of the volume specific surface area (S_v) area carried out with Svensson's method at LKAB's mineral processing laboratory.

Sample	10 Min Rod mill [cm^{-1}]	10 Min Rod mill + 25 Min Ball mill [cm^{-1}]	10 Min Rod mill + 35 Min Ball mill [cm^{-1}]
6382 (B1)	3003	6342	7770
6365 (B2)	2885	6356	7155
6354 (D3)	2633	6790	7688

6.3.1.2 Specific surface of samples for characterization of ore type B2

For the samples selected for characterization of the high-SiO_2 ore type B2, the specific surface area was determined by the Svensson's method (Chapter 5.5.3) at LKAB's mineral processing laboratory. The results of the determination of the volume specific surface area (S_v) and calculated mass specific surface area (S_m) are displayed in Table 10. It should be noted, that determination of the specific surface area was not carried out on these samples in after the grinding tests at the laboratory of the Institute of Mineral Processing.

Table 10. Measurement results of determination of the volume specific [cm^{-1}] surface area (S_v) and calculated mass specific [cm^2/g] surface area (S_m) at LKAB's mineral processing laboratory.

Sample	Methode 10 minutes		Methode 10+25 minutes		Methode 10+35 minutes	
	S_v [cm^{-1}]	S_m [cm^{-2}/g]	S_v [cm^{-1}]	S_m [cm^{-2}/g]	S_v [cm^{-1}]	S_m [cm^{-2}/g]
6252	3575	746	6680	1397	7897	1652
6351	3988	790	8190	1599	9835	1902
6363	2516	527	5977	1256	7124	1497
6367	2434	498	5764	1179	6883	1408
6370	5092	1140	6923	1594	8258	1901
6387	3208	666	6677	1388	7773	1613

6.3.2 Shape factor

The shape factor (*f*) is defined as a proportional factor relating the reciprocal of the surface equivalent particle size (k_e) to the volume specific surface area (S_v) given in *Equation* 13:

$$f = k_e \cdot S_v \qquad \textit{(Eq. 13)}$$

The equivalent particle size [k_e] can be derived from *Equation 19* if the distribution function is given as the potential distribution (GGS distribution). GGS-modulus can be calculated from *Equation* 14. It should be noted that *Equation* 14 is only valid for GGS distribution. RRS (Rosin-Rammler) or other distribution display other k_e and Equations:

$$k_e = \left(\frac{1}{n} - 1\right) \cdot \frac{D_u - D_l}{\frac{D_l}{k_l} - \frac{D_u}{k_u}} \qquad \textit{(Eq. 14)}$$

$$n = \frac{lg\frac{D_u}{D_l}}{lg\frac{k_u}{k_l}} \qquad \textit{(Eq. 15)}$$

k_e…… Surface equivalent particle size [m]

n…… GGS-modulus of the particle size class

D_u , D_o….. cumulative passing at the upper and lower particle size limit

k_u , k_l…… upper and lower particle size limit [m]

Table 11. Shape factors for the particle size class 100/40 µm (shape factor for sphere = 6).

	Shape factor		
	< 3.15 mm	**< 0.5 mm**	**< 0.1 mm**
6382 (B1)	7.92	9.64	7.29
6365 (B2)	7.57	8.11	7.88
6354 (D3)	8.15	8.04	7.65

The shape factor, displayed in Table 11, is assumed to remain constant for all of the particle size classes. It can also be assumed that the sum of the measured specific surface area of the size classes 100/40 µm and < 40 µm make up at least 90% of the total specific surface area of the sample. The specific surface area of the remaining particle size classes can be estimated from their surface equivalent [k_e] and the shape factor [f]. There are two earlier determinations of the shape factor of magnetite ore from the Kiirunavaara deposit by Rohmoser et al. (2007): 7.83 and 9.41, which correspond well with the shape factors determined in this study. Unfortunately, information on the ore type of these samples is lacking in their report. Wartbichler (2014) has also determined the shape factor for the magnetite-hematite ore (martite) from the Kiirunavaara deposit after several comminution stages and it varies between 6.77 and 7.16 (mean 6.8). For more information, see Boehm (2010).

6.3.3 P_{80} values

6.3.3.1 P_{80} values for comminution products at the laboratory of the Institute of Mineral Processing

Particle size distribution can also be used to interpolate P_{80} values after each comminution stage at LKAB's mineral processing laboratory. P_{80} values are displayed for samples 6382, 6365 and 6354 in Table 12. In the internal reports at LKAB, k(80) is used for the 80% passing instead of P_{80}. The P_{80} values are used to estimate SiO_2 grade in the Davis magnetic tube concentrate at P_{80} = 45 µm (80% passing 45 µm) (Drugge 2009, Niiranen & Fredriksson 2012). Furthermore, P_{80} values are needed to estimate the recession time of the material in the laboratory ball mill to get P_{80} = 45 µm.

Table 12. Interpolated P_{80} values after each grinding stage at LKAB's mineral processing laboratory.

Sample	Ore type	P_{80} [µm]		
		10 Min / Rod mill	25 Min / Ball mill	35 Min / Ball mill
6382	B1	133	62	51
6365	B2	108	57	49
6354	D3	241	50	39

The particle size distribution after the grinding tests has also been used to interpolate P_{80} values after each grinding stage carried out at the laboratory of the Institute of Mineral Processing the same way as at LKAB's mineral processing laboratory. The values are displayed in Table 13.

Table 13. Interpolated P_{80} values for the feed and comminution products after each grinding stage at the laboratory of the Institute of Mineral Processing.

Sample	Ore type	P_{80} [µm]		
		Feed (As received)	Rod mill	Ball mill
6382	B1	85	398	83
6365	B2	196	367	83
6354	D3	223	387	81

6.3.3.2 P_{80} values related to characterization of ore type B2

The P_{80} (product, 80% passing) values has also been interpolated by the mineral processing tests at LKAB's mineral processing laboratory based on the particle size distribution. The P_{80} values for the processing mineral tests carried out in Malmberget and Leoben are displayed in Table 14.

Table 14. Comparison of P_{80} values (80% passing) interpolated from the particle size distribution after each grinding stage at LKAB's mineral processing laboratory and at the laboratory of the Institute of Mineral Processing (Appendix 16).

LKAB's mineral processing laboratory

Method	6252	6351	6363	6367	6370	6387
10 minutes	124.12	103.47	113.84	161.87	129.36	186.31
10+25 minutes	50.96	53.43	62.37	68.02	57.62	50.5
10+35 minutes	42.61	44.71	50.65	53.59	49.14	42.13

Institute of Mineral Processing, University of Leoben

Method	6252	6351	6363	6367	6370	6387
10 minutes	147.91	115.30	129.83	185.91	156.12	200.57
10+15 minutes	78.74	81.63	93.60	102.12	92.67	83.04
10+25 minutes	67.02	73.37	83.07	92.15	81.66	68.61
10+35 minutes	57.92	69.10	76.52	81.97	77.18	59.53

These P_{80} values resulting from comminution in the laboratory rod mill for ten minutes and the laboratory ball mill for 25 minutes and 35 minutes will be used to estimate the necessary time for comminution to obtain P_{80} = 45 µm based on the screen analysis carried out at LKAB's mineral processing laboratory. Furthermore, the estimated grinding time for P_{80} = 45 µm will be used to estimate the total consumption of energy at the beneficiation plants in Kiruna (Bergström & Anttila 1973, Drugge 2009). The P_{80} values also serves to predict the SiO_2 grade by P_{80} = 45 µm in the DT concentrate based on the chemical assays on SiO_2 after the Davis magnetic tube tests at the laboratory scale (Malm 2009, Drugge 2009, Niiranen & Fredriksson 2012).

It should be noted that P_{80} values are higher when comparing the comminution tests at the laboratory of the Institute of Mineral Processing and the values related to the tests concerning from the "Silica in the Mine" project. Furthermore, it can be noted that the P_{80} value in both tests are lower in the case of samples 6252, 6351 and 6387. This characteristics is obviously also related to the grindability of the different subtypes of ore type B2. In Figure 42 the distribution of all P_{80} values for entire sample population is displayed determined at LKAB's mineral processing laboratory. It should be noted that the results for samples 6252, 6351 and 6387 are slightly lower and slightly higher than for samples 6363, 6367 and 6370 for the reference value for P_{80} = 45 µm related to the beneficiation process in Kiruna (Adolfsson 1996, Drugge 2009, Niiranen & Fredriksson 2012).

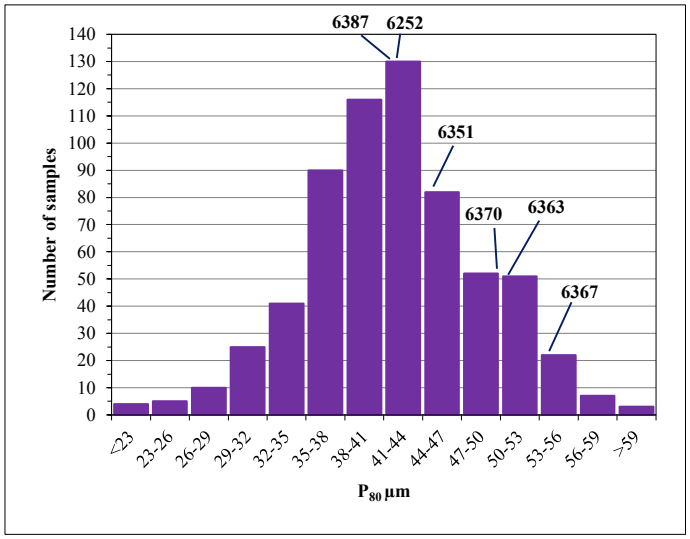

Figure 42. Distribution of P_{80} values after comminution tests carried out at LKAB's mineral processing laboratory based on data from 632 samples, which are classified as ore type B2 by geologists during core logging. Mean = 42, Median = 42, Std. Deviation = 7, Variance = 48.

6.3.3.3 P_{80} values related to the "Silica in the Mine" project

The P_{80} (product, 80% passing) values have been interpolated by the mineral processing tests at LKAB's mineral processing laboratory based on the particle size distribution. The P_{80} values for the selected samples are displayed in Table 15 (see Figures 38, 39, and 40). Statistical parameters for the whole population are displayed in Table 16.

Table 15. P_{80} values for selected samples interpolated at LKAB's mineral processing laboratory. As a method 10 minutes corresponds to the comminution of 10 minutes in the laboratory rod mill, 10+25 minutes and 10+35 minutes correspond to the comminution of 10 minutes in the laboratory rod mill, and 25 minutes and 35 minutes, respectively, in the laboratory ball mill.

Method	**6255** (B1) [µm]	**6365** (B1) [µm]	**6384** (B1) [µm]	**6386** (B1) [µm]	**6397** (B1) [µm]	**6440** (B1) [µm]
10 minutes	125	151	125	151	168	135
10+25 minutes	52	63	64	60	60	47
10+35 minutes	44	55	52	51	50	35

Method	**6359** (B2) [µm]	**6361** (B2) [µm]	**6385** (B2) [µm]	**6396** (B2) [µm]	**6400** (B2) [µm]	**6412** (B2) [µm]
10 minutes	124	99	259	149	162	267
10+25 minutes	54	52	62	60	53	59
10+35 minutes	46	44	51	51	52	46

Method	**6254** (D3) [µm]	**6351** (D3) [µm]	**6369** (D1) [µm]	**6440** (D3) [µm]	**8028** (D5) [µm]	**8030** (D3) [µm]
10 minutes	119	96	104	97	124	210
10+25 minutes	60	50	58	37	59	77
10+35 minutes	50	42	48	26	49	63

Although P_{80} values are a parameter for dispersity, in this study and in relation to the "Silica in the Mine" project, they are used as a basis for the two essential mineral processing parameters as described in previous chapter.

Table 16. Statistical characterization of P_{80} values based on information from comminution tests. 767 samples represent ore type B1, 632 samples the high-SiO_2 ore type B2, and 259 samples the high-P ore type D. The comminution times of 10, 10+25, and 10+35 minutes correspond to the same values as in Table 15.

B1	10 min	10+25 min	10+35 min
Min	61	23	6
Max	165	61	51
Mean	174	56	43
Median	154	55	43
Stdev	78	10	7
Variance	6048	92	47

B2	10 min	10+25 min	10+35 min
Min	53	26	10
Max	534	200	60
Mean	159	55	42
Median	144	54	42
Stdev	61	12	7
Variance	3690	135	48

D	10 min	10+25 min	10+35 min
Min	65	26	13
Max	542	156	143
Mean	168	53	40
Median	140	52	40
Stdev	83	12	11
Variance	6886	150	131

7. ENERGY CONSUMPTION

7.1 Optimized Comminution Sequence (OCS)

7.1.1 Preface

The objective of energy-efficient mechanical comminution is to fragmentize a set of particles of a given maximum size and a known size distribution to a defined lower maximum particle size at the minimum amount of supplied energy. The energy consumption can be directly correlated to the generated amount of the fine particles. An overproduction of fine material reflects a waste of energy because the fine material already produced causes energy dissipation by compaction while present in the comminution tool. Pre-screening serves to separate the existing fines in the feed, thus directing the energy supplied by the comminution tool to the coarse particles. The accurate intermediate screening removes the fine particles soon after their creation. High circulating load causes a short retention time of the particles within the comminution tool, resulting in a smaller number of stress events per particle and cycle. The net energy consumption and the specific surface area of selected particle size classes of the comminution product are measured at each stage, as well as the particle size distribution of the feed and the comminution product (Boehm et al. 2002).

The measurement of the net-energy consumption for the comminution of the oversize material at each stage, as well as the determination of the specific surface area of the comminution products, provide the data to construct the energy-register diagram. According to Steiner (1990, 1996), the energy register is

defined as the minimum amount of energy that has to be expended per mass unit for the comminution from the entirely non-fragmentized state to the desired maximum particle size. Vice versa the difference between two energy registers delivers the specific energy consumption.

Several sequential comminution steps can be realized at the laboratory scale at the reasonable degree of approximation to the model process as presented in Figure 43. To obtain the energy register function, the accumulated mass specific energy consumption (Δe) is plotted versus the mass specific surface area (S_m) of the assigned product. If the measured data set can be approximated by a linear function, then the slope is known as the Rittinger coefficient (R). The natural breakage characteristics (NBC) and the Rittinger coefficient are parameters for the material independent of the used comminution tools (Steiner 1991, Boehm et al. 2002). It can be used for the characterization of the comminution behaviour of a given material as in this study. The particle shape factor (Table 11) and the minimum particle size of mechanical fragmentation complete the set of material parameters.

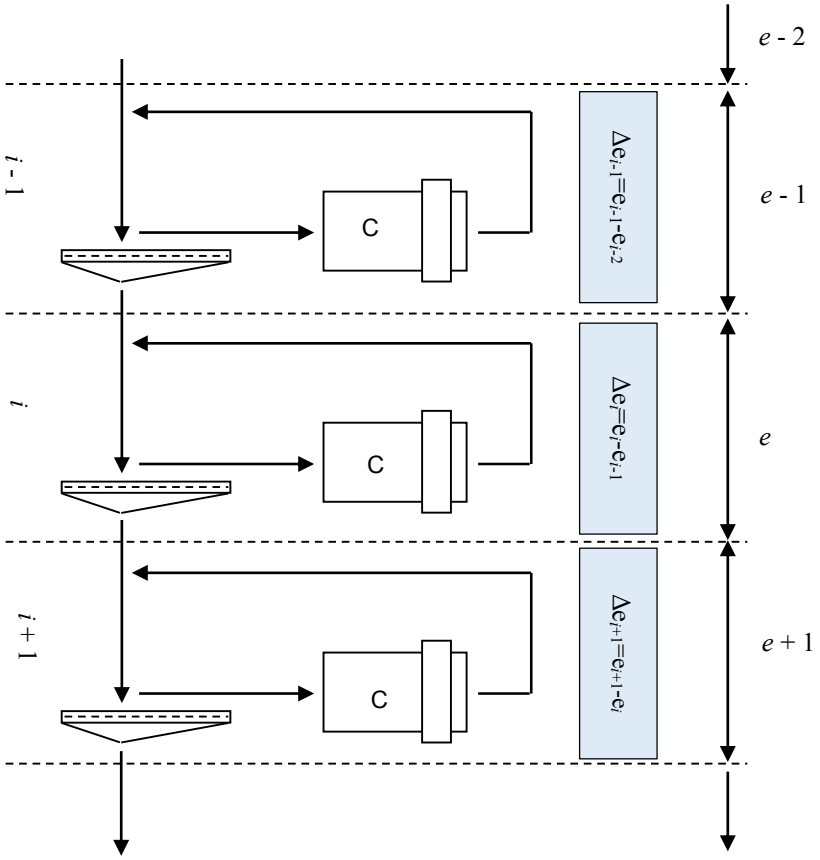

Figure 43. Flow sheet of the optimized comminution sequence, combined of several stages with pre-screening, where C = comminution machine, Δe_i = specific energy consumption in the i-stage, e_i = energy register related to the comminution product of the i-stage (Steiner 1990, Steiner 1996).

According to the empirical data collected at the Institute of Mineral Processing, the measured/estimated values from the step-wise optimized comminution confirms the hypothesis of proportionality between the energy consumption and the new created specific surface formulated by Peter Ritter von Rittinger (Steiner 1991, Boehm et al. 2002, Rohrmoser et al. 2007, Wartbichler 2014). In the case of non-energy-

optimized comminution, the plot of mass specific surface of the comminution products versus the accumulated energy consumption is characterized by a curve of decreasing inclination (Fig 44). Thus, the Rittinger's hypothesis represents the limiting case of an energy-optimized comminution for apparatus or comminution circuit, where the material is stressed mainly by compressive strength and impact.

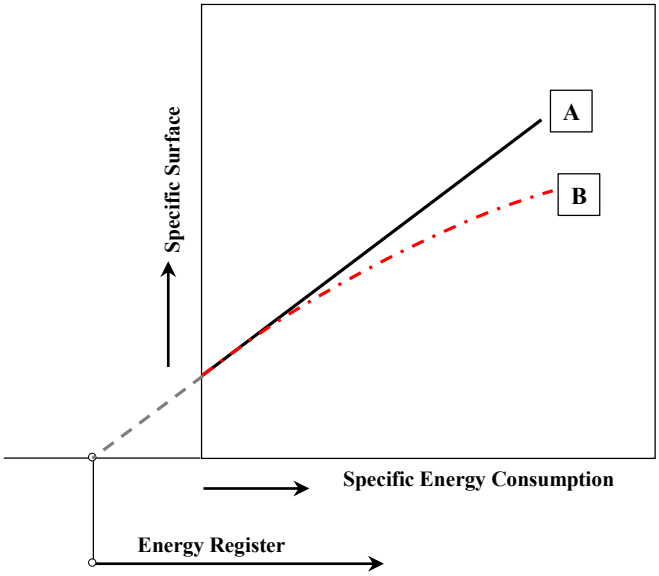

Figure 44. Simplified energy register functions for the energy-optimized comminution by OCS (A) and for the non-energy-optimized (technical) comminution (B) after Steiner (1998) and Boehm et al. (2002).

7.1.2 Energy consumption (laboratory rod mill)

According to Steiner (1996) the net power draw (E) of a tumbling mill remains constant as shown in *Equation* 16. It serves as a formalism to estimate the mass specific energy consumption (Δe) for the laboratory rod mill used for grinding tests at the laboratory of the Institute of Mineral Processing given in *Equation* 17. The following parameters are expected to be rather constant: bulk volume fraction of the mill charge inside the mill chamber, frictional conditions within the mill charge, the boundary between the charge and the shell of the tumbling mill, and the ratio of centrifugal acceleration at the perimeter of the mill chamber.

$$E = c_p \cdot M_G \cdot g \cdot D_i \cdot \frac{U}{M_F} \qquad \textit{(Eq. 16)}$$

$$\Delta e = \frac{E}{M_F} \qquad \textit{(Eq. 17)}$$

E……	Net power draw [J]
C_p…….	Power number
M_G……	Mass of the grinding media
g……	Gravity acceleration [9.81 m/s^2]
D_i……	Inside diameter of the mill [m]

U…… Number of the revolutions

M_F…… Mass of the fine material (product)

C_p is known as the power number (or Steiner factor), derived under assumption of both geometric and kinematic similarity may be expected to remain rather constant and it is distributed in general in the range C_p = 0.8 to 1.3 (Steiner 1996) . For this case, the power number C_p = 1.2 is used for the laboratory rod mill, derived from a series of calibration measurements (Boehm et al. 2002). The ratio U/M_F (= number of mill revolutions U divided by the mass of fine product M_F) is called the "specific number of revolutions" (Steiner 1996). For the calculation of the net power draw (E) , the mean of the specific number of revolutions (M_F/U) was used (Fig. 45, Tables 17, 18, and 19).

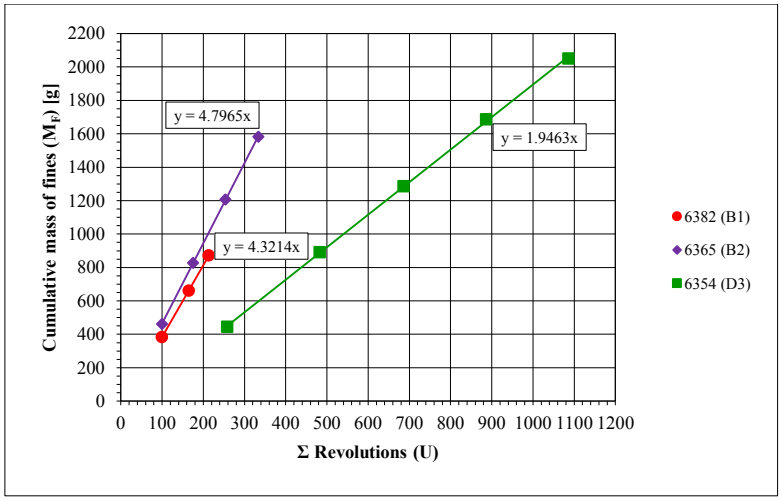

Figure 45. The specific production of fine material (M_F /U) for samples 6382 (B1), 6365 (B2), and 6354 (D3) as a function of the sum of revolutions and cumulated mass of generated fine material in the laboratory rod mill. Numeric data is displayed in Appendix 4.

However, it should be mentioned that the small amount of the sample material for the comminution tests was insufficient to make it possible to run multiple comminution cycles. The net power draw for crushing the material down to the –3 mm using a jaw crusher and a MK 25 mortar crusher was not determined, but it will be discussed in next the chapter, relating to the energy register function. Using *Equation* 16, the net power draw can be calculated for the laboratory rod mill displayed in Tables 17, 18, and 19. This data will be then used for the calculation of the total energy consumption in the OCS.

Table 17. Estimation of the net power draw for sample 6382 (B1) grinded in the laboratory rod mill at the laboratory of the Institute of Mineral Processing; g/U corresponds production of fine material per a revolution.

Sample 6382 (B1)

n_{Mean}	1.240353 s^{-1}	Mass of grinding media (M_G)	7.802 kg
n_c	1.796 s^{-1}	Mill internal diameter (D)	0.154 m
n/n_c,	69.06%	Power number (C_P)	1.2
		Specific production of fine material (M_F / U)	4.321 g/U
Net power draw:			
$E = C_p \cdot g \cdot D \cdot M_G \cdot U/M_F \cdot 1000$			3273 J/kg

Table 18. Estimation of the net power draw for sample 6365 (B2) grinded in the laboratory rod mill at the laboratory of the Institute of Mineral Processing; g/U corresponds production of fine material per a revolution.

Sample 6365 (B2)

n_{Mean}	1.240353 s^{-1}	Mass of grinding media (M_G)	7.802 kg
n_c	1.796 s^{-1}	Mill internal diameter (D)	0.154 m
n/n_c,	69.06%	Power number (C_P)	1.2
		Specific production of fine material (M_F / U)	4.797 g/U
Net power draw:			
$E = C_p \cdot g \cdot D \cdot M_G \cdot U/M_F \cdot 1000$			2949 J/kg

Table 19. Estimation of the net power draw for sample 6354 (D3) grinded in the laboratory rod mill at the laboratory of the Institute of Mineral Processing; g/U corresponds production of fine material per a revolution.

Sample 6354 (D3)

n_{Mean}	1.240353 s^{-1}	Mass of grinding media (M_G)	7.802 kg
n_c	1.796 s^{-1}	Mill internal diameter (D)	0.154 m
n/n_c,	69.06%	Power number, C_P,	1.2
		Specific production of fine material (M_F / U)	1.946 g/U
Net power draw:			
$E = C_p \cdot g \cdot D \cdot M_G \cdot U/M_F \cdot 1000$			7267 J/kg

The mass specific energy consumption (Δe) for samples grinded in the laboratory rod mill can be calculated from *Equation* 17, as displayed in Table 20. The net power draw for ore type D is significantly higher than for ore types B1 and B2. It should be noted that this applies only to the comminution in the laboratory ball mill. Furthermore, it is not known if there are several subtypes of ore type D with different grindability, as is the case for ore type B2.

Table 20. Mass specific energy consumption (Δe) for samples 6382 (B1), 6365 (B2) and 6354 (D3) to get 100% < 3.15 mm to 100% < 0.5 mm (laboratory rod mill). The entire data is given Appendix 18 and data for screen analysis is in Appendix 15.

Sample	**6382** (B1)	**6365** (B2)	**6354** (D3)
3.15 / 0.5 mm [wt.%]	27.82	49.69	61.55
< 0.5 mm [wt.%]	72.18	50.31	38.45
E [J/kg]	3273	2949	7267
Δe [J/g]	0.911	1.47	4.47
[J/kg]	911	1465	4473
[kWh/t]	0.25	0.41	1.24

7.1.3 Energy consumption (laboratory ball mill)

For the measurement of the total consumption of energy supplied to the ball mill, a torque sensor type Hottinger Baldwin T1 with a measuring and a recording unit was available at the laboratory of the Institute of Mineral Processing. With this equipment, the measuring shaft is bolted to the drive shaft between the electric drive and the mill over two rigid couplings. Four rotating gauges are placed in a Wheatstone bridge circuit onto the actual measuring body so that they are either stretched or compressed by measuring torque. The technical data for this laboratory tumbling mill is displayed in Table 3.

The ultimate goal of the power draw measurement is the determination of the net power draw of the mill, i.e., the power demand to tumbling the mill charge. To obtain reliable results, calibration procedure corrections are necessary (Steiner 1996). Also, for the comminution tests with the laboratory ball mill related to this study, the ball mill was calibrated empty with various external loads to determine the mean of the torque both before and after every comminution sequence. After calibration, the measurement structure for the measurement data provided the conversion of the signals in a torsional and integral by recorder averaging of the time course of the torque over the measurement's period of time. The relationship between torsion and output voltage of the alleged bridge circuit was determined before each measurement and defined by torque load. The net torque during the comminution time is used for the estimation of the specific energy consumption of the ground material. The calibration data for the mean torque is displayed in Appendix 7 and integration units from the recorder are given in Appendix 17. The value of mean torque (ΔM_D) is estimated using *Equations* 18 and 19:

$$C = b \cdot B \qquad (Eq.\ 18)$$

$$\Delta M_D = C \cdot \Delta\left(\frac{IE}{t}\right) \qquad (Eq.\ 19)$$

b.....	Mean torque (Appendix 7).
B……	1.25 (constant)
IE……	Integration units from recorder (Appendix 17)
t……	Retention time of material in the mill

When the mean net torque (ΔM_D) is estimated and the number of revolutions (U) was recorded by the comminution (Appendix 17), the net energy consumption (ΔE) for the total mass of the feed can be estimated from *Equation* 20 and the power (N) from *Equation* 21.

$$\Delta E = 2 \cdot \pi \cdot \Delta M_D \cdot U \qquad (Eq.\ 20)$$

$$N = \frac{\Delta E}{t} \qquad (Eq.\ 21)$$

7.1.4 Mass specific energy consumption

As in the case of the laboratory rod mill, the mass specific energy consumption (*Δe*) can be estimated for the each comminution cycles in the laboratory ball mill using *Equation* 22, where M_F is the mass of generated fine material, which is obtained from the mass of the feed by means of the screen analysis. The estimation of the total consumption of energy and the mass specific consumption of energy is displayed in Table 21 and presented graphically in Figure 46, based on data from the comminution tests in a laboratory ball mill in closed circuit (see also Appendix 17 and 18):

$$\Delta e = \frac{\Delta E}{M_F} \qquad (Eq.\ 22)$$

Table 21. The mass specific energy consumption (*Δe*) for samples 6382 (B1), 6365 (B2) and 6354 (D3), to get 100% < 0.5 mm to 100 % < 0.1 mm. The entire data is given Appendix 18 and data for screen analysis is in Appendix 15.

Sample	**6382** (B1)	**6365** (B2)	**6354** (D3)
0.5 / 0.1 mm [wt.%]	62.94	58.27	59.56
< 0.1 mm [wt.%]	37.06	41.73	40.44
Δe' [J/kg]	42891	28941	26670
Δe [J/kg]	26995	16863	15885
[J/g]	27.00	16.86	15.89
[kWh/t]	7.50	8.04	4.41

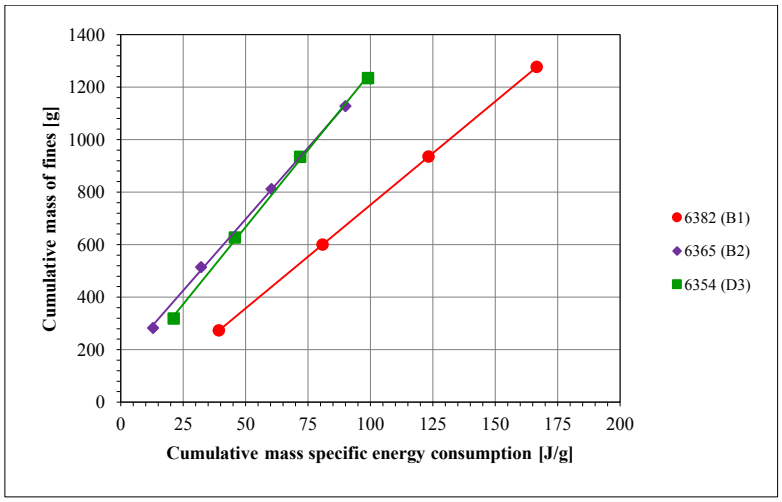

Figure 46. Mass specific energy consumption for samples 6382 (B1), 6365 (B2) and 6354 (D3) based on data from the comminution tests in the laboratory ball mill at the laboratory of the Institute of Mineral Processing. Numeric data is displayed in Appendix 17.

When looking at the mass specific energy consumption (*Δe*), some conclusions can be made in relation to the grindability of the three different ore types. Ore type B1, represented by sample 6382, clearly seems to differ from the other two ore types, B2, represented by sample 6365, and D3, represented by sample 6354, when grinding in the laboratory ball mill. Ore type B1 seems to be characterized by higher comminution resistance. In other words, clearly more energy is needed to produce the same amount of

fine material by grinding compared to the other ore types, B2 and D3. Both the mass specific (S_m) and the volume specific surface area (S_v) are lower for ore type B1, in fraction 100/40 µm, but higher in fraction < 40 µm compared to the other ore types, B2 and D3 (Fig. 46, Table 21). This result will be studied in more detail in Chapter 11.

7.1.5 Rittinger coefficient

The point of the Rittinger theory of comminution is that there is assumed to be a proportionality between the energy input and the creation of new surface. First published by Rittinger in 1867, it states that the increase of the specific surface related to the energy consumption is called the "Rittinger coefficient", no matter what the existing relation between the energy input and the surface production is. It can be defined as the ratio of the increase of the volume specific surface (Δa) to the volume specific net energy consumption (Δe). However, it is well known that this equation cannot be confirmed for any type of comminution system, especially not for the energy inefficient open circuit designs, where a clear decrease in surface development with increasing energy input is observed (curve B, Fig. 44). But for energy-optimized comminution circuit according OCS-method, obeying the principles are relevant. First, the OCS-method consists a large number of comminution stages with a small size reduction ration. Second, the adjustment of the comminution tool is optimized in relation to the feed size. Third, the comminution circuit is closed design and the circulating load is high. However, during the experimental tests, the Rittinger's hypothesis might be confirmed especially for the compressive and impact stress (Steiner 1991). According to Steiner (1991), the Rittinger coefficient (R) of proportionality of raw mineral material usually covers a range between 10 and 150 cm^2/J.

7.1.6 Energy register diagrams

As indicated in Chapter 7.1, the energy register function of any comminution step, such as a crusher, a laboratory ball mill and a laboratory rod mill, can be calculated from the accumulation of the specific energy consumption and the successive size-reduction steps (Appendices 8 and 23). These values are assigned to the mass specific surface of the comminution products and are used to construct the energy register diagrams (Fig. 47 and 48) (Boehm et al. 2002, Rohmoser et al. 2007, Wartbichler 2014). The energy register of the comminution products of the first two stages (1^{st}: crushing stage with a jaw crusher, 2^{nd}: crushing stage with cone crusher at LKAB's mineral processing laboratory) can be obtained by linear extrapolation (Fig. 47).

For all samples, representing different ore types, the succession of the points can be approximated by a straight line (Fig. 47). In addition, the Rittinger coefficient can be obtained through estimation of the inclination of the linear approximation (Fig. 48 A, B, and C). It should be noted that these three samples, representing the three main ore types of the Kiirunavaara deposit, show a difference in their breakage

behaviour under the controlled comminution tests according to the principles of the OCS. This will be discussed in detail in Chapter 11.

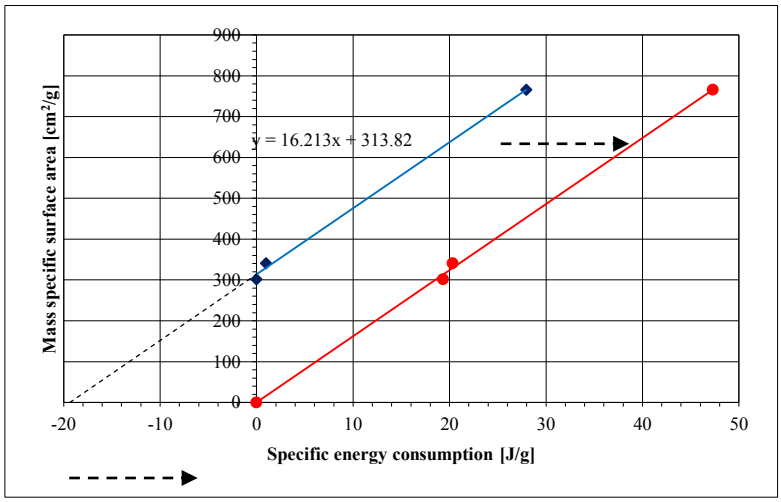

Figure 47. The linear extrapolation of the energy register function for sample 6382 (B1). Numeric data is displayed in Appendix 18 (see also Fig. 44).

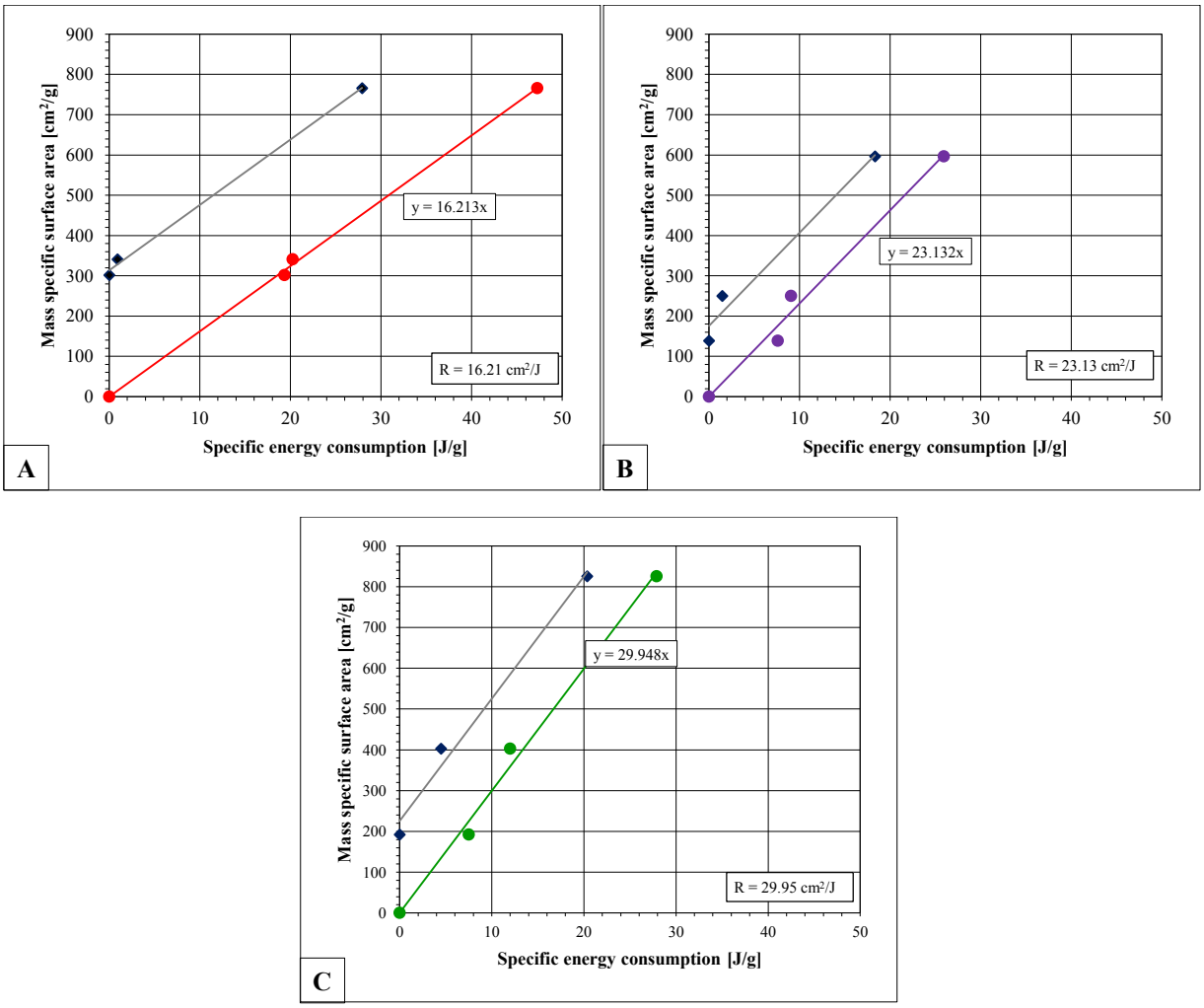

Figure 48. Energy register function of (A) sample 6382 (B1), (B) sample 6365 (B2), and (C) sample 6354 (D3). Numeric data is displayed in Appendix 18. R = Rittinger coefficient [cm²/J].

When looking the energy register presented in Figures 48 A, B and C, the slope of the energy register function seems to be flatter than compared to the earlier investigations of Rohmoser et al. (2007) and Wartbichler (2014). There seems to be a clear difference between the comminution stages carried out by the laboratory rod mill and laboratory ball mill. This will be discussed in detail in Chapter 11 (Conclusions and discussion).

7.2 Energy consumption in open comminution circuit used for characterization of ore type B2

7.2.1 Energy consumption (laboratory rod mill)

The net power consumption of a tumbling mill remains constant and *Equation* 23, derived by Steiner (1996), serves a formalism to estimate the energy consumption for a laboratory rod mill and is used to evaluate comminution tests at the laboratory of the Institute of Mineral Processing as already presented in Chapter 7.1.2:

$$E = C_p \cdot M_k \cdot g \cdot D_i \cdot U \qquad (Eq.\ 23)$$

E……	Net power draw [J/kg].
C_p……	Power number (or Steiner factor).
M_K……	Mass of grinding media [kg].
g……	Gravity acceleration 9.81 [m/s^2].
D_i……	Inside diameter of the mill [m].
U……	Number of revolution.

C_p was determined from calibration measurements (laser aberration measurement) by Steiner (1996). The specific energy was calculated at C_p = 1.1 referring to the energy transferred from the grinding media into the product, i.e. the energy input into material (M_{MK}). The total power consumption necessary for moving the total charge (grinding media and product) is calculated by a factor C_p = 1.2, i.e. the energy in the grinding chamber ($M_{MK} + M_{Feed}$). These factors are derived at a degree of filling (*DoF*) of 40 vol.% and a percentage of critical speed (n_c) of 70%. Furthermore, the following parameters are expected to be rather constant according to Steiner (1996): the bulk volume fraction of the mill charge inside the mill chamber, frictional conditions within the mill charge and the boundary between the charge and the shell of tumbling mill and the ratio of centrifugal acceleration at the perimeter of mill chamber. As far as the conditions of kinetic and kinematic similarity criteria are fulfilled (n/n_c = 0.7 and *DoF* = 40 vol.%), the data derived from the formula (*Equation* 23) can be directly used for mill design. For this particular case, the power number C_p = 1.2 for the laboratory rod mill will be used as derived from a series of calibration measurements (Steiner 1996, Boehm et al. 2002). The data is displayed in Table 22.

Table 22. The net power draw (*E*) for the laboratory rod mill by comminution tests carried out at the laboratory of the Institute of Mineral Processing (Steiner 1996).

Sample	C_p	M_k [kg]	g [ms^{-2}]	D_i [m]	U	E (Energy) [J]
6252	1.2	6.0011	9.81	0.152	550	5905.92
6351	1.2	6.0011	9.81	0.152	500	5369.02
6363	1.2	6.0011	9.81	0.152	750	8053.52
6367	1.2	6.0011	9.81	0.152	400	4295.21
6370	1.2	6.0011	9.81	0.152	350	3758.31
6387	1.2	6.0011	9.81	0.152	400	4295.21

The mass specific energy consumption (Δe) for this comminution stage can be estimated from *Equation* 24 (Steiner 1996),where M_F corresponds to the mass [kg] of the fine material (< 125 µm) generated and *E* to the net power draw [J]:

$$\Delta e = \frac{E}{M_F} \qquad (Eq.\ 24)$$

The estimation for the mass specific energy consumption (Δe) is shown in Table 23 based on the comminution tests in a laboratory rod mill in open circuit, where *E* is the net power draw (*Eq. 23*) and M_F the mass of fine material generated during the comminution (< 125 µm in this particular case), which is obtained from the mass of the feed based on the screen analysis (Appendix 16).

Table 23. The net power draw (*E*) and the mass specific energy consumption (Δe) for M_F (generated fine material during the comminution, < 125 µm) based on the comminution tests in the laboratory rod mill at the Institute of Mineral Processing.

Sample	Feed [g]	M_F [g]	E (Energy) [J]	Δe (Energy to mass) [J/g]	[kWh/t]
6252	678.4	507.14	5905.92	11.65	3.24
6351	591.2	504.62	5369.02	10.64	2.96
6363	798.8	626.62	8053.52	12.85	3.57
6367	591.6	381.58	4295.21	11.26	3.13
6370	549.9	391.24	3758.31	9.61	2.67
6387	591.8	394.52	4295.21	10.89	3.03

7.2.2 Energy consumption (laboratory ball mill)

For the measurement of the total consumption of energy supplied to the ball mill, a torque sensor type Hottinger Baldwin T1 was available at the mineral processing laboratory of the Institute of Mineral Processing. In this equipment, the measuring shaft is bolted to the drive shaft between the electric drive and the mill over two rigid couplings. Four rotating gauges are placed in a Wheatstone bridge circuit onto the actual measuring body so that they are either stretched or compressed by measuring torque. The torque, proportional to the measurement signal, is passed to recording equipment in millivolts per volt of constant supply voltage via a signal amplifier. The recording equipment consists of a measuring unit and a recording unit. The technical data for this laboratory tumbling mill is displayed in Table 2.

After calibration, the measurement structure the processing software for the measurement data provides the automatic conversion of the voltage signals in a torsional and integral averaging of the time course of the torque over the measurement's period of time. The calibration data for the laboratory ball mill is displayed in Appendix 8. The relationship between torsion and output voltage of the alleged bridge circuit is determined before each measurement and defined by moment load. The mean torque during the comminution time is used for the estimation of the specific energy consumption of the ground material. In addition, the energy consumption for open comminution circuit can be estimated from *Equation* 25:

$$\Delta E = 2\pi \cdot \Delta M_D \cdot U \qquad (Eq.\ 25)$$

Where ΔM_D is the mean net torque moment and U the number of revolutions. The results for each comminution stage are shown in Table 24, where the ΔE is calculated for the total mass of feed.

Table 24. Measured values of the total energy consumption (ΔE) based on the comminution tests (open circuit) in the laboratory ball mill carried out at the laboratory of the Institute of Mineral Processing.

Sample	Comm. stage	Time [min]	U [1]	Feed [g]	ΔM_D [Nm]	ΔE (Energy) [J]
6252	1	15	957	1416.6	3.693	22438.57
	2	25	1596	1416.5		37008.54
	3	35	2232	1416.1		51296.58
6351	1	15	957	1395.5	3.475	21253.56
	2	25	1596	1395.2		34661.99
	3	35	2232	1395.0		48155.27
6363	1	15	957	1456.7	3.509	21304.22
	2	25	1596	1456.6		35109.66
	3	35	2232	1456.7		48833.81
6367	1	15	957	1490.0	3.689	22415.37
	2	25	1596	1489.9		36969.85
	3	35	2232	1490.1		51242.48
6370	1	15	957	1338.6	3.526	21244.53
	2	25	1596	1338.6		35385.25
	3	35	2232	1338.5		49301.09
6387	1	15	957	1504.0	3.610	22001.36
	2	25	1596	1504.1		36132.22
	3	35	2232	1504.5		50020.71

As in the case of the laboratory ball mill at the laboratory of the Institute of Mineral Processing, the mass specific energy consumption (w_m) can be estimated for the three different comminution stages (15, 25 and 35 minutes) using *Equation* 26 where M_F is the mass of generated fine material (in this particular case < 40 μm), which is obtained from the mass of the feed by means of the screen analysis. The estimation of the total consumption of energy and the mass specific consumption of energy is shown in Table 25 based on the comminution tests in a laboratory ball mill in open circuit.

$$w_m = \frac{\Delta E}{M_F} \qquad (Eq.\ 26)$$

When comparing the total energy consumption (ΔE) to the mass specific energy consumption (w_m), shown in Table 25, a difference can be noted between the two subtypes B2-a and B2-b which were defined in Chapters 8.3 and 8.4 based on their mineralogy.

Table 25. Total consumption of energy (ΔE) and the mass specific energy consumption (w_m) for M_F (generated fine material during the comminution, < 40 µm) based on the comminution tests with the laboratory ball mill at the laboratory of the Institute of Mineral Processing. Comminution times were 15, 25 and 35 minutes.

Sample	Comm. stage	Time [min]	Feed [g]	M_F [g]	Energy [J]	W_m (Energy to mass) [J/g]	[kWh/t]
6252	1	15	1416.6	679.93	22438.57	33.00	9.17
	2	25	1416.5	796.22	37008.54	46.48	12.91
	3	35	1416.1	926.17	51296.58	55.39	15.39
6351	1	15	1395.5	599.68	21253.56	35.44	9.85
	2	25	1395.2	625.75	34661.99	55.39	15.39
	3	35	1395.0	777.74	48155.27	61.92	17.20
6363	1	15	1456.7	699.18	21304.22	30.47	8.46
	2	25	1456.6	818.76	35109.66	42.88	11.91
	3	35	1456.7	952.72	48833.81	51.26	14.24
6367	1	15	1490.0	400.8	22415.37	55.93	15.54
	2	25	1489.9	543.77	36969.85	67.99	18.89
	3	35	1490.1	545.13	51242.48	94.00	26.11
6370	1	15	1338.6	532.15	21244.53	39.92	11.09
	2	25	1338.6	604.25	35385.25	58.56	16.27
	3	35	1338.5	653.81	49301.09	75.41	20.95
6387	1	15	1504.0	733.4	22001.36	30.00	8.33
	2	25	1504.1	875.83	36132.22	41.26	11.46
	3	35	1504.5	932.81	50020.71	53.62	14.90

The total consumption of energy (ΔE) is quite equal both for samples 6252, 6363, and 6387 representing subtype B2-a, and for samples 6351, 6367 and 6370 representing subtype B2-b. However, comparing the mass specific energy consumption (w_m) for the finest fraction (< 40 µm) between these two subtypes, a clear difference can be noted. The mass specific energy consumption (w_m) shown in Table 25 is significantly lower for subtype B2-a than for the subtype B2-b. It seems to be apparent that there exists a link between the mineralogy, actinolite ± phlogopite in the subtype B2-a versus quartz, phlogopite and albite in the subtype B2-b, and grindability (i.e. breakage characteristics). Besides the different mineralogy, ore type B2 frequently shows lower density than ore type B1, although the porosity seems to be low or absent in ore type B2 compared to ore type B1 (Aupers 2014). That can be explained by significant difference between the density of magnetite (5.1–5.2 g/cm^3) and density of silicates (e.g., actinolite 3.02–3.44 g/cm^3, phlogopite 2.76–2.90 g/cm^3, titanite 3.45–3.55 g/cm^3, quartz 2.65 g/cm^3), which are typical for ore type B2 as has already been stated.

7.2.4 Correlation between mass specific energy consumption and P_{80}

The assumed linear correlation between P_{80} values and comminution time in a laboratory ball is used to estimate the total consumption of energy to get P_{80} = 45 µm (Chapter 7.3.1) related to the "Silica in the Mine" project and will be described in detail in the next chapter. It has also already been mentioned that the comminution tests have been carried out as an open comminution system without pre-screening at the laboratory of the Institute of Mineral Processing. If it is assumed that every comminution event corresponding one stage in the closed comminution system of OCS (Steiner 1996, Steiner 1998) with the estimation of mass specific energy consumption (w_m), some conclusions can be drawn. In Figure 49, the mass specific energy consumption (J/g) and P_{80} values are compared for samples 6252, 6363, and 6387 (subtype B2-a) after comminution in a laboratory roll mill (10 minutes) and a laboratory ball mill (15, 25 and 35 minutes) and in Figure 50 for samples 6351, 6367 and 6370 (subtype B2-b). Numeric data is displayed in Tables 14, 24 and 25.

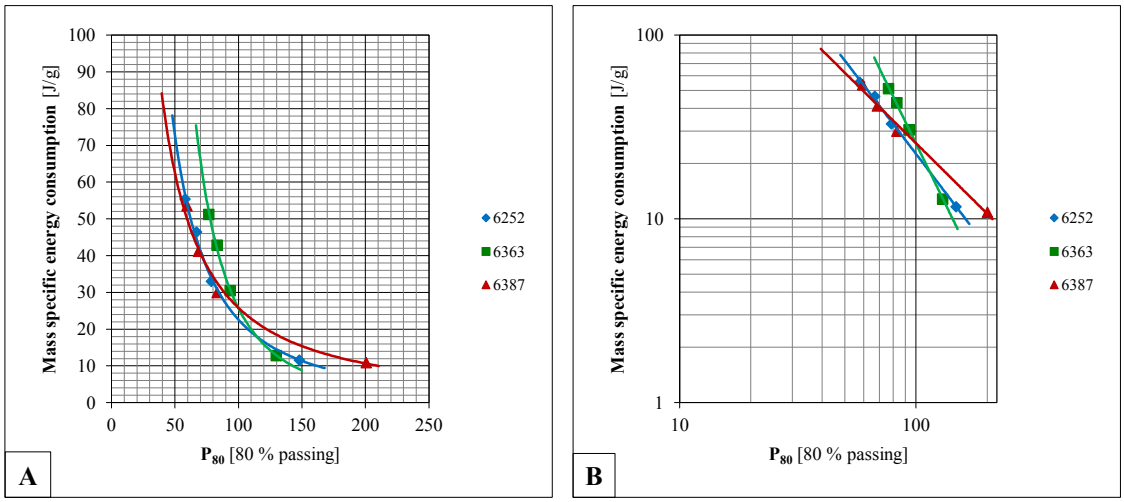

Figure 49. Comparison of the P_{80} and the mass specific energy [J/g] using a power function after comminution for samples 6252, 6363 and 6387 (subtype B2-a) in a laboratory rod mill (10 minutes) and in a laboratory ball mill (15, 25 and 35 minutes) at the laboratory of the Institute of Mineral Processing (A = linear scale, B = logarithmic scale).

In the case of comminution in a laboratory ball mill (15, 25 and 35 minutes), the correlation between the mass specific energy consumption (w_m) and the P_{80} value can be given as a power function (Table 26). Furthermore, the consumption of the total mass specific energy consumption required to reach P_{80} = 45 µm can be interpolated based on the correlation between the mass specific energy consumption and P_{80} values after different stages of comminution in a laboratory ball mill. When comparing the data, which are displayed numerically in Tables 14 (P_{80}), 24 and 25 (w_m), as well as graphically in Figures 49 and 50, some observations can be made regarding the energy consumption related to the comminution of ore type B2 and, in particular, the subtypes B2-a and B2-b. First of all, if looking at the mass specific energy consumption (w_m), it can be noted that energy consumption (P_{80} = 45 µm) for the subtype B2-a is clearly lower than of the subtype B2-b.

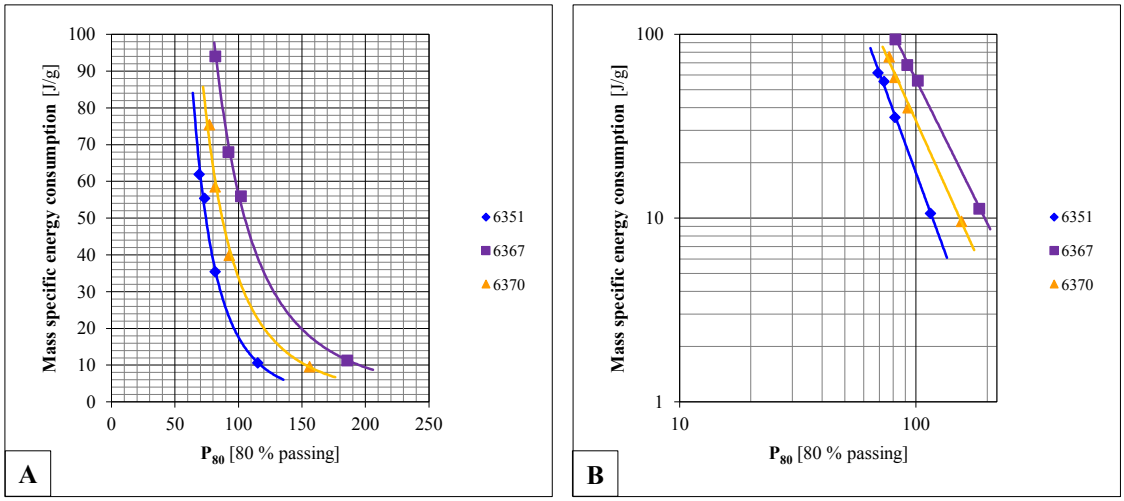

Figure 50. Comparison of the P_{80} and the mass specific energy [J/g] using a power function after comminution for samples 6351, 6367 and 6370 (subtype B2-b) in a laboratory rod mill (10 minutes) and in a laboratory ball mill (15, 25 and 35 minutes) of the Institute of Mineral Processing (A = linear scale, B = logarithmic scale).

Table 26. The correlation given as a power function between the mass specific energy consumption (w_m) and P_{80} values after different stages of comminution (15, 25 and 35 minutes) in a laboratory ball mill.

Sample	Ore type	Correlation	R^2	w_m to P_{80} = 45 µm [J/g]
6252	B2-a	$y = 53.84 \cdot 10^3 \cdot x^{-1.69}$	0.998	86.53
6351	B2-b	$y = 19.03 \cdot 10^7 \cdot x^{-3.52}$	0.997	288.46
6363	B2-a	$y = 49.91 \cdot 10^5 \cdot x^{-2,64}$	1.000	215.63
6367	B2-b	$y = 86.07 \cdot 10^5 \cdot x^{-2.59}$	0.999	449.83
6370	B2-b	$y = 17.41 \cdot 10^6 \cdot x^{-2.86}$	0.997	325.61
6387	B2-a	$y = 91.13 \cdot 10^2 \cdot x^{-1.27}$	0.991	72.46

In a comparison of the graphical representation of the mass specific energy consumption (w_m) and of the P_{80} value (Fig. 49), a significant jump can be noted in the P_{80} values related to the subtype B2-a in the case of comminution in a laboratory rod mill (10 minutes) and in a laboratory ball mill (15 minutes). In addition, the mass specific energy consumption (w_m) is significantly lower to get P_{80} = 45 µm compared to the mass specific energy consumption related to the subtype B2-b (Table 26). Furthermore, it can be noted that the clear jump in the P_{80} values does not exist in the case of subtype B2-b (Fig. 50). On the basis the of mass specific energy consumption (w_m), sample 6363 can presumably be attributed to subtype B2-a (Table 26). Some degree of overlap between these subtypes has been observed as well as in the case of the modal mineralogy.

The reason for this different breakage characteristics can be the aforementioned difference in the mineralogy between the two subtypes. In addition, Aupers (2014) has described in his work a brecciation of magnetite in ore type B2 in some cases. These characteristics are not yet well known and require further investigations as they may have some impact on the breakage characteristics of this ore type.

7.3 Energy consumption related to the "Silica in the Mine" project

7.3.1 Preface

Bergström and Anttila (1973) carried out comminution tests in an open comminution system to compare the results of grinding with rod mill, ball mill, and pebble mill with waste pebbles. Further, their target was to determine the efficiency of the mills, the energy consumption and conversion ratio at the laboratory scale, and at pilot scale and further at industrial scale at the beneficiation plant based on these tests. Their work included experiments in three different methods to determine the grinding capacity of mills, which was divided into three subsections: estimation according to empirically developed formula, braking test, and comminution experiment. In a talk: "A Theory for Wear in Wet Rod Mills and Cascade Mills" by Fahlström-Andrén (IMPC 1964), empirical formulas were given for calculating the mill effect when the weight of grinding media is known (*Equation* 27):

$$M_r = 0.121 \cdot \frac{P}{n_c \cdot D^{0.6}} \qquad (Eq.\ 27)$$

M_r…… Mass of grinding media [ton] by effect P

P…… Effect of a mill [kW_{brutto} value in operation]

n_c…… Mill speed in percent of critical speed [a decimal number]

D…… Efficient mill diameter [m]

Using these formulas given in *Equations* 28, 29, and 30, the efficiency of the pilot mills was calculated by Bergström and Anttila (1973) as follows:

$$P = \frac{M_r \cdot n_c \cdot D^{0.6}}{0.121} \qquad (Eq.\ 28)$$

$$I_D = \frac{P_{indicated\ from\ mill}}{P} \qquad (Eq.\ 29)$$

$$\eta = \frac{P_{netto}}{P_{indicated\ from\ mill}} \qquad (Eq.\ 30)$$

P…… $P_{netto} = 0.85$

I_D…… Calculated divisor for effect of experimental mills indicated from operating mills at large scale

H…… Efficiency of an operating mills (assumed to be 0.85 for this case)

The principle of braking tests carried out by Bergström and Anttila (1973) was that a brake band is a charged mill shell exterior with progressively increasing load (Fig. 51). If the mill is running in the load

direction, the brake band is influenced by the force of the mill rotation and gravity of the load. The grinder casts mechanical power converted to electrical power, which corresponds to the mill target power or net effect.

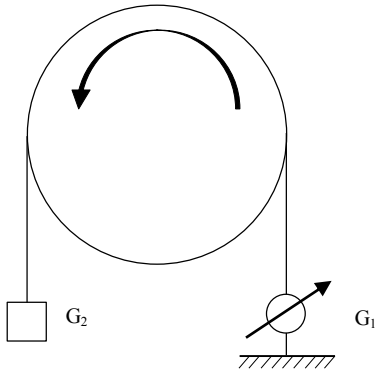

Figure 51. Principle of the brake test where G_1 is an indication of dynamometer and G_2 is the counterweight (Bergström & Anttila 1973).

At the same time, the mill power meter was read and the efficiency was estimated. The comminution tests were carried out to compare the results with a tumbling mill, operating mill, Bond mill, and pilot-scale mill using steel rods as well as steel balls as grinding media. Because the comminution of the same ore with the equal comminution process and equal total energy input into mills of different dimensions, the size reduction ratio varied with respect to P_{80} values, volume of newly formed fine fraction, and specific surface area. For results, the comminution effects in an open circuit for laboratory, pilot, and operating mills were compared with respect to these factors. However, the results, displayed in Table 27, should be examined critically from case to case.

Table 27. Results of comparison of the energy consumption after comminution by rod mills, ball mills, and pebble mills (Bergström & Anttila 1973).

Mill Type	Rod Mill			Ball Mill			Pebble Mill		
	Ø [m]	η	I_D	Ø [m]	η	I_D	Ø [m]	η	I_D
Operation	2.7	0.85	1.0	3.0	0.85	1.0	1.5	0.85	1.0
Pilot	0.6-1.0	0.58	1.5	1.0	0.63	1.3		~ 0.63	~ 1.3
Bond	0.3	0.43	2.0	0.3	0.60	1.4		~ 0.43	~ 2.0
Tumbling	0.2	10 min → 5 kWh/ton		0.2	10 min → 6.5 kWh/ton				

The observation and results, reported by Bergström and Anttila (1973), were a basis for the comminution test and the estimation of the energy consumption concerning the "Silica in the Mine" project (Adolfsson 1996, Drugge 2009).

7.3.2 Principle of the estimation of the energy consumption

By establishing a linear relationship between the comminution time in the laboratory ball mill, 25 and 35 minutes, respectively, and P_{80} values (Fig. 52), a needed comminution time can be interpolated to obtain $P_{80} = 45$ µm using an equation of a straight line (*Equation* 31*)* passing through two distinct points $P_1(x_1 , y_1)$ and $P_2(x_2, y_2)$ as follows (Pentikäinen 1978):

$$y - y_1 = m(x - x_1) \qquad (Eq.\ 31)$$

Its slope (m) is given by *Equation* 32 with x_2 not equal to x_1:

$$m = \frac{y_2 - y_1}{x_2 - x_1} \qquad (Eq.\ 32)$$

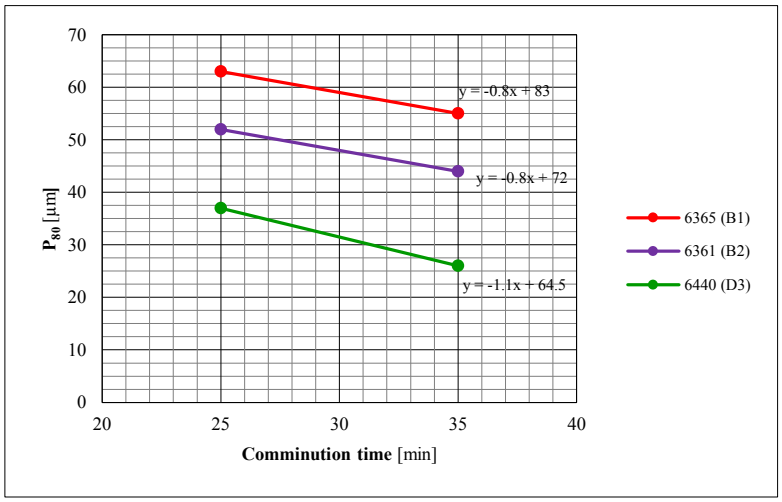

Figure 52. Principle of interpolation of the comminution time at the laboratory scale to obtain P_{80} = 45 µm using the laboratory ball mill.

Estimating the energy consumption to obtain P_{80} = 45 µm is done using *Equation* 33. This methodology for the estimation of the total energy consumption has its origin in the investigations carried out by Bergström and Anttila (1973) and Adolfsson (1996):

$$E = A + \tau \cdot B \pm 0.47\ [\frac{kWh}{t}] \qquad (Eq.\ 33)$$

E……	Energy consumption to obtain P_{80} = 45 µm
A……	5 [kWh/t] constant for a rod mill
τ……	Comminution time [min] a laboratory ball mill
B……	0.65 [kwh/t/min] constant
0.47 $[\frac{kWh}{t}]$	Total error

The possible error of the energy consumption is mainly dependent on the variation in the right comminution time in the laboratory ball mill to obtain P_{80} = 45 µm. The repeatability and reproducibility of the determination on P_{80} values and the accuracy of the model for determination will not described in detail here, but they are described in detail in the report by Drugge (2009). Furthermore, a confidence interval of 95% for the error can be estimated from *Equation* 34 as follows (Drugge 2009):

$$\frac{\pm 1.96 \cdot s_{P(80)lab}}{\sqrt{n}} = \frac{\pm 1.96 \cdot 0.299152}{\sqrt{4}} = \pm 0.293169\ \mu m \qquad (Eq.\ 34)$$

By the estimation of the comminution time to obtain P_{80} = 45 µm, the differences in the dispersity were back-calculated to the time differences and eventually to the differences in the energy consumption. The result corresponds to a margin of error of ± 0.19 kWh/t. The systematic error at 0.46 µm corresponds to 0.28 kWh/t, which is added to get the total error, providing the total error of ± 0.47 kWh/t in *Equation* 36 (Drugge 2009). It should be noted, that in accordance with the estimation of the error in the case SiO_2 grade, the standard deviations of the four values are consistently applied. Furthermore, it should also be pointed out that this estimation of the energy consumption given in *Equation* 36 is adapted to the beneficiation plants in Kiruna and thus does not directly suitable for use in other comminution systems. However, the principle may be applied to other systems.

7.3.3 Estimation of the energy consumption for selected samples

In Tables 28, 29, and 30 the estimated energy consumption (*E)* is given for the selected samples which represent the main ore types in the Kiirunavaara deposit using the linear correlation between P_{80} values and comminution time to interpolate the needed comminution time obtain P_{80} = 45 µm. The graphical presentation is given as histograms for the samples analyzed until yet. Statistic parameters are given in Table 31.

Table 28. Estimated energy consumption at the industrial scale based on *Equation* 33 for selected samples representing ore type B1.

Sample	**Ore type**	**Method**	**P_{80}** [µm]	**Comm. time** P_{80}= 45 µm, [min]	**E** (Plant) P_{80}= 45 µm, [kWh/t]	**E** (Plant) P_{80}= 45 µm, [J/g]
6255	B1	10 10+25 10+35	125 52 44	33.75	26.94 ± 0.47	96.98 ± 1.69
6365	B1	10 10+25 10+35	151 63 55	47.50	35.88 ± 0.47	129.15 ± 1.69
6384	B1	10 10+25 10+35	125 64 52	40.83	31.54 ± 0.47	113.55 ± 1.69
6386	B1	10 10+25 10+35	151 60 51	41.67	32.08 ± 0.47	115.50 ± 1.69
6397	B1	10 10+25 10+35	168 60 50	40.00	31.00 ± 0.47	111.60 ± 1.69
6440	B1	10 10+25 10+35	135 47 35	26.67	22.33 ± 0.47	80.40 ± 1.69

Table 29. Estimated energy consumption at the industrial scale based on *Equation* 33 for selected samples representing ore type B2.

Sample	**Ore type**	**Method**	**P_{80}** [µm]	**Comm. time** P_{80}= 45 µm, [min]	**E** (Plant) P_{80}= 45 µm, [kWh/t]	**E** (Plant) P_{80}= 45 µm, [J/g]
6359	B2	10 10+25 10+35	124 54 46	36.25	28.56 ± 0.47	102.83 ± 1.69
6361	B2	10 10+25 10+35	99 52 44	33.75	26.94 ± 0.47	96.98 ± 1.69
6385	B2	10 10+25 10+35	259 62 51	40.45	31.30 ± 0.47	112.66 ± 1.69
6396	B2	10 10+25 10+35	149 60 51	41.67	32.08 ± 0.47	115.50 ± 1.69
6400	B2	10 10+25 10+35	162 53 52	105.00	73.25 ± 0.47	263.70 ± 1.69
6412	B2	10 10+25 10+35	267 59 46	35.77	28.25 ± 0.47	101.70 ± 1.69

Table 30. Estimated energy consumption at the industrial scale based on *Equation* 33 for selected samples representing ore type D.

Sample	**Ore type**	**Method**	**P_{80}** [µm]	**Comm. time** P_{80}= 45 µm, [min]	**E** (Plant) P_{80}= 45 µm, [kWh/t]	**E** (Plant) P_{80}= 45 µm, [J/g]
6254	D3	10 10+25 10+35	119 60 50	40.00	31.00 ± 0.47	111.60 ± 1.69
6351	D3	10 10+25 10+35	96 50 42	31.25	25.31 ± 0.47	91.13 ± 1.69
6369	D1	10 10+25 10+35	104 58 48	38.00	29.70 ± 0.47	106.92 ± 1.69
6440	D3	10 10+25 10+35	97 37 26	17.73	16.52 ± 0.47	59.48 ± 1.69
8028	D5	10 10+25 10+35	124 59 49	39.00	30.35 ± 0.47	109.26 ± 1.69
8030	D3	10 10+25 10+35	210 77 63	47.86	36.11 ± 0.47	129.99 ± 1.69

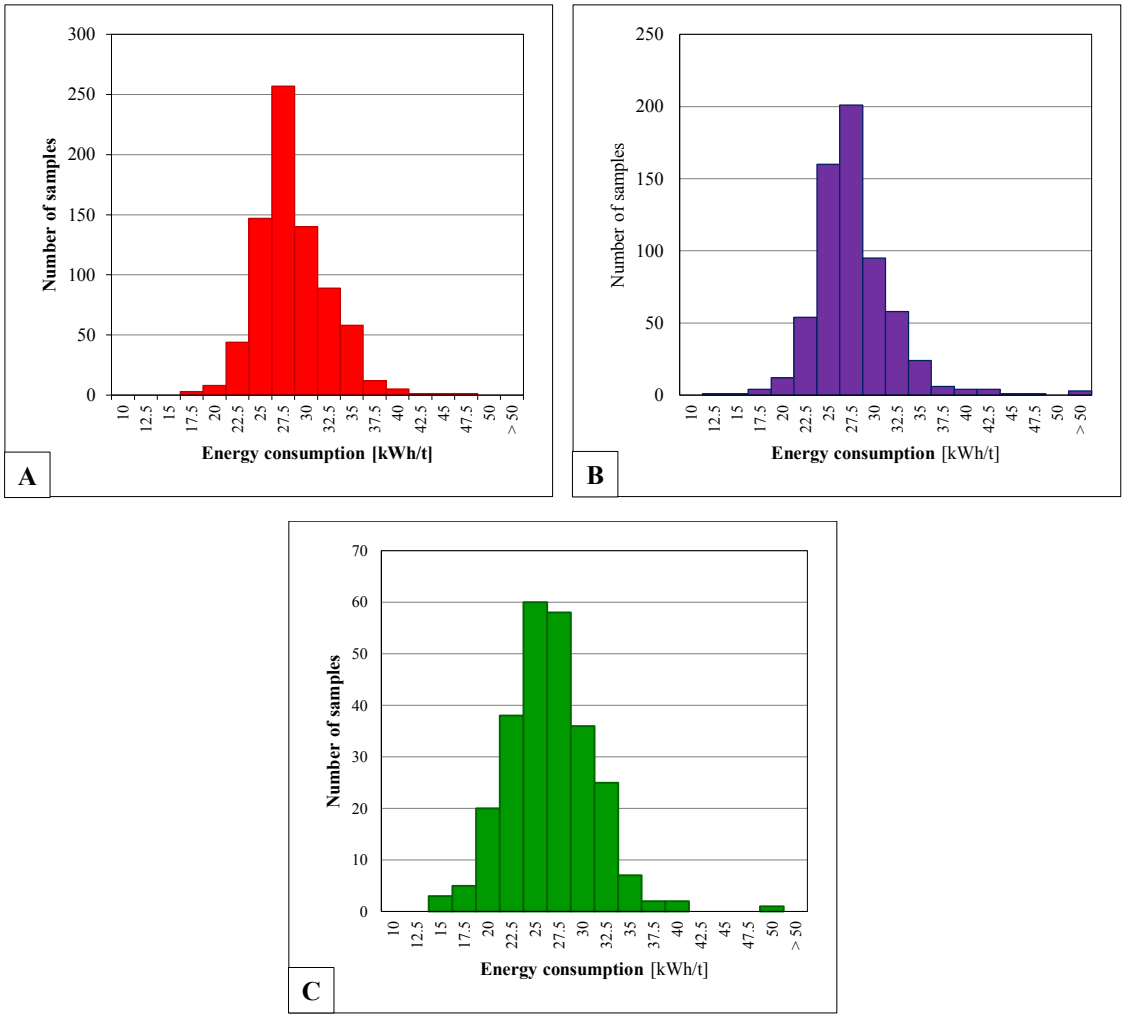

Figure 53. Histograms of the estimated energy consumption for entire population. (A) Ore type B1 (769 samples), (B) ore type B2 (632 samples), and (C) ore type D (259 samples). Statistic parameters are given in Table 31.

Table 31. Statistic parameters of the estimated energy consumption related to the "Silica in the Mine" project.

Ore type	B1	B2	D
Min	15.34	10.86	12.52
Max	47.40	121.24	48.20
Mean	27.25	26.79	25.33
Median	26.68	26.07	25.13
Stdev	3.78	6.85	4.52
Variance	14.29	46.98	20.42

In general it can be noted that there are no significant difference in the energy consumption to obtain P_{80} = 45 µm between the main ore types in the Kiirunavaara deposit. The energy consumption for the high-P ore type D is slightly lower that for ore types B1 and B2 thus also the comminution resistance can be regarded lower. There is also more variation in the energy consumption related to ore type D compare to ore types B1 and B2. Sample 6400 representing ore type B2 is clearly different from behalf of other samples because its significantly higher energy consumption to obtain P_{80} = 45 µm. There are also some other samples of ore type B2 that show very high energy consumption. There seems to be only slightly difference in P_{80} values between the comminution for 25 and 35 minutes, respectively. This may be

related to special breakage characteristic of some ore samples which will be discussed in detail in Chapter 11.

8. MINERALOGICAL CHARACTERIZATION OF ORE TYPE B2

8.1 Automated mineralogy

8.1.1 Optical microscopy versus automated mineralogy

Optical microscopy allows for the qualitative, as well as quantitative, description of the rock samples and their mineralogy. Optical mineralogy is still a widely used technique for the identification of minerals, although automated mineralogy and petrography for process mineralogy are currently undergoing rapid development(e.g. Gu, Y. 2003, Fandrich et al. 2007, Andersen et al. 2009). Optical mineralogy allows for the identification of minerals by their characteristic optical behavior, especially when viewed under magnification on a petrographic polarizing microscope using combinations of transmitted and reflected light sources in both polarized and un-polarized states. Ore minerals (such as sulfides, oxides and precious metals) are best viewed in reflected light as they tend to be opaque. Gangue minerals (such as silicates, carbonates and phosphates) are mostly translucent.

Aside from the mineral identification, the amount or grade of the minerals (modal mineralogy) in the sample can also be determined by optical microscopy using the point counting method (e.g., Freund 1966, Hedin 1992, Butcher 2010). Textures can also be observed and recorded photographically (photo-micrographs) and they are typically used to report and illustrate the features in a sample. A clear advantage of optical microscopy is that it offers the opportunity to get a relatively quick overview of the mineralogy in a sample. Furthermore, a relatively cheap prognosis can be obtained for both unbroken ore as well as for grains and particles. In many cases optical microscopy alone might be sufficient, but like all techniques, optical microscopy can be used in combination with other techniques for better certainty (Butcher 2010, Nordstrand 2012, Wartbichler 2014).

Combining optical microscopy with image analysis quickens the method quantitative mineralogical investigations, but a positive identification of minerals is not always easy. This is especially true when a sample consists of very fine-grained grains or particles. Although advances in technical development have recently improved the quality of quantitative analysis with XRD (*x-ray diffraction*), the technique is still sensitive to crystal size, orientation of the sample, crystallinity and the variation of the chemical composition of a mixture, which may contain multiple phases (Rietveld 1969). Modern, automated mineralogy provides significantly faster quantitative analysis on the modal mineralogy and texture (e.g., Gu 2003, Moen 2006, Butcher 2010, Liipo et al. 2012). However, optical mineralogy can be recommended in order to get a quick overview and preliminary information about the expected minerals in a sample from a deposit before the use of automated mineral analysis such as QEMSCAN

(*Quantitative Evaluation of Minerals by Scanning Electron Microscopy*) and MLA (*Mineral Liberation Analysis*). These methods are often expensive and time consuming.

8.1.2. Principle of the automated systems for mineralogical characterization

When the scanning electron microscope (SEM) and later, the electron microprobe micro-analyzers (EPMA) were introduced about 40 years ago, they revolutionized mineralogical investigations and quantitative mineralogical analysis (Butcher 2010). Automated systems for mineralogical characterization based on SEM-EDS (*Energy-dispersive Scanning Electron Microscopy*) such as QEMSCAN (*Quantitative Evaluation of Minerals by Scanning Electron Microscopy*) and MLA (*Mineral Liberation Analysis*) are of increasing importance for process mineralogy and mineral processing operations because of their ability to collect large amounts of statistically valid quantitative data on e.g. the distribution of minerals, modal mineralogy, mineral associations and textures in relatively short periods of time (Andersen et al. 2009). Providing quantitative mineralogical, structural and textural data, these methods have more or less replaced the point counting of minerals in thin sections, earlier frequently used in optical mineralogy. The latter is time consuming and often requires a competent mineralogist or geologist (Butcher 2010).

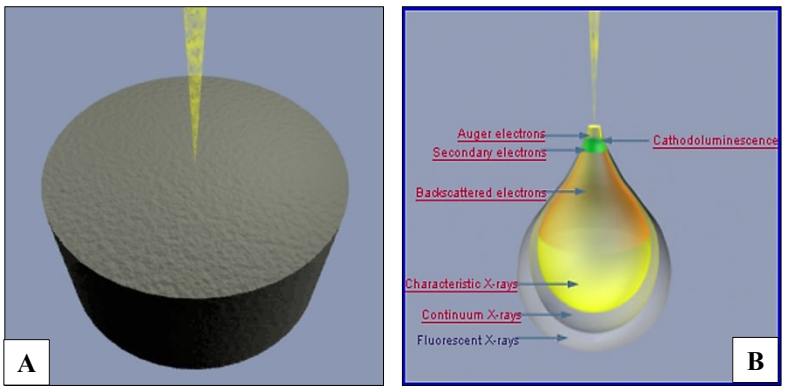

Figure 54. Schematic picture of the interactions of an electron beam and a sample (FEI; Krusemann 2012 a).

The technology behind automated mineralogy, i.e. scanning electron microscopy (SEM), is based on an electron beam, generated in a vacuum, which is the scanned over a sample (Fig. 54 A). The electron beam interacts with the near surface region of a sample to the depth of approximately a few microns (µm), depending on both the accelerating voltage and the density (atomic number) of material being sampled. Numerous signals are generated as a result of this interaction. Those can be detected by appropriate detectors, to provide information on a sample (Fig. 54 B). Low energy secondary electron emission, backscattered electron emission, characteristic x-ray emission and cathode-luminescence can be regarded as the most significant of these signals. Furthermore, some other signals such as Auger electrons, continuum X-rays, fluorescent X-rays, transmitted electrons and absorbed electrons are generated (FEI Krusemann 2012 a). The principles of QEMSCAN® technology are based on image analysis using a combination of signals from backscatter electron detectors, X-ray detectors and

secondary electron detectors. Backscattered electrons will recognize mineral or other phases based on the density contrast (atomic number) and compositional differences from X-ray spectra. This information is used for creating digital mineral images of the sample based on chemical composition (Gottlieb et al. 2000, Sutherland et al. 2000, FEI Krusemann 2012 a).

To be able to identify the minerals and phases in the samples, every analyzed pixel and obtained X-ray spectra is compared to a known database of the mineral compositions called SIP (*Species Identification Protocol*) (Gottlieb et al. 2000, FEI Krusemann 2012 b). The SIP consists of a table of entries (*SIP Profiles*), each with a set of criteria specified by a user which are used to match to the scanned elemental composition data and BSE (*Back Scatter Emission*) brightness to a mineral species. As each point (pixel) on a sample is scanned, its spectrum is converted to elemental information which is compared to the entries in the SIP list until one (the first hit) is found with parameters matching that of the scanned material. It should be noted that the order of entries in the SIP table is very important, as spectra are mapped to SIP entries by scanning the SIP table sequentially from top to bottom (FEI; Krusemann 2012 b).

8.1.3 QEMSCAN® Analysis

The portion of the mineralogical investigations related to this study was carried out using the QEMSCAN® E430 Pro (Carl Zeiss SEM) at LKAB's metallurgical laboratory in Luleå (Fig. 55).

Figure 55. QEMSCAN® E430 Pro (Carl Zeiss SEM) at LKAB's metallurgical laboratory in Luleå (Photo: LKAB).

The QEMSCAN® is equipped with four silicon drift detectors (SDD) for energy-dispersive X-ray spectroscopy (EDX) based on a system developed by CSIRO in the early 1980's and known as quantitative evaluation of minerals by scanning electron microscopy (QEM*SEM) (Grant et al. 1977, Miller et al. 1982, Pirrie et al. 2004). The latest product of this system is known as QEMSCAN® and is complete automation solution from sample preparation through analysis to data reporting (Butcher 2011, FEI Krusemann 2012 a).The QEMSCAN® is equipped with a number of different measurement modes such as PMA (*Particle Mineral Analysis*), BMA (*Bulk Mineral analysis*) and TMS (*Trace Mineral*

Search). Depending on the purpose of a project, any number or combination of measurement modes can be selected to achieve the desired results (FEI Krusemann 2012 c). During the analysis, X-ray spectra are collected at user-defined pixel spacing and are acquired very rapidly (ca. 10 ms per pixel). The back scatter electrons recognize the particles based on the density (atomic number) and topographical information. The compositional information from the X-ray spectra creates a digital pixel map of each particle based on the chemical composition (Gu 2003, Goodall et al. 2005, Butcher 2010, FEI Krusemann 2012 c). In this fashion the near-surface qualitative elemental composition of each particle is systematically mapped, assigned to a mineral name or chemical compound/species, and a digital pixel map of each particle is created (Fig. 56).

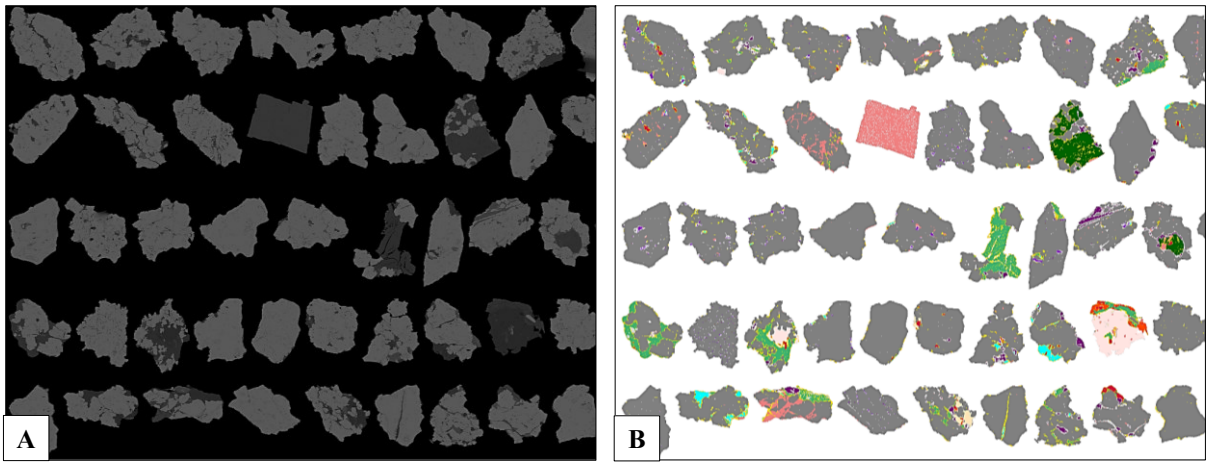

Figure 56. (A) Backscattered electron image (BSE) on sample 6351 (fraction 0.315/0.1 mm); (B) the same picture as a color-coded mineral map (digital image) with false colours after processing with iDiscover 5.3 software (grey = magnetite).

8.1.4 Mineralogical investigations at LKAB's metallurgical laboratory

The samples for this study were prepared for QEMSCAN® analysis at LKAB's metallurgical laboratory as polished resin-impregnated blocks ca. 30 mm in diameter (Fig. 57 A) and coated with conductive carbon. First, the samples were homogenized by multiple splitting and then mixed with graphite (Fig. 57 B). The graphite is used as a supporting matrix to ensures the dispersion of the particles across the block as well as to ensure a random orientation. The graphite also minimizes the segregation of the particles resulted by the density separation. The graphite particles should have the same or slightly smaller size than the particles of interest (Pirrie & Rollinson 2011).

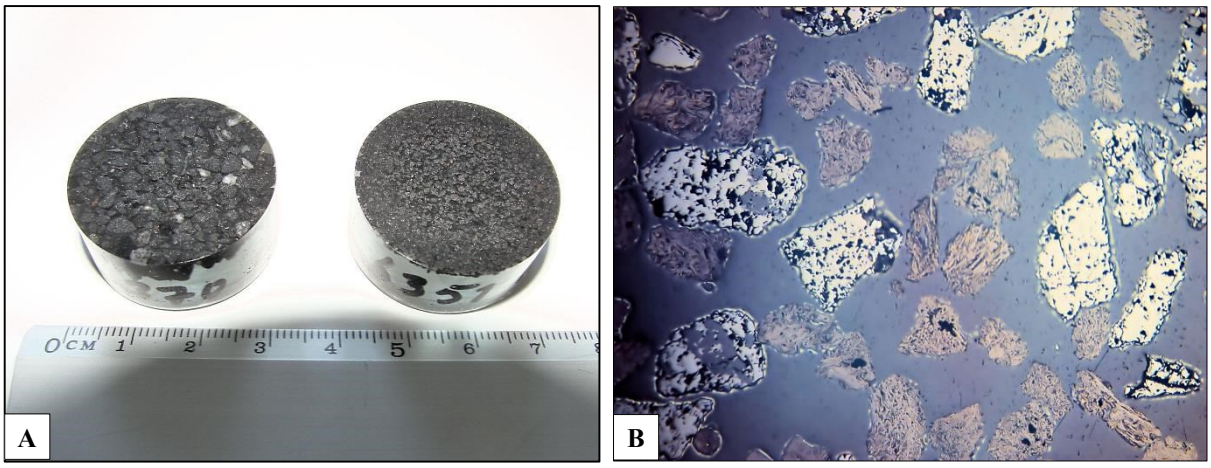

Figure 57. (A) Polished 30 mm resin blocks (samples 6370 and 6351, without coating); (B) Magnetite particles (light grey) mixed with graphite particles (brownish grey) for an automated mineral analysis by QEMSCAN®.

Typically, approximately 1 g of a sample is required to prepare this kind of resin block. However, the mass of a sample for the analysis will be influenced by a number of factors including the particle size and the density of the sample, the concentration of the minerals of interest and the overall aims of the analysis. For instance, the coarser the particle size, the fewer the number of the particles in an individual resin block. To have a statistically valid data set (e.g. modal mineralogy, liberation characteristics), numerous sub-samples would be needed to be prepared and analyzed especially in the case of coarser particles (Pirrie & Rollinson 2011). In most studies, 300 identified particles are usually as a minimum for the statistically valid modal mineralogy. In this study, it will commonly be around 5000 particles, especially in the finest fractions.

For the mineralogical analysis with QEMSCAN® the measurement mode of Particle Mineral Analysis (PMA), in which the combination of the signals from the back scatter electron detectors (BSE) and the X-ray detectors are used, was selected. Particle Mineral Analysis (PMA) can be regarded as an optimal mode for obtaining the data on the distribution of minerals, the degree of liberation and the textural characteristics. Furthermore, it obtains data on modal mineralogy, chemical assays as well as grain size (FEI Krusemann 2012 a). For this study, a pixel spacing of 2.5 µm and a line spacing of 2.5 µm were used and approximately 5000 to 6000 particles per sample were measured in the fine particle size classes (< 0.315 mm).

All analytical data were processed off line by using an integrated software application to QEMSCAN® system called iDiscover 5.3. For analysis and interpretation of the data, three SIP-Lists (Secondary Lists) were created for the mineralogical and mineral liberation analyses (Fig. 58) in this study.

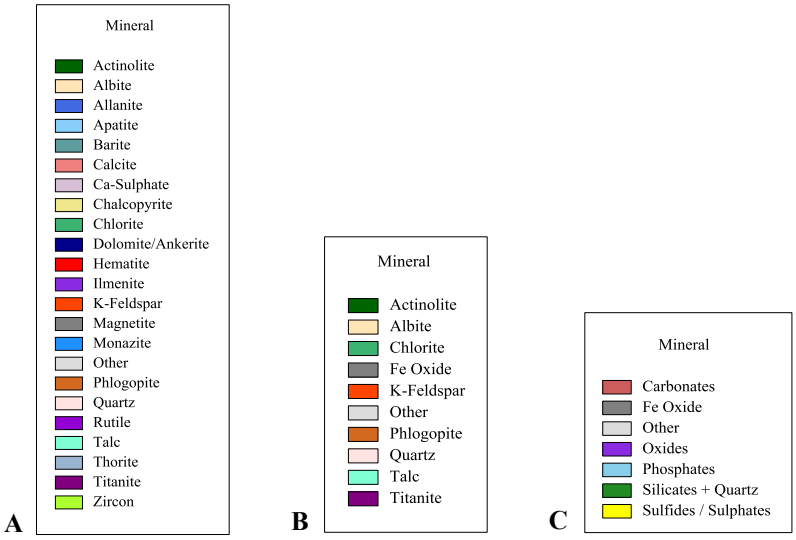

Figure 58. Selected minerals in the secondary SIP Lists (Species Identification Protocol) used for mineralogical investigation (A), and (B) and (C) for mineral liberation analysis. Created by iDiscover 5.3 software (FEI).

The data from the analyses carried out by QEMSCAN® was used to understand the modal mineralogy of ore type B2 and the mineralogy and the distribution of the silicates, as well as Si (silicon), in the different particle size classes after comminution tests. A second target of the analysis was to study the degree of the liberation of the magnetite and silicates. The results of the mineralogical investigation will be represented in detail in this chapter. It should be pointed out that further on in this study quartz will be considered to belong to the silicate group (i.e. silicate minerals) for practical reasons as in Deer et al. (2004). They define quartz to belong to the framework silicates along with other silica minerals, feldspathoids and zeolites. Others, such as Strunz (1941), have grouped quartz with the oxide groups (Class 4 by Strunz).

8.1.5 EMPA analyses on SiO_2-bearing minerals

iExplorer is a part of the iDiscover software suite which is used for the interactive analysis of measurements from a QEMSCAN instrument, in which significantly more information can be stored pertaining to the samples and measurements relative to the QEMSCAN instrument. These include, for example, external chemical assays, mass-flow information, chemistry and the density of minerals or phases, all of which is essential data for iExplorer calculations and creating reports. This type of additional external information can be imported either using Samples Explorer manually input of additional data or by using an Excel spreadsheet (FEI Krusemann 2012 c).

More information about the mineral chemistry can be yielded by a single point analyses using wavelength dispersive spectrometry on the EPMA (*Electron Probe Micro-Analysis*). Aupers (2014) carried out analyses on ten samples, of which samples 6099, 6702 and 6715 represent the high-SiO_2 ore type B2. His study to quantify the mineral chemistry of selected minerals (magnetite, ilmenite, rutile, pyroxene, amphibole and hematite, biotite, chlorite, talc, titanite and allanite) was carried out using a

JEOL JXA-8530F electron microprobe at the Helmholtz-Institute for Resource Technology in Freiberg, Germany. Nordstrand (2012) has carried a total of 503 analyses on 198 mineral grains of different ore types of the Kiirunavaara deposit using a CAMECA SX100 electron microprobe at the Geological Survey of Finland in Espoo.

Table 32. Essential SiO_2-bearing minerals of ore type B2 identified in this study and the silicon (Si) and silica (SiO_2) grade based on EMPA analysis carried out by Nordstrand (2012) and Aupers (2014). See also Appendix 19.

Mineral	Chemical Formula	Si wt.%	SiO_2 wt.%
Actinolite	$Ca_2(Mg,Fe^{2+})_5Si_8O_{22}(OH)_2$	25.11	53.72
Albite	$NaAlSi_3O_8$	31.99	68.43
Chlorite	$(Fe^{2+},Mg,Al)_6(Si,Al)_4O_{10}(OH)_8$	13.36	28.58
K-Feldspar	$KAlSi_3O_8$	30.27	64.75
Phlogopite	$KMg_3(Si_3Al)O_{10}(F,OH)_2$	19.75	42.25
Quartz	SiO_2	46.75	100.00
Talc	$Mg_3Si_4O_{10}(OH)_2$	28.69	61.37
Titanite	$CaTiSiO_5$	14.26	30.50

This additional mineral chemistry data based on these EMPA analyses (Nordstrand 2102, Aupers 2014) was used to define the chemical composition of the minerals and is given in Appendix 19. In Table 32 the Si (wt.%) and SiO_2 (wt.%) are displayed. This data is essential for the mineralogical and liberation analysis of silicates. The mineral chemistry data and the associated density of the minerals was imported to iExplorer (Datastore). The additional required for mineralogical analysis with iDiscover software on raw data yielded by the QEMSCAN and for generating reports such on modal mineralogy, element distribution and liberation analysis for this study.

8.1.6 Assay reconciliation

To check the reliability of the measurements with the QEMSCAN method, a comparison called assay reconciliation can be made between the external chemical assays (XRF, XRD) imported into iExplore and the calculated assays based on mineral modal analyses from the QEMSCAN (SIP protocol) together with the chemical composition of the minerals (EMPA). The comparison can be displayed both for selected fractions or entire samples (FEI Krusemann 2012 c). Assay reconciliation provides the possibility to identify potentially anomalous measurements. The assay reconciliation charts created by iDiscover on the different fractions (as received/6 fractions; ball mill/4 fractions) of samples 6252, 6351, 6363, 6367, 6370 and 6387 is presented in Figures 59 A–D. In an assay reconciliation chart the external chemical assay data in given on the X-axis based on XRF analyses on the feed and on the different fractions after screen analysis and the calculated assays from the QEMSCAN are plotted on the Y-axis based on SIP protocols (Fig. 58) and mineral chemistry (Appendix19). In the assay reconciliation charts in Figures 59 A and 59 B show a correlation between silicon (Si) and iron (Fe) which can be regarded as the most important elements in this study.

The assay reconciliation chart for magnesium (Mg) and titanium (Ti) is displayed in Figure 59 C and for aluminum (Al), potassium (K) and manganese (Mn) is shown in Figure 59 D. These elements are partly or wholly concentrated in different silicate minerals such as actinolite (Mg, Fe), phlogopite (Al, K, Mg) and titanite (Ti). When comparing various elements, it is apparent that some of the elements show clearly more deviation. For instance, silicon (Si) in Figure 59 A and magnesium (Mg) in Figure 59 C deviate to a greater degree compared to other elements such as titanium (Ti) in Figure 59 C and potassium (K) in Figure 59 D.

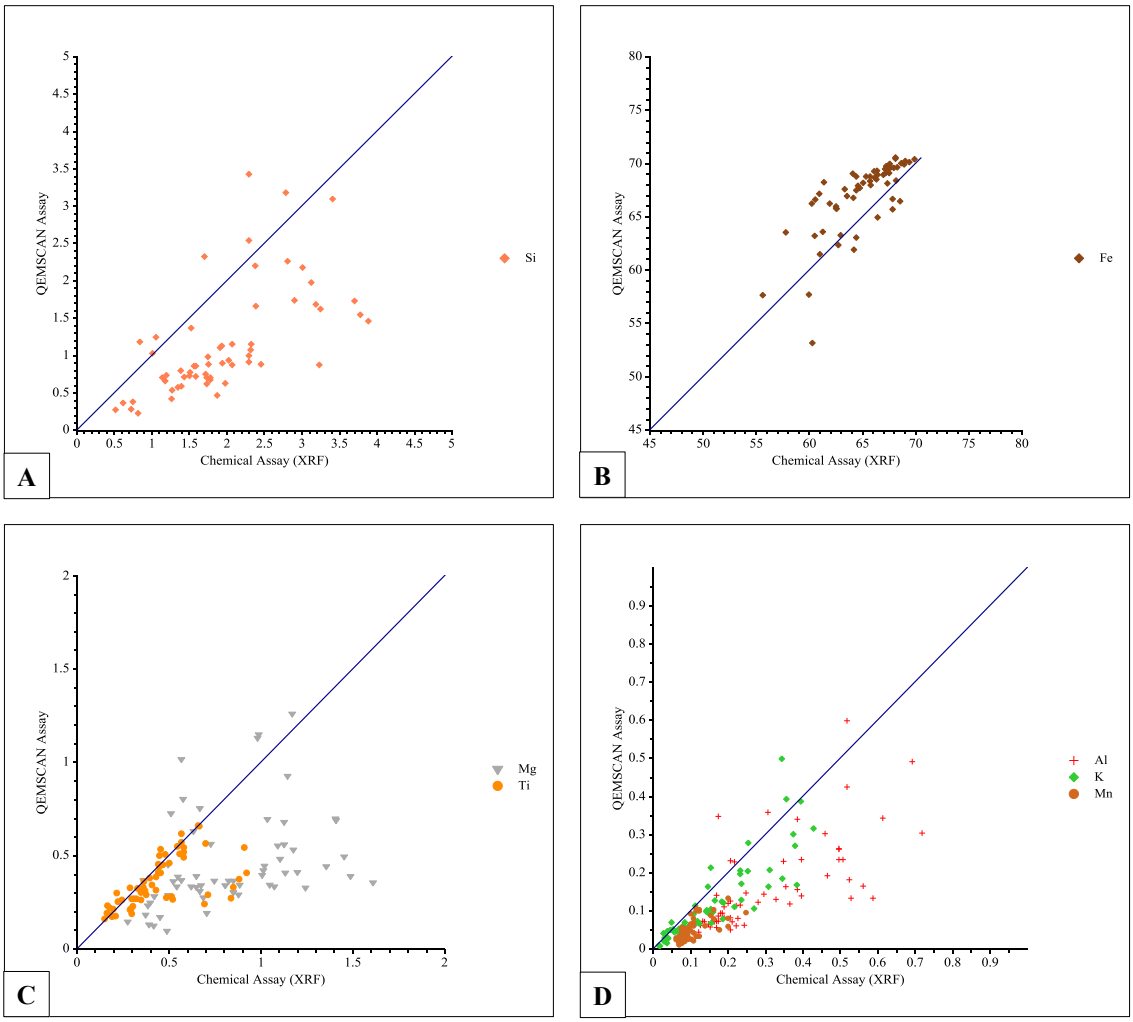

Figure 59. Comparison of the chemical assays on Si (A); Fe (B); Mg, Ti (C) and Al, K, Mn (D) grades for samples 6252, 6351, 6363, 6367, 6370 and 6387 (Fractions) generated from XRF and QEMSCAN.

The reasons for the deviation may be manifold, but the most likely interpretation is the use of an old and inaccurate SIP-List (Malm, updated latest on 04.07.2010), which was used for QEMSCAN analysis carried out at LKAB's metallurgical laboratory in the spring of 2011. The SIP-List mentioned above was the first one used by LKAB and actually created for analyzing pellets and slag. As a result, the creation of the primary SIP-List (Malm complete) and the first secondary SIP-Lists proved to be difficult

and time consuming. Furthermore, the some inhomogeneity of the samples may contribute to the deviation of chemical assays carried out by QEMSCAN and XRF at LKAB's chemical laboratory.

8.1.7 Identification of magnetite and hematite

The sensitivity of the QEMSCAN analysis is poor in the case of different iron oxide phases such as magnetite, hematite, goethite (Donskoi et al. 2011, Wartbichler 2014). Although the latest QEMSCAN system can distinguish between major iron oxides and oxyhydroxides, it can still misidentify minerals with close chemical composition and with similar BSE signal, e.g., magnetite as hematite and hematite as vitreous goethite (Donskoi et al. 2011). In Figure 60, one magnetite particle is represented as a BSE image (A) and as a processed false color image using the secondary SIP List. There are still some pixels which are classified as hematite because of the low BSE intensity although they are clearly magnetite. The low BSE intensity is caused by fractures in the magnetite particle. Hematite is present in most samples, but is not frequently occuring (< 1% by volume).

In this study two methods were used to handle the problem with magnetite and hematite. The first method used, is the Boundary Phase Processor, which belongs to the standard tool in iDiscover software (FEI Krusemann 2012 c). It allows for the adjustment of the pixels in each particle (hematite vs. magnetite), to eliminate solitary hematite pixels that are result from boundary-phase artifacts or ambiguous measurements but which can be clearly identified as magnetite based on the BSE image (Fig. 60 A and B).

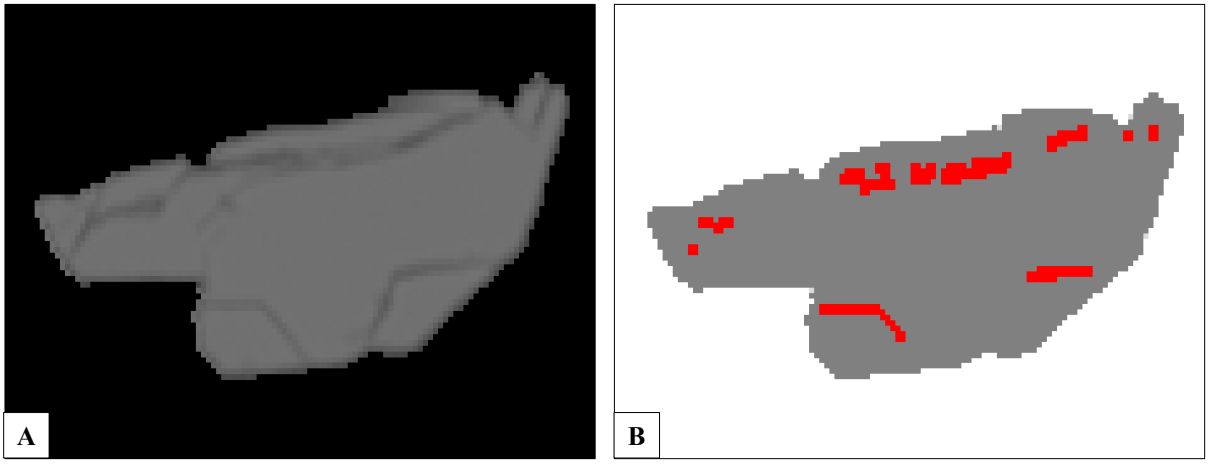

Figure 60. (A) BSE (Back Scattered Electron) image on a magnetite particle (Sample 6351; particle size class 0.315/0.1 mm); (B) Same particle processed with a SIP List presented in Figure 58 A.

The second method is to create a secondary list in which all of the different phases of iron oxides are placed under one group such as Fe Oxide in the secondary SIP Lists presented in Figures 58 A and 58 B. This method is frequently used by processing QEMSCAN data from the practical point of view at LKAB. Further in this study the "Fe Oxide" grouping when referring to QEMSCAN data will be regarded as equivalent to magnetite. In most cases, other phases of Fe oxides, such as hematite and

goethite are of negligible quantity in the Kiirunavaara ore deposit. They are not expected to have no significant impact on the results of analysis.

8.2 Modal mineralogy

Modal mineralogy, i.e. the grade of minerals, has traditionally been determined by optical microscopy with point counting techniques. However, as mentioned earlier, it is time consuming (Petruk 2000) and the quality of the investigation depends on the skill of the point counter (Butcher 2010). As mentioned in Chapter 8.1.1, optical mineralogy is relatively quick and often is also a cheap way to get qualitative information on the mineralogy of the samples. Using optical mineralogy, a modal mineralogy is typically represented in volume percent. The expected mineral composition of the samples is also crucial data to have before using automated mineral analysis systems, which commonly are more expensive. QEMSCAN and MLA have a clear advantage in the investigation of quantitative mineralogy, elemental deportment or when carrying out a mineral liberation analysis. In these cases it is preferable to use weight percent for representing the mineralogical data.

The first step in identifying the silicates and determining the modal mineralogy of ore type B2 was a petrographic polarizing microscope (Nikon Eclipse E600) in this study at LKAB's mineral processing laboratory. It should be noted that no point count analysis was carried out on these samples. The modal mineralogy was determined in more detail by using QEMSCAN® E430 Pro (Carl Zeiss SEM) at LKAB's metallurgical laboratory. The overview of the modal mineralogy in the samples is presented in Figure 61 and the numeric data is displayed in Table 33.

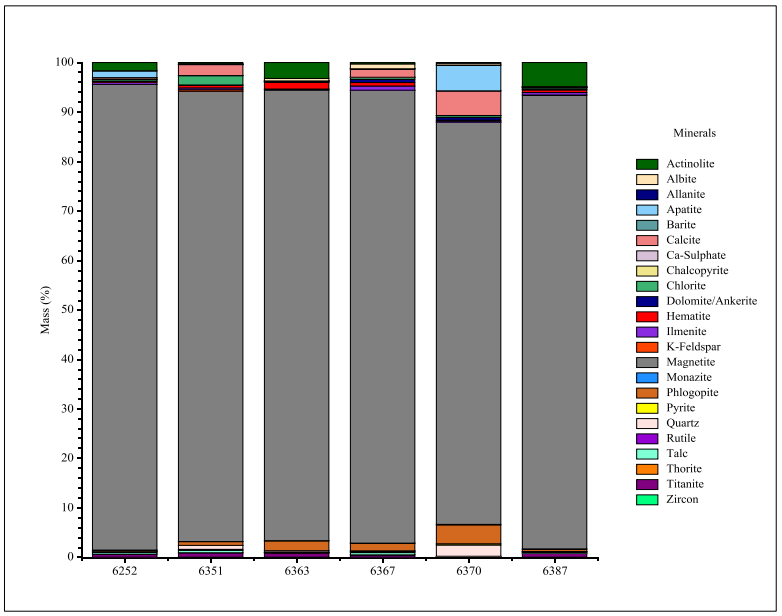

Figure 61. Modal mineralogy (total sample) of samples 6252, 6351, 6363, 6367, 6370 and 6387 (wt.% in the sample) determined by QEMSCAN® at LKAB's metallurgical laboratory in Luleå.

Table 33. Modal mineralogy of samples 6252, 6351, 6363, 6367, 6370 and 6387 determined by QEMSCAN® at LKAB's metallurgical laboratory in Luleå.

Mineral	6252 wt.% in sample	6351 wt.% in sample	6363 wt.% in sample	6367 wt.% in sample	6370 wt.% in sample	6387 wt.% in sample
Actinolite	1.64	0.25	3.20	0.26	0.11	4.85
Albite	0.00	0.07	0.51	0.97	0.38	0.02
Allanite	0.00	0.00	0.00	0.00	0.01	0.00
Apatite	1.38	0.08	0.02	0.03	5.19	0.03
Calcite	0.33	2.22	0.13	1.69	4.98	0.16
Chalcopyrite	0.00	0.01	0.00	0.01	0.03	0.00
Chlorite	0.35	1.89	0.09	0.39	0.38	0.36
Dolomite/Ankerite	0.00	0.07	0.00	0.66	0.53	0.09
Hematite	0.24	0.53	1.38	0.69	0.16	0.53
Ilmenite	0.42	0.36	0.15	0.86	0.25	0.50
K feldspar	0.00	0.32	0.00	0.05	0.05	0.00
Magnetite	93.76	90.84	91.01	91.36	81.19	91.44
Monazite	0.03	0.03	0.03	0.02	0.10	0.05
Phlogopite	0.65	0.86	2.01	1.64	3.82	0.74
Pyrite	0.00	0.03	0.02	0.05	0.25	0.04
Quartz	0.08	0.86	0.48	0.19	2.36	0.08
Rutile	0.11	0.19	0.03	0.19	0.12	0.09
Talc	0.37	0.49	0.02	0.45	0.00	0.23
Titanite	0.61	0.90	0.89	0.47	0.06	0.79
Other	0.01	0.00	0.00	0.00	0.00	0.00
Total	100.00	100.00	100.00	99.99	99.99	100.00

The magnetite content is approximately 81.19 to 93.76 wt.% (alternatively 70.51 to 89.08 vol.%) in the samples selected for this study. Magnetite is the dominant mineral in all the samples and the silicates make up only a small part of the modal mineralogy. Besides magnetite the following ore minerals are identified in the deposit: hematite (Fe_2O_3), ilmenite ($FeTiO_3$), pyrite (FeS_2) and chalcopyrite ($CuFeS_2$), but they are normally less abundant in the ore (Niiranen 2012 b, Nordstrand 2012, Aupers 2014). Recently, molybdenite (MoS_2) has also been described (Aupers 2014).

8.3 Modal mineralogy of silicates

As already was mentioned, the most significant SiO_2-bearing minerals in ore type B2 are actinolite, phlogopite, chlorite, titanite, and quartz. In some cases, talc and feldspar, mostly albite but also K-feldspar, can be of importance (Fig. 62). Zircon, allanite and thorite, which were identified in only a few cases, are uncommon. In this Chapter 3.3 the mineralogy of these silicate minerals and quartz was described in detail, in particular, actinolite, phlogopite, and titanite, because they are the main source of SiO_2 in the crude ore, in some cases also quartz, chlorite and albite are of significance. Furthermore, in some cases talc can also be an important source of SiO_2 in the crude ore. Other minerals containing SiO_2 such as potassium feldspar, allanite, thorite and zircon, are uncommon and occur very sporadically. Therefore it can be assumed that these minerals may have no significant impact on SiO_2 grade in the crude ore or in the magnetite concentrate. Therefore these minerals will be described only briefly.

Besides ilmenite, titanite is also an important source of TiO_2, especially in ore type B2 (Niiranen 2012 b, Aupers 2014).

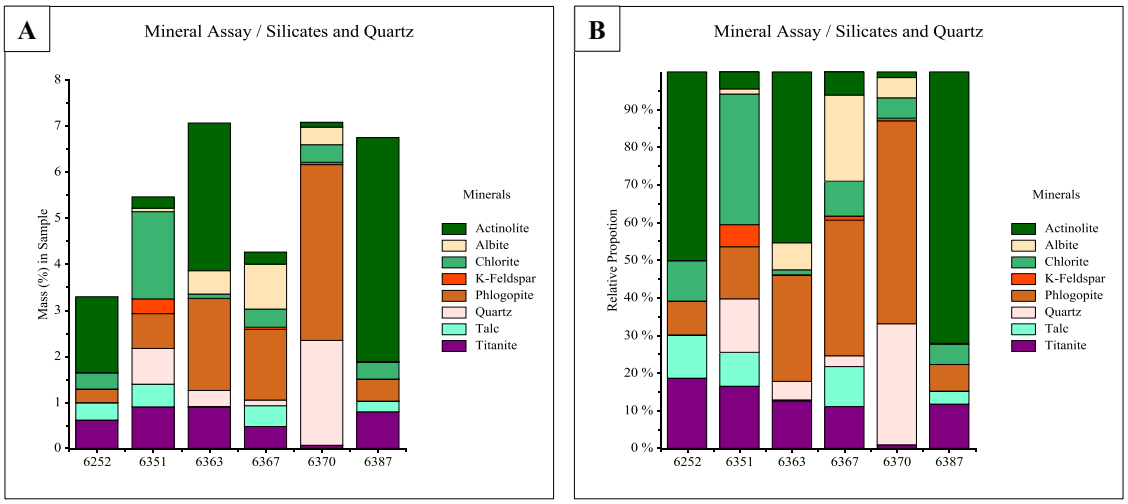

Figure 62. Modal mineralogy of SiO_2-bearing minerals in samples 6252, 6351, 6363, 6367, 6370, and 6387 (total samples). (A) Mass (wt.% in the sample; see also Table 18); (B) Samples normalized to 100%.

Based on their silicate mineralogy (modal mineralogy), the SiO_2-rich ore type B2 seems to have two different subtypes (Fig. 62). The samples 6252, 6363, and 6387 represent a subtype in which actinolite is the dominating silicate und thus also the main source of SiO_2. The mineralogy is more complicated in samples 6351, 6367, and 6370, in which phlogopite, quartz, chlorite and in some cases also albite are significant silicates. These samples seem to represent the second subtype.

8.4 Distribution of SiO_2-bearing minerals

One of the objectives of the "Silica in Mine" project is to predict the SiO_2 grade in magnetite concentrate. This problem with silicates, and thus SiO_2, appears to be linked, above all, to the high-silica ore type B2 (Niiranen 2012 b, Niiranen & Böhm 2013, Aupers 2014). As already described (Adolfsson 2008, Adolfsson & Fredriksson 2011) the aim of the process at the beneficiation plants in Kiruna is to liberate apatite and silicates (comminution) and free the ore of phosphorous (reverse apatite flotation) and silica (WLIMS) to highest possible degree and, wet low intensity magnetic separation (WLIMS) is regarded as the crucial component of the separation process. In this chapter, the distribution of the SiO_2-bearing minerals in the samples will be discussed in detail. The distribution of silicates is represented in Figure 63 (A-F) in the four finest fractions (particle size classes), whereas the combined corresponds an entire sample. The numeric data on the distribution of minerals in the samples is given in Appendix 20.

For the mineral distribution charts, iDiscover software compares the mass of mineral across each mineral and size fractions and combines data also as an un-sized sample (Table 34). In addition to providing mineralogical (phase) assignment for each particle based upon the BSE data or the elemental composition, the system also automatically provides data on the area of each particle (size). It should be

noted that with samples prepared as polished blocks as in this study, the particle size analysis is based upon the assumption that area equals volume and that the grains are spherical (FEI Krusemann 2012 c). However, these investigations and estimations are not always straightforward, partly because of a problem known as the stereological error (Fandrich et al. 1998, Spencer & Sutherland 2000, Böhm et al. 2015), and partly because the ill-defined nature of mineral grains and particles such as mixed spectra or random effect. In this study, the stereology is understood as the three-dimensional interpretation of two-dimensional cross sections of particles in the polished grain mount used in mineralogical and liberation analyses carried out by QEMSCAN at LKAB's metallurgical laboratory.

Table 34. Principle for the calculation of the distribution of minerals in a particle size class (fraction) and in an entire sample. As example particle size class > 80 µm of sample 6252 is used after comminution in a laboratory rod mill (10 minutes) and in a laboratory ball mill (35 minutes).

Sample 6252	**Fraction** > 80 µm			**Mass of Fraction** [29.78 g]	**Mass of Sample** [495.1 g]	
Mineral	**Volume**	**Density**	**Mass**	**wt.% in Fraction**	**wt%. in Sample**	**Normalized** (in Fraction)
Actinolite	0.19624	3.04	0.5966	2.003	0.120	60.86
Albite	0.00051	2.62	0.0013	0.004	0.000	0.14
Allanite	0.00000	3.75	0.0000	0.000	0.000	0.00
Chlorite	0.04564	2.65	0.1209	0.406	0.024	12.34
K-Feldspar	0.00007	2.55	0.0002	0.001	0.000	0.02
Phlogopite	0.04579	2.80	0.1282	0.431	0.026	13.08
Quartz	0.00381	2.62	0.0100	0.033	0.002	1.02
Talc	0.00483	2.75	0.0133	0.045	0.003	1.35
Thorite	0.00003	3.48	0.0001	0.000	0.000	0.01
Titanite	0.02048	5.35	0.1096	0.368	0.022	11.18
Zircon	0.00000	4.65	0.0000	0.000	0.000	0.00
	0.31740		0.9802	3.291	0.198	100.00

Furthermore, in this study the volume of the particles (minerals) is assumed to be equal to the area of the mineral concerned as determined by QEMSCAN. In addition, the density of the minerals, as well as the mass of the particle size class (fraction) and the mass of the entire sample, which have been entered into iExplorer software, are necessary for the most of the calculations.

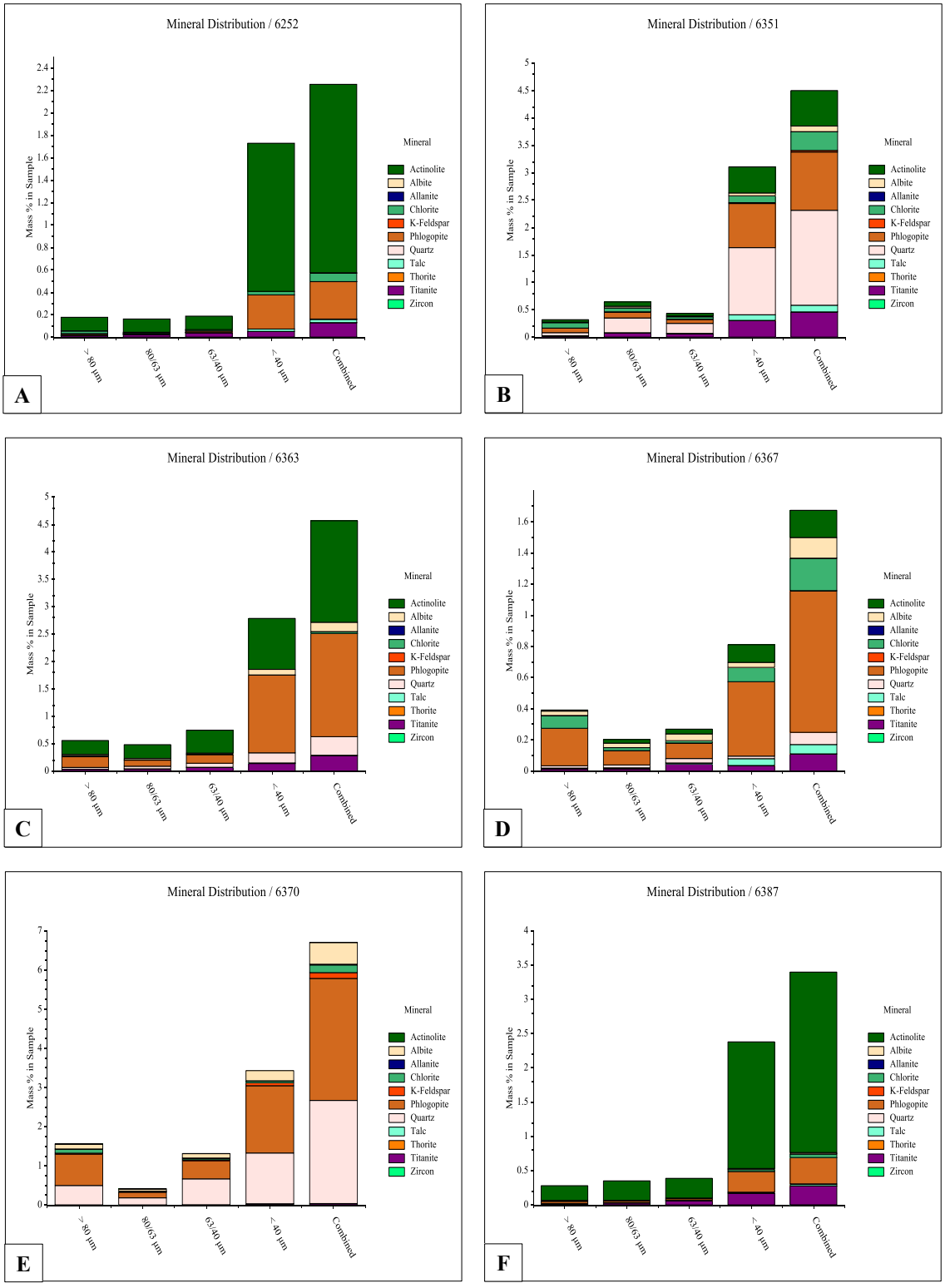

Figure 63. Distribution (wt.% in sample) of silicates in the different size fractions of samples 6252 (A), 6351 (B), 6363 (C), 6367 (D), 6370 (E) and 6387 (F) after crushing and comminution in the laboratory rod mill (10 minutes) and in the laboratory ball mill (35 minutes). Numeric data is displayed in Appendix 20.

In these charts (Fig. 63), the focus is on the silicates and no attention is paid to the oxides (including magnetite), carbonates and phosphates. From attached Fig 64 and Appendix 20, several conclusions can be drawn. First, the content of SiO_2-bearing minerals (silicates) varies between different samples.

Sample 6252 (Fig. 63 A) and sample 6367 (Fig. 63 D) can be regarded as poor in silicates. On the contrary, sample 6370 (Fig. 63 E) is rich in silicates and quartz. Second, it can be concluded that actinolite, phlogopite and even quartz are clearly the dominant SiO_2-bearing minerals in these samples. In contrast, the occurrence of albite, allanite, K-Feldspar, talc, and titanite is of a lesser extent and of varying quantity, although titanite is present in the most of the samples.

If this is generally true, ore type of B2 requires more mineralogical investigations in order to construct a 3D geological model based on the ore types as defined by the mineralogy. Furthermore, the silicates, especially actinolite, seem to have been enriched in the finest fraction (< 40 μm) after crushing and comminution in the laboratory rod mill (10 minutes) and in the laboratory ball mill (35 minutes). It must be kept in mind that the content of silicon (Si) / silica (SiO_2) is dependent on the type of silicates (quartz with 100 wt.% SiO_2 as absolute maximum; Deer et al. 2001), which of course has an impact on SiO_2 grade in the concentrate. This is also closely related to the liberation of magnetite and the mineralogy of the middlings, which is discussed in more detailed in Chapter 9.

Based on the analysis data by QEMSCAN, it can be concluded that there is no even distribution of the dominant silicates (actinolite, phlogopite and quartz), but that there are two subtypes within ore type B2 based on the mineralogical data (see also Fig. 62, 63, 64, and 65; Appendix 20). The first one, tentatively named as subtype B2-a, is characterized by actinolite ± phlogopite and is represented by samples 6252, 6363 and 6387. The latter subtype, tentatively named as subtype B2-b, is characterized by phlogopite and quartz and is presented by samples 6351, 6363 and 6370. This possible split-up of ore type B2 into the two subtypes mentioned above, requires further mineralogical investigations with, above all, a larger number of samples combined with the mineral processing tests. The same applies to their distribution within the Kiirunavaara iron ore deposit. The division of ore type B2 into two subtypes, B2-a and B2-b, will be used in rest of this study.

Based on the observations, it should be paid attention to three essential characteristics of high-SiO_2 ore type B2. First, how is the distribution of SiO_2-bearing minerals in the different particle size classes. Second, how is grindability affected by the mineralogy of the ore. Third, the liberation and intergrowth of SiO_2-bearing minerals and Fe Oxides (almost entirely magnetite) and how they behave during the magnetic separation (Chapter 9 and 10). Furthermore, the data on the generation of the finest material (< 20 μm) during the comminution, may also be of importance. These questions will be discussed in detail in Chapter 7.2 (energy consumption related to ore type B2) and in Chapter 9 (liberation analysis) and compared with data on mineralogy and mineral characterization of the silicates presented in this chapter. For the liberation analysis (see Chapter 9), it is essential to study the distribution of the essential SiO_2-bearing minerals in different fractions (> 80 μm, 80/63 μm, 63/40 μm, < 40 μm) after comminution in different levels of dispersity. The three finest fractions (80/63 μm, 63/40 μm, and < 40 μm) of samples 6252, 6351, 6370, and 6387 were selected for magnetic separation tests by the Davis magnetic tube. This data is also essential for the liberation analysis.

8.5 Deportment of silicon (Si)

Traditional bulk geochemical analysis techniques such as ICP (*Inductively Coupled Plasma*) or XRF (*X-Ray Fluorescence*) do not offer the capability to measure the deportment of elements in different minerals or phases. XRD (*X-Ray Diffraction*) and automated mineralogy such as QEMSCAN and MLA can do just that. Automated mineralogy can be regarded as a turnkey solution for elemental and mineral deportment analysis. Furthermore, elemental deportment also entails the comprehensive understanding of minerals and mineral chemistry that don't necessarily contribute to the grade of the ore or affect the efficiency of processing.

As a result, elemental and mineral deportment has become an essential requirement for ore characterization projects in the last several years (Agorhom et al. 2012, Smythe et al. 2013). As previously mentioned, the requirements for an elemental distribution analysis are mass flow, mass-% of each particle size class (fraction) and chemical composition and the density of the minerals or phases, all of which are imported into iExplorer (Datastore). In general, an elemental deportment analysis involves the quantitative investigation of the relationship between one or more elements and the host (mineral or phase), in which these elements occur in significant concentrations.

An elemental deportment allows comparison of the contribution of a selected element, in this case silicon (Si), within various minerals to the total content for the element of interest across size fractions (FEI Butcher 2012 c). In the charts, the comparison of the elemental mass of silicon is presented across the four finest fractions (> 80 µm, 80/63 µm, 63/40 µm, < 40 µm) for samples 6252, 6363, and 6387 (Fig. 64) and for samples 6351, 6367, and 6370 (Fig. 65). The numeric data is given in Appendix 21. In this analysis on the elemental deportment of silicon (Si), the initial classification and division of ore type B2 into two subtypes, B2-a and B2-b, will be used as defined in the previous chapter.

In Figures 64, C, and E, the elemental deportment of silicon (Si) is represented for the subtype B2-a as the total mass and in Figures 64 B, D, and F the same data is normalized to 100%. The elemental deportment of silicon (Si) is represented for the subtype B2-b in Figure 65 in the same manner. When looking at the subtype B2-a, actinolite is clearly the most important SiO_2-bearing mineral within this subtype. This is particularly true for samples 6251 and 6387. In sample 6363, phlogopite, and to some extent quartz, are also essential sources of silicon (Si). On the basis of mineralogy, this sample can presumably be attributed to subtype B2-a, although there may be some degree of overlap between these subtypes

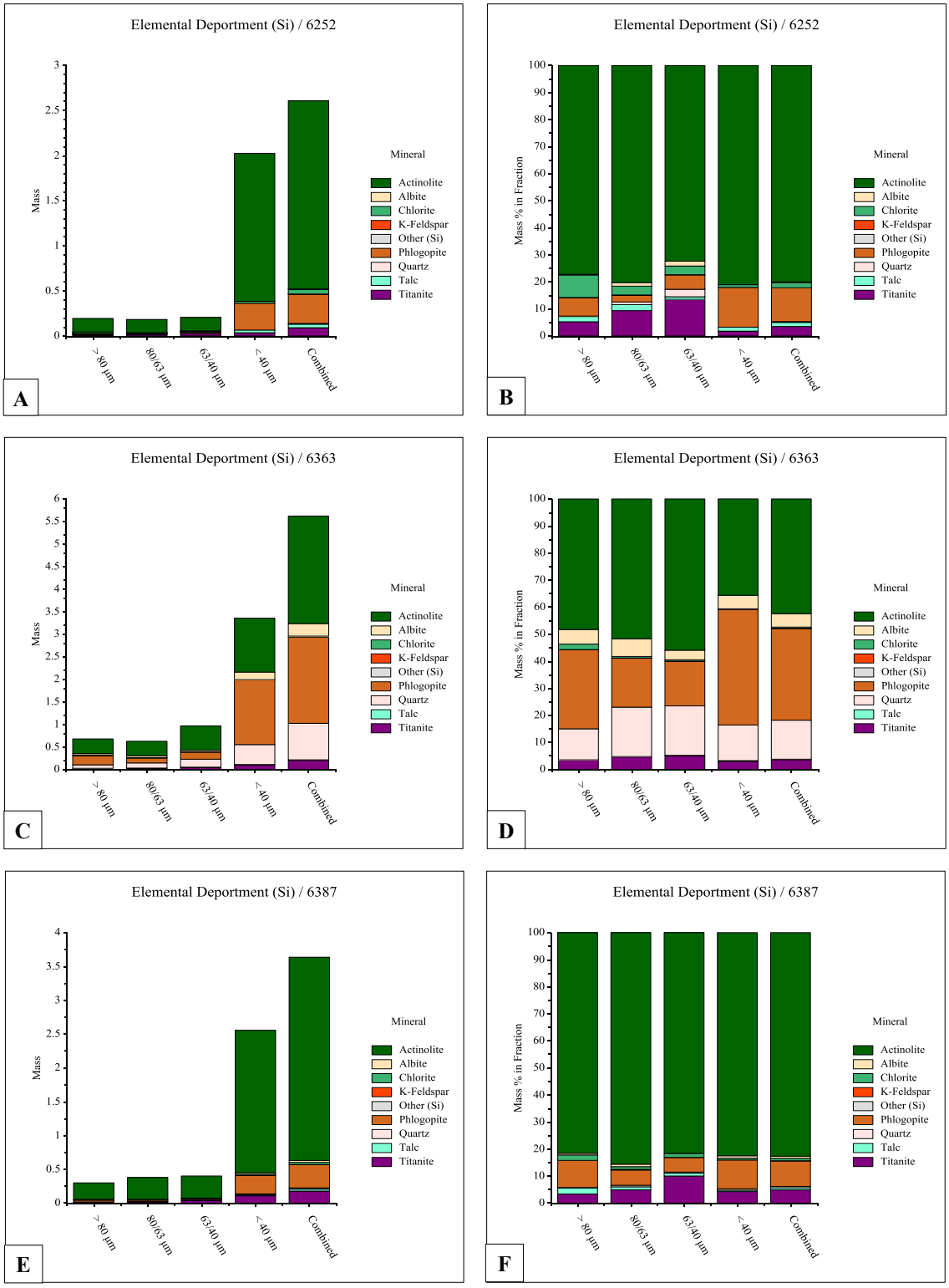

Figure 64. Deportment of silicon (Si) in samples 6252, 6363, and 6387 representing the actinolite dominated subtype (B2-a). (A), (C), and (E) represent the absolute mass of Si in the samples. (B), (D) and (F) represent the same samples normalized to 100%.

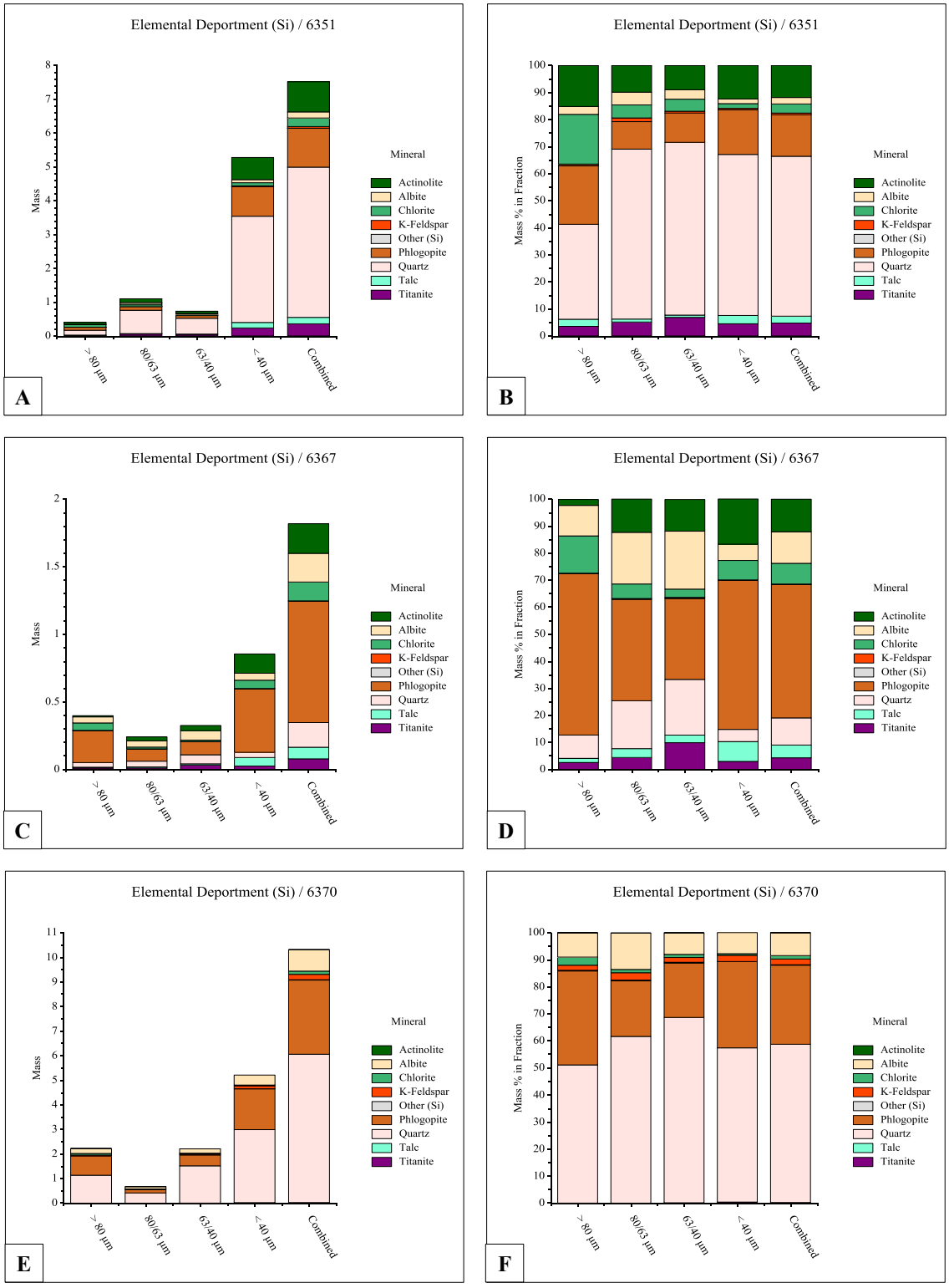

Figure 65. Deportment of silicon (Si) in samples 6351, 6367, and 6370 representing the quartz and phlogopite dominated subtype (B2-b), (A), (C) and (E) represent the absolute mass of Si in the samples. (B), (D), and (F) represent the same samples normalized to 100%.

The other subtype, B2-b, clearly differs in mineralogy relative to subtype B2-a. In samples 6351 and 6370, quartz is the main SiO_2-bearing mineral, although it is not as dominant in modal mineralogy (Fig. 62 and 63, Appendix 20) and not a common mineral in the deposit based on earlier investigations

(Nordstrand 2012, Niiranen 2012 b, Aupers 2014). However, quartz is rich in silicon (Table 32) which can be an explanation for this characteristic. In sample 6363, the main SiO_2-bearing mineral is phlogopite but chlorite and albite can contain up to 25% of the silicon (Si) in the different fractions. The different mineralogy of SiO_2-bearing minerals and their liberation and recovery will be discussed in Chapter 10. It is also evident that titanite occurs in each sample, representing both subtypes B2-a and B2-b, but it seems to be of little to no importance as a source of silicon (Si). However, aside from ilmenite and rutile, titanite can be regarded as one of the main sources of titanium (Ti) especially in ore type B2.

9. LIBERATION ANALYSIS

9.1 Preface

Mineral liberation analysis has always been a crucial part of the characterization of an ore for mineral processing (Lamberg 2010, Liipo et al. 2012, Lamberg & Lund 2012). A series of analytical methods are used to study liberation and the intergrowth of valuable minerals and gangue in process mineralogy and mineral processing. In this study, two methods are used: separation with the Davis magnetic tube (Chapter 5.1) and QEMSCAN (Chapter 8.1). The mineralogical approach was selected for liberation analysis with a focus on parameters like modal mineralogy, mineral associations and particle size distribution (fractions). They can be regarded as an important characteristic in process mineralogical point of view because of their relation to the degree of liberation, behavior in the magnetic separation and, not least, to understand the occasionally high SiO_2 grade in the magnetite concentrate at the beneficiation plants in Kiruna. In particular, this applies to ore type B2, which is rich in SiO_2 and the amount of which is predicted to increase in the deeper parts of the Kiirunavaara ore body.

In process mineralogy, the degree of liberation of a mineral is generally calculated from examining 2D sections (grain mounts) of a statistically representative set of particles (often large amount of particles) containing the mineral of interest. The degree of liberation is typically based on the area–% of the mineral grains of interest, which can further be estimated to wt.% or vol.% based on the pre-defined density of the minerals and / or pre-defined narrow particle size classes. Wills (2006) defines the degree of liberation as a percentage of the mineral of interest occurring as free particles in the material such as concentrate, mill product, etc. in relation to the total content of this mineral. Schubert (1988) defines the degree of liberation as presented in *Equation* 35 based on the method described by Gaudin (1939), in which the particles are classified into narrow particle size classes as liberated particles and binary, ternary etc. intergrowths and evaluated. The degree of liberation A_{ij} of a mineral phase (i) in a particle size class (j) is given in *Equation* 35:

$$A_{ij} = \frac{N_{fr}}{N_{fr} + N_{eq}} \cdot 100 \qquad \text{in \%} \qquad (Eq.\ 35)$$

Where N_{fr} corresponds to the number of liberated particles and N_{eq} to the number of the equivalent particles in the particle size class *j*. Furthermore, using the degree of liberation A_{ij}, *Equation* 36 gives the degree of liberation for the total sample as follows:

$$A = \frac{\sum_{i=1}^{N} A_i \mu_{3,i} c_i}{100\ \hat{c}} \qquad \text{in \%} \qquad (Eq.\ 36)$$

Where $\mu_{3,i}$ is the mass of the particle size class (fraction), c_i is the grade of the valuable mineral in the particle size class *i* and $\hat{c}$ is the medium grade of the valuable mineral in the total sample. However, the degree of liberation is not enough to understand and predict the behaviour of the particles and minerals in a process where different types of mixed particles are present and behave in a unique way (Lamberg & Vianna, 2007). For example, in Kiruna, where methods of the mineral processing at LKAB today are comprised of wet low intensity magnetic separation (WLIMS) and reversed apatite flotation. In the future, it may be necessary to consider other process options, such as silicate flotation, because of the increasing SiO_2 grade. This study will provide additional, relevant information to consider a solution to the problem of increasing silica grade.

9.2 Intergrowths of magnetite

9.2.1 intergrowths of magnetite and gangue mineral

The analysis and the comparison of mineral associations for non-liberated particles is challenging, especially in the case of ternary particles when not using automated mineralogy. Lund (2013) has described it for the iron ore deposit in Malmberget but it can also be adapted for the Kiirunavaara ore as follow: if just comparing the mass proportion of magnetite with, for example actinolite, the figure is affected by the degree of liberation of magnetite and the grade of actinolite in the samples. If the degree of liberation of magnetite is high, as in the case in this study, the binary association of magnetite and actinolite should be low. Similarly if the grade of actinolite is low in the sample the mass proportion of the binary intergrowth of magnetite - actinolite particles will also be low.

The mineral associations of magnetite and different gangue minerals associations - binary and ternary - for samples 6252 (A), 6363 (B), and 6387 (C), representing the subtype B2-a, is shown in Figure 66 and for samples 6351 (A), 6367 (B), and 6387 (C) representing the subtype B2-b in Figure 67 (numeric data is given in Appendix 22). A particle is called ternary if it consists of three minerals or phases (although the term ternary also encompasses particles with more than three minerals). Binary is, on the other hand, a term for a particle containing only two minerals or phases. When examining the mineral associations after comminution and before the Davis magnetic tube test, the two finest fractions (63/40 µm and < 40 µm) are of special interest. When comparing these two subtypes of ore type B2 with each other it is apparent that the intergrowth of magnetite and the silicate minerals are the most common type.

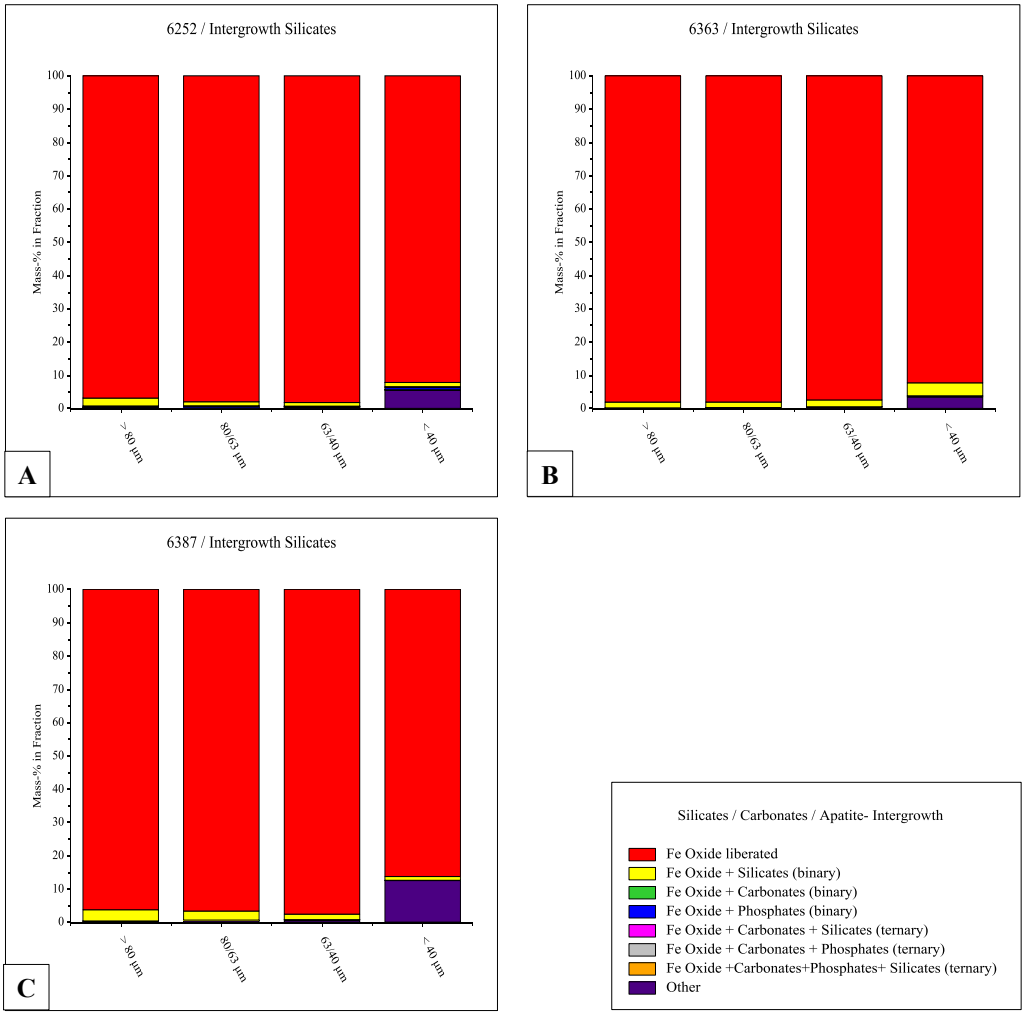

Figure 66. Intergrowth of magnetite (Fe Oxide) and different gangue mineral associations for samples 6252 (A), 6363 (B) and 6387 (C) representing the subtype B2-a after crushing, comminution in a laboratory rod mill (10 minutes) and in a laboratory ball mill (35 minutes) at the laboratory of the Institute of Mineral Processing.

In Figures 66 and 67 is also an "Other" group presented. This group consists mostly of fully liberated gangue minerals or gangue mineral associations (Fig. 68 and 69). They are not examined in more detail in this study, but each sample is clearly enriched in the finest fraction (< 40 µm). The next most common binary mineral associations are magnetite with apatite or with carbonates. However, they are not minerals of importance for the problem of high SiO_2 grades in the magnetite concentrate. Furthermore, binary associations of apatite with carbonate and liberated apatite will be removed to a large extent in the process during the apatite flotation. This seems to be the case for the low grade middlings with binary associations of magnetite and apatite, because the P grade in the magnetite concentrate is as low as 0.025% (LKAB 2014).

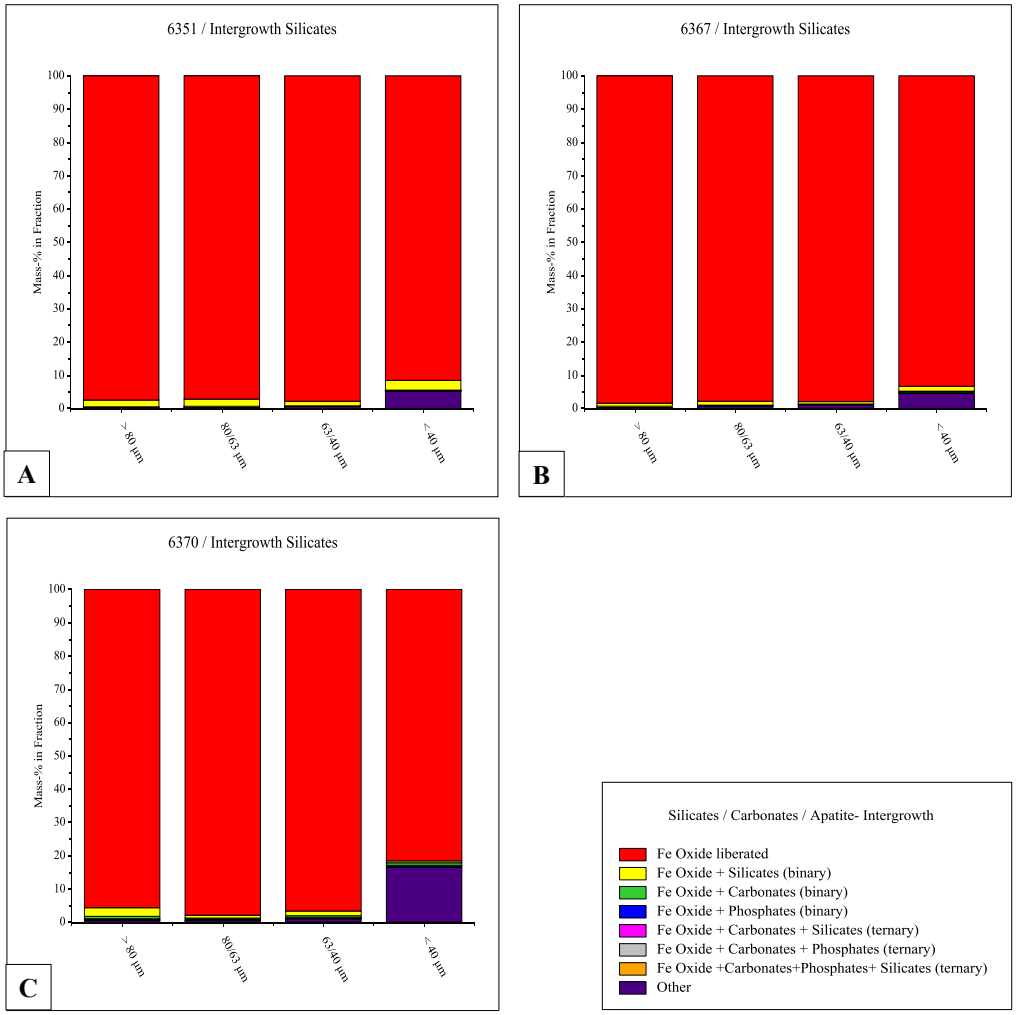

Figure 67. Intergrowth of magnetite (Fe Oxide) and different gangue mineral associations for the samples 6351 (A), 6367 (B), and 6370 (C) representing the subtype B2-b after crushing, comminution in a laboratory rod mill (10 minutes) and in a laboratory ball mill (35 min) at the laboratory of the Institute of Mineral Processing.

Figure 68. Fully liberated gangue minerals after crushing and comminution in a laboratory rod mill (10 minutes) and in a laboratory ball mill (35 minutes) at the laboratory of the Institute of Mineral Processing. Sample 6363, fraction 63/40 µm, mineralogy after SIP-List presented in Figure 58 A.

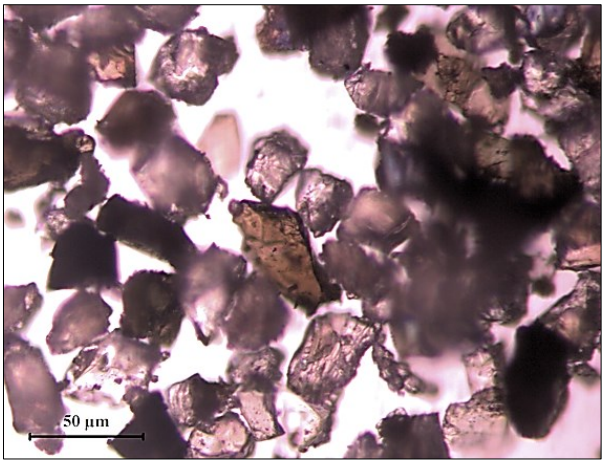

Figure 69. Fully liberated gangue minerals (silicates and apatite) in the waste (non-magnetics) after the Davis magnetite tube separation. Sample 6370, fraction 63/40 µm.

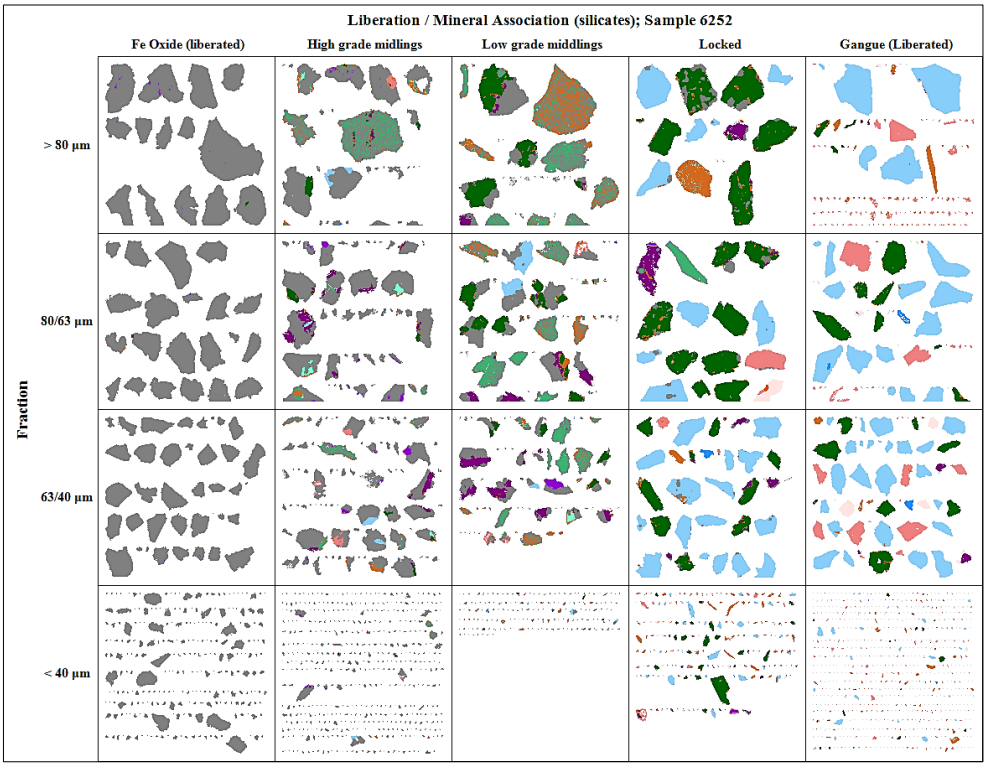

Figure 70. Mineral associations of magnetite with various gangue minerals for sample 6252 (subtype 2B-a) with respect to different fractions and classification used by LKAB (liberated magnetite, high grade and low grade middlings, locked and liberated gangue), mineralogy after SIP-List presented in Figure 58 A.

In Figure 70, the mineral associations of magnetite and varoius minerals is presented for sample 6252 (subtype B2-a) with respect to different fractions and classificiations used by LKAB (liberated magnetite, high grade and low grade middlings, locked and liberated gangue). As earlier noted, sample 6252 is characterized by low energy comsumption to obtain P_{80} = 45 µm and a poor recovery of silica. As a conclusion it can be said that there are large amounts of binary intergrowths of magnetite and varoius silicate minerals, most often with actinolite, phlogopite, chlorite and titanite, which will be

discussed in detail in the next Chapter. Alternately the liberation of gangue mineral (mostly apatite and carbonate, but also some phlogopite and actinolite) is good. In this respect the most interesting are the two finest fractions (63/40 µm and < 40 µm) because these are equivalent to the corresponding particle size (P_{80} < 45 µm) in the magnetite concentrate at the beneficiation plants of the Kiirunavaara site.

9.2.2 Intergrowth of magnetite with silicate minerals

In this chapter, the two different subtypes of the high-SiO_2 ore type B2 are studied separately. Moreover, only binary intergrowths such as magnetite and actinolite and magnetite and phlogopite will be taken account into because of the intergrowths of magnetite and two or more silicate (ternary) appearing to be uncommon based on the data from QEMSCAN analysis. The binary mineral associations of magnetite (Fe Oxide) and silicate minerals for the subtype B2-a is presented as wt.% in fraction in Figure 71 and for the subtype B2-b in Figure 72. Equivalent numeric data is displayed in Appendix 23.

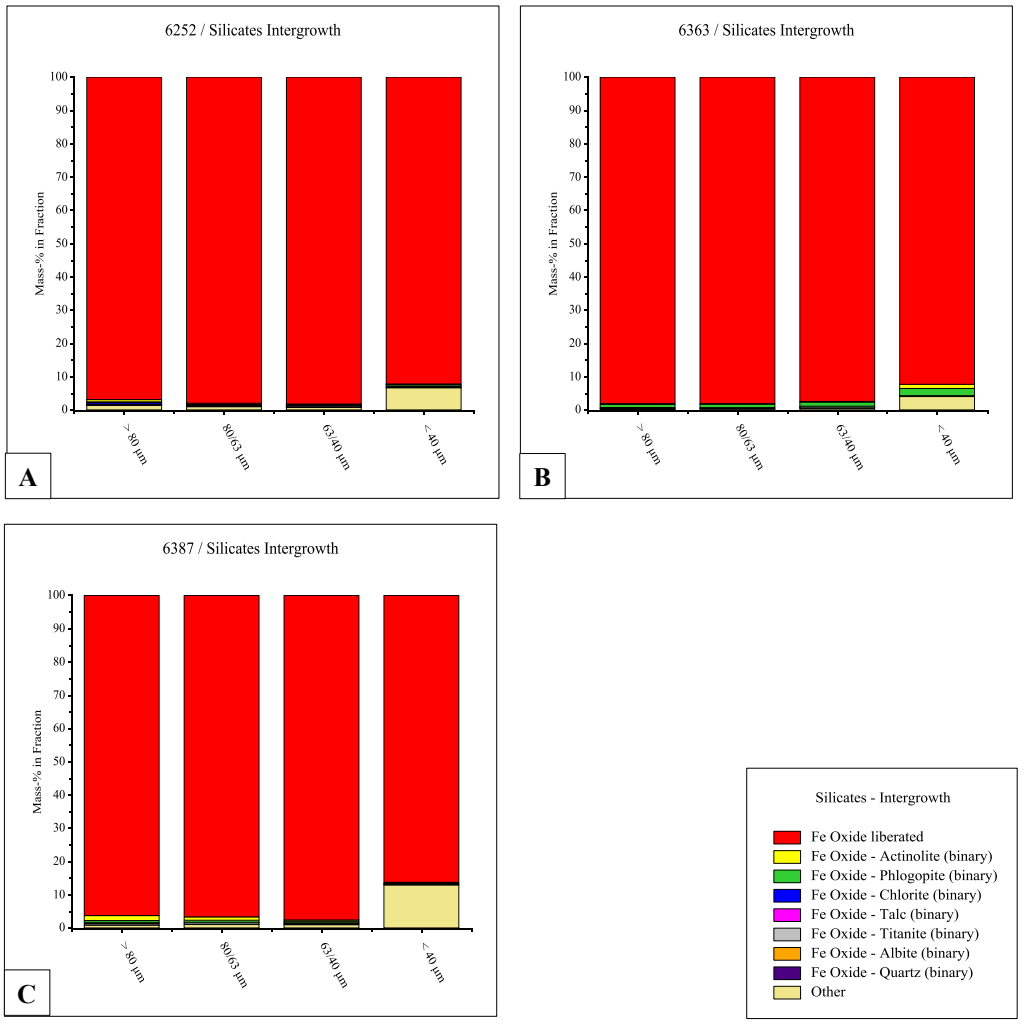

Figure 71. Binary intergrowths of magnetite (Fe Oxide) and various silicates for samples 6252 (A), 6363 (B), and 6387 (C) representing subtype B2-a after crushing, comminution in a laboratory rod mill (10 minutes) and in a laboratory ball mill (35 min).

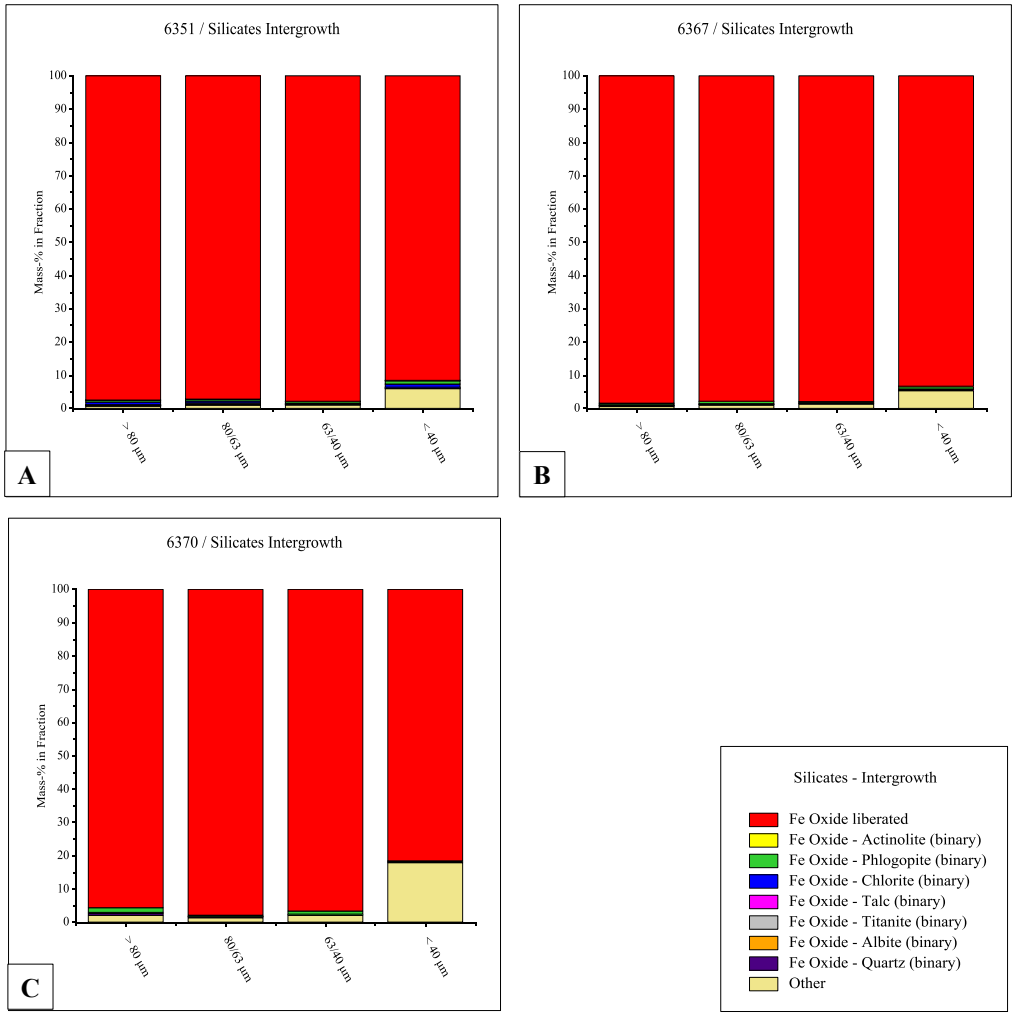

Figure 72. Binary intergrowths of magnetite (Fe Oxide) and different silicates for samples 6351 (A), 6367 (B), and 6370 (C) from subtype B2-b after crushing, comminution in a laboratory rod mill (10 minutes) and in a laboratory ball mill (35 min).

Based on the results, some conclusions can be drawn from the degree of liberation of magnetite and silicates as well as from the binary intergrowths. As was noted, the degree of liberation of magnetite is high or even very high in these samples and even the degree of liberation of gangue minerals (Fig. 68 and 69). However, it must be kept in mind that there might be some degree of overestimation related to the liberation of magnetite when automated mineralogy is used. First of all, the "Other" group is significant in the finest particle size class (< 40 µm), which is an indication of a high degree of liberation of silicates as well as other gangue minerals such as phosphates, carbonates and sulphides (Fig. 71 and 72). It can also be noted that the high degree of liberation of the valueable minerals or gangue minerals will not always be necessary and, In particular, it should be noted that there is considerable growth in the "Other" class between the two finest fractions (63/40 µm and < 40 µm). This suggest that the ore must be ground into very fine fractions, in some cases, it can even be unwanted (Schubert 1988, Wills 2006). An example is given for magnetic and gravity separation by Wills (2006) in which high recovery can be achieved, when the valuable minerals are poorly liberated or enclosed (degree of liberation equal

zero).Second, there seems to be a clear difference between the two subtypes B2-a and B2-b in binary intergrowths of magnetite and silicates. In the subtype B2-a (samples 6252, 6363, and 6387), intergrowths of magnetite and actinolite are the most common, but an intergrowth of magnetite and phlogopite can also occur. On the contrary, in the subtype B2-b (samples 6351, 6367, and 6370) intergrowths of magnetite and phlogopite, but also of magnetite and chlorite, are common because chlorite is an alteration product of phlogopite.

The binary intergrowths of magnetite and actinolite, but also intergrowth of magnetite and phlogopite in some cases, can be regarded as the most important and presumably also the most common type intergrowths in the case of magnetic separation (Fig. 73). In some case the amount of binary intergrowths of magnetite and chlorite, magnetite and titanite and even magnetite and quartz may be relevant in terms of SiO_2 grade in the magnetic concentrate. Binary intergrowths of magnetite and talc or magnetite and albite can be expected to have much less significant role concluded from results of this study.

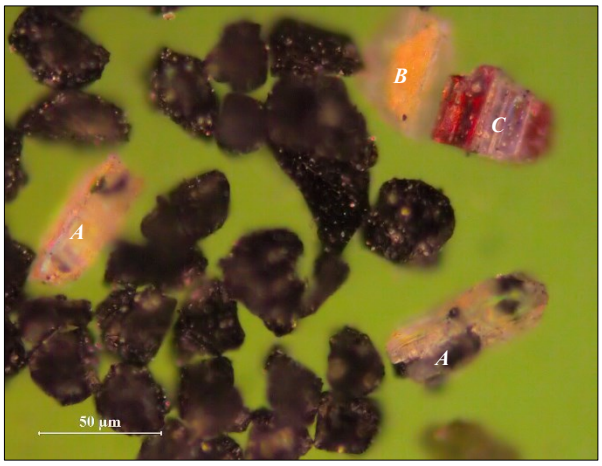

Figure 73. Fully liberated magnetite particles (dark), intergrowth of very fine-grained magnetite and actinolite (A), liberated actinolite (B), (C) liberated titanite (?). Sample 6367, particle size class 63/40 µm (in transmitted and reflected light).

9.3 Liberation analysis based on the Henry-Reinhardt charts

9.3.1 Principle of the Henry-Reinhardt charts

The Henry-Reinhardt chart can be regarded as a graphic combination of the mineralogical or chemical information and seperability of physical parameters. In his book, Heidenreich (1954) describes the basics of the Henry-Reinhardt chart, which was initially created to determine the different quality classes of coal. The relevant properties for coal are the specific gravity and the ash content (Heidenreich 1954). The specific gravity can be determined by the so-called sink and float analysis, in which the liquids of known density are used. In the next step, the ash content is determined for every quality class. These parameters can be used to define the coal into different quality classes.

While, the Henry-Reinhardt chart is not often used in mineral processing (Drzymała 2007), in this study it is used for liberation analysis to determine the grade and content of silica (SiO_2) for samples 6382, 6365, and 6354, representing the three main ore types of the Kiirunavaara deposit. It is also used for liberation analysis for samples representing the high-SiO_2 ore type B2 to complete the liberation analysis carried out be automated mineralogy. A Henry-Reinhardt chart serves to characterize an ore for its amenability to separation or technical processing by combining technically relevant separation properties such as density, magnetization and size with mineralogical or chemical information. Further, the Henry-Reinhardt chart provides the characterization of the intergrowths, as well as liberation and the best separation results possible by the exploiting a separation property (Böhm 2009, Böhm 2011, Kogelbauer & Böhm 2009).

The Henry-Reinhardt chart provides also information on the best possible separation result at a given physical property setting, as well as the intergrowth characteristics (liberation). In Figure 74, a simplified Henry-Reinhardt chart with (basic) intergrowth curves is presented. The red intergrowth curve (A) indicates a good separability with the selected property. The black intergrowth curve (B) indicates that separation will be very poor with selected properties. In this study, it reflects of a high degree of liberation between magnetite and silicates, which are the most important gangue minerals in the high-silica ore type B2, and the only source of SiO_2 in the Kiirunavaara deposit.

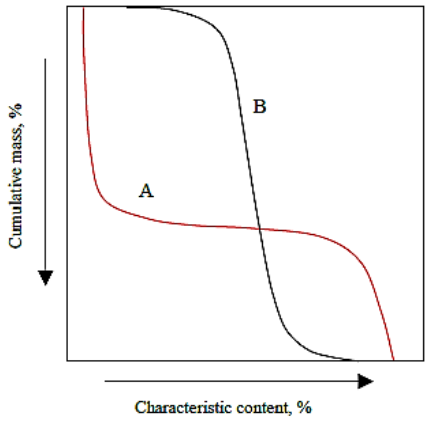

Figure 74. Simplified Henry-Reinhardt chart with (basic) intergrowth curves (Heidenreich 1954): (A) Separation is possible with the selected property; (B) No or very poor separation is possible because of low degree of liberation or no amenability to the separation.

For this study, the used property for separation with the Davis magnetic tube, was the self-evident magnetization of the particles. The varying degree of magnetization, by means of external magnetic fields and, consisting of different grades of magnetic minerals can be used to split sets of particles into classes of given boundaries of magnetization. For magnetization there are several methods that can be used, depending on the susceptibility of the particles in a magnetic field. For paramagnetic particles the Franz Isodynamic Separator can be used, and for the ferromagnetic particles the Davies magnetic tube or pick up method are suitable (Böhm 2009, Böhm 2011). The pick-up method was also tested with

sample 6354 for the particle size class 100/40 µm, but it turned out to be unsuitable for the Kiirunavaara ore because of the extremely high content of magnetite. Wartbichler (2014) has, however, used the pick-up method successfully when studying the separation of hematite and magnetite in the martite ore from the Kiirunavaara deposit. More information about the principles and use of the pick-up method can be found by Böhm (2009) and Wartbichler (2014). Furthermore, it can be noted that LKAB also validates the process with respect to the wet low intensity magnetic separation (WLIMS) by comparing the actual silica levels in the process with the silica levels in the Davis magnetic tube concentrate (Malm 2009, Adolfsson & Fredriksson 2011).

9.3.2. Construction of the Henry-Reinhardt chart

The data for the construction of the Henry-Reinhardt chart can be collected in one or several steps. For example, the first step is the property analysis (fractioning), and the second step the chemical and/or mineralogical analysis. Fractioning can also include several steps. Sample 6354 (D3) serves an example. The first step was the determination of the particle size classes by screening. The second step was the fractioning with the Davies magnetic tube, where several current intensities were used within the size classes 100/40 µm and < 40 µm. After the Davis magnetic tube tests at the mineral processing laboratory in Leoben, each fraction was dried and weighed (Appendix 10) and the chemical assays were carried out for every fraction at the laboratory of Labtium Oy (Appendix 12). By analysing a defined characteristic grade in each fraction, such as SiO_2, TiO_2, or P grades for sample 6354, the Henry-Reinhardt chart can be drawn. The data needed for the construction of a Henry-Reinhardt chart for sample 6354 (Fig 78 B) is displayed in Table 35.

Table 35. Data (sample 6354; fraction < 40 µm) from the Davis magnetic tube tests for the construction of the Henry-Reinhardt chart by Heidenreich (1954) and Böhm (2011); (MP = concentrate, magnetic particles; W = waste, non-magnetic particles, $\overline{x}$ = average grade).

Class	BASIC INTERGROWTH CURVE					CUMULATIVE CURVES					
						Magnetics (retaining)			*Non-magnetics (passing)*		
	I_E	**Mass**	**Mass**	**SiO_2**	**Units**	**Mass (Σ)**	**Grade ($\overline{x}$)**	**Units (Σ)**	**Mass (Σ)**	**Grade ($\overline{x}$)**	**Units (Σ)**
	[A]	[g]	[%]	[%]	[%²]	[%]	[%]	[%²]	[%]	[%]	[%²]
						-	-	-	100	2.65	265.34
I	0.12 (*MP*)	0.82	2.76	1.01	2.79	2.76	1.01	2.79	97.24	2.70	257.69
II	0.18 (*MP*)	18.92	63.68	0.54	34.39	66.44	0.56	37.18	33.56	6.80	90.61
III	0.225 (*MP*)	4.51	15.18	1.28	19.45	81.62	0.69	56.63	18.38	11.36	124.98
IV	1.78 (*MP*)	0.26	0.88	7.87	6.89	82.50	0.77	63.52	17.50	11.53	198.80
V	>1.78 (*W*)	5.20	17.50	11.53	201.82	100.00	2.65	265.34	0.00	0.00	0.00
		29.71	100.00	2.65	265.34						

It should be noted that there was not enough material in the Davis magnetic tube concentrate (magnetics) for two samples (sample 6382, fraction 100/40 µm, 1.78 A, and sample 6365, fraction 100/40 µm, 1.78 A) to carry out the chemical analysis. Furthermore, there was a contamination through distilled water

during the analysis at Labtium's laboratory, which had an impact on the aluminium (Al) and calcium (Ca) grades. However, Al and Ca are of no interest for this study.

9.3.3 Henry-Reinhardt charts for samples 6382 (B1), 6365 (B2), and 6354 (D3)

The mineralogy of silicates in the Kiirunavaara ore deposit is well known for the high-SiO_2 ore type B2 (Niiranen 2012 b, Aupers 2014). There is not so detailed information about the mineralogy of the silicates in ore type B1 and ore type D (Nordstrand 2012, Aupers 2014). However, it can be assumed that there is no significant difference in the mineralogy of silicates between different ore types, but rather in their quantity. It can also be assumed that the same silicates are present in ore types B1 and D as in the high-silica ore type B2. The most common silicates in ore type B1 are the minerals of the mica group, mostly phlogopite, which is also a common mineral in subtype B2-b of ore type B2. Other minerals representing silicates, directly associated with magnetite, are minerals of the amphibole group, mostly actinolite, titanite, and quartz. Minerals of the amphibole group are abundant in larger aggregates and are typically coarse-grained (> 500 μm) (Aupers 2014).

The high-SiO_2 ore type B2 is more inhomogeneous than B1 and characterized by a higher portion of gangue minerals, of which the silicates are dominating. Gangue minerals are often finely disseminated or directly associated with magnetite. Also, porosity and break outs are more abundant in this ore type, and the number of disruptions in magnetite locally decreases towards gangue minerals. These areas are also characterized by a lower grade of porosity and less intergrowths of magnetite and gangue, mostly silicates (Niiranen 2012 a, Aupers 2014). In ore type B2, the most important SiO_2-bearing minerals in the deposit are actinolite, phlogopite, chlorite, titanite, and quartz. In some cases also talc, and alkali feldspars, mostly albite can occur. Zircon, allanite and thorite, which were identified in only a few cases, are uncommon. Based on their silicate mineralogy, ore type B2 seems to have two different subtypes. The first one is dominated by actinolite, in which actinolite is also the main source of SiO_2. The mineralogy of the second subtype is more complicated, in which phlogopite, quartz, chlorite and in some cases also albite are significant silicates. Generally, it should be noted that ore type B1 shows lower SiO_2 grade than ore type B2 and the high-phosphorous ore type D.

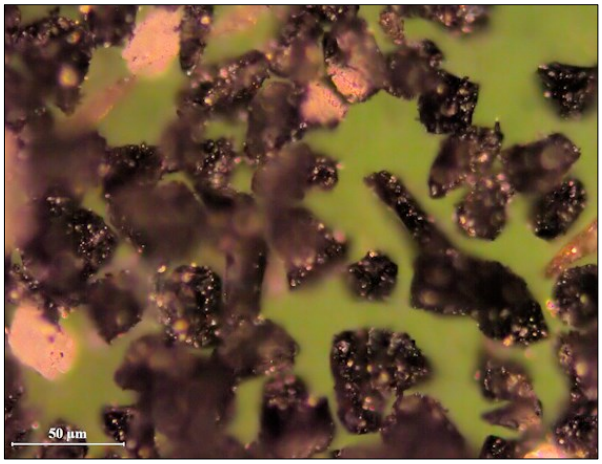

Figure 75. Fully liberated magnetite particles (dark) and silicates (transparent) and obviously carbonates (pink). Sample 6367, representing ore type B2, particle size class 63/40 µm (in transmitted and reflected light).

Not only the degree of the liberation of magnetite seems to be high or even very high for most of the samples, especially in the finest fractions, 100/40 µm and < 40 µm (Fig. 75). When comparing these ore types to each other it is apparent that the intergrowths of magnetite and the silicate minerals are the most common types. Especially, the binary intergrowths of magnetite and actinolite are the most common, but binary intergrowths of magnetite and phlogopite and magnetite and titanite can also occur.

In relation to ore type B1, based on data from the Davis magnetic tube tests and presented as the Henry-Reinhardt charts in Figures 76 A and 76 B, the following conclusions can be made. As has already been noted, ore type B1 is normally very homogeneous and has generally low SiO_2 grade. The most common SiO_2-bearing mineral is this ore type is phlogopite, which seems to occur more seldom as intergrowths with magnetite. This means that the degree of liberation of magnetite and gangue minerals is high or even very high. Furthermore, the separability by the Davis magnetic tube, which corresponds to the wet low magnetic separation (WLIMS), is good. When considering the problem with increasing SiO_2 grade in the incoming crude ore, ore type B1, as homogenous and with a rather low in SiO_2 content, seems to be trouble-free.

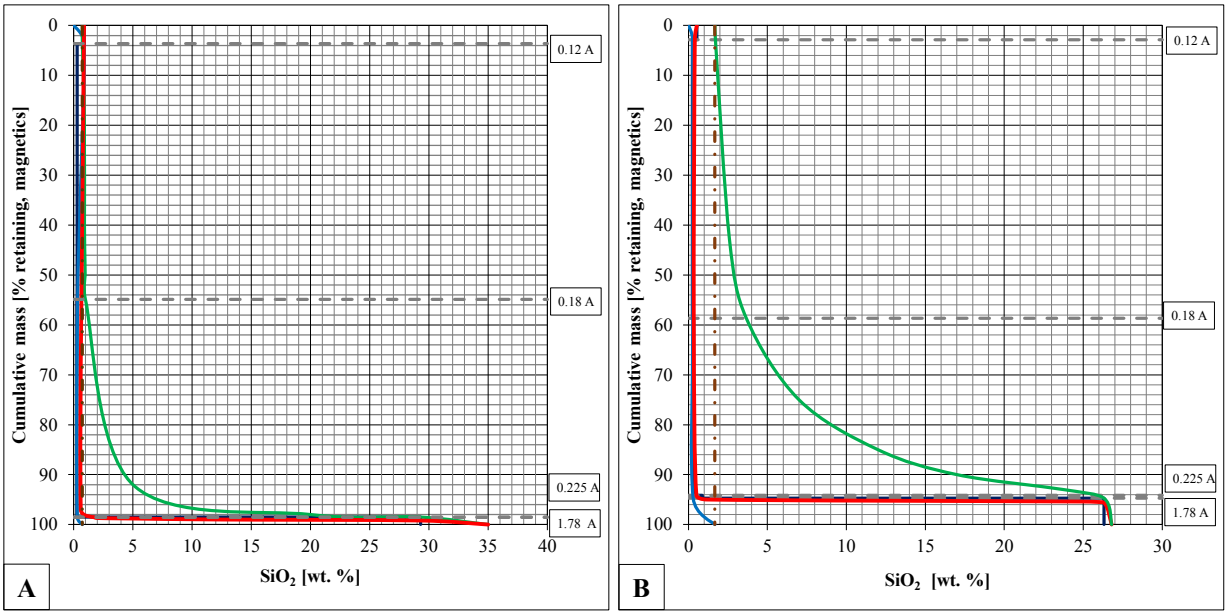

Figure 76. Henry-Reinhardt charts on the two finest fractions (A) 100/40µm; (B) < 40µm for sample 6382 (B1) based on data from the Davis magnetic tube tests. Basic intergrowth curve of magnetics = red, cumulative curve for magnetics = blue, cumulative curve for non-magnetics = green, dotted dark brown line = average SiO_2 grade.

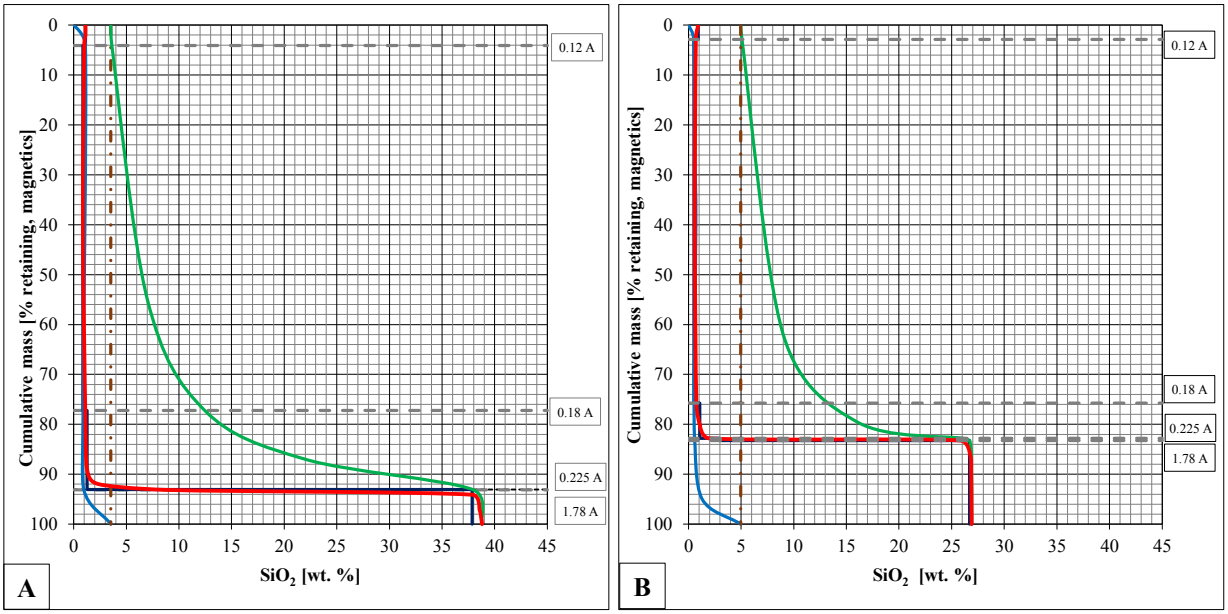

Figure 77. Henry-Reinhardt charts on the two finest fractions (A) 100/40µm; (B) < 40µm for sample 6365 (B2) based on data from the Davis magnetic tube tests (for explanation see Fig. 76).

The degree of liberation of magnetite seems to be high even for sample 6365, representing the high-silica ore type B2, based on the data from the Henry-Reinhardt charts presented in Figures 77 A and 77 B. Even the degree of liberation of gangue minerals, in this case silicates, seems to be high. However, there is clearly a higher SiO_2 grades in the magnetite concentrate after the Davis magnetic tube tests, as in the case of ore type B1. It can be concluded that in some cases there may be a poor separation of some silicates by the Davis magnetic tube tests, mostly actinolite, especially for the samples belonging to

subtype B2-a, compared to subtype B2-b, which causes an elevated grade of SiO_2 in the Davis magnetic tube concentrate. This will be discussed in detail in Chapters 9.4 and 9.5.

Ore type D is the third main ore type in the Kiirunavaara deposit. It represents, with its three subtypes D1, D3 and D5, the most P-rich parts of the deposit, especially from the northern most part, known as "Lake Ore". As with ore type B2, ore type D is more inhomogeneous that ore type B1 and shows a variable appearance both at macroscale and microscale (Aupers 2014). Besides apatite, which is the dominating gangue mineral in this ore type, phlogopite and actinolite can occur. Talc and albite are more uncommon. In some cases, this ore type can contain a larger amount of green actinolite, which can sometimes be quite fine-grained.

In the past, this ore type has been considered to be the most problematic due to the elevated SiO_2 grade in the magnetite concentrate. Based on data from previous investigations, including this one, ore type D can be regarded as "softer" than the other ore types, and this may have a direct impact on the liberation of silicates during the comminution, especially in the autogenous mills.

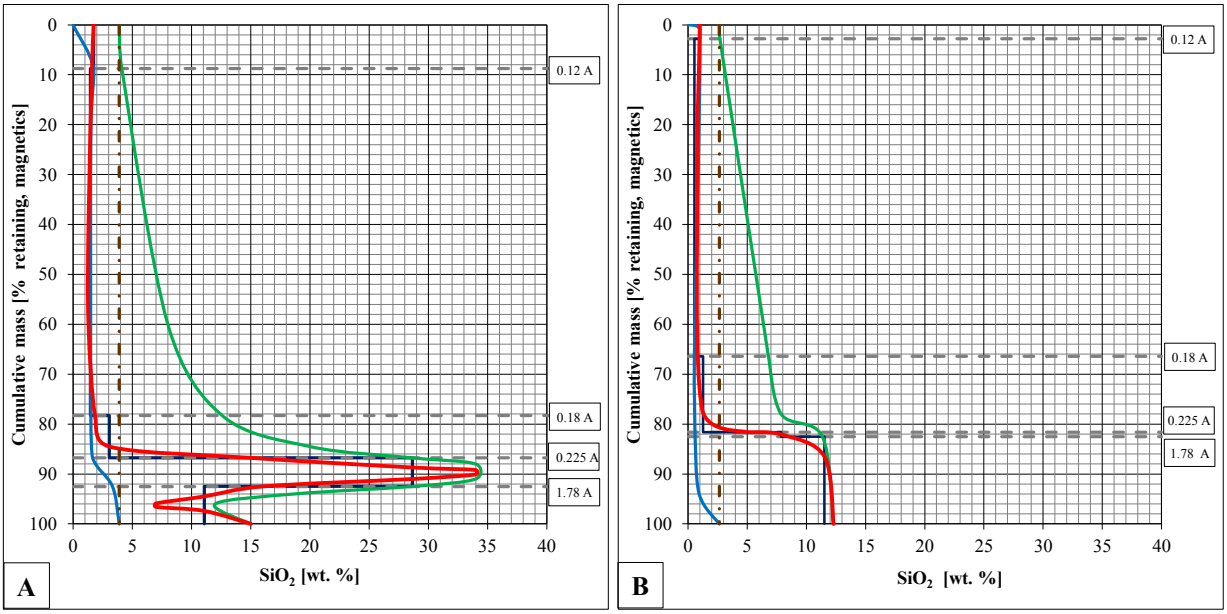

Figure 78. Henry-Reinhardt charts on the two finest fractions (A) 100/40µm; (B) < 40µm for sample 6354 (D3), based on data from the Davis magnetic tube tests (for explanation see Fig. 76).

When looking at the infornmation from the Henry-Reinhardt charts presented in Figure 78 A and B, it can be noted that the liberation and separation of the silicates is poorer compared to ore types B1 and B2. Especially, in the fraction 100/40 µm, the liberation of the silicates seems to be very poor. The large amount, almost 50% of SiO_2, is concentrated in the magnetics when separated by the Davis magnetic tube using a current intensity of 1.78 A (Fig. 78 A). This is clear evidence that there is a large amount of unliberated particles (intergrowths with magnetite and silicates) in this fraction. However, in the finest fraction, < 40 µm, the degree of liberation is significantly higher, but still there some small amount of unliberated magnetite particles.

No mineralogical analysis on the magnetite concentrate has been carried out, but it can be assumed that in the case of these unliberated magnetite particles, they are intergrowths of magnetite and actinolite. This characteristic in the liberation of magnetite and the intergrowths of magnetite and actinolite has been found to be in relation to the fine-grained inclusions of magnetite in actinolite (Niiranen 2012 a, Aupers 2014). Typical for this type is a structure of needle-like, euhedral actinolite crystals, which are likely a pseudomorph of pyroxene (Fig. 7 B). Furthermore, a very fine-grained, green mineral, apparently actinolite, has been described in ore type D (Fig. 8 C) by Aupers (2014). Thus, it can also be expected that this type of actinolite can most likely can occur as fine-grained intergrowths with magnetite. It should be noted that the amount of high-phosphorous ore type D significantly decreases in the deeper part of the Kiirunavaara deposit, based on information from the 3D resource model generated from exploration and grade control drilling (Niiranen & Böhm 2012, Niiranen & Fredriksson 2014). Therefore, it can be concluded that ore type D will have less impact lon the SiO_2 grade in the crude ore in the future, although the liberation of magnetite and silicates seems to be poorer compared to the other main ore types.

9.3.4 Henry-Reinhardt charts for ore type B2

In Chapter10.2, the mineral associations and the degree of liberation of magnetite and especially the intergrowths of magnetite and silicates were studied in detail. In this chapter, the magnetic separation of the comminution product will be studied with a focus on the separation of magnetite and silicates in relation to the high-SiO_2 ore type B2. For the separation with the Davis magnetic tube carried out at the mineral processing laboratory of the Institute of Mineral Processing, the three finest fractions (80/63 µm, 63/40 µm, < 40 µm) out of four samples were selected after the comminution in the laboratory rod mill and in the laboratory ball mill. Of the selected samples, 5252 and 6387 represent the subtype B2-a and samples 6351and 6370 the subtype 2B-b. The next step was the fractioning of each size class with the Davis magnetic tube at three current intensities 0.1 A, 0.2 A and 1.8 A. The third step was the determination of the mass and chemical assays on the genereated magnetic fractions and the waste (non-magnetics). Output data for the Davis magnetic tube tests and the chemical assays on the magnetics (magnetic concentrate) and waste are given in Appendix 11 and Appendix 13. The results of the magnetic separation tests carried out with the Davis magnetic tube will be preseneted in this chapter by the Henry-Reinhardt charts with comments.

The Henry-Reinhardt charts on the two finest particle size classes for samples 6252 and 6387, representing subtype B2-a, are presented in Figures 79 and 80. The Henry-Reinhardt charts for samples 6351 and 6370, representing subtype B2-b, are presented in Figures 81 and 82. The Henry-Reinhardt charts for the coarsest particle size class (80/63 µm) are displayed in Appendix 24.

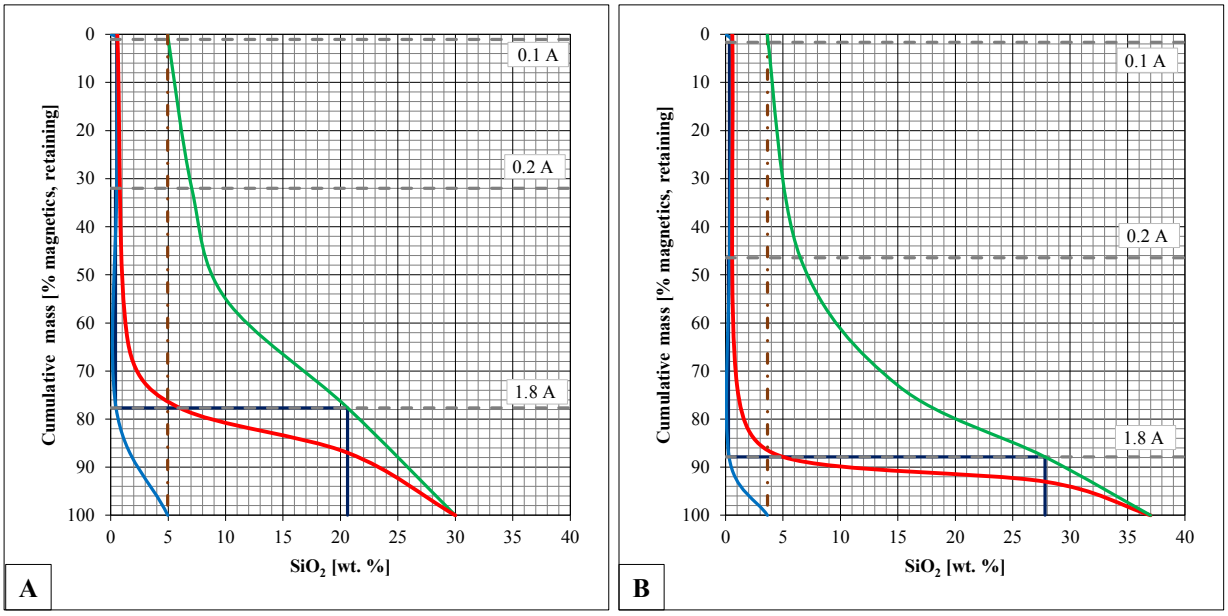

Figure 79. Henry-Reinhardt charts on the two finest fractions (A) 63/40µm; (B) < 40µm for sample 6252 representing the subtype B2-a based on data from the Davis magnetic tube tests (for explanation see Fig. 76).

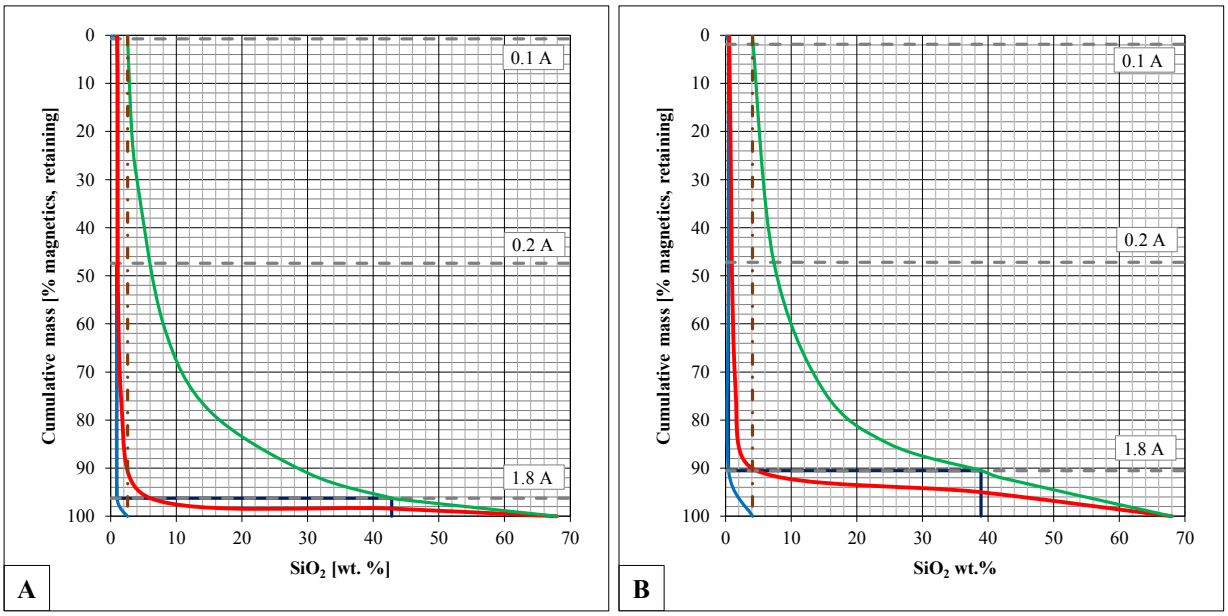

Figure 80. Henry-Reinhardt charts on the two finest fractions (A) 63/40µm; (B) < 40µm for sample 6387 representing the subtype B2-a based on data from the Davis magnetic tube tests (for explanation see Fig. 76).

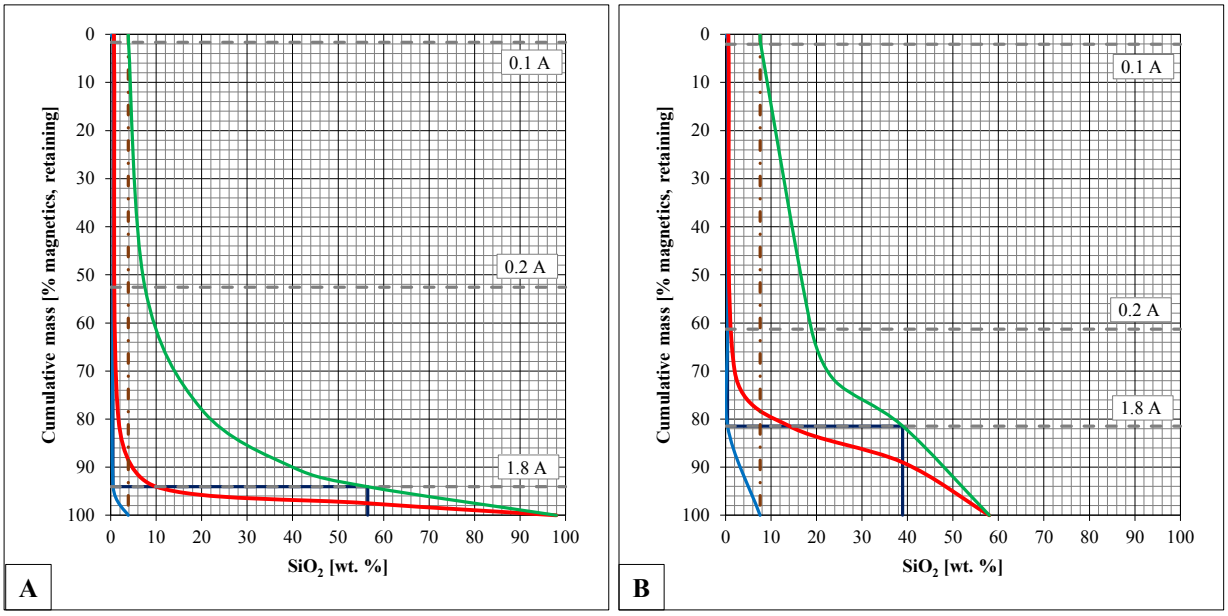

Figure 81. Henry-Reinhardt charts on the two finest fractions (A) 63/40µm; (B) < 40µm for sample 6351 representing the subtype B2-b based on data from the Davis magnetic tube tests (for explanation see Fig. 76).

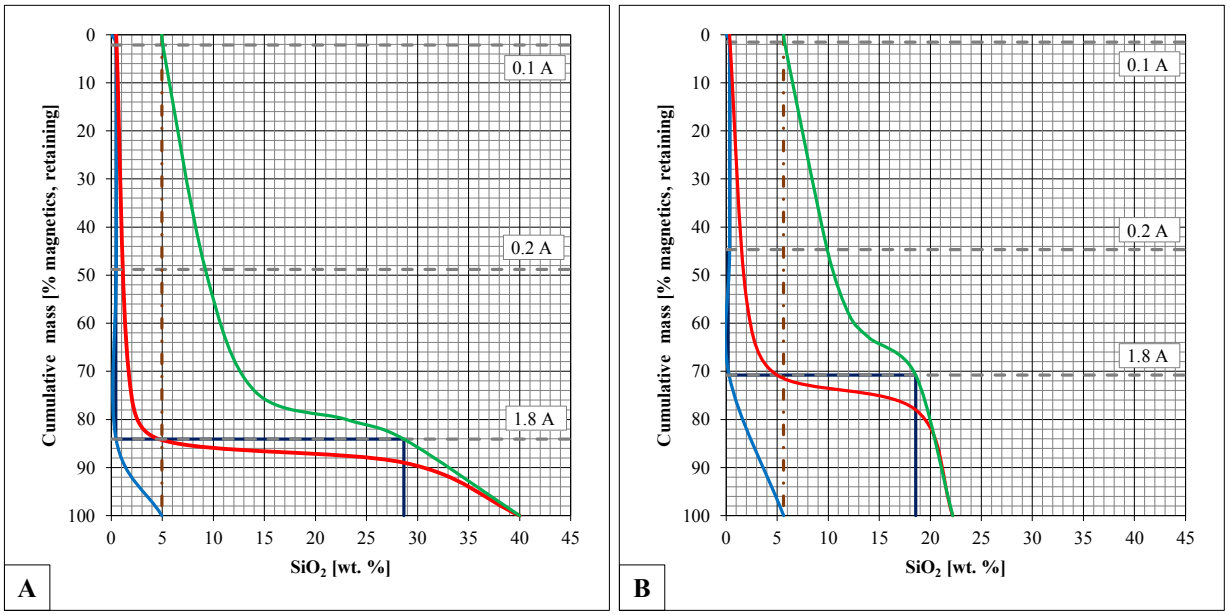

Figure 82. Henry-Reinhardt charts on the two finest fractions (A) 63/40µm; (B) < 40µm for sample 6370 representing the subtype B2-b based on data from the Davis magnetic tube tests (for explanation see Fig. 76).

When interpreting the Henry-Reinhardt charts presented in Figures 79 to 82, it is clear that the degree of liberation and thus the amenability to separation of magnetite and silicates (SiO_2) is good. It is also apparent that the degree of liberation increases when particle size decreases. Furthermore, the separation of magnetics (magnetite) and non-magnetics (mostly silicates) and the recovery of SiO_2 increases when the particle size decreases. The liberation of magnetite is also high or very high (> 97 wt.%), especially in the finest particle size classes (63/40 µm and < 40µm). Concerning the two subtypes of ore type B2 (B2-a and B2-b), no obvious difference was observed during separation with the Davis magnetic tube.

However, one must acknowledge the differences between laboratory scale tests (Davis magnetite tube) and large scale magnetic separation when interpreting the separation and recovery data (SiO_2) based on the Davis magnetic tube results. It has been found out that in the Davis magnetic tube tests, the concentrate is somewhat lower in SiO_2 than the SiO_2 grade in the concentrate (magnetics) after processing based on the empirical data collected from the processes at the beneficiation plant KA1 in Kiruna (Malm 2009, Drugge 2009).

9.4 Liberation analysis with QEMSCAN®

The introduction of scanning electron microscope (SEM) analysis combined with image analysis such as MLA and QEMSCAN, generally called automated mineralogy, has revolutionized the mineralogical investigations and liberation analysis and became a common technique for measuring the liberation spectrum of mineral particle populations in the last 20 to 30 years (Fandrich et al. 1998, Butcher 2010, Gu et al. 2014). This is because the size of the mineral particles or grains and the degree of liberation are essential parameters for process mineralogy and mineral processing. Automated mineralogy provides a basis for making estimations of these important parameters (Sutherland 2007). It also provides a tool for the investigation and comparison of mineral associations for non-liberated particles (middlings and locked particles) presented in Figure 83, which can be challenging without automated mineralogy (Lund 2013).

One of the main tasks of comminution is to release, or liberate the valuable minerals from the gangue minerals at the coarsest particle size and by the lowest possible consumption of energy (Schubert 1988, Wills 2006). A particle is considered as liberated if it consists purely of the mineral of interest. At LKAB's mineral processing laboratory, particles are usually classified into classes of specific incremental steps based on the degree of liberation of Fe oxides (magnetite) as follow (wt.% in Fraction): 100–90% → liberated, 90–60% → high-grade middlings, 60–30% → low-grade middlings, 30–0% → locked (see also Fig. 83). However, in some cases the ore must be grinded even finer because of the nature of the next process stage or specific requirements for the concentrate. For example, the magnetite ore in Malmberget is intensively metamorphosed, granoblastic and texturally is relatively coarse compared to the magnetite ore in the Kiirunavaara deposit and the liberation size is reasonably larger (Lund 2013). Regarding the Kiirunavaara deposit, the crystal shape of the magnetite is characteristically subhedral isometric and in massive parts of the ore body, the microstructure is granoblastic with often well-developed triple junctions at grain boundaries (Aupers 2014). As a triple junction refers to a texture where the majority of the grains meet in threes along lines and the junction lines appear as a point (Misra 2000).

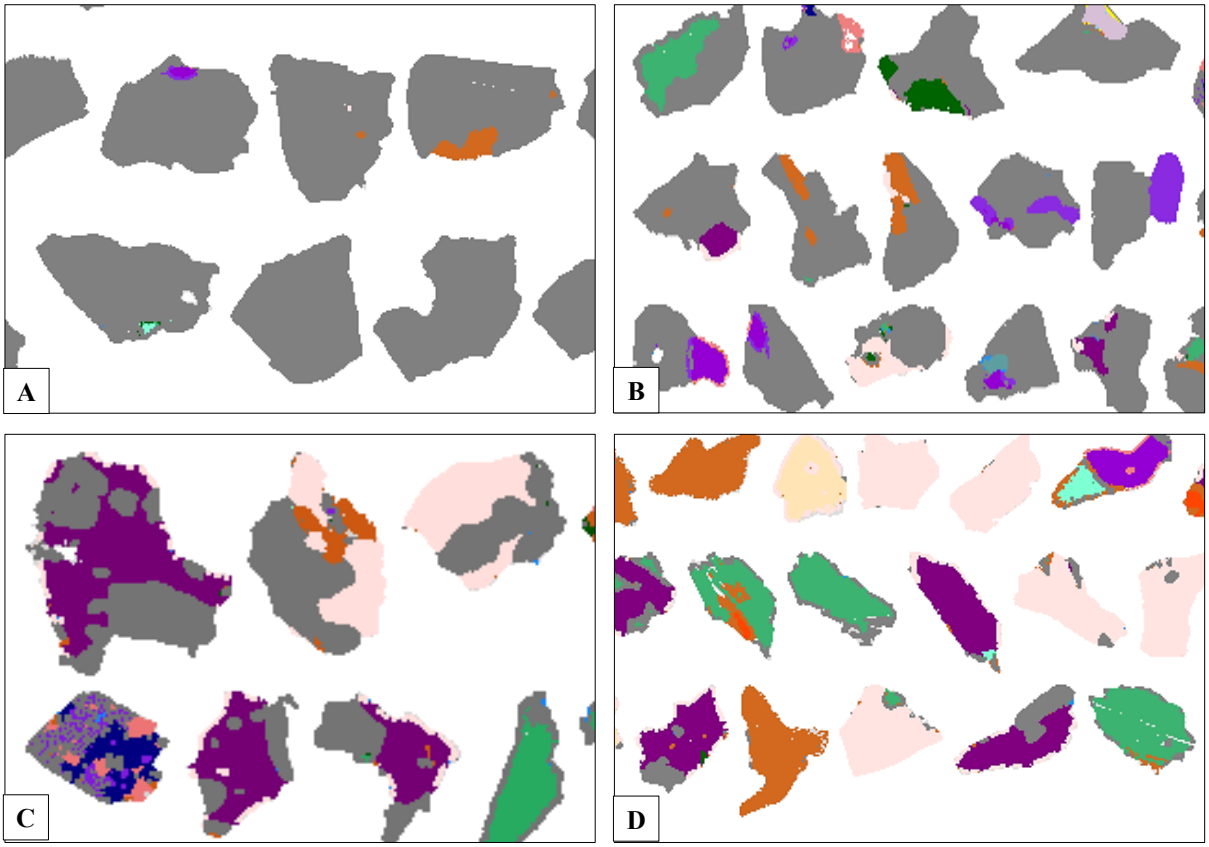

Figure 83. Mineral associations of liberated and non-liberated particles. Sample 6351, fraction 63/40 µm. Mineralogy after SIP-List presented in Figure 58 A. (A) Liberated (100-90%), (B) High grade middlings (90-60%), (C) Low grade middlings (60-30%) and (D) Locked (30-0%).

Apart from investigating the modal mineralogy of the samples, QEMSCAN is used to analyse the liberation of magnetite and, to study the intergrowth between magnetite and the relevant silicate minerals. It is also worth noting that a description of Fe oxides was used for the analysis of liberation and intergrowths for this study, because the resolution of QEMSCAN is incomplete for the case of different Fe oxide phases (Chapter 7.4). However, in practice Fe oxides consist almost exclusively of magnetite as noted earlier from optical microscopy analysis. Also previously mentioned, the division of ore type B2 into two subtypes B2-a and B2-b, is also used in this analysis. The liberation of magnetite for the samples belonging to the subtype B2-a characterized by actinolite and a low total consumption of energy is presented in Figure 84 and for the samples belonging to the subtype B2-b characterized by quartz, albite and phlogopite and a high total consumption of energy is presented in Figure 85. The numeric data is displayed in Appendix 25.

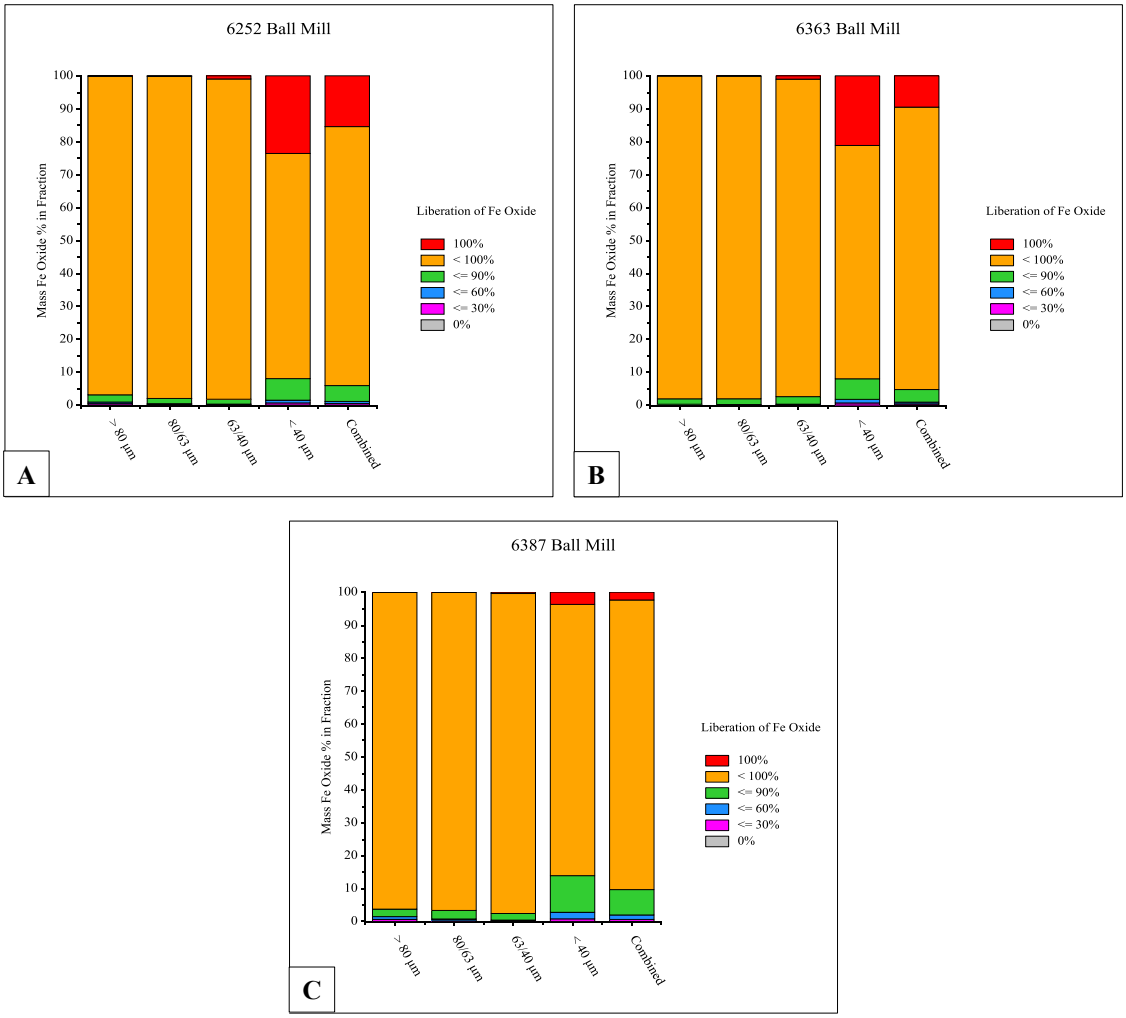

Figure 84. Liberation of magnetite (Fe Oxide) for samples 6252 (A), 6363 (B) and 6387 (C) representing the subtype B2-a after crushing and comminution in the laboratory rod mill (10 minutes) and in the laboratory ball mill (35 minutes) at the laboratory of the Institute of Mineral Processing.

When looking at the high degree of liberation (> 90 wt.%) of magnetite (Fig. 84 and 85), especially in the finest particle size classes (63/40 µm and < 40 µm), magnetite (regarded as equal Fe oxide) can be regarded as fully liberated according to the current classification used by LKAB. Furthermore, no clear difference in the degree of liberation of magnetite can be observed between the two subtypes of ore type B2. Only in samples 6370 (subtype 2B-b) and 6387 (subtype 2B-b) is the amount of the fully liberated particles (100%) somewhat less than in the other samples. Similarly, in the case of these two samples, no enrichment of material in the finest particle size class can be observed.

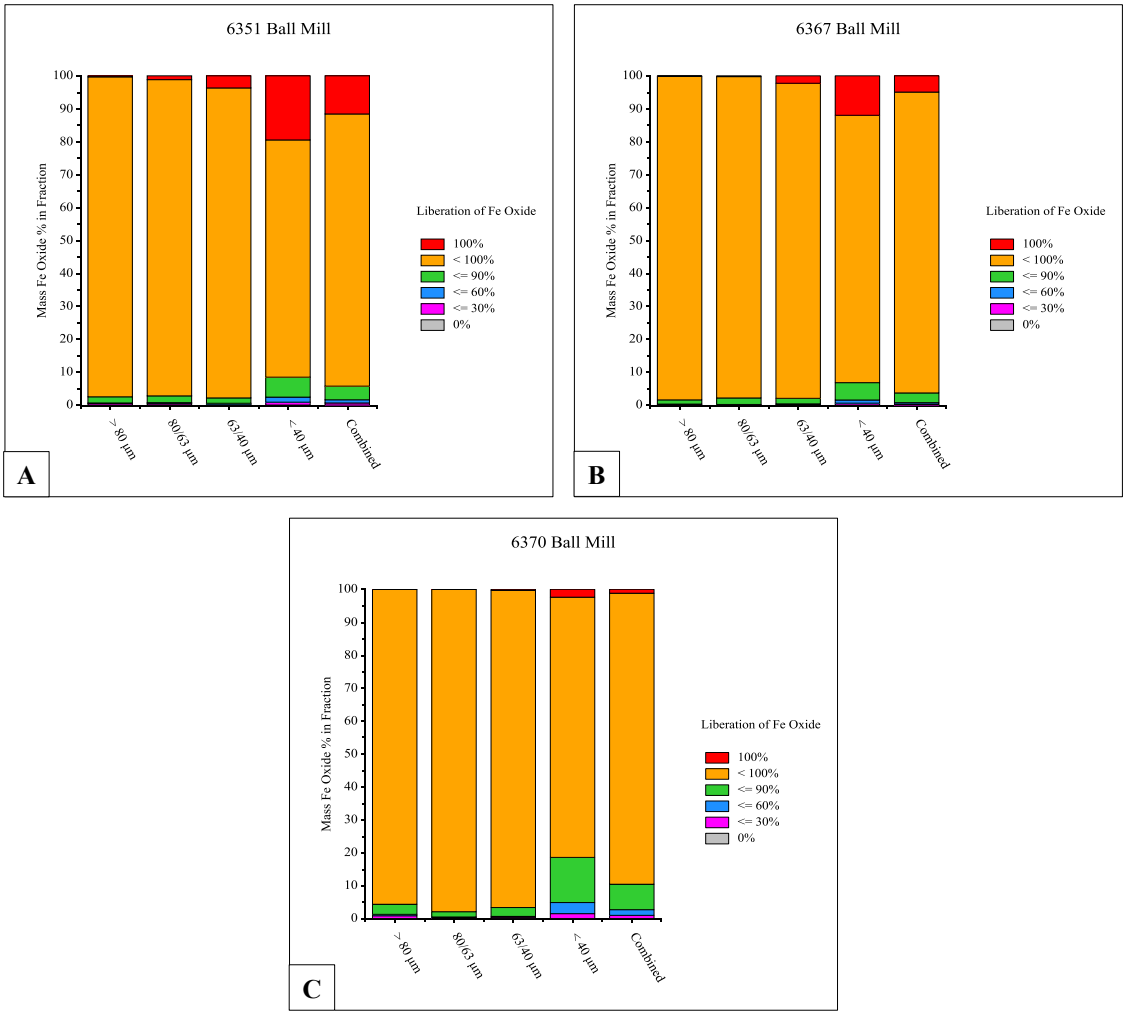

Figure 85. Liberation of magnetite (Fe Oxide) for samples 6351 (A), 6367 (B) and 6370 (C) representing the subtype B2-b after crushing and comminution in the laboratory rod mill (10 minutes) and in the laboratory ball mill (35 minutes) at the laboratory of the Institute of Mineral Processing.

However, in this investigation, the grain size of various silicate minerals and the intergrowth of magnetite with gangue minerals has not been studied in the samples *in situ*. It can be concluded that apparently neither mineralogy nor the total consumption of energy has a direct effect on the degree of liberation of magnetite in ore type B2. Likewise, the particle size (compare the P_{80} value) does not appear to directly affect the degree of liberation. It should be pointed out that there might be some degree of overestimation related to the liberation of magnetite (i.e. the measured grade of liberation could be higher than the real grade). The overestimation of the degree of liberation resulting from a stereological error can be dependent on various factors such as particle composition, texture and the type of measurement modus such as areal PMA (areal, used in this study) or BMA (linear). It is important to keep in mind that a particle could be composite but appear liberated, which can lead to an overestimation of the degree of liberation. As already has been noted, numerous methods have been proposed and tested for correcting this error (Fandrich et al. 1998, Spencer & Sutherland 2000). However, it is generally accepted that there might be a bias towards liberation in some cases. Similarly, the particle and grain

size measured in 2D is usually smaller that in 3D (Gu et al. 2012). In this study with focus on the liberation of magnetite and silicates, no stereological correction methods for these mostly binary mineralogical systems were used because some of them are not appropriate for real mineralogical textures or their implications are beyond the scope of this project. For that reason, it is assumed that in this study a statistically large number of particles (5000 to 6000 in the finest fractions) correspond to the actual liberation rate, or very near of it.

9.5 Separation of magnetite and silicates

The intergrowth of magnetite and actinolite is presumably the most important with regarded to magnetic separation and further the SiO_2 grade in the magnetite concentrate at the beneficiation plants. In the subtype B2-b intergrowth of magnetite and phlogopite, but also of magnetite and chlorite seems to be common. Furthermore, albite, quartz and also partly actinolite seems to be often fully liberated (Fig. 86). It has been noted that there occur two different types of actinolite in ore type B2.

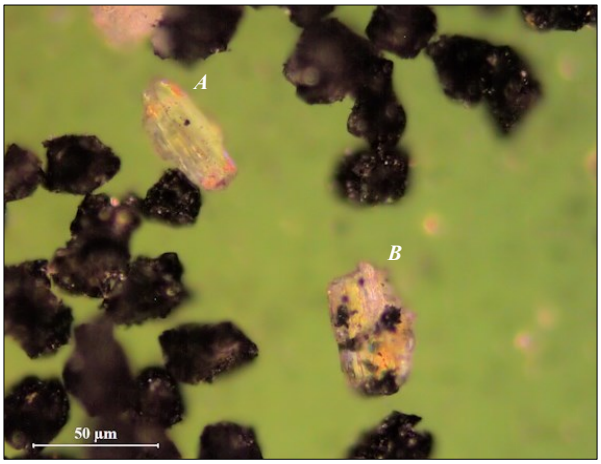

Figure 86. Two different types (generations) of actinolite in sample 6387, particle size class 63/40 µm after grinding and before the Davis magnetic tube separation.

A part of it occurs as large coarse crystals which are partly euhedral, partly subhedral and without significant inclusions of magnetite (*A* in Fig. 86). The most likely the actinolite particle with magnetite intergrowth (*B* in Fig. 86) belongs to the second type of actinolite which is regarded to be a pseudomorph of clinopyroxen (Nordstrand 2012, Niiranen 2012 b, Aupers 2014). It can be concluded that there is a poor separation of the some silicates by the Davis magnetic tube tests, mostly actinolite, for the samples belonging to the subtype B2-a compared to the subtype B2-b which causes an elevated grade of SiO_2 in the Davis magnetic tube concentrate (magnetic fraction, Fig. 87).

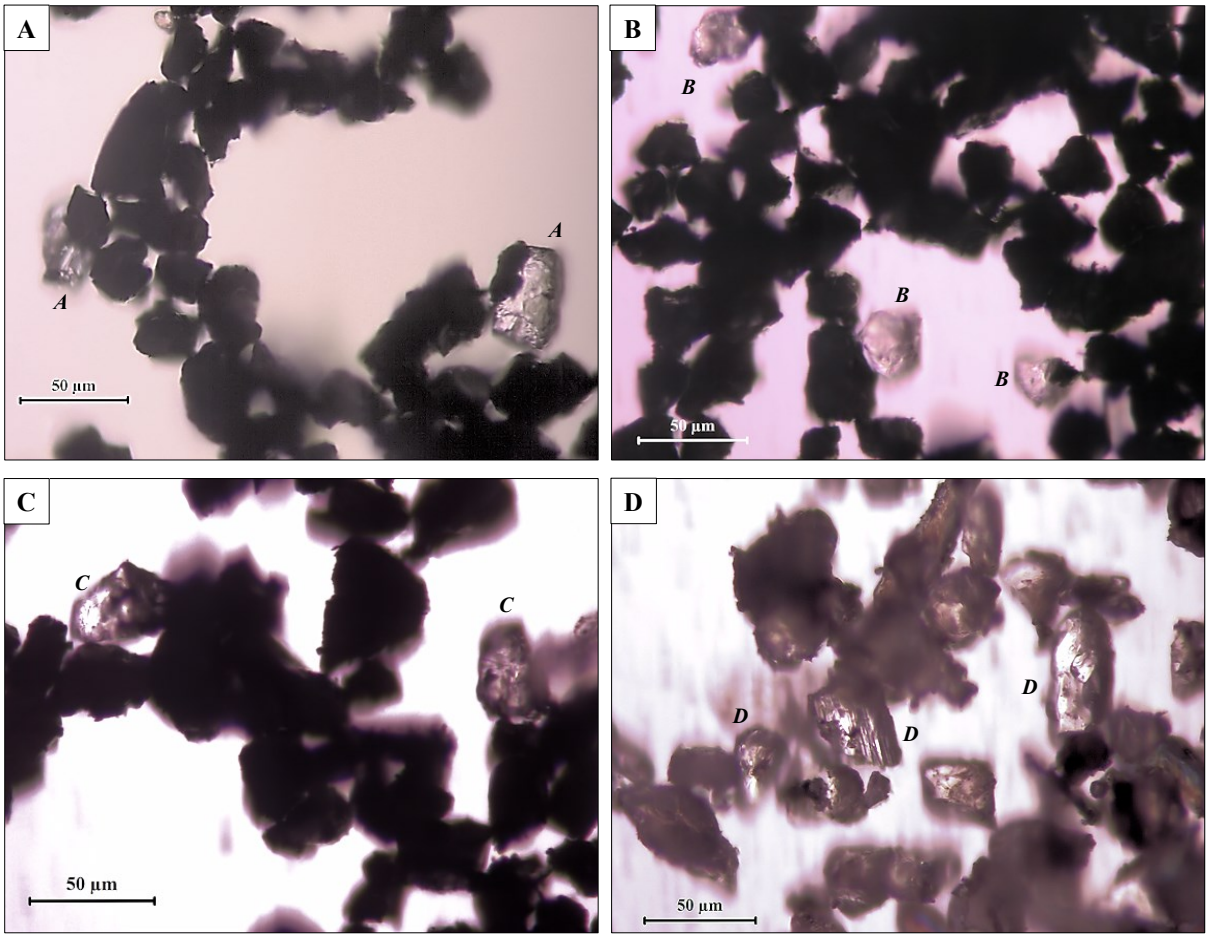

Figure 87. Magnetics (magnetite concentrate) and non-magnetics (waste) of sample 6252 after separation with the Davis magnetite tube, particle size class 63/40 µm (black = magnetite, transparent = silicate, apatite; transmitted light): (A) Magnetics, 0.1 A; (B) Magnetics, 0.2 A; (C) Magnetics, 1.8 A; (D) Non-magnetics, 1.8 A.

This is can be regarded to be characteristic for actinolite which probably is a pseudomorph of pyroxene (clinopyroxene) based on the results of this study. In Figure 87 A, representing sample 6252 (subtype B2-a) two actinolite particles with coarse intergrowth of actinolite and magnetite (*A*) are presented. The concentrate was yield by the lowest amperage (0.1 A) which is correlated to the low intensity of the magnetic field. The conclusion is that in the low intensity of magnetic field, only the actinolite particles with coarse magnetite inclusions (*A*) were forced to the concentrate by separation. When the intensity of the magnetic field increases because of the higher amperage, 0.2 A for the concentrate presented in Figure87 B and 1.8 A for the concentrate presented in Figure 87 C, the actinolite particles with finer, but in some cases also denser, magnetite inclusions (*B* and *C*) were forced to the concentrate by separation with the Davis magnetic tube. However, there are still some actinolite particles (*D*) with very fine-grained magnetite inclusions in the non-magnetic fractions (waste) presented in Figure 87 D. It can be expected that even they will be forced to the magnetic concentre when the intensity of magnetic field strength will be increased additionally.

It should be noted that also in some samples, such as sample 6351 in Figure 88 (particle size class 63/40 µm) representing the subtype B2-b, some actinolite particles with magnetite inclusions can occur in the magnetic fraction (concentrate) after separation by the Davis magnetic tube. This indicates that in the sample, a small amount of actinolite with magnetite inclusions (pseudomorph after pyroxen) can occur although the major part of actinolite represents the coarse-grained type.

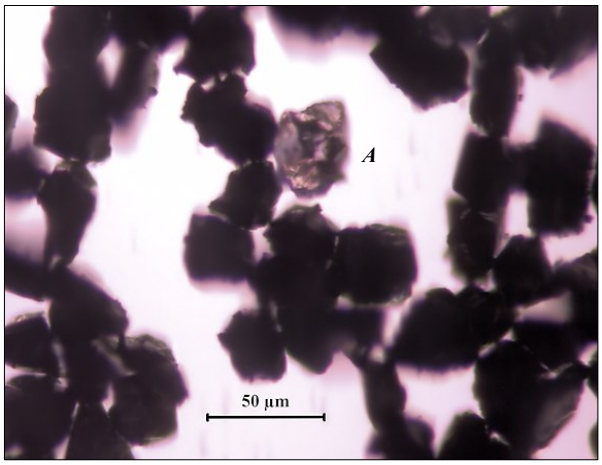

Figure 88. Actinolite particle with small inclusions of magnetite (A) in the magnetics after separation with the Davis magnetite tube (0.1 A). Sample 6351, particle size class 63/40 µm (transmitted light).

Figure 89. A large actinolite particle with small inclusions of magnetite (A) and two liberated quartz particles (B) in the magnetics after separation with the Davis magnetite tube (1.8 A). Sample 6370, particle size class 63/40 µm (transmitted light).

One special characteristics is that fully liberated quartz particles which can occur in the magnetite concentrate (Fig. 89) after separation by the Davis magnetic tube. They have been also observed in the magnetite concentrate in the beneficiation plant in Kiruna in the past (Adolfsson 2014). It is clear that they increase the SiO_2 grade in the concentrate significantly, because the quartz is chemically pure SiO_2. It can be concluded that there is a need to carry out further study to find out the reason or mechanism contribute the occurrence of the fully liberated quartz particles in the concentrate.

10. PREDICTION OF SiO_2 GRADE FROM LABORATY SCALE TO INDUSTRIAL SCALE

10.1 Estimation of SiO_2 at P_{80} = 45 µm at the laboratory scale

By establishing a linear relationship between SiO_2 grade and P_{80}, the SiO_2 grade can be determined in the concentrate after comminution with a laboratory tumbling mill and DT test at P_{80} = 45 µm. The principle is shown in Figure 90 for samples 6440 (B1), 6361 (B2), and 6351 (D3) representing the main ore types of the Kiirunavaara deposit.

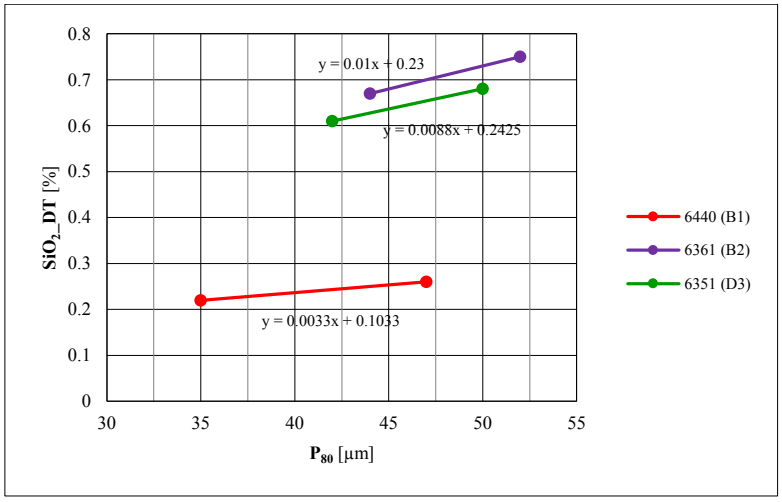

Figure 90. Principle of estimation of SiO_2 grade in the DT concentrate at the laboratory scale. Only the values (Tables 37, 38, and 39) after comminution in the laboratory rod mill for 25 and 35 minutes, respectively, are displayed in the chart.

The SiO_2 grade by P_{80} = 45 µm can be estimated using an equation of a straight line (*Equation* 37*)* passing through two distinct points $P_1(x_1 , y_1)$ and $P_2 (x_2, y_2)$ as follows (Pentikäinen 1978):

$$y - y_1 = m(x - x_1) \qquad (Eq.\ 37)$$

Its slope (m) is given by *Equation* 38 with x_2 not equal to x_1:

$$m = \frac{y_2 - y_1}{x_2 - x_1} \qquad (Eq.\ 38)$$

These equations (*Eq. 37* and *Eq. 38*) also has been used for the estimation of the comminution time in the laboratory ball mill to obtain P_{80} = 45 µm, which are then used to estimate the energy consumption (Chapter 7.3).

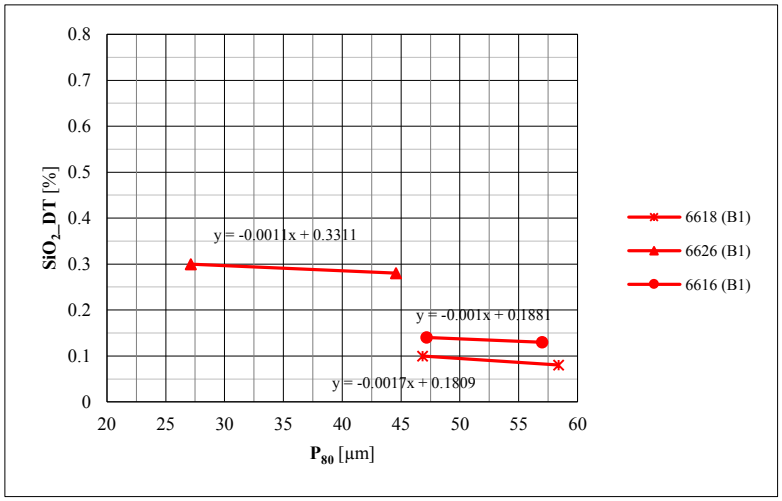

Figure 91. Three samples showing an deviant behaviour of SiO_2 in the DT concentrate.

The case presented in Figure 90 can be regarded as a normal case for the estimation of SiO_2 grade in the DT concentrate at the laboratory scale. It means that the liberation of magnetite and also silicates increase as a function of the comminution time. In Figure 91, however, three samples representing ore type B1 show a deviant behaviour. It means that, when P_{80} value increases, the SiO_2 grade also increases in the DT concentrate. This occurs not often and is typical for the samples representing ore type B1 and which show low or very low SiO_2 grade in the feed. Furthermore, it can be assumed that this deviant behaviour of the SiO_2 has no significant impact on the results of the estimation, mostly because the SiO_2 grades are low.

There can be three different explanations for this. First, with regards to the SiO_2 grade in the feed, slight differences may be observed in the same sample for the mineral processing tests at LKAB's mineral processing laboratory (Tables 36, 37, and 38). Obviously, this might depend on the fact that after crushing, mixing, and splitting, three separate sub-samples of 2 kg were selected, so that the small differences in chemical assays can indicate some degree of minor inhomogeneity in the samples. In the future, it will be recommended to combine the samples, homogenize them, and split them evenly after the comminution with a laboratory rod mill before the second comminution circuit with a laboratory ball mill, the mineral processing tests, and the chemical assays. In this fashion, it is possible to minimize the impact of inhomogeneity on the samples in the results and obtain less varying data.

Second, there might also be differences in the SiO_2 grade in the DT concentrate because of the uncertainty of the XRF analysis. The uncertainty for XRF analysis on the SiO_2 in relation to magnetite and hematite ore at LKAB's chemical laboratory varies with ± 0.02% SiO_2 (Linder 2015). The impact of uncertainty is certainly larger when the SiO_2 grade in the samples is low. Third, fully liberated quartz particles have observed in the magnetite concentrate after separation by the Davis magnetic tube. They also have been observed in the magnetite concentrate in the beneficiation plant in Kiruna in the past (Adolfsson 2014). It is clear that they increase the SiO_2 grade in the concentrate because the quartz is chemically pure SiO_2. Based on the liberation analysis, carried out in relation to the study with focus on

the high silica ore type B2, it can be concluded that there is a need to carry out further study to find out the reason or mechanism that contribute to the occurrence of the fully liberated quartz particles in the concentrate.

10.2 Comparison of SiO_2 grade between laboratory scale and industrial scale

By comparing the SiO_2 grade in the magnetite concentrate from the DT tests at laboratory scale and SiO_2 grade in the DT concentrate from the beneficiation plant after magnetic separation (WLIMS) at the same state of dispersity, a link between the laboratory and industrial scale can be created. To connect the SiO_2 grade in the DT concentrate from the laboratory tests and concentrate from the beneficiation plant KA1, a total amount of samples of 120 kg was collected from the feed material for the primary mill at Section 22. Sampling has also occurred from the cyclone overflow as well as after magnetic separation before apatite flotation. Sampling was made during normal operation and for a total time of 3 hours. The DT concentrate from the latter sampling was used as the reference for the industrial scale. The samples were analysed chemically and physically. The SiO_2 grade in the DT concentrate in the samples after magnetic separation was determined, likewise the dispersity of the concentrate (P_{80}). Samples taken from the feed for the primary mill an section 22, were used to develop and optimize comminution tests at the laboratory scale with respect to variation and to provide reference material for developing a simulation function between the laboratory scale and industrial scale (Drugge 2009).

It should be noted that dispersity will probably vary in the additional samples withdrawn from operation in the future. The simulation calculations for the SiO_2 grade between the laboratory scale and the industrial scale will consistently be used at a dispersity of 80% < 45 µm. An assumption was then made that the difference between laboratory scale and the industrial scale should be constant in the range of 75% to 85% < 45 µm (P values). This assumption justifies the model (simulation function) developed at the dispersity of 83.4% < 45 µm. Furthermore, it can be considered valid and stable despite the estimations of SiO_2 grade in the concentrate, and total energy consumption will be performed at 80% < 45 µm (P_{80} = 45 µm) (Drugge 2009). In Table 36, a point estimation of the SiO_2 grade is presented in the DT concentrate from the laboratory tests and from the beneficiation plant, and the difference between them by dispersity is 83.4% < µm.

Table 36. Point estimation of the SiO_2 grade in the concentrate from the beneficiation plant and from the laboratory tests. Asterisk (*) denotes the estimated value.

	SiO_2 [%] in DT conc.	**Dispersity** [% < 45 µm]
Lab. scale	0.33318	83.4*
Operat. scale	0.52	83.4
Difference	0.1868	

Because the SiO_2 grade in the concentrate from the beneficiation plant indicates two decimal places, and because the XRF analysis varies with ± 0.02% SiO_2 (Linder 2015), the final SiO_2 grade in the concentrate is similarly displayed in two decimal places. The difference is then stated that at 0.19%

(Drugge 2009). It should, however, be recommended to make additional sampling and comminution tests as reference to define the possible variation and difference in the SiO_2 grade between the laboratory and industrial scale at constant dispersity (P value).

10.3 Function for estimation of SiO_2 grade from the laboratory scale to industrial scale

To construct the function for the estimation of the SiO_2 between the laboratory scale and industrial scale, the SiO_2 grades engage at the same dispersity. Based on the data from the reference material sampled from the beneficiation plant KA1 (Drugge 2009), it can be concluded that concentrate from the industrial scale (after magnetic separation) showed the dispersity amounted to 83.4% < 45 µm. In Figure 92, the SiO_2 grade in the DT concentrate, Fraction < 45 µm, after comminution with the laboratory ball mill as a function of the dispersity. Regression lines are based on the data from Operator A and B (Drugge 2009).

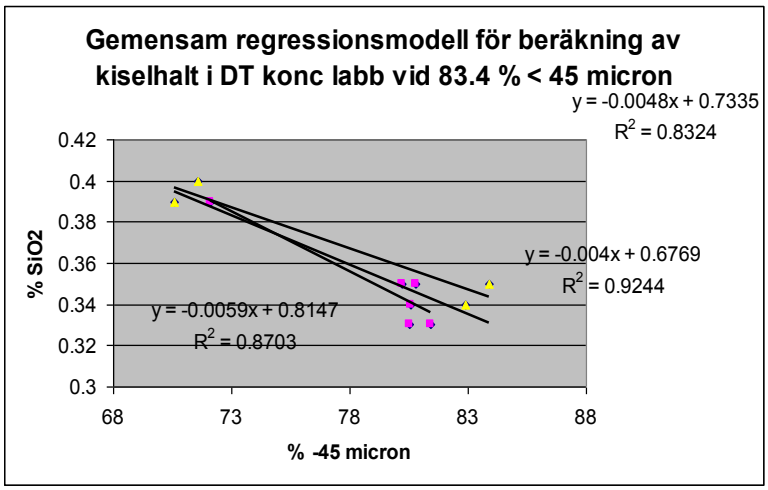

Figure 92. SiO_2 grade in the DT concentrate, Fraction < 45 µm, after comminution with the laboratory ball mill as a function of the dispersity (Drugge 2009).

In Figure 23, individual and combined regression lines are displayed. The combined regression line (y = - 0.0048 · x + 0.7335) is based on entire data and shows $R^2 = 0.83$. The SiO_2 grade for the combined function can then be estimated at dispersity of $P_{83.4}$ < 45 µm when x = 83.4 is substituted in *Equation* 39 as follows:

$$y = -0.0048 \cdot x + 0.7335 \qquad (Eq.\ 39)$$

The substitution gives a y value of 0.33318% for the SiO_2 grade in the concentrate from DT tests at the laboratory scale. The SiO_2 grade in the DT concentrate from the industrial scale is 0.52% by $P_{83.4}$ < 45 µm. The difference in the SiO_2 grades between the laboratory scale and the industrial scale then amounts to 0.187% SiO_2. The difference of 0.187% SiO_2 between the laboratory scale and the industrial scale is assumed to be constant in the range of 75% to 85% < 45µm. The model should be enhanced by making additional sampling and tests at the beneficiation plants (Drugge 2009). The function for the estimation of the SiO_2 can be given in *Equation* 40 as follows:

$$Y = X + 0.1868\, SiO_2\% \qquad (Eq.\ 40)$$

Y…… SiO_2 grade in the DT concentrate at the industrial scale

X…… SiO_2 grade in the DT concentrate at the laboratory scale

To estimate the variation of the model in relation to data from the laboratory scale and the industrial scale, these cases were studied separately by Drugge (2009). The variations at the laboratory scale are given as $s_{SiO2\ (labb)}$ and at the industrial scale as $s_{SiO2\ (drift)}$. By establishing a 95% confidence interval for the difference between the mean value of the SiO_2 grade at the industrial scale in relation to the mean value for the corresponding SiO_2 grade at the laboratory scale, the overall error can be estimated. Because $s_{SiO2\ (labb)}$ is not a value of reproducibility of the standard deviation but only a value of repeatability value, the systematic error will be added as well due to several operators (reproducibility term). Reading the F-test of the variances, it cannot be ruled out with 95% probability that they come from the same distribution. Thus, it can be concluded as follow (*Equation* 41), according Drugge (2009):

$$\sigma^2_{SiO2\ (labb)} = \sigma^2_{SiO2(drift)} = \sigma^2 \qquad (Eq.\ 41)$$

If $\bar{x}_1$, $\bar{x}_2$, s_1^2, and s_2^2 are the mean of the sample mean and the sample variance for the SiO_2 grade at the industrial scale (1) and at the laboratory scale (2) of the two samples of population $n_1 = 5$ and $n_2 = 4$ from two independent normal distributions with unknown but equal variances, then a 95% confidence interval for the difference between the mean values $\mu_1 - \mu_2$ can be estimated, as given in *Equation* 42:

$$\bar{x}_1\text{-}\bar{x}_2\text{-}t_{\alpha/2,n1+n2-2}\, s_p\sqrt{\frac{1}{n_1}+\frac{1}{n_2}} \le \mu_1 - \mu_2 \le \bar{x}_1\text{-}\bar{x}_2\text{+}t_{\alpha/2,n1+n2-2}s_p\sqrt{\frac{1}{n_1}+\frac{1}{n_2}} \qquad (Eq.\ 42)$$

$$s_p = \sqrt{[(n_1-1)s_1^2 + (n_2-1)s_2^2]\cdot(n_1+n_2-2)^{-1}} \qquad (Eq.\ 43)$$

where s_p corresponds to an estimation of common population of the standard deviation, and $t_{\alpha/2,n1+n2-2}$ represents the upper percentile point of the t-distribution with degrees of freedom of $n_1 + n_2 - 2$, known as "pooled estimation" (*Equation* 43). The substitution of the values gives a confidence interval of [0.16;0.21]% (Drugge 2009).

The difference from the middle of the interval 0.187% shares in the upper and lower range limit, respectively, is 0.025% shares. To these values, the systematic error of 0.0126% shares is added. The total error can be estimated as 0.025 + 0.0126 = 0.0376% ≈ 0.04%. In percentage terms, it represents an error of 21%, which should be added to results from the DT tests at the laboratory scale. The entire function for the estimation the SiO_2 in the DT concentrate at the industrial scale from the SiO_2 grade in the DT concentrate at the laboratory scale can be given as in *Equation* 44 (Drugge 2009):

$$Y = X + 0.187\%\ [SiO_2] \pm 0.04\%\ \lfloor SiO_2 \rfloor \qquad (Eq.\ 44)$$

Because the SiO_2 grade in the DT concentrate is a function of dispersity (P), ΔP_{80} values will correspond to ΔSiO_2 values. However, it should be noted because depending on the slope (gradient) of the regression lines, this entails more or less of an error in the dependent variable. In most cases, this error can be assumed to be negligible due to small inclination (Drugge 2009).

10.4 SiO_2 grade at industrial scale

Principles of the estimation of the SiO_2 grade in the DT concentrate at the laboratory scale to the industrial scale were presented in previous chapters. In Tables 37, 38, and 39, the estimation for the selected samples is presented. In the first stage, the SiO_2 grade is estimated at P_{80} = 45 µm using the linear approximation of the SiO_2 as a function of the P_{80} values after the comminution time of 25 and 35 minutes, respectively, in the laboratory ball mill.

Table 37. Data for estimation of the SiO_2 grade in the DT concentrate at P_{80} = 45 µm at the laboratory scale and industrial scale at the beneficiation plant for the selected samples representing ore type B1. As method 10+25 corresponds to comminution for 10 minutes in the laboratory rod mill and 25 minutes in the laboratory ball mill, 10+35 corresponds 10 and 35 minutes, respectively.

Sample	**Ore type**	**Method**	**P_{80}** [µm]	**SiO_2** (Feed) [%]	**SiO_2_DT** [%]	**SiO_2_DT** P_{80}= 45 µm, [%]	**SiO_2_DT** (Plant) [%]
6255	B1	10	125	3.75	1.01	0.39	0.57 ± 0.04
		10+25	52	3.80	0.43		
		10+35	44	3.77	0.38		
6365	B1	10	151	1.83	0.45	0.20	0.38 ± 0.04
		10+25	63	1.92	0.22		
		10+35	55	1.92	0.21		
6384	B1	10	125	5.92	0.9	0.38	0.57 ± 0.04
		10+25	64	6.38	0.38		
		10+35	52	6.45	0.38		
6386	B1	10	151	2.14	0.86	0.50	0.68 ± 0.04
		10+25	60	2.26	0.58		
		10+35	51	2.29	0.53		
6397	B1	10	168	2.91	0.62	0.32	0.50 ± 0.04
		10+25	60	2.85	0.36		
		10+35	50	3.00	0.33		
6440	B1	10	135	2.02	0.45	0.25	0.44 ± 0.04
		10+25	47	2.03	0.26		
		10+35	35	2.12	0.22		

When looking at the estimated SiO_2 grades at P_{80} = 45 µm, it is clear that ore type B1 seems to be low in SiO_2 after mineral processing at the beneficiation plant (Table 37). Although it should be mentioned that SiO_2 in the DT concentrate carried out at the beneficiation plant after magnetic separation and before flotation might be lower than the actual SiO_2 grades in the KPC (Kiruna pellets concentrate) (Malm 2009).

Table 38. Data for estimation of the SiO_2 grade in the DT concentrate at P_{80} = 45 µm at the laboratory scale and industrial scale at the beneficiation plant for the selected samples representing ore type B2. As method 10+25 corresponds to comminution for 10 minutes in the laboratory rod mill and 25 minutes in the laboratory ball mill, 10+35 corresponds 10 and 35 minutes, respectively.

Sample	**Ore type**	**Method**	**P_{80}** [µm]	**SiO_2** (Feed) [%]	**SiO_2_DT** [%]	**SiO_2_DT** (Lab) P_{80}= 45 µm, [%]	**SiO_2_DT** (Plant) [%]
6359	B2	10	124	3.88	1.16	0.40	0.59 ± 0.04
		10+25	54	4.12	0.47		
		10+35	46	4.25	0.41		
6361	B2	10	99	5.34	1.28	0.68	0.87 ± 0.04
		10+25	52	5.59	0.75		
		10+35	44	5.53	0.67		
6385	B2	10	259	2.94	1.08	0.51	0.69 ± 0.04
		10+25	62	3.13	0.63		
		10+35	51	3.08	0.55		
6396	B2	10	149	4.22	0.73	0.25	0.44 ± 0.04
		10+25	60	4.42	0.32		
		10+35	51	4.24	0.28		
6400	B2	10	162	6.16	1.83	0.52	0.71 ± 0.04
		10+25	53	6.25	0.76		
		10+35	52	6.45	0.73		
6412	B2	10	267	1.55	0.44	0.21	0.40 ± 0.04
		10+25	59	1.63	0.23		
		10+35	46	1.72	0.21		

Table 39. Data for estimation of the SiO_2 grade in the DT concentrate at P_{80} = 45 µm at the laboratory scale and industrial scale at the beneficiation plant for the selected samples representing ore type D. As method 10+25 corresponds to comminution for 10 minutes in the laboratory rod mill and 25 minutes in the laboratory ball mill, 10+35 corresponds 10 and 35 minutes, respectively.

Sample	**Ore type**	**Method**	**P_{80}** [µm]	**SiO_2** (Feed) [%]	**SiO_2_DT** [%]	**SiO_2_DT** (Lab) P_{80}= 45 µm, [%]	**SiO_2_DT** (Plant) [%]
6254	D3	10	119	2.33	0.59	0.25	0.43 ± 0.04
		10+25	60	2.44	0.29		
		10+35	50	2.44	0.26		
6351	D3	10	96	4.59	1.49	0.64	0.82 ± 0.04
		10+25	50	4.71	0.68		
		10+35	42	4.79	0.61		
6369	D1	10	104	3.54	0.64	0.27	0.46 ± 0.04
		10+25	58	3.33	0.31		
		10+35	48	3.68	0.28		
6440	D3	10	97	2.10	0.79	0.73	0.92 ± 0.04
		10+25	37	2.29	0.57		
		10+35	26	2.30	0.35		
8028	D5	10	124	0.88	0.32	0.20	0.39 ± 0.04
		10+25	59	0.86	0.23		
		10+35	49	0.79	0.21		
8030	D3	10	210	2.20	0.32	0.03	0.22 ± 0.04
		10+25	77	2.24	0.17		
		10+35	63	2.29	0.11		

When looking at the SiO_2 grades in ore types B2 and D, there is clearly more variation (Tables 38 and 39). Especially, samples 6385 (B2) and 6440 (D3) show high estimated SiO_2 grades in the concentrate, although the feed shows not exceptionally high SiO_2 grade. Furthermore, samples 6361 and 6400 representing ore type B2 show high SiO_2 grade in the DT concentrate estimated to the beneficiation plant. Ore type B2 is rich in silicates, the most common of which are actinolite, titanite, phlogopite, and, in some cases quartz, chlorite, and albite. Based on information of the study of Aupers (2014), a significant amount of mostly fine-grained silicates can occur in some samples representing the high-P ore type D. The most common of these silicate mineral seems to be amphiboles (actinolite), phlogopite, and talc. In general, the gangue mineralogy seems to be similar to the subtypes of ore type D.

If a general limit value for SiO_2 at the industrial scale is considered to be 0.55% at the beneficiation plant KA3 in Kiruna, then it can be concluded that most of the samples representing ore type B1, are below this limit value (Fig. 93).

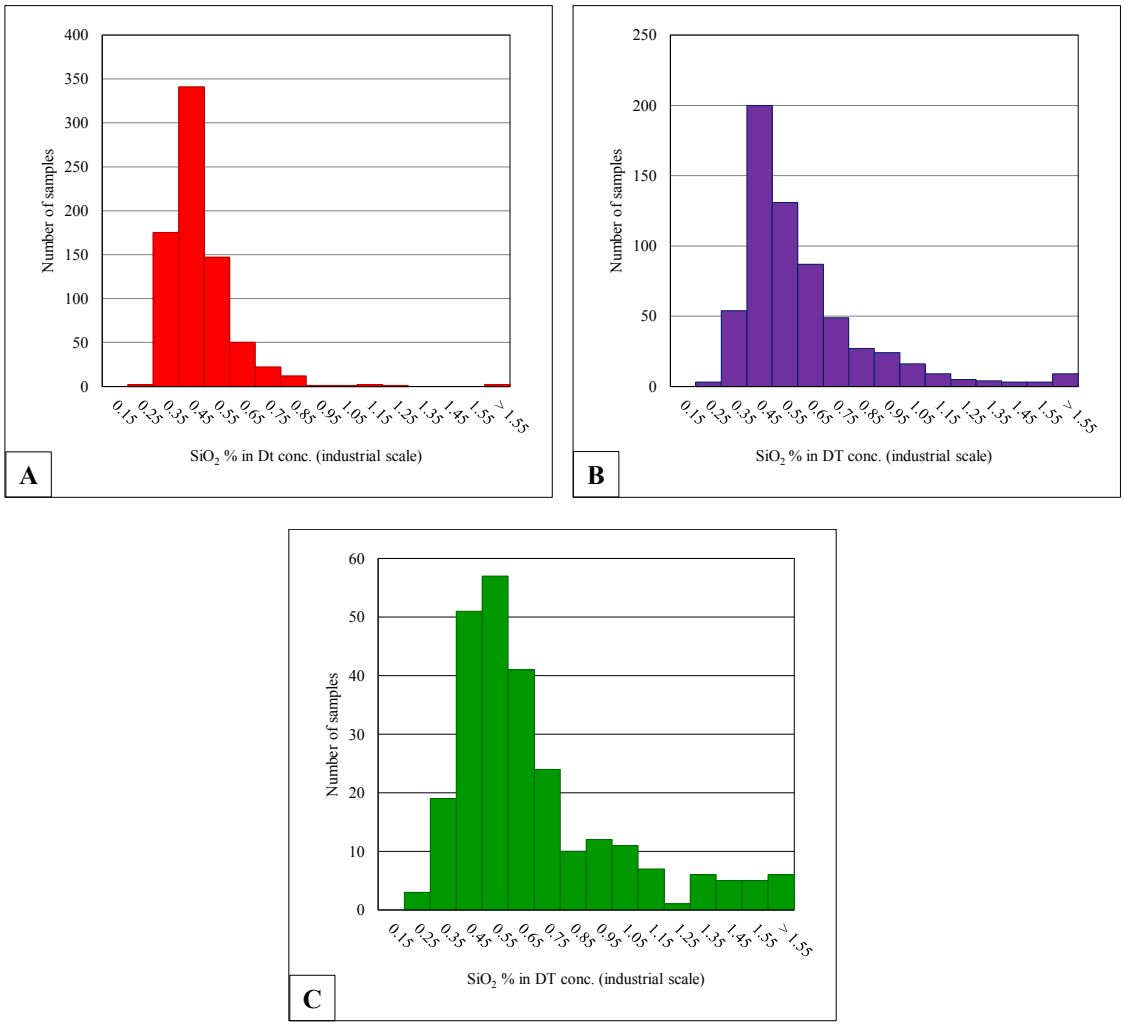

Figure 93. Distribution of SiO_2 in the whole sample population. (A) Ore type B1 (756 samples), (B) Ore type B2 (624 samples) and (C) Ore type D (258 samples). Statistic parameters are displayed in Table 40.

In addition, there seems to be homogenous distribution of SiO_2 values and little variation in the DT concentrate estimated to the industrial scale. In the case of the samples representing B2 ore, significantly more samples show the SiO_2 grade that is higher than 0.55%. They show also more distribution. The largest variation in the SiO_2 grades show the samples representing the high-P ore type D.

Table 40. Statistic parameters for SiO_2 grade estimated to the industrial scale for ore types B1, B2, and D.

Ore type	B1	B2	D
Min	0.22	0.19	0.22
Max	2.70	4.55	2.17
Mean	0.43	0.57	0.65
Median	0.40	0.49	0.55
Stdev	0.15	0.32	0.34
Variance	0.02	0.10	0.11

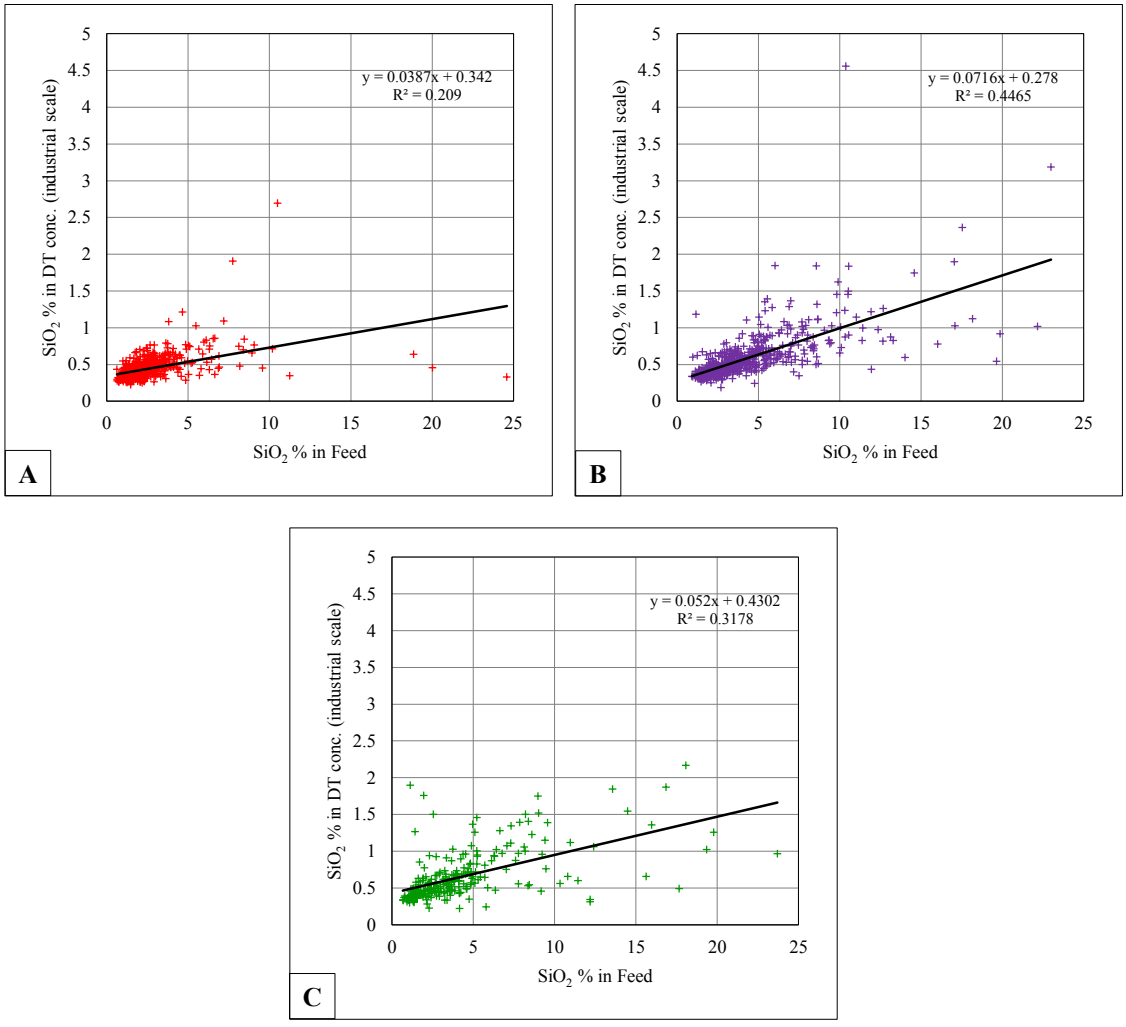

Figure 94. The estimated SiO_2 % in DT concentrate at the industrial scale vs. the SiO_2 % in the feed. (A) Ore type B1 (756 samples), (B) Ore type B2 (624 samples) and (C) Ore type D (258 samples).

In Figure 94, the estimated SiO_2 grade in the DT concentrate at the industrial scale versus the SiO_2 grade in the feed are shown. Also in this case, ore type B1 seems to be more homogenous as the high-silica

ore type B2 and high-phosphorous ore type D. There is no clear correlation between the SiO_2 grade in the feed and the SiO_2 grade in the DT concentrate. However, the slope of the regression line seems to be steeper for ore types B2 and D. That can be an indication that the SiO_2 grade in the feed might have more impact on the SiO_2 grade in the concentrate in the case of ore type B2 and D. It should be noted that the amount of ore type D decreases in the deeper parts of the ore deposit, while the amount of ore type B2 increases. Based on the data given in Tables 37, 38 , and 39 and information in Figure 94, the SiO_2 grade in the DT concentrate at the industrial scale cannot be directly predicted from the SiO_2 grade in the feed in the most cases. Furthermore, it seems to obvious that the problem of high silica in the magnetite is dependent mainly on the type of ore, and in particular of ore type B2.

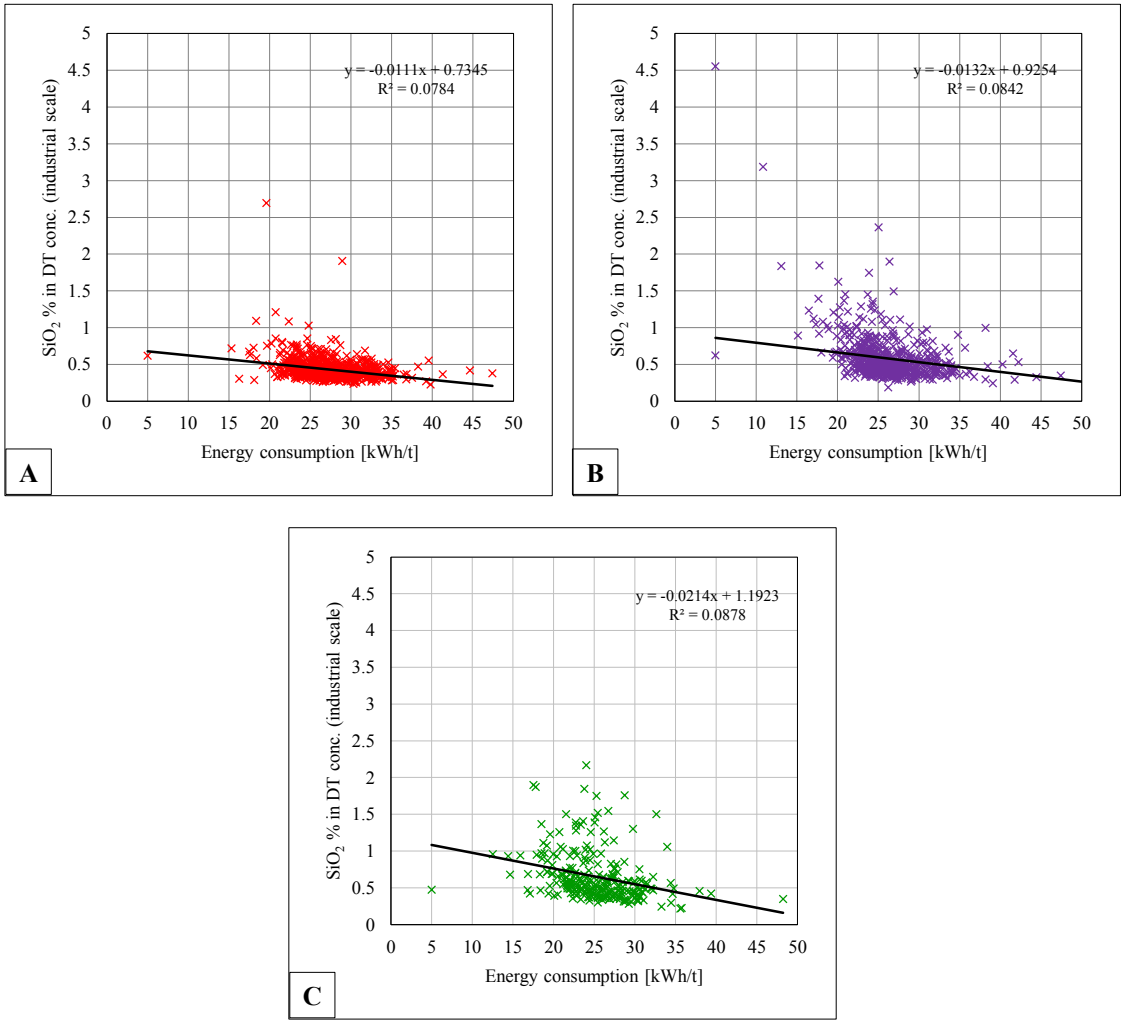

Figure 95. Comparison of the SiO_2 grade in the DT concentrate at the industrial scale and the estimated energy consumption related to the "Silica in the Mine" project. (A) Ore type B1, (B2) Ore type B2, and (C) Ore type D.

There also does not appear to be any clear correlation between the energy consumption at the industrial scale to obtain P_{80} = 45 µm and SiO_2 grade in the magnetite concentrate based on data from mineral processing tests carried out in relation to the "Silica in the Mine" project (Fig. 95). However, there seems to be some indications that there is a connection between the SiO_2 grade and energy consumption.

Especially, in the case of the high-SiO_2 ore type B2 a clear correlation between the mineralogy and the energy consumption has been showed (Chapter 7.2). Otherwise, there are more variations in ore types B2 and D than in ore type B1.

11. DISCUSSION AND CONCLUSIONS

The aim of this study was to characterize the main ore types (B1, B2, D) of the Kiirunavaara deposit from a mineral processing point of view. The comminution and mineral processing tests were carried out at the laboratory of the Institute of Mineral Processing, Montanuniversitaet Leoben. The focus of this study was on the investigation the differences in the breakage characteristics of the main ore types of the Kiirunavaara iron ore deposit, such as specific energy consumption and specific surface area. Furthermore, the essential part of this study was the mineralogical investigations using automated mineralogy (QEMSCAN®) to study the modal mineralogy, the distribution of silicates in the different particle size classes after comminution, the deportment of silicon (Si) between various silicates and degree of liberation and intergrowth of magnetite and silicates with the focus on the high-SiO_2 ore type B2.

For the comminution tests in the laboratory rod mill and in the laboratory ball mill, combined with a particle size analysis of the products, a test procedure was used known as the "Optimized Comminution Sequence" (OCS) developed by Steiner at the Institute of Mineral Processing at the Montanuniversitaet Leoben. It can be concluded that on the basis of the results of the comminution tests carried out at the laboratory of the Institute of Mineral Processing, new and valuable information was obtained from the behaviour of different ore types during the comminution. Furthermore, it should be noted that based on the differences in OCS used for the comminution tests in relation to this study and the open comminution system used for the comminution tests at LKAB's mineral processing laboratory in relation to the "Silica in the Mine" project, no direct comparison can be done. In addition, it should be recommended that comminution tests based on the OCS should be used to complete and to control the comminution tests developed for the "Silica in the Mine" project carried out at LKAB's mineral processing laboratory in the future.

To obtain the energy register function based on the data from comminution tests of the three samples (6382, 6365, 6354), presented in Figure 96, the accumulated mass specific energy consumption (Δe) is plotted versus the mass specific surface area (S_m) of the assigned product. If the measured data set can be approximated by a linear function then the slope is known as the Rittinger coefficient (R).

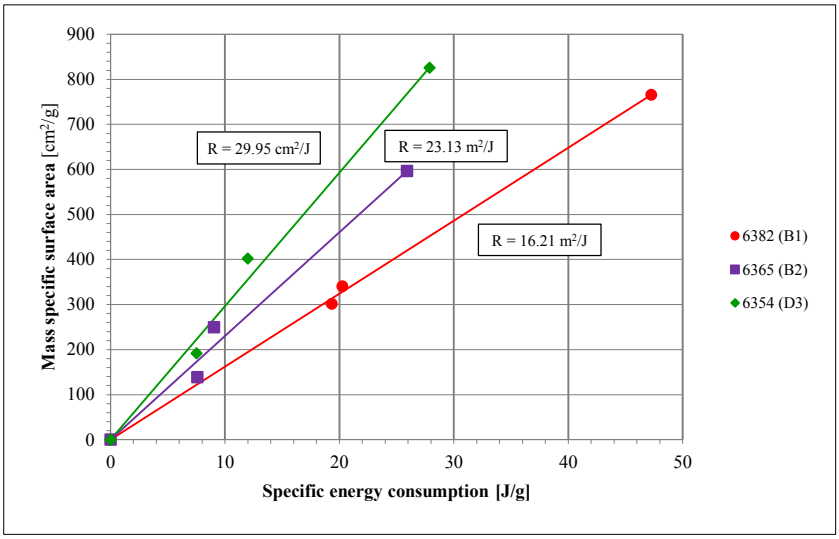

Figure 96. Comparison of the energy register functions of samples 6382 (B1), 6365 (B2) and 6354 (D3). R = Rittinger coefficient [cm^2/J].

It can be concluded that these three samples, representing the three main ore types of the Kiirunavaara deposit, show a difference in their breakage behaviour under the controlled comminution tests according to the principles of OCS. This conclusion is based on the ore characterization data defined by the differences in the particle size distribution within comminution products, as well as in differences in the mass specific energy consumption. Based on the results from the comminution tests at the laboratory of the Institute of Mineral Processing, Montanuniversitaet Leoben, the characteristic value of the Rittinger coefficient (R) can be used to make conclusions on the breakage resistance of the different ore types in technical fragmentation. It should be noted that ore type B1 is heavier to fragment based on the low value of the Rittinger coefficient. Furthermore, in the case of sample 6382 (B1), the mass specific surface area (S_m) is significantly higher in the finest particle size class than the equivalent value of sample 6365 (B2). However, the Rittinger coefficient is lower for sample 6382 representing ore type B1. The values of the Rittinger coefficient are nearer to each other for ore types B2 and D3, from which it can be interpreted that these ore types are easier to fragment. On the other hand, this characteristic was already known based on empirical knowledge and earlier grinding tests regarding the iron ore of the Kiirunavaara deposit. It should be noted, however, that each of the ore types is represented by a single sample, so very far-reaching conclusions cannot be made.

In their study, Rohmoser et al. (2007), have determined the Rittinger coefficient for two samples from Kiirunavaara iron ore deposit as follows: R = 46 [cm^2/J] for sample M3 and R = 30 [cm^2/J] for sample M4, which can be compared with the Rittinger coefficient obtained in this study. However, they gave no information of the ore type for these samples. Wartbichler (2014) determined in his study the Rittiger coefficient R = 40.24 [cm^2/J] for the martite (hematite-magnetite) ore from the northern part of the Kiirunavaara deposit. However, these comminution tests carried out by Rohmoser et al. (2007) and Wartbichler (2014) consisted only comminution stages with the crushers and the laboratory rod mill.

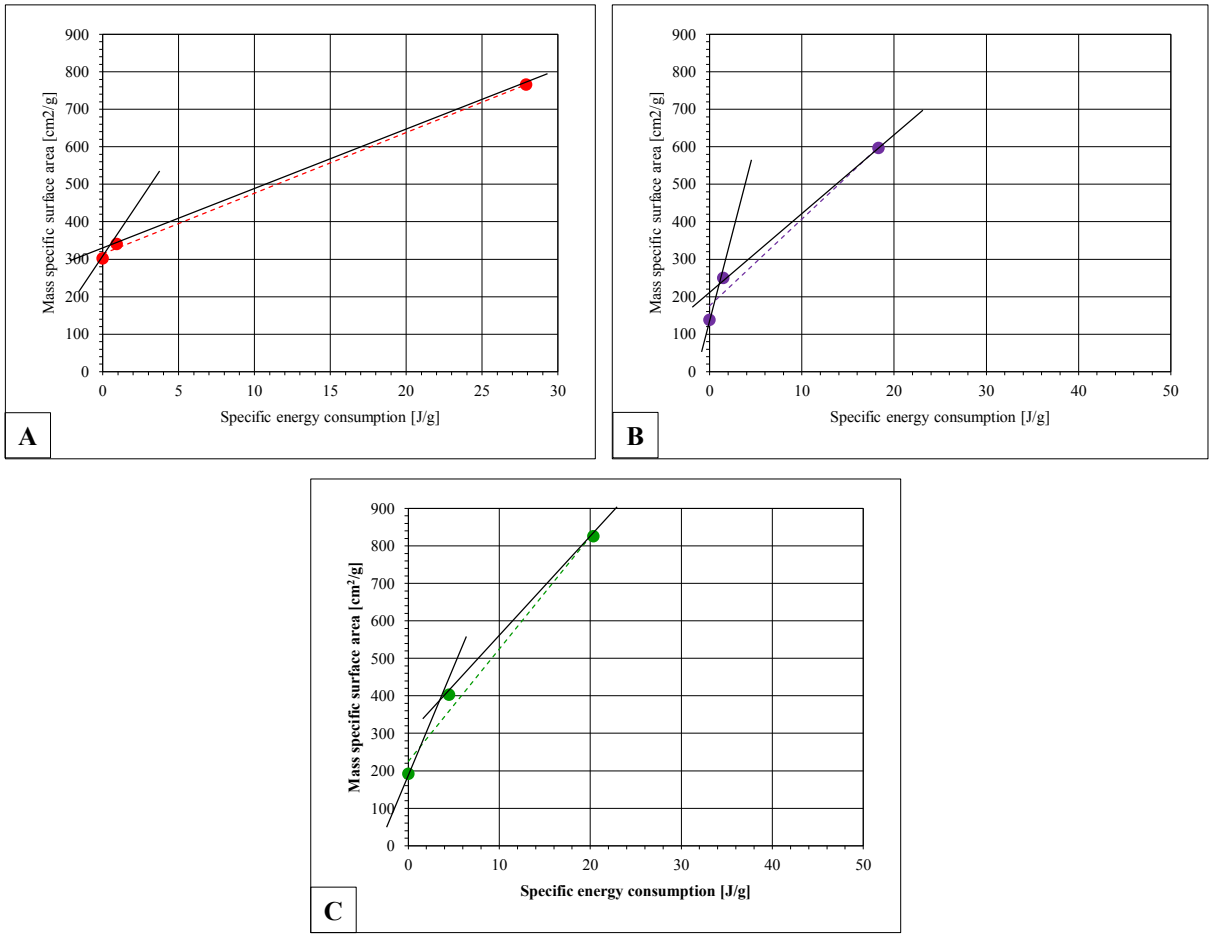

Figure 97. Another interpretation for the energy register function (black line) of (A) sample 6382 (B1), (B) sample 6365 (B2), and (C) sample 6354 (D3).

It is significant to note based on the information from the comminution tests that there might be a deviant breakage characteristic in relation to the magnetite-apatite ore from the Kiirunavaara deposit. When looking at the charts presented in Figure 97, the energy register might have a kink point when the comminution was carried out in the laboratory ball mill. Especially, this characteristics seems to be obvious in case of samples 6382 (Fig. 97 A) and 6365 (Fig. 97 B) representing ore types B1 and B2, respectively. Similar results were obtained in comminution tests carried out with focus on ore type B2 at the laboratory of the Institute of Mineral Processing in summer of 2010 (Chapter 7.2).

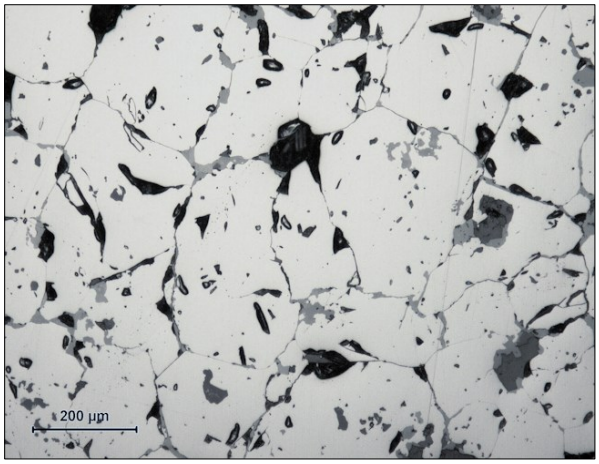

Figure 98. Magnetite ore with well-preserved, obviously primary crystal structure. Sample 6057, reflected light.

This feature can be explained with the crystal structure of magnetite in the ore from the Kiirunavaa deposit (Fig. 98). Up to a certain particle size, the ore structure is broken down along the interfaces of the magnetite crystals. Thus the magnetite crystals and/or particle are liberated, the specific energy consumption increases to generate equal amount specific surface area, which is indicated by the flatter slope of the energy register based on the comminution test. The critical particle size seems be to approximately 200 µm based on the information from this study. It can be concluded that the consumption of the energy to obtain a certain specific surface area is not only dependent on the material itself, but it can obviously be dependent also on the particle and/or crystal structure. However, it should be pointed out that there is a possibility that each of the main ore types contains several subtypes with different breakage characteristics, such as grain size or variations in mineralogy within in the same ore type. This characteristic has already been discovered in the case of ore type B2, which can be split into two different sub types, B2-a and B2-b, based on the mineralogy but also on the breakage characteristic.

The information on elemental and mineral deportment in samples and in particle size classes is a critical requirement for many ore characterization projects. One of the main targets of this study was to investigate the SiO_2-bearing minerals and the modal mineralogy (i.e., the grade of the minerals) with a focus on the high-SiO_2 ore type B2 based on the optical mineralogy and analysis with automated mineralogy (QEMSCAN®) at LKAB's metallurgical laboratory in Luleå. The most important SiO_2-bearing minerals in the Kiirunavaara deposit are actinolite, phlogopite, chlorite, titanite and quartz, but in some cases also talc, and alkali feldspars, mostly albite. A main result of the mineralogical investigations related to this study was the discovery of two separate subtypes within ore type B2 based on the mineralogical data, which also seem to differ in mineral processing properties. The first one, tentatively named the subtype B2-a, is characterized by actinolite and the second one, tentatively named the subtype B2-b is characterized by phlogopite and quartz, but also in some cases by albite. The possible split-up of ore type B2 into these subtypes and their distribution within the Kiirunavaara deposit requires, however, additional mineralogical and geological investigations. On the deportment of silicon (Si), the initial classification of the ore type B2 into two subtypes is used. In the subtype B2-a, actinolite as a

dominant mineral clearly contains the most silicon (Si). However, in some cases phlogopite can also contain significant amount of Si. Quartz and phlogopite are the most common silicate minerals in the subtype B2-b containing also the most of Si in this sub-type. Quartz seems to be a rather common mineral in the deposit based on the data of modal mineralogy, which can be an explanation for the enrichment of Si in the subtype B2-b.

A mineral liberation analysis can be regarded as a crucial part of modern process mineralogy. To carry out a mineral liberation analysis by using the traditional Davis magnetic tube test work and automated mineralogy was the third target of this study. Without modern automated mineralogy based on SEM-EDS technics a liberation analysis and a comparison of mineral associations for non-liberated particles can be challenging, especially in the case of ternary particles. In ore type B2 the binary intergrowths of magnetite and the silicate minerals seem to be the most common type of mineral association discovered. The intergrowths of magnetite and two or more silicates (ternary) appear to be rare. The degree of the liberation of magnetite seems to be high for most of the samples especially in the finest particle size classes and magnetite can be regarded as fully liberated according to the current classification used by LKAB (> 90% liberated) in most cases based on information evaluated with the Henry-Reinhardt charts and QEMSCAN® analysis . It should be kept in mind that there can be some overestimation of the degree of liberation because of a stereological error, which can be dependent on various factors such as particle composition, texture or the type of measurement when using automated mineralogy.

In conclusion, there seems to be a characteristic difference between the two subtypes B2-a and B2-b related to the binary intergrowths of magnetite and silicates. Intergrowths of magnetite and actinolite is the most common in the subtype B2-a, but also intergrowths of magnetite and phlogopite seem to occur in some cases in both subtypes. Furthermore, it seems to be obvious that there exists also a link between the mineralogy and grindability (i.e., breakage characteristics) in these two subtypes. This characteristics of ore type B2 is not yet well known and requires, however, additional investigations. Based on this study, it can be concluded that the problem with the high SiO_2 grade in the magnetite concentrate at the beneficiation plants in the Kiirunavaara site seems to be closely related to fine-grained intergrowths of magnetite and actinolite (Fig. 99 A and B; see also Chapter 3.3.2 and Chapter 9.5).

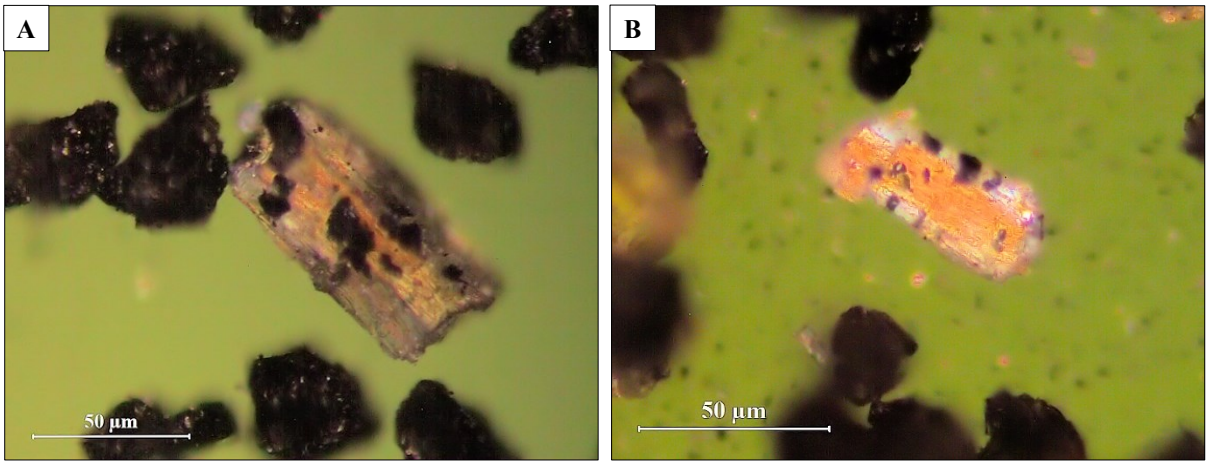

Figure 99. Actinolite particles with fine-grained magnetite inclusions. Both (A) sample 6252 and (B) sample 6387 represent the subtype B2-a (in transmitted and reflected light; polarized state).

Two recommendations will be given based on the results from this study in order to find out more information about the problematic silica in the crude ore. Firstly, it is advisable to carry out an extensive large-scale sampling program in the different stages of the process at the beneficiation plants in the Kiirunavaara site, especially after comminution circuit and before and after wet low magnetic separation (WLIMS) when repeated high SiO_2 grades are measured in the magnetite concentrate or when significant fluctuations in SiO_2 grades in the crude ore noted. Thus it seems to possible that magnetic separation (WLIMS) can't help to decrease of SiO_2 (significant variations and/or high SiO_2 grade in the feed, variations in the silicate mineralogy, the amount of different ore types in the feed, et c.). This information will be essential for the characterization and identification of the silica problem, which is undoubtedly, at least to some extent, related to the mineralogy of the silicates in the ore (liberation and intergrowths). Special attentions should be paid on ore type B2 and especially to the subtype B2-a, characterized by actinolite with magnetite inclusions. Even if liberated, actinolite particles with magnetic inclusions and in some cases also fully liberated quartz particles will end up in the magnetite concentrate. It is clear that they increase the SiO_2 grade in the concentrate significantly, because the quartz is chemically pure SiO_2. It is obvious that there is a need to carry out further study to find out the reason or mechanism contribute the occurrence of the fully liberated quartz particles in the concentrate.

Currently, only two different ore types in the Kiirunavaara deposit, low-phosphorous ore (B) and high-phosphorous ore (D), are separated in the 3D geological model and in the block model, of which the former includes both ore type B1 (low SiO_2) and ore type B2 (high-silica). By the drill core logging, as well as by geological mapping underground, ore types B1 and B2 are separated from each other and stored in a database. Secondly, it is recommended that the current 3D geological model should be reconstructed with the ore types B1 and B separated into different domains. Considerations should also be made to separate the two subtypes, B2-a and B2-b, in the drill core logging and in the geological modeling. These two points will likely aid in the making of reliable predictions of the amount of high-silica ore and the silica grade in the crude ore as well as in the magnetite concentrate based on the mineral

processing tests in the “Silica in the Mine” project. This applies in particular to the subtype B2-a, which seems to be closely related to the high SiO_2 problem. Because ore type B1 seems to be more homogenous and, in general, low in silica and because the amount of high phosphorous ore type D is decreasing in the deeper parts of the deposit, more focus should be laid on ore type B2 via sampling of the drill cores obtained by exploration drilling and mineral processing tests. In this manner the total number of samples can be reduced which reduces the time needed for the tests and personnel at LKAB’s mineral processing laboratory and, naturally, lowers the costs. Furthermore, when taking into account the particular mineralogy of the silicates and the mineral processing characteristics of ore type B2 defined in this study, this information is a good basis for designing pilot plant tests related to potential silicate flotation at the beneficiation plants in the Kiirunavaara site.

REFERENCES

Adolfsson, G. (1995): MITU Project – Column flotation of silicate minerals from iron ore. *LKAB Rapport 95–774, (Internal Report in Swedish), 15 p with appendices.*

Adolfsson, G. (1996): Projekt 3 gruvor. Uppföljning gruva färdig produkt B2-rågods från olika områden. *LKAB Utredning 96-702 (Internal report in Swedish), 10 p.*

Adolfsson, G. (2008): Uppföljning av kisel Gruva – färdig produkt. *LKAB Report 08-766, (Internal Report in Swedish), 21 p.*

Adolfsson, G. & Fredriksson A. (2011): Reduction of Silica in LKAB Pellets through Different Mineral Processing Unit Operations. *Conference in Minerals Engineering, Luleå University of Technology, Preprints.*

Adolfsson, G. (2014): *personal communication.*

Agorhom, E. A., Swierczek, Z., Skinner, W. and Zanin, M. (2012): Combined QXRD-QEMSCAN mineralogical analysis of a porphyry copper-gold ore for the optimization of the flotation strategy. *Paper No. 335, XXVI International Mineral Processing Congress (IMPC 2012), New Delhi India, pp. 99–111.*

Andersen, J.C.Ø, Rollison, G.K., Snook, B., Herrington, R. & Fairhurst, R.J. (2009): Use of QEMSCAN® for the characterization of Ni-rich and Ni- poor goethite in laterite ores. *Minerals Engineering 22, pp. 1119–1129.*

Andréasson, G. (1997): Magnetsepareringens effekter av malm från nivå 765 Kiirunavaaragruvan – mineralogisk studie. *University of Uppsala, Master thesis, 61 p., (in Swedish).*

Aupers, K. (2014): Gangue mineralogy and deportment of deleterious elements in the iron ore of the Kiirunavaara deposit, Sweden. *TU Bergakademie Freiberg, Master Thesis (unpubl.) with appendices, 151 p.*

Bergman, S., Kubler, L. & Martinsson, O. (2001): Description of regional geological and geophysical maps of northern Norrbotten County (east of the Caledonian orogen). *Geological Survey of Sweden SGU Ba 56, 110 pp.*

Bergström, B. & Anttila, A. (1973): MALNING: Försök i laboratorie- och pilotskala jämfört med driftsmalning. *Intern Utredning 6/52 (Internal Report in Swedish), 10 p.*

Butcher, A. (2010): A Practical Guide to Some Aspects of Mineralogy that Affect Flotation. *Spectrum Series 16, Flotation Plant Optimisation, pp. 83–93.*

Boehm, A., Mayerhofer, R. & Oefner, W. (2002): Optimized Comminution Sequence. Natural Breakage Characteristic. Energy register Function. *Technical Report No. 22. EU Project: Less Fines Production in aggregate and industrial minerals industry. Project No: GRD-2000-25224. 27 p.*

Böhm, A. (2009): Theoretische Aspekte der Magnetscheidung für Praxis. *BHM 154. Jahrgang: pp. 145–151, (in German).*

Böhm, A. (2011): The Henry Reinhardt Diagram, *Presentation at LKAB in Kiruna, 12th January 2011.*

Böhm, A., Wartbichler, M. & Niiranen, K. (2015): Entwicklungstendenzen in der Verwachsungsanalyse. *BHM Berg-und Hüttenmännische Monatshefte, 160 (6), pp.247-256, (in German).*

Cliff, R. A., Rickard, D. & Blake, K. (1990): Isotope Systematics of the Kiruna magnetite Ores, Sweden. Part 1. Age of the Ore. *Economic geology, Vol. 85, pp. 1770–1776.*

Deer, W. A., Howie, R. A. & Zussman, J. (1997 a): Rock-Forming Minerals - Single-chain silicates. *Volume 2A, Second edition. The Geological Society, London, 668 p*

Deer, W. A., Howie, R. A. & Zussman, J. (1997 b): Rock-Forming Minerals - Double-chain silicates. *Volume 2B, Second edition. The Geological Society, London, 764 p.*

Deer, W. A., Howie, R. A. & Zussman, J. (2001): Rock-Forming Minerals - Framework silicates (Feldspars). *Volume 4A, Second edition. The Geological Society, London, 972 p.*

Deer, W. A., Howie, R. A., Wise, W. S. & Zussman, J. (2004): Rock-Forming Minerals - Framework silicates: Silica Minerals, Feldpathoids and the Zeolites. *Volume 4B, Second edition. The Geological Society, London, 982 p*

Deer, W. A., Howie, R. A. & Zussman, J. (2009): Rock-Forming Minerals – Layered Silicates Excluding Micas and Clay Minerals. *Volume 3B, Second edition. The Geological Society, London, 314 p.*

Didic, M. (2003): Jämförelse mellan Svenssons - yta, Malvern och konventionell siktning m a p precision / repeterbarhet. *LKAB Report 03-718, (Internal Report in Swedish), 8 pp.*

Didic, M. & Norén, B. (2003): One –line partikelstorleksmätning i KA 1 m h a Laserdiffration. *LKAB Report 03-741, (Internal Report in Swedish), 18 pp.*

Donskoi, E., Manuel, J. R., Austin, P., Poliakov, A., Peterson, M. J. & Hapugoda, S. (2011): Comparative Study of Iron Ore Characterisation by Optical Image Analysis and QEMSCAN™. *Iron Ore Conference 2011, Perth, The AUSIMM Publication Series No 6/2011, pp. 213–222.*

Drugge, L. (2009): Validering av metod för simulering av framtida anrikningsresultat. *LKAB Utredning 09-775 (Internal Report in Swedish), 65 p.*

Drugge, L. (2010): Validering av malkroppscharger for anrikningssimulering 091215. *LKAB Utredning (Internal Report in Swedish), 65 p.*

Drzymała, J. (2007): Mineral Processing – Foundations of theory and practice of minerallury. *Oficyna Wydawnicza PWr., 509 p.*

Ekström, M & Ekström, T. (1997): Petrografisk beskrivning av sidoberget i Kiirunavaara. *Ekströms Mineral AB, Stockholm, 22 p., (in Swedish)*.

Everitt, B. (1998): The Cambridge Dictionary of Statistics. *Cambridge, UK New York: Cambridge University Press.*

Fagerberg, B. & Ornstein, H. (1962): Borrkärnegods från Leveäniemi, Makroskopisk kartering ur anrikningsteknisk synvinkel. *LKAB Report 62-100, (Internal Report in Swedish), 6 pp.*

Fandrich, R. G., Schneider, C.L. & Gay, S. L. (1998): Two stereological correction methods: allocation method and kernel transformation method. *Minerals Engineering 11, pp. 707–711.*

Fandrich, R., Ying, G., Burrows, D. & Moeller, K. (2007): Modern SEM-based mineral liberation analysis. *International Journal of Mineral Processing Vol. 84, Issues 1–4, pp. 310–320.*

Farrell, J. N., Miller, A. D. & Gaze, R. L. (2011): Geometallurgical Sampling and Resource Estimation for Magnetite Deposits. *The First AusIMM Geometallurgy Conference, Brisbane. In Proceedings, pp. 311–319.*

Fleet, M. F., (2003): Rock-Forming Minerals - Micas, Volume 3A, second edition (edit. Deer et al. 2003), *The Geological Society, London, 758 p.*

Freund, H. (edit.) (1966): Handbuch der Mikroskopie in der Technik. Instrumente für Auflicht-Mikroskopie, Band I / Teil 2. *Umschau Verlag,, 699 p, (in German).*

Frietsch, R. & Perdahl, J.-A. (1995): Rare earth elements in apatite and magnetite in Kiruna-type iron ores and some other iron ore types. *Ore Geology Reviews, Volym 9, pp. 489–510.*

Gaudin, A. M. (1939): Principles of Mineral Dressing. *New York / London: McGraw Hill Book Co., Inc. 1939.*

Geijer, P. (1910): Igneous rocks and iron ores of Kiirunavaara, Luossavaara och Tuolluvaara. *Scientific and practical researches in Lapland arranged by Luossavaara-Kiirunavaara Aktiebolag, Stockholm. 278 p.*

Geijer, P. (1931): The iron ores of Kiruna type: geographical distribution, geological characters, and origin. *Sveriges Geol. Unders., Ser. C (367) 39 p.*

Goodall, W. R., Scales, P. J. & Butcher, A. R. (2005): The use of QEMSCAN® and diagnostic leaching in the characterization of visible gold in complex ores. *Mineral Engineering 18, pp. 877–886.*

Gottlieb, P., Wilkie, G., Sutherland. D., Ho-Tun, E., Suthers, S., Perera, K., Jenkins, B., Spencer, S., Butcher, A. & Rayner, J. (2000): Using Quantitative Electron Microscopy for Process Mineral Application. *JOM Journal of Metals 52, pp.24–25.*

Grant, G., Hall, J. S., Reid, A. F. and Zuiderwyk, M. (1977): Characterization of particulate and composite mineral grains by on-line computer processing of SEM Images, in *Proceedings 15th APCOM Symposium, Brisbane, pp. 159–170.*

Gu Y. (2003): Automated Scanning Electron Microscope Based Mineral Liberation Analysis. *Journal of Minerals & Materials Characterization & Engineering, Vol. 2, No. 1, pp. 33–41.*

Gu, Y., Schouwstra, R. P. & Wang, D. (2012): A comparison between 2D and 3D particle size measurement. *Proceedings, Process Mineralogy 2012, MEI Conference, South Africa.*

Gu, Y., Schouwstra, R. P. & Rule C. (2014): The value of automated mineralogy. *Minerals Engineering 58, pp. 100–103.*

Hansson, K-E. (2001): Hematit i Sjömalmen. *LKAB Rapport PB 01-049 (Internal Report in Swedish), 13 p.*

Hedin, J-O. (1992): SiO_2 –problemet i KUJ – en mineralogisk studie i makroskopisk och mikroskopisk skala. Del I och II. *LKAB Rapport KG 92-114 (Internal Report in Swedish), 15 p.*

Heidenreich, H. (1954): Die Erfolgsrechnung im Aufbereitungsbetrieb. *Verlag Glückauf GmbH, Essen pp.1–3, (in German).*

Henley K. J. (1983): Ore dressing mineralogy – a review of techniques, applications and development. *ICAM 81, Spec. Publ Geo. S. Afr. 7, pp 175–200.*

Höfig, T. (2014) : *Personal communication.*

Jarousseau, B. & Pålsson, B. (2000): Mineralogical study of the Lake Ore. *Luleå University of Technology, Division of Mineral Processing, 38 p.*

Keeney, F. & Walters, S.G. (2011): A Methodology for Geometallurgical Mapping and Orebody Modelling. *The First AusIMM Geometallurgy Conference, Brisbane. In Proceedings pp. 217–225.*

Kittler, P., Liebezeit, V., Ehring, K., Macmillan, E. & Lower, C. (2011): 'It seemed like a Good Idea at the Time…' Common Mistakes in Geometallurgy. *The First AusIMM Geometallurgy Conference, Brisbane, pp. 133–138.*

Knights, J. (2001): Optical Assessment Impurities in Kiruna Iron Ore, *LKAB, R&D Labs, Malmberget, J K Tech Job 1147 (Internal Report), 47 p.*

Kogelbauer, A & Böhm, A. (2009): Trockene Schwachfeld-Magnetscheidung im Feinkornbereich am Beispiel des Pelletierprojekts am Erzberg. *BHM 154. Jahrgang, pp. 164–170, (in German).*

Krusemann, H. (2012 a): QEMSCAN™ - The Scanning Electron Microscope, *FEI Handbook, 33 p.*

Krusemann, H. (2012 b): QEMSCAN Manual 5_SIP Editor. *FEI Handbook, 52 p.*

Krusemann, H. (2012 c): QEMSCAN Manual 4_iExplorer. *FEI Handbook, 303 p.*

Lamberg, P. & Vianna, S. (2007): A Technique for Tracking Multiphase Mineral. *Particles in Flotation Circuits: 7th Meeting of the Southern Hemisphere on the Mineral Technology, Ouro Preto, Brazil, Proceedings, pp.195–241.*

Lamberg, P. (2010): The use of mineral liberation data with property-based models in simulating mineral processes. *Process Mineralogy '10, South Africa, Proceedings, pp. 69-83.*

Lamberg, P. & Lund, C. (2012): Taking Liberation Information into a Geometallurgical Model – Case Study Malmberget, Northern Sweden. *Process Mineralogy '12, South Africa, Proceedings.*

Leake, B. E., Woolley, A.R., Arps, C.E.S., Birch, W.D., Gilbert, M.C., Grice, J.D., Hawthorne, F. C., Kato, A., Kisch, H. J., Krivovichev, V. G., Linthout, K., Laird, J. & Youzhi, G. (1997): Nomenclature of amphiboles: report of the subcommittee on amphiboles of the International Mineralogical Association, Commission on New Minerals and Mineral Names. *The Canadian Mineralogist, 35, pp. 219–246.*

Liipo, J., Lang, C., Burgess, S., Otterstrom, H., Person, H. & Lamberg, P. (2012): Automated mineral liberation analysis using INCAMineral. *Process Mineralogy '12, South Africa, Proceedings.*

LKAB (2014): *LKAB Products 2014, 57 p.*

Loberg, B. E. H. & Horndahl, A-K. (1983): Ferride geochemistry of Swedish Precambrian Iron Ores, *Mineralium Deposita 18, pp. 48–504.*

Lund, C. (2013): Mineralogical, Chemical and textural Characterisation of the Malmberget Iron Ore Deposit for a geometallurgical Model. *Luleå University of Technology, Doctoral Thesis with manuscripts, 97 p.*

Malm, L. (2009): Dingstube – analyser KA 090406. *LKAB Meddelande 09-128 (Internal Report in Swedish), 3 p.*

Malvern (2015): Malvern Mastersizer [on line]. Available from [Accessed: 25. June 2015] http://www.malvern.com/labeng/products/mastersizer/ms2000/mastersizer2000.htm

Martinsson, O. (2004): Geology and Metallogeny of the Northern Norrbotten Fe-Cu-Au Province. *Society of Economic Geologists, Guidebook Series, Volume 33, pp. 131–148.*

Martinsson, O. (2011): REE i LKAB:s järnmalmer – Projekt Kiirunavaara och Lappmalmen, (*Internal Report in Swedish*), 29 p.

Martinsson, O., Öberg, E. & Fredriksson, A. (2012): Apatite for extraction – Mineralogy of apatite and REE in the Kiirunavaara Fe-deposit. *Paper No. 476, International Mineral Processing Congress IMPC 2012, New Delhi, pp. 3287–3297*.

Miller, P. R., Reid, A. F. & Zuiderwyk, M. (1982): QEM*SEM image analysis in the determination of modal assays , mineral associations and mineral liberation, *Presented to XIV International mineral processing Congress (IMPC), Toronto*.

Misra, K. C. (2000): Understanding Mineral Deposits. *Kluwer Academic Publisher, p. 847.*

Moen, K. (2007): En kartleggning av silikat fördelning og opptreden i ulike jernmalmkonsentrat. *NTNU (Norges teknisk-naturvitenskaplige universitet), Trondheim. Reported to LKAB, 30 p. (in Swedish).*

Newton, M. J. & Graham, J.M. (2011: Spatial Modelling and Optimisation of Geometallurgical Indices. *The First AusIMM International Geometallurgy Conference, Brisbane. In Proceedings, pp. 247–261.*

Niiranen, K. (2006): The Deep Parts of the Kiirunavaara Apatite-magnetite Ore Body in Kiruna, Northern Sweden and the Impact of Future mining on the Township of Kiruna. *6th International Mining Geology Conference, Darwin, AusImm, Proceedings, pp. 57–67.*

Niiranen, K. & Fredriksson, A. (2012): A Systematic Approach of Geometallurgical Mapping of the Kiirunavaara Iron Ore. *Conference in Minerals Engineering, Luleå University of Technology, Preprints, pp. 81–90.*

Niiranen, K. & Böhm, A. (2012): A Systematic Characterization of the Ore Body for Minerals Processing at Kiirunavaara Iron Ore mine operated by LKAB in Kiruna, Northern Sweden. *Paper No. 1039, XXVI International Mineral Processing Congress (IMPC 2012), New Delhi India, pp. 3856–3864*.

Niiranen, K. (2012 a): Produktstromkontrolle des Aufgabestroms in die Aufbereitung bei LKAB in Kiruna, Nordschweden. *BHM Berg-und Hüttenmännische Monatshefte, 157(6-7), pp. 264-268, (in German).*

Niiranen, K. (2012 b): Mikroskopische Untersuchungen (LKAB, Malmberget) über die Mineralogie der Silikatminerale von ausgesuchten Eisenerzproben vom Erztyp B2 aus Kiruna und vergleichende Untersuchungen mit QEMSCAN-Mikroskopie (LKAB, Luleå). *Institute of Geology, Montanuniversitatet Leoben, Austria 30 p. (in German, unpubl.).*

Niiranen, K. & Böhm, A. (2013): Geometallurgical Characterization of ore type B2 (high silica ore) at the Kiirunavaara iron ore deposit, Northern Sweden. *Proceedings Vol. 1, 12th Biennial SGA Meeting, Uppsala, Sweden, S. 352–355.*

Niiranen, K. & Fredriksson, A. (2014): Geometallurgy at LKAB. *Paper No. 295, XXVII International Mineral Processing Congress (IMPC 2014), pp. 248–256.*

Niiranen, K. (2014): Titan (Ti) und Vanadium (V) – Mineralogische und geochemische Studie an diese Elemente in der Apatit-Magnetit-Lagerstätte am Kiirunavaara. *Institute of Geology, Montanuniversitaet Leoben, Austria 52 p. (in German, unpubl.).*

Nordstrand, J. (2012): Mineral Chemistry of Gangue Minerals Kiirunavaara iron ore, *Luleå University of Technology, Master Thesis, 45 p.*

Pentikäinen, T. (1978): Matematiikan kaavoja. *114 p.*

Perdahl, J-A. (1994): Geochemistry of Host Rocks and Ore at the Kiirunavaara Deposit, *Subproject, Department of Applied Geology, Luleå University of Technology, 10 p.*

Petruk, W. (2000): Applied Mineralogy in the Mining Industry. *Elsevier Science BV, Amsterdam, 288 p.*

Pirrie, D., Butcher, A.R., Power, M.R., Gottlieb, P. & Miller, G.L. (2004): Rapid quantitative mineral and phase analysis using automated scanning electron microscopy (QemSCAN); potential applications in forensic geoscience. *In: Pye, K. & Croft, D. (eds.) Geological Society, London, Special Publication, 232, pp. 123–136.*

Pirrie, D. & Rollinson, G. K. (2011): Unlocking the applications of automated mineral analysis. *Geology Today, Vol. 27, pp. 235–244.*

Quinteiro, C. (2008): Uppföljning: SiO_2 i råmalmen från KUJ till färdigt produkt. *LKAB Rapport 08–765 (Internal Report in Swedish), 19 p.*

Rapiscan (2013): Satmagan 135 [online]. Available from http://www.rapiscansystems.com/en/products/bpi/productssatmagan_135 . *[Accessed: 1. April 2013].*

Rietveld, H. M. (1969): A Profile Refinement Method for Nuclear and Magnetic Structures*: Journal of Applied Crystallography, v. 2, pp. 65-71.*

Romer, R. L, Martinsson, O. & Perdahl, J-A. (1994): Geochronology of the Kiruna iron ores and hydrothermal alterations. *Economic Geology Volume 89, pp 1249–1261.*

Rutanen, H. (2012): *Personal communication.*

Pålsson, B. I. & Fredriksson A. (2012): Beneficiation of REE containing Minerals. *Conference in Minerals Engineering, Luleå University of Technology, Preprints, pp.98–118.*

Schubert, H. (1988): Aufbereitung fester mineralischer Rohstoffe. *Band 1, Überarbeitete 4. Auflage, 363 p., (in German).*

Schulz, N. F. (1963): Determination of the Magnetic Separation Characteristic with the Davis magnetic Tube, *The Rocky Mountain Minerals Conference - SME (Society of Mining Engineers), Preprints, 21 p.*

Schulz, N.F. (1964): Mineral Beneficiation - Determination of the Magnetic Separation Characteristic with the Davis magnetic Tube, *AIME Transactions, Vol. 229, pp. 211–216.*

Smith, M. P., Storey, C. D., Jeffries, T. E. & Ryan, C. (2009): In Situ U-Pb and Trace Element Analysis of Accessory Minerals in the Kiruna District, Norrbotten, Sweden: New Constraints on the Timing and Origin of Mineralization. *Journal of Petrology, 50(11), pp. 2063–2094.*

Smythe, D. M, Lombard, A. & Coetzee, L. L. (2013): Rare Earth Element deportment studies utilising QEMSCAN technology, *Minerals Engineering 52, pp. 52–61.*

Spencer, S. & Sutherland, D. (2000): Stereological Correction of Mineral Liberation Grade Distributions estimated by Single Sectioning of Particles. *Image Analysis & Stereology 19, pp. 175–182.*

Steiner, H. J. (1990): Rahmengesetzmäßigkeiten der natürlichen Bruchcharakteristik von Mineralen und Gesteinen, *Erzmetall 43, No. 10, pp. 435–440.*

Steiner, H. J. (1991): The significance of the Rittinger equation in present-day comminution technology. *Proceedings of the XVIIth International Mineral Processing Congress, Dresden, Vol. 1. Polygraphischer Bereich, Bergakademie Freiberg/Sa, Freiberg, 1991, pp. 177–188.*

Steiner, H. J. (1996): Characterization of laboratory-scale tumbling mills, *Int. Journal of Mineral. Processing. 44-45, pp. 373–382.*

Steiner, H. J. (1998): Zerkleinerungstechnische Eigenschaften von Gesteinen, *Sonderdruck aus Felsbau 16, No.5, pp. 320–325., (in German).*

Storey, C. D., Smith, M. P. & Jeffries, T. E. (2007): In situ LA-ICP-MS U-Pb dating of metavolcanics of Norrbotten, Sweden: Record of extended geological histories in complex titanite grains. *Chemical Geology, Volym 240, pp. 163–181.*

Strunz, H. (1941): Mineralogische Tabellen. *Leipzig: Akademische Verlagsgesellschaft Becker & Erler, 287p., (in German).*

Ståhlström, A. (2008): Mikroskoperingsrapport på KPC. *LKAB Rapport 05–120 (Internal Report in Swedish), 7 p.*

Sutherland, D. (2007): Estimation of mineral grain size using automated mineralogy. *Minerals Engineering, Vol 20. Issue 5, pp. 452-460.*

Sutherland, D. N., Gottlieb, P. & Butcher A. R. (2000): Mineral characterization in the 21st century. *Minerals & Metals Challenges beyond 2000, IMM.*

J. Svensson (1949): Bestämmning av specifika ytan på kross- och malgods enligt permeabilitets-metoden. *Jernkontorets Ann. 133, pp. 33-86 (in Swedish).*

Teipel, U. & Winter, H. (2011): Reduzierte Abweichung – Less deviation. *AT Mineral Processing, Vol. 52 06-2011, pp. 45–53, (in German).*

Waara, M. (2013): Kontroll av fältstyrka på Dings tube. *LKAB Rapport KS2013-0218-M (Internal Report in Swedish), 2 p.*

Walters, S. G. (2009): New research initiatives in geometallurgical integration – moving towards a common operating language. *The Seventh International Mining Geology Conference 2009, The Australasian Institute of Mining and Metallurgy, Melbourne. In Proceedings, pp 19–22.*

Wartbichler, M. (2014): Raw Material Characterization of a Martite Ore: Case Study Kiirunavaara Deposit; Sweden. *Montanuniversitaet Leoben, MasterThesis (unpubl.), 70 p. with Appendices.*

Westhues, A., Hanchar, J.M., Whitehouse, M.J & Martinsson, O. (2013): In situ U-PB and whole rock Nd data for the Kiruna iron oxide apatite deposits and their host rocks, Norrbotten Sweden. *Proceedings Vol. 3, 12th Biennial SGA Meeting, Uppsala, Sweden, pp. 1394–1397.*

Wills, B.A. (2006): Mineral Processing Technology, (*edit. Napier-Munn, T.J.), Elsevier, 444 p.*

Wimmer, M. & Niiranen, K. (2005): Das Magnetit-Apatit-Erz von Kiruna (Nordschweden); Gewinnung, Aufbereitung und Veredlung. *Bergbau 9/2005 (Zeitschrift für Rohstoffgewinnung, Energie, Umwelt), pp. 396-406, (in German).*

Wimmer, M. (2012): Towards Understanding Breakage and Flow in Sublevel Caving (SLC). *Luleå University of Technology, Doctoral Thesis, 100 p.*

LIST OF FIGURES

Figure 1. SiO_2 (in situ) estimated from the resource block model for the Kiirunavaara mine (LKAB). x-axis corresponds the mining level (z) in the coordinate system used in the mine. 1

Figure 2. Former Leveäniemi open pit after it has been emptied of water in 2014 (Photo: LKAB). 2

Figure 3. Identification protocol on a drill core containing chemical assays of iron (Fe-analys), ore type and structure (Kärnstruktur) and section boundaries for the proposed mining pallets (Sektionslängd). Hematit = hematite; Malm = ore; Gråberg = waste (Fagerberg & Ornstein 1962). 3

Figure 4. Schematic picture combing of the mining lay out and a mining block containing mineral processing parameters for the Leveäniemi open pit (Fagerberg & Ornstein 1962). 3

Figure 5. Schematic picture of the Kiirunavaara orebody, seen from north (Picture: LKAB). 7

Figure 6. Ore type B1 (drill core ø ca. 29 mm). (A) Sample 6127: some veinlets of gangue minerals (actinolite, talc) cutting the ore; (B) Sample 6524: some very fine cracks filled by carbonate minerals cutting the ore; (C) Sample 6139: fine-grained calcite, phlogopite, titanite and sulphides between magnetite crystals (Photo: K. Aupers). 9

Figure 7. Ore type B2 (drill core ø ca. 29 mm). (A) Sample 6200: coarse-grained, green actinolite brecciates magnetite. (B) Sample 6196: euhedral actinolite as finely disseminated in the magnetite ore. (C) 6245: stockwork-like appearance of silicate minerals, mostly green actinolite (Photo: K. Aupers). 10

Figure 8. Ore type D (drill core ø ca. 29 mm). (A) Sample 6287: subtype D1, fine veinlets of apatite associated with calcite in magnetite, creating a network-like structure. (B) Sample 6453: subtype D3, high amounts of apatite associated with magnetite. (C) Sample 6138: subtype D5, "schlieren"-like structure of apatite-rich layers and greenish minerals (actinolite?) described by Geijer (1910) (Photo: K. Aupers). 10

Figure 9. (A) Coarse-grained, subhedral, almost colorless actinolite in brecciated magnetite ore (Sample 6387.3; transmitted light); (B) large needle-like subhedral/euhedral actinolite crystals with fine-grained magnetite inclusions (Sample 6252.4, reflected light). 12

Figure 10. Chemical classification scheme of amphibole group minerals (after Leake et al. 1997). All the analyzed samples fall into the actinolite group (Aupers 2014). The green dotted line marks the EPMA analyses carried out by Nordstrand (2012). 13

Figure 11. (A) Coarse-grained, colorless Mg-rich phlogopite (Sample B2-6172; transmitted light; Photo: K. Aupers); (B) Dark brown Fe-rich phlogopite (transmitted light; Photo: J. Nordstrand). 14

Figure 12. Oxide concentration (SiO_2 and TiO_2) in phlogopite in different ore types based on EPMA analysis (Aupers 2014). Oxide concentrations in ore types B1 and B2 (squares) show variations in TiO_2 concentrations within a sample, while D-type ores (crosses) display constant TiO_2 values. 14

Figure 13. Chlorite as an alteration product of phlogopite in transmitted light. (Photo: K. Aupers (A) and J. Nordstrand (B)). 15

Figure 14. (A) Fine-grained titanite as interstitial to granular magnetite and between magnetite and silicates (reflected light; see blue arrows); (B) Coarse-grained titanite as subhedral to euhedral crystals (transmitted light). 16

Figure 15. (A) Quartz grains (Qz) with carbonate (Crb) in sample 6370.2 (transmitted light); (B) Undulose extinction of quartz grains (transmitted light; polarized state)..... 17

Figure 16. Albite (light brown) and K-Feldspar (red) in a particle together with phlogopite and quartz; (A) BSE image; (B) Processed with a secondary SIP List presented in Figure 58 B. Sample 6370, Fraction 1.0/0.5 mm. 17

Figure 17. (A) Fine-grained talc (Talc) with colorless actinolite between magnetite (Mag) grains (transmitted light); (B) massive, fine-grained talc (Talc) as an aggregate with phlogopite (Phl) (transmitted light). 18

Figure 18. (A) Particle size distribution (PSD) for samples 6382 (B1), 6365 (B2), and 6354(D3) after crushing -3 mm at LKAB's mineral processing laboratory. (B) The same particle size distribution presented in Figure 18 A, but in the format of internal reports used at LKAB (cumulative mass, % passing is non-logarithmic). Numeric data available on CD. 20

Figure 19. Scheme of the closed comminution circuit design with pre-screening (S = screening, C = Comminution tool) by Steiner (1990, 1996). 21

Figure 20. The laboratory rod mill at the laboratory of the Institute of Mineral Processing, Montanuniversitatet Leoben (Photo: M. Wartbichler). 22

Figure 21. Particle size distribution of the samples selected for the mineral processing tests and mineralogical investigation representing ore type B2 after crushing to –3 mm at LKAB's mineral processing laboratory. Numeric data available on CD. 24

Figure 22. Comparison of the particle size distribution of samples 6252 and 6363 after comminution in the laboratory rod mill (10 minutes) at LKAB's mineral processing laboratory (Mbgt) and in the laboratory rod mill (550 and 750 rounds) at the laboratory of the Institute of Mineral Processing (Leo). 25

Figure 23. Laboratory tumbling mill used for the comminution tests with steel rods or steel balls as grinding media, at LKAB's mineral processing laboratory in Malmberget. 26

Figure 24. The apparatus for the Davis magnetic tube tests at the laboratory at the Institute of Mineral Processing, Montanuniversitaet Leoben (Photo: A. Böhm). 28

Figure 25. The cumulative frequency curve for sample 6354 (D3) based on data from the Davis magnetic tube tests. (two particle size classes after the comminution with the laboratory ball mill 0.1/0.04 mm and < 0.04 mm) displayed in Table 5..... 30

Figure 26. Apparatus for the Davis magnetic tube tests at LKAB's mineral processing laboratory in Malmberget. 31

Figure 27. He-gas Pycnometer (Type AccuPyc 1330) at the laboratory of the Institute of Mineral Processing (Photo: M. Wartbichler). 32

Figure 28. Permaran® (A) and Blaine (B) apparatuses used for the determination of the specific surface area at the laboratory of the Institute of Mineral Processing. 35

Figure 29. Apparatus for the determination of specific surface area by Svensson's method at LKAB's mineral processing laboratory in Malmberget. 36

Figure 30. Satmagan by Outokumpu at the laboratory of the Institute of Mineral Processing (Photo: M. Wartbichler) 38

Figure 31. Results of the determination of magnetite content (wt.%) by Satmagan at the laboratory of the Institute of Mineral Processing. (A) The feed material classified into four particle size classes by screening; (B) Comminution products after grinding in the laboratory rod mill classified into four particle size classes by screening; (C) and (D) the Davis magnetic tube concentrate (m = magnetics) and waste (w = non-magnetics) 39

Figure 32. PSD of sample 6382 (B1) before pre-screening (as received), after the 3rd cycle in the laboratory rod mill and the 3rd and 4th cycles (combined) in the laboratory ball mill at the laboratory of the Institute of Mineral Processing. 42

Figure 33. PSD of sample 6365 (B2) before pre-screening (as received), after the 3rd and 4th cycles (combined) in the laboratory rod mill and the 3rd and 4th cycles (combined) in the laboratory ball mill at the laboratory of the Institute of Mineral Processing. 42

Figure 34. PSD of samples 6354 (D3) before pre-screening (as received), after the 4th and 5th cycles (combined) in the laboratory rod mill and the 3rd and 4th cycles (combined) in the laboratory ball mill at the laboratory of the Institute of Mineral Processing. 42

Figure 35. PSD of sample 6382 (B1, see Fig. 32). The blue dotted line presents the expected PSD for crushing according to OSC mode. 43

Figure 36. The particle size distribution for samples 6252 (A) and 6367 (B) after each comminution stage at the laboratory of the Institute of Mineral Processing. 43

Figure 37. The particle size distribution for samples 6252 (A) and 6367 (B) after different comminution stages at LKAB's mineral processing laboratory related the "Silica in the Mine" project. 44

Figure 38. Particle size distribution for samples representing ore type B1 after (A), ore type B2 (B), and ore type (D) after comminution time of 10 minutes in the laboratory rod mill at LKAB's mineral processing laboratory related to the "Silica in the Mine" project. Numeric data available on CD. 45

Figure 39. Particle size distribution for samples representing ore type B1 (A), ore type B2 (B), and ore type (D) after comminution time of 10 minutes in the laboratory rod mill and 25 minutes in the laboratory ball mill at LKAB's mineral processing laboratory related to the "Silica in the Mine" project. Numeric data available on CD. 46

Figure 40. Particle size distribution for samples representing ore type B1 (A), ore type B2 (B), and ore type (D) after comminution time of 10 minutes in the laboratory rod mill and 35 minutes in the laboratory ball mill at LKAB's mineral processing laboratory related to the "Silica in the Mine" project. Numeric data available on CD. 47

Figure 41. Comparison of particle size distribution for sample 6255 (ore type B1) determined by a screen analysis (Sc) and Malvern Mastersizer 2000 (Ma) at LKAB's mineral processing laboratory. 48

Figure 42. Distribution of P_{80} values after comminution tests carried out at LKAB's mineral processing laboratory based on data from 632 samples, which are classified as ore type B2 by geologists during core logging. Mean = 42, Median = 42, Std. Deviation = 7, Variance = 48. 53

Figure 43. Flow sheet of the optimized comminution sequence, combined of several stages with pre-screening, where C = comminution machine, Δe_i = specific energy consumption in the i-stage, e_i = energy register related to the comminution product of the i-stage (Steiner 1990, Steiner 1996). 55

Figure 44. Simplified energy register functions for the energy-optimized comminution by OCS (A) and for the non-energy-optimized (technical) comminution (B) after Steiner (1998) and Boehm et al. (2002). 56

Figure 45. The specific production of fine material (M_F /U) for samples 6382 (B1), 6365 (B2), and 6354 (D3) as a function of the sum of revolutions and cumulated mass of generated fine material in the laboratory rod mill. Numeric data is displayed in Appendix 4. 57

Figure 46. Mass specific energy consumption for samples 6382 (B1), 6365 (B2) and 6354 (D3) based on data from the comminution tests in the laboratory ball mill at the laboratory of the Institute of Mineral Processing. Numeric data is displayed in Appendix 17. 60

Figure 47. The linear extrapolation of the energy register function for sample 6382 (B1). Numeric data is displayed in Appendix 18 (see also Fig. 44). 62

Figure 48. Energy register function of (A) sample 6382 (B1), (B) sample 6365 (B2), and (C) sample 6354 (D3). Numeric data is displayed in Appendix 18. R = Rittinger coefficient [cm^2/J]. 62

Figure 49. Comparison of the P_{80} and the mass specific energy [J/g] using a power function after comminution for samples 6252, 6363 and 6387 (subtype B2-a) in a laboratory rod mill (10 minutes) and in a laboratory ball mill (15, 25 and 35 minutes) at the laboratory of the Institute of Mineral Processing (A = linear scale, B = logarithmic scale). 67

Figure 50. Comparison of the P_{80} and the mass specific energy [J/g] using a power function after comminution for samples 6351, 6367 and 6370 (subtype B2-b) in a laboratory rod mill (10 minutes) and in a laboratory ball mill (15, 25 and 35 minutes) of the Institute of Mineral Processing (A = linear scale, B = logarithmic scale). 68

Figure 51. Principle of the brake test where G_1 is an indication of dynamometer and G_2 is the counterweight (Bergström & Anttila 1973). 70

Figure 52. Principle of interpolation of the comminution time at the laboratory scale to obtain P_{80} = 45 µm using the laboratory ball mill. 71

Figure 53. Histograms of the estimated energy consumption for entire population. (A) Ore type B1 (769 samples), (B) ore type B2 (632 samples), and (C) ore type D (259 samples). Statistic parameters are given in Table 31. 74

Figure 54. Schematic picture of the interactions of an electron beam and a sample (FEI; Krusemann 2012 a). 76

Figure 55. QEMSCAN® E430 Pro (Carl Zeiss SEM) at LKAB's metallurgical laboratory in Luleå (Photo: LKAB). 77

Figure 56. (A) Backscattered electron image (BSE) on sample 6351 (fraction 0.315/0.1 mm); (B) the same picture as a color-coded mineral map (digital image) with false colours after processing with iDiscover 5.3 software (grey = magnetite). 78

Figure 57. (A) Polished 30 mm resin blocks (samples 6370 and 6351, without coating); (B) Magnetite particles (light grey) mixed with graphite particles (brownish grey) for an automated mineral analysis by QEMSCAN®. 79

Figure 58. Selected minerals in the secondary SIP Lists (Species Identification Protocol) used for mineralogical investigation (A), and (B) and (C) for mineral liberation analysis. Created by iDiscover 5.3 software (FEI)..... 80

Figure 59. Comparison of the chemical assays on Si (A); Fe (B); Mg, Ti (C) and Al, K, Mn (D) grades for samples 6252, 6351, 6363, 6367, 6370 and 6387 (Fractions) generated from XRF and QEMSCAN. 82

Figure 60. (A) BSE (Back Scattered Electron) image on a magnetite particle (Sample 6351; particle size class 0.315/0.1 mm); (B) Same particle processed with a SIP List presented in Figure 58 A. 83

Figure 61. Modal mineralogy (total sample) of samples 6252, 6351, 6363, 6367, 6370 and 6387 (wt.% in the sample) determined by QEMSCAN® at LKAB's metallurgical laboratory in Luleå. 84

Figure 62. Modal mineralogy of SiO_2-bearing minerals in samples 6252, 6351, 6363, 6367, 6370, and 6387 (total samples). (A) Mass (wt.% in the sample; see also Table 18); (B) Samples normalized to 100%..... 86

Figure 63. Distribution (wt.% in sample) of silicates in the different size fractions of samples 6252 (A), 6351 (B), 6363 (C), 6367 (D), 6370 (E) and 6387 (F) after crushing and comminution in the laboratory rod mill (10 minutes) and in the laboratory ball mill (35 minutes). Numeric data is displayed in Appendix 20. 88

Figure 64. Deportment of silicon (Si) in samples 6252, 6363, and 6387 representing the actinolite dominated subtype (B2-a). (A), (C), and (E) represent the absolute mass of Si in the samples. (B), (D) and (F) represent the same samples normalized to 100%. 91

Figure 65. Deportment of silicon (Si) in samples 6351, 6367, and 6370 representing the quartz and phlogopite dominated subtype (B2-b), (A), (C) and (E) represent the absolute mass of Si in the samples. (B), (D), and (F) represent the same samples normalized to 100%..... 92

Figure 66. Intergrowth of magnetite (Fe Oxide) and different gangue mineral associations for samples 6252 (A), 6363 (B) and 6387 (C) representing the subtype B2-a after crushing, comminution in a laboratory rod mill (10 minutes) and in a laboratory ball mill (35 minutes) at the laboratory of the Institute of Mineral Processing..... 95

Figure 67. Intergrowth of magnetite (Fe Oxide) and different gangue mineral associations for the samples 6351 (A), 6367 (B), and 6370 (C) representing the subtype B2-b after crushing, comminution in a laboratory rod mill (10 minutes) and in a laboratory ball mill (35 min) at the laboratory of the Institute of Mineral Processing. 96

Figure 68. Fully liberated gangue minerals after crushing and comminution in a laboratory rod mill (10 minutes) and in a laboratory ball mill (35 minutes) at the laboratory of the Institute of Mineral Processing. Sample 6363, fraction 63/40 µm, mineralogy after SIP-List presented in Figure 58 A. ... 96

Figure 69. Fully liberated gangue minerals (silicates and apatite) in the waste (non-magnetics) after the Davis magnetite tube separation. Sample 6370, fraction 63/40 µm. 97

Figure 70. Mineral associations of magnetite with various gangue minerals for sample 6252 (subtype 2B-a) with respect to different fractions and classification used by LKAB (liberated magnetite, high grade and low grade middlings, locked and liberated gangue), mineralogy after SIP-List presented in Figure 58 A. 97

Figure 71. Binary intergrowths of magnetite (Fe Oxide) and various silicates for samples 6252 (A), 6363 (B), and 6387 (C) representing subtype B2-a after crushing, comminution in a laboratory rod mill (10 minutes) and in a laboratory ball mill (35 min). 98

Figure 72. Binary intergrowths of magnetite (Fe Oxide) and different silicates for samples 6351 (A), 6367 (B), and 6370 (C) from subtype B2-b after crushing, comminution in a laboratory rod mill (10 minutes) and in a laboratory ball mill (35 min). 99

Figure 73. Fully liberated magnetite particles (dark), intergrowth of very fine-grained magnetite and actinolite (A), liberated actinolite (B), (C) liberated titanite (?). Sample 6367, particle size class 63/40 µm (in transmitted and reflected light). 100

Figure 74. Simplified Henry-Reinhardt chart with (basic) intergrowth curves (Heidenreich 1954): (A) Separation is possible with the selected property; (B) No or very poor separation is possible because of low degree of liberation or no amenability to the separation. 101

Figure 75. Fully liberated magnetite particles (dark) and silicates (transparent) and obviously carbonates (pink). Sample 6367, representing ore type B2, particle size class 63/40 µm (in transmitted and reflected light). 104

Figure 76. Henry-Reinhardt charts on the two finest fractions (A) 100/40µm; (B) < 40µm for sample 6382 (B1) based on data from the Davis magnetic tube tests. Basic intergrowth curve of magnetics = red, cumulative curve for magnetics = blue, cumulative curve for non-magnetics = green, dotted dark brown line = average SiO_2 grade. 105

Figure 77. Henry-Reinhardt charts on the two finest fractions (A) 100/40µm; (B) < 40µm for sample 6365 (B2) based on data from the Davis magnetic tube tests (for explanation see Fig. 76). 105

Figure 78. Henry-Reinhardt charts on the two finest fractions (A) 100/40µm; (B) < 40µm for sample 6354 (D3), based on data from the Davis magnetic tube tests (for explanation see Fig. 76). 106

Figure 79. Henry-Reinhardt charts on the two finest fractions (A) 63/40µm; (B) < 40µm for sample 6252 representing the subtype B2-a based on data from the Davis magnetic tube tests (for explanation see Fig. 76). 108

Figure 80. Henry-Reinhardt charts on the two finest fractions (A) 63/40µm; (B) < 40µm for sample 6387 representing the subtype B2-a based on data from the Davis magnetic tube tests (for explanation see Fig. 76). 108

Figure 81. Henry-Reinhardt charts on the two finest fractions (A) 63/40µm; (B) < 40µm for sample 6351 representing the subtype B2-b based on data from the Davis magnetic tube tests (for explanation see Fig. 76). 109

Figure 82. Henry-Reinhardt charts on the two finest fractions (A) 63/40µm; (B) < 40µm for sample 6370 representing the subtype B2-b based on data from the Davis magnetic tube tests (for explanation see Fig. 76). 109

Figure 83. Mineral associations of liberated and non-liberated particles. Sample 6351, fraction 63/40 µm. Mineralogy after SIP-List presented in Figure 58 A. (A) Liberated (100-90%), (B) High grade middlings (90-60%), (C) Low grade middlings (60-30%) and (D) Locked (30-0%). 111

Figure 84. Liberation of magnetite (Fe Oxide) for samples 6252 (A), 6363 (B) and 6387 (C) representing the subtype B2-a after crushing and comminution in the laboratory rod mill (10 minutes) and in the laboratory ball mill (35 minutes) at the laboratory of the Institute of Mineral Processing. 112

Figure 85. Liberation of magnetite (Fe Oxide) for samples 6351 (A), 6367 (B) and 6370 (C) representing the subtype B2-b after crushing and comminution in the laboratory rod mill (10 minutes) and in the laboratory ball mill (35 minutes) at the laboratory of the Institute of Mineral Processing. 113

Figure 86. Two different types (generations) of actinolite in sample 6387, particle size class 63/40 µm after grinding and before the Davis magnetic tube separation. 114

Figure 87. Magnetics (magnetite concentrate) and non-magnetics (waste) of sample 6252 after separation with the Davis magnetite tube, particle size class 63/40 µm (black = magnetite, transparent = silicate, apatite; transmitted light): (A) Magnetics, 0.1 A; (B) Magnetics, 0.2 A; (C) Magnetics, 1.8 A; (D) Non-magnetics, 1.8 A. 115

Figure 88. Actinolite particle with small inclusions of magnetite (A) in the magnetics after separation with the Davis magnetite tube (0.1 A). Sample 6351, particle size class 63/40 µm (transmitted light). 116

Figure 89. A large actinolite particle with small inclusions of magnetite (A) and two liberated quartz particles (B) in the magnetics after separation with the Davis magnetite tube (1.8 A). Sample 6370, particle size class 63/40 µm (transmitted light)..... 116

Figure 90. Principle of estimation of SiO_2 grade in the DT concentrate at the laboratory scale. Only the values (Tables 37, 38, and 39) after comminution in the laboratory rod mill for 25 and 35 minutes, respectively, are displayed in the chart..... 117

Figure 91. Three samples showing an deviant behaviour of SiO_2 in the DT concentrate. 118

Figure 92. SiO_2 grade in the DT concentrate, Fraction < 45 µm, after comminution with the laboratory ball mill as a function of the dispersity (Drugge 2009). 120

Figure 93. Distribution of SiO_2 in the whole sample population. (A) Ore type B1 (756 samples), (B) Ore type B2 (624 samples) and (C) Ore type D (258 samples). Statistic parameters are displayed in Table 40. 124

Figure 94. The estimated SiO_2 % in DT concentrate at the industrial scale vs. the SiO_2 % in the feed. (A) Ore type B1 (756 samples), (B) Ore type B2 (624 samples) and (C) Ore type D (258 samples). 125

Figure 95. Comparison of the SiO_2 grade in the DT concentrate at the industrial scale and the estimated energy consumption related to the "Silica in the Mine" project. (A) Ore type B1, (B2) Ore type B2, and (C) Ore type D. 126

Figure 96. Comparison of the energy register functions of samples 6382 (B1), 6365 (B2) and 6354 (D3). R = Rittinger coefficient [cm^2/J]. 128

Figure 97. Another interpretation for the energy register function (black line) of (A) sample 6382 (B1), (B) sample 6365 (B2), and (C) sample 6354 (D3). 129

Figure 98. Magnetite ore with well-preserved, obviously primary crystal structure. Sample 6057, reflected light. 130

Figure 99. Actinolite particles with fine-grained magnetite inclusions. Both (A) sample 6252 and (B) sample 6387 represent the subtype B2-a (in transmitted and reflected light; polarized state). 132

LIST OF TABELS

Table 1. Limit values, % Fe and % P, for different ore types of the Kiirunavaara deposit (Niiranen 2006, Niiranen & Fredriksson 2012) and mean values for SiO_2 estimated from the Oracle database (LKAB). 8

Table 2. Technical data for the laboratory rod mill (Fig. 22) and the laboratory ball mill used for the comminution tests at the laboratory of the Institute of Mineral Processing, Montanuniversitatet Leoben. For critical speed see Equation 1. 22

Table 3. Technical data for the laboratory tumbling mill, with steel rods or balls, as grinding media used for the comminution tests related to the "Silica in the Mine" project at LKAB's mineral processing laboratory (Drugge 2009, Drugge 2010). 27

Table 4. Detailed data for the steel rods used for comminution tests in the laboratory tumbling mill at LKAB's mineral processing laboratory. 27

Table 5. The mass fractions of property and Fe and SiO_2 grade for two particle size classes of sample 6354 for cumulative frequency curve from the Davis magnetic tube tests. 29

Table 6. Measurement results of the specific gravity determined with He-gas Pycnometer (type AccuPyc 1330) at the laboratory of the Institute of Mineral Processing. 33

Table 7. Measurement results of the volume specific surface area (S_v) at the laboratory of the Institute of Mineral Processing, Montanuniversitaet Leoben. As received corresponds the feed material after crushing. 49

Table 8. Measurement results of the mass specific surface area (S_m) at the laboratory of the Institute of Mineral Processing, Montanuniversitaet Leoben. As received corresponds the feed material after crushing. 49

Table 9. Measurement results of the volume specific surface area (S_v) area carried out with Svensson's method at LKAB's mineral processing laboratory. 49

Table 10. Measurement results of determination of the volume specific [cm^{-1}] surface area (S_v) and calculated mass specific [cm^2/g] surface area (S_m) at LKAB's mineral processing laboratory. 50

Table 11. Shape factors for the particle size class 100/40 µm (shape factor for sphere = 6). 50

Table 12. Interpolated P_{80} values after each grinding stage at LKAB's mineral processing laboratory. 51

Table 13. Interpolated P_{80} values for the feed and comminution products after each grinding stage at the laboratory of the Institute of Mineral Processing. 51

Table 14. Comparison of P_{80} values (80% passing) interpolated from the particle size distribution after each grinding stage at LKAB's mineral processing laboratory and at the laboratory of the Institute of Mineral Processing (Appendix 16). 52

Table 15. P_{80} values for selected samples interpolated at LKAB's mineral processing laboratory. As a method 10 minutes corresponds to the comminution of 10 minutes in the laboratory rod mill, 10+25 minutes and 10+35 minutes correspond to the comminution of 10 minutes in the laboratory rod mill, and 25 minutes and 35 minutes, respectively, in the laboratory ball mill. 53

Table 16. Statistical characterization of P_{80} values based on information from comminution tests. 767 samples represent ore type B1, 632 samples the high-SiO_2 ore type B2, and 259 samples the high-P ore type D. The comminution times of 10, 10+25, and 10+35 minutes correspond to the same values as in Table 15. 54

Table 17. Estimation of the net power draw for sample 6382 (B1) grinded in the laboratory rod mill at the laboratory of the Institute of Mineral Processing; g/U corresponds production of fine material per a revolution. 58

Table 18. Estimation of the net power draw for sample 6365 (B2) grinded in the laboratory rod mill at the laboratory of the Institute of Mineral Processing; g/U corresponds production of fine material per a revolution. 58

Table 19. Estimation of the net power draw for sample 6354 (D3) grinded in the laboratory rod mill at the laboratory of the Institute of Mineral Processing; g/U corresponds production of fine material per a revolution. 58

Table 20. Mass specific energy consumption (Δe) for samples 6382 (B1), 6365 (B2) and 6354 (D3) to get 100% < 3.15 mm to 100% < 0.5 mm (laboratory rod mill). The entire data is given Appendix 18 and data for screen analysis is in Appendix 15. 58

Table 21. The mass specific energy consumption (Δe) for samples 6382 (B1), 6365 (B2) and 6354 (D3), to get 100% < 0.5 mm to 100 % < 0.1 mm. The entire data is given Appendix 18 and data for screen analysis is in Appendix 15..... 60

Table 22. The net power draw (E) for the laboratory rod mill by comminution tests carried out at the laboratory of the Institute of Mineral Processing (Steiner 1996). 64

Table 23. The net power draw (E) and the mass specific energy consumption (Δe) for M_F (generated fine material during the comminution, < 125 μm) based on the comminution tests in the laboratory rod mill at the Institute of Mineral Processing. 64

Table 24. Measured values of the total energy consumption (ΔE) based on the comminution tests (open circuit) in the laboratory ball mill carried out at the laboratory of the Institute of Mineral Processing. 65

Table 25. Total consumption of energy (ΔE) and the mass specific energy consumption (w_m) for M_F (generated fine material during the comminution, < 40 μm) based on the comminution tests with the laboratory ball mill at the laboratory of the Institute of Mineral Processing. Comminution times were 15, 25 and 35 minutes..... 66

Table 26. The correlation given as a power function between the mass specific energy consumption (w_m) and P_{80} values after different stages of comminution (15, 25 and 35 minutes) in a laboratory ball mill. 68

Table 27. Results of comparison of the energy consumption after comminution by rod mills, ball mills, and pebble mills (Bergström & Anttila 1973). 70

Table 28. Estimated energy consumption at the industrial scale based on Equation 33 for selected samples representing ore type B1. 72

Table 29. Estimated energy consumption at the industrial scale based on Equation 33 for selected samples representing ore type B2. 73

Table 30. Estimated energy consumption at the industrial scale based on Equation 33 for selected samples representing ore type D. 73

Table 31. Statistic parameters of the estimated energy consumption related to the "Silica in the Mine" project. 74

Table 32. Essential SiO_2-bearing minerals of ore type B2 identified in this study and the silicon (Si) and silica (SiO_2) grade based on EMPA analysis carried out by Nordstrand (2012) and Aupers (2014). See also Appendix 19. 81

Table 33. Modal mineralogy of samples 6252, 6351, 6363, 6367, 6370 and 6387 determined by QEMSCAN® at LKAB's metallurgical laboratory in Luleå. 85

Table 34. Principle for the calculation of the distribution of minerals in a particle size class (fraction) and in an entire sample. As example particle size class > 80 µm of sample 6252 is used after comminution in a laboratory rod mill (10 minutes) and in a laboratory ball mill (35 minutes). 87

Table 35. Data (sample 6354; fraction < 40 µm) from the Davis magnetic tube tests for the construction of the Henry-Reinhardt chart by Heidenreich (1954) and Böhm (2011); (MP = concentrate, magnetic particles; W = waste, non-magnetic particles, $\bar{x}$ = average grade). 102

Table 36. Point estimation of the SiO_2 grade in the concentrate from the beneficiation plant and from the laboratory tests. Asterisk (*) denotes the estimated value. 119

Table 37. Data for estimation of the SiO_2 grade in the DT concentrate at P_{80} = 45 µm at the laboratory scale and industrial scale at the beneficiation plant for the selected samples representing ore type B1. As method 10+25 corresponds to comminution for 10 minutes in the laboratory rod mill and 25 minutes in the laboratory ball mill, 10+35 corresponds 10 and 35 minutes, respectively. 122

Table 38. Data for estimation of the SiO_2 grade in the DT concentrate at P_{80} = 45 µm at the laboratory scale and industrial scale at the beneficiation plant for the selected samples representing ore type B2. As method 10+25 corresponds to comminution for 10 minutes in the laboratory rod mill and 25 minutes in the laboratory ball mill, 10+35 corresponds 10 and 35 minutes, respectively. 123

Table 39. Data for estimation of the SiO_2 grade in the DT concentrate at P_{80} = 45 µm at the laboratory scale and industrial scale at the beneficiation plant for the selected samples representing ore type D. As method 10+25 corresponds to comminution for 10 minutes in the laboratory rod mill and 25 minutes in the laboratory ball mill, 10+35 corresponds 10 and 35 minutes, respectively. 123

Appendix 1. Simplified flow sheet on the mineral processing tests related to the "Silica in Mine" project carried out at LKAB's mineral processing laboratory (Drugge 2009, Niiranen & Fredriksson 2012, Niiranen & Böhm 2012).

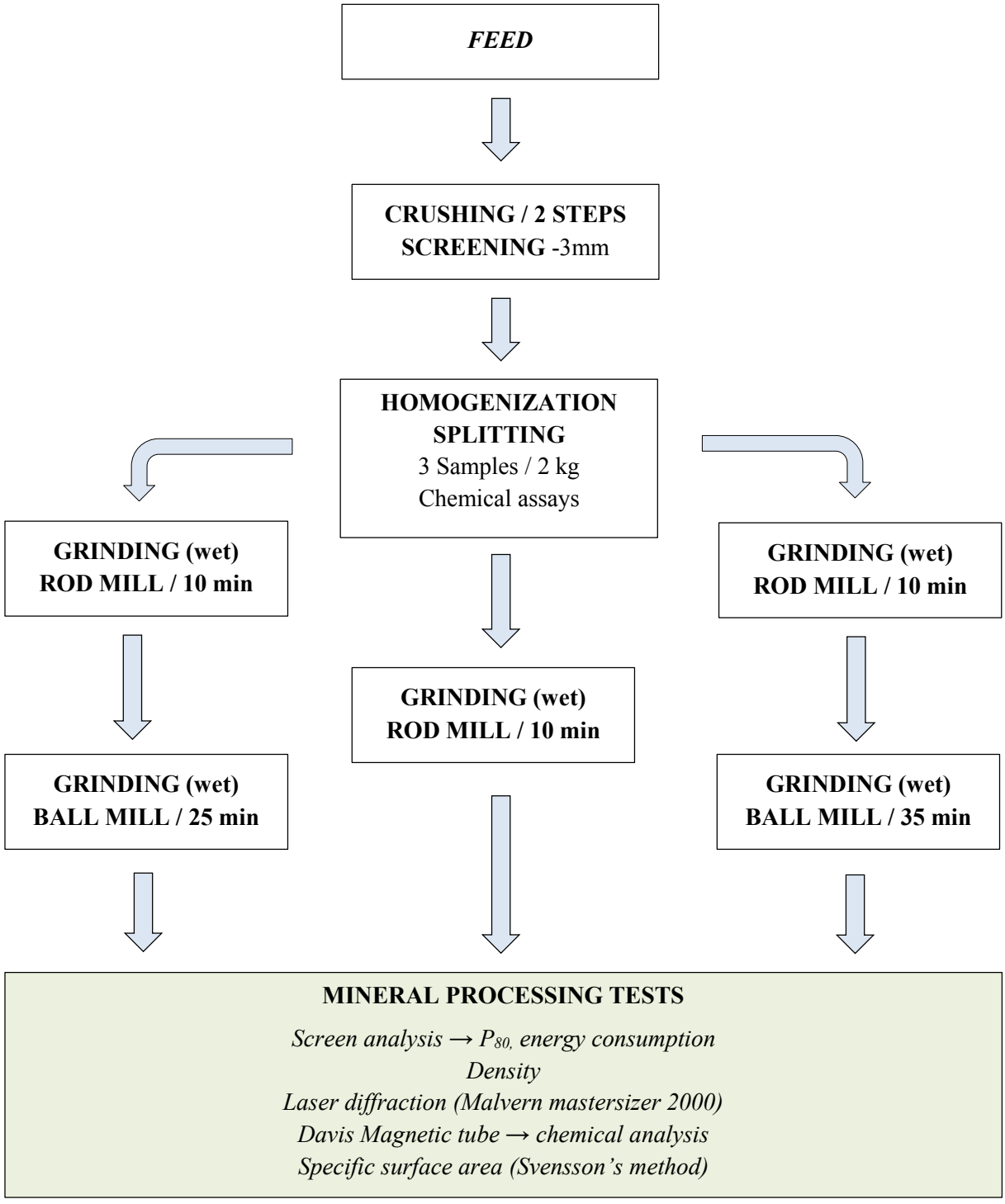

Appendix 2. Simplified scheme of the methods used for the systematic characterization of ore type B2 (high-silica ore) from the process mineralogical perspective developed at the laboratory of the Institute of Mineral Processing.

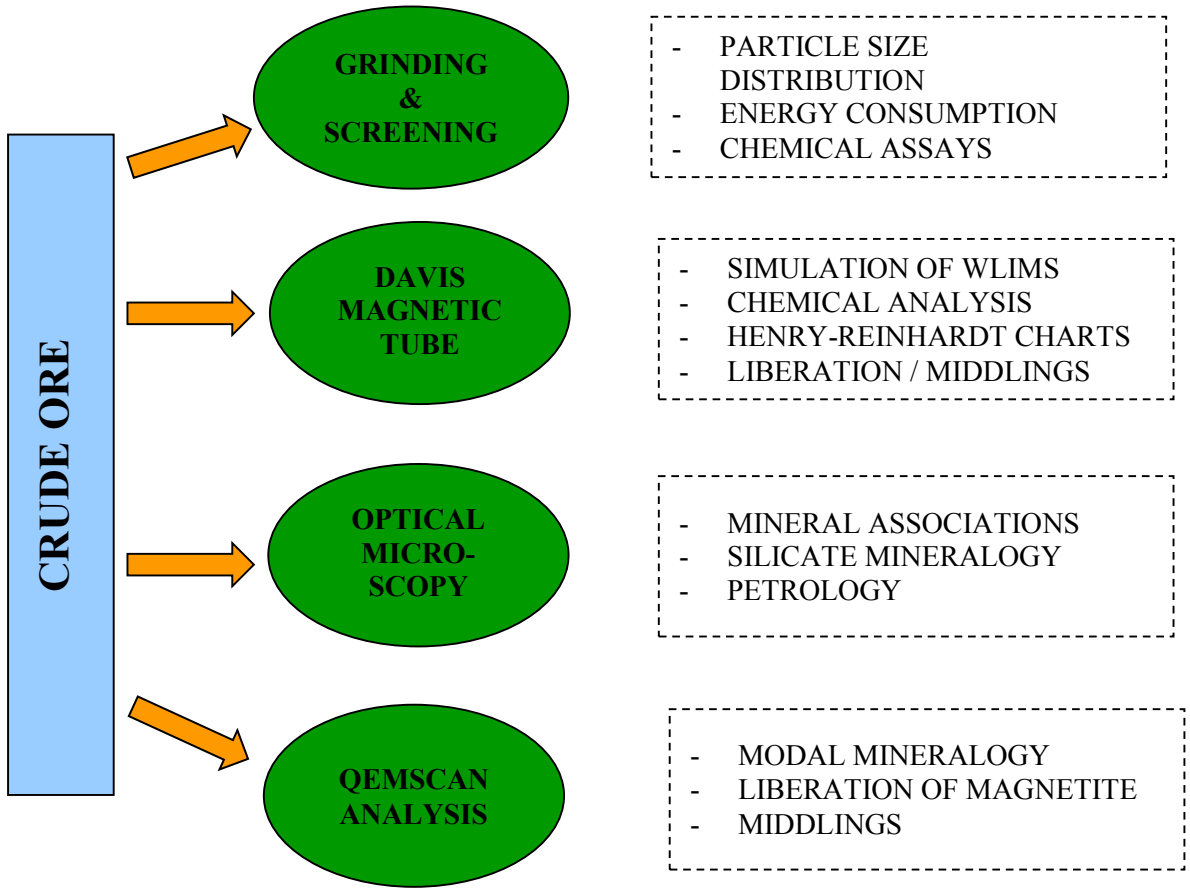

Appendix 3. Setup for the OCS (Optimized Comminution System) consisting a laboratory rod mill and a laboratory ball mill with pre-screening used for the comminution tests at the laboratory of the Institute of Mineral Processing, Montanuniversitatet Leoben.

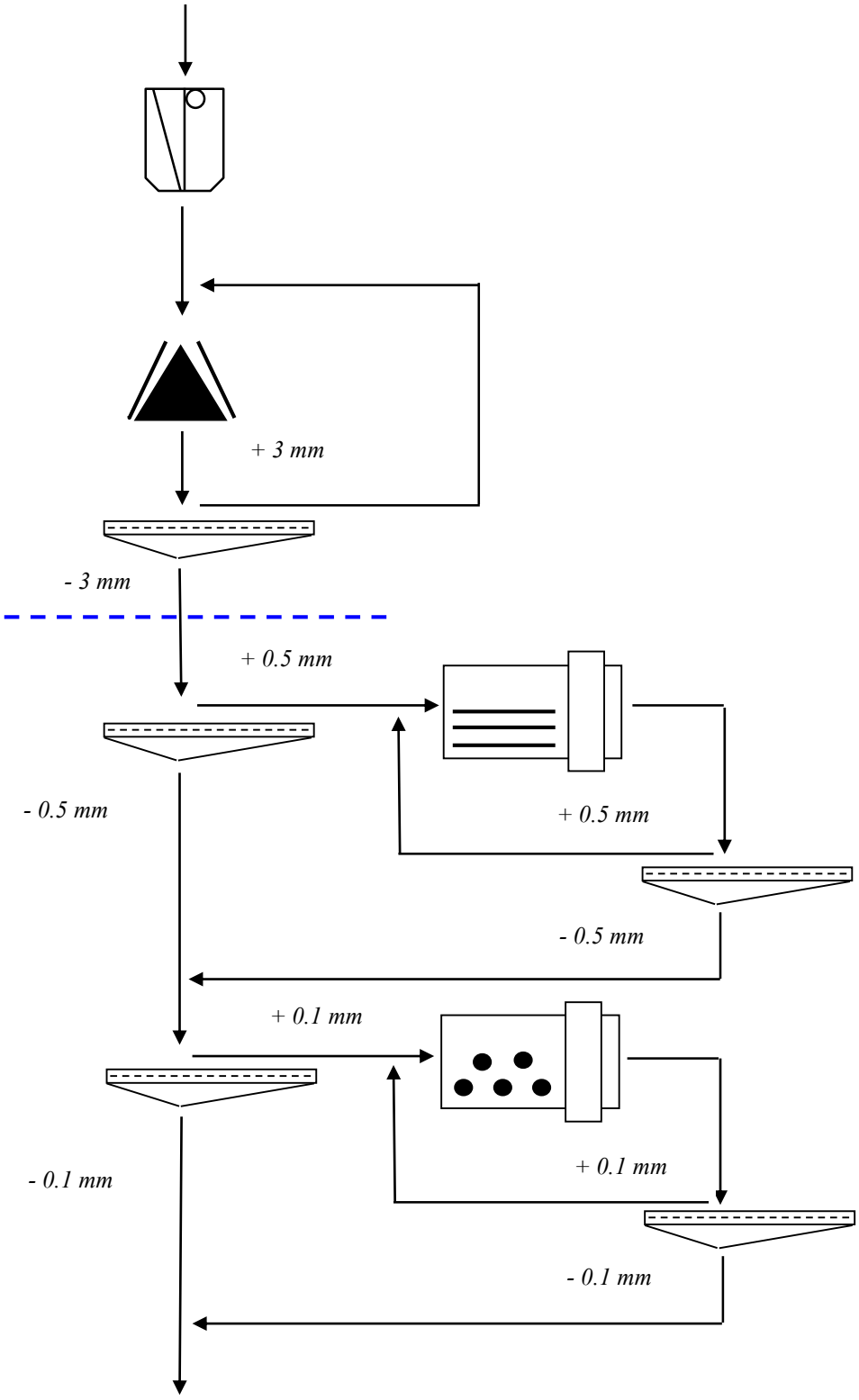

Appendix 4. Input and output data for the comminution tests carried out with the laboratory rod mill and the laboratory ball mill according the Optimized Comminution Sequence (OCS) the laboratory of the Institute of Mineral Processing, Montanuniversitaet Leoben.

Sample	Charge	Number of revolutions		Feed	Coarse material >500 µm	Fine material < 500 µm		Circulating load	Specific production of Fein material
		[Δ]	[Σ]	[g]	[g]	[Δ]	[Σ]	[%]	[g/U]
6382 (B1) **Rod mill**	1	100	100	500.0	116.3	381.0	381.0	30.3	3.81
	2	65	165	500.0	221.8	277.2	658.2	79.7	4.26
	3	48	213	421.4	211.0	209.3	935.4	100.3	4.36
6365 (B2) **Rod mill**	1	100	100	769.0	304.7	461.4	461.4	66.0	4.61
	2	75	175	769.0	401.6	366.2	827.6	109.0	4.90
	3	79	254	769.0	388.6	379.3	1206.9	102.9	4.82
	4	80	334	769.0	389.0	376.9	1583.8	102.0	4.75
6354 (D3) **Rod mill**	1	258	258	797.0	339.9	445.2	455.2	74.4	1.73
	2	225	483	797.1	355.6	445.5	890.7	80.6	1.98
	3	203	686	797.4	399.1	394.8	1285.5	99.3	1.94
	4	201	887	797.0	394.3	401.1	2075.1	97.9	2.00
	5	199	1086	797.0	432.1	364.9	2440.0	118.4	1.83

Sample	Charge	Number of revolutions		Feed	Coarse material >100 µm	Fine material < 100µm		Circulating load	Specific production of Fein material
		[Δ]	[Σ]	[g]	[g]	[Δ]	[Σ]	[%]	[g/U]
6382 (B1) **Ball mill**	1	495	495	1214.0	939.1	273.6	273.6	342	0.56
	2	615	1110	1214.0	882.0	372.0	600.6	266	0.54
	3	643	1753	1214.0	877.9	334.6	935.2	261	0.52
	4	664	2417	1207.0	861.5	341.1	1276.3	249	0.52
6365 (B2) **Ball mill**	1	163	163	1163.0	867.1	283.6	283.6	305	1.74
	2	191	354	1163.0	928.1	231.0	514.6	402	1.22
	3	367	721	1163.0	854.2	297.6	812.2	287	0.81
	4	410	1131	1163.0	843.1	315.8	1128	264	0.78
6354 (D3) **Ball mill**	1	300	300	1114.0	794.9	319.1	319.1	71.4	1.06
	2	330	630	1114.0	806.2	307.8	626.9	253	0.93
	3	340	970	1114.0	809.4	304.6	931.5	263	0.90
	4	350	1320	1114.0	814.7	299.3	1230.8	267	0.86

Appendix 5. The flow sheets with mass balance of comminution tests carried out according the optimized comminution system (OCS) at the laboratory of the Institute of Mineral Processing. (A) Sample 6382, ore type B1; (B) 6365, ore type B2; (C) 6354, ore type D3.

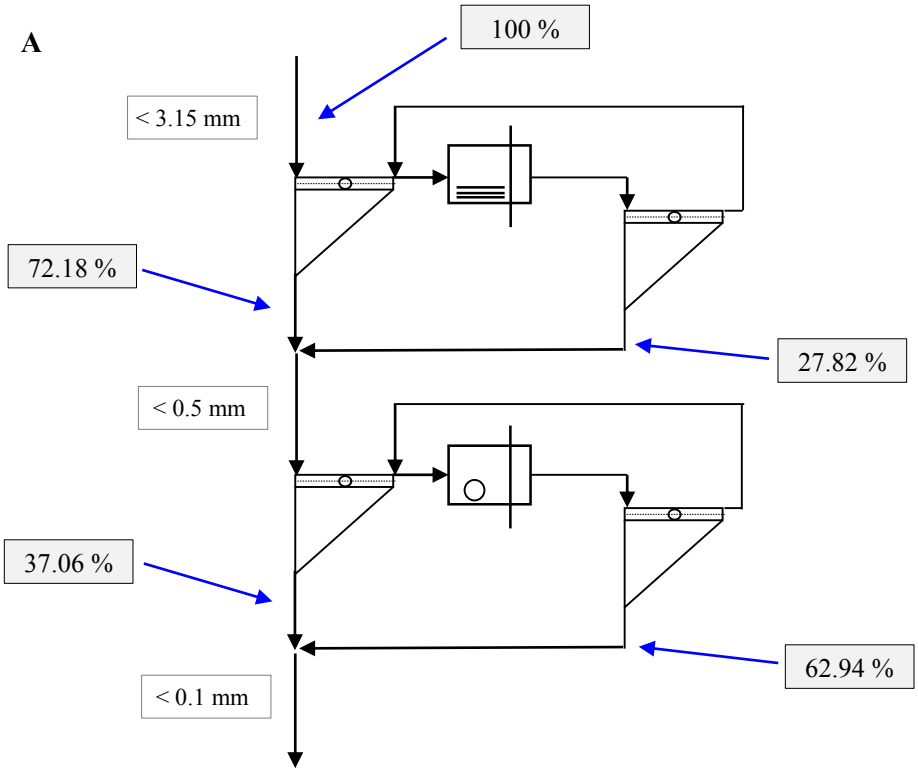

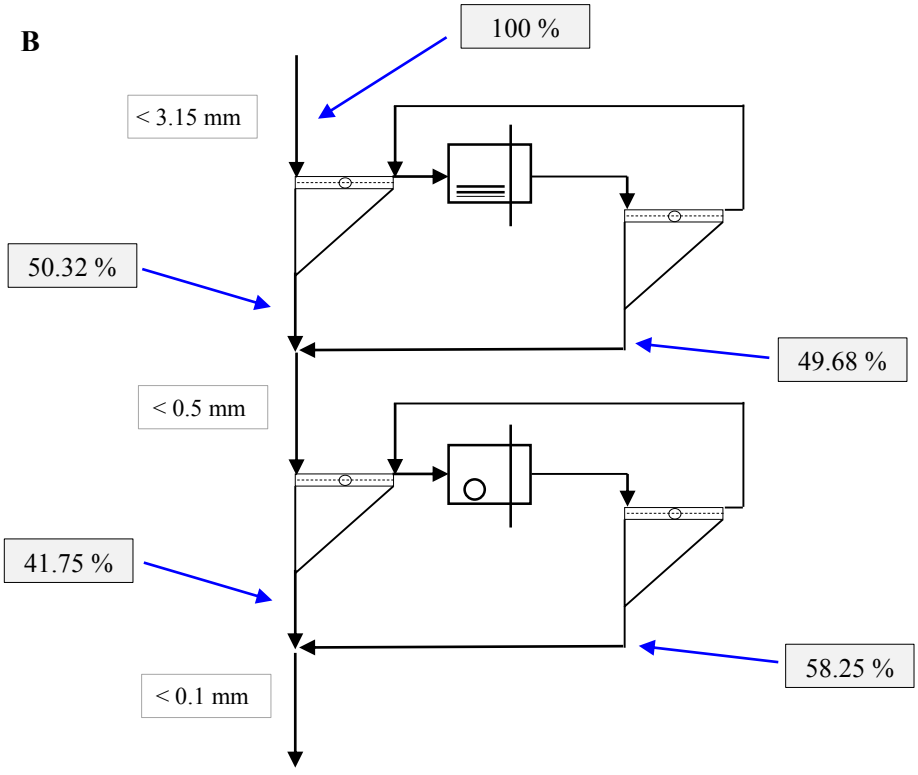

C

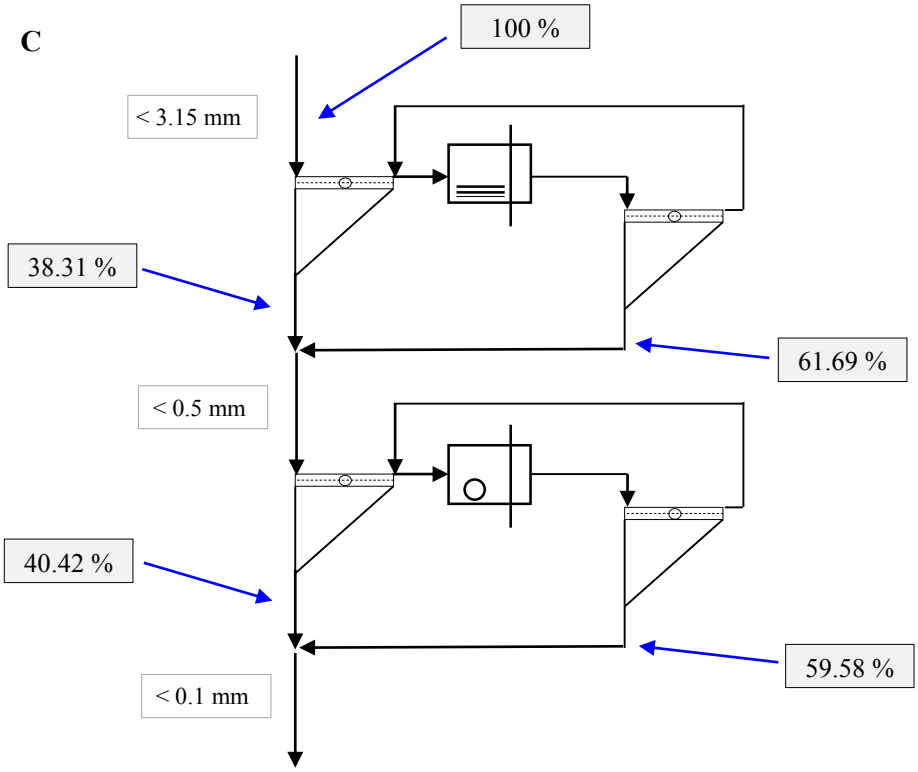

Appendix 6. The calibration of the ball mill before and after comminution sequence **(A)** for sample 6382 (B1), **(B)** for sample 6365 (B2), and **(C)** for sample 6354 (D3) the comminution tests carried out according the "OCS" with the laboratory ball mill at the laboratory of the Institute of Mineral Processing.

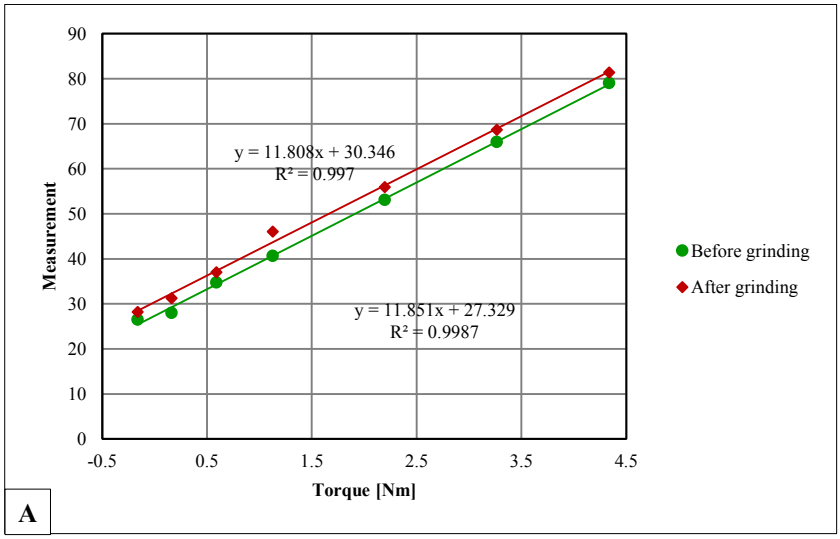

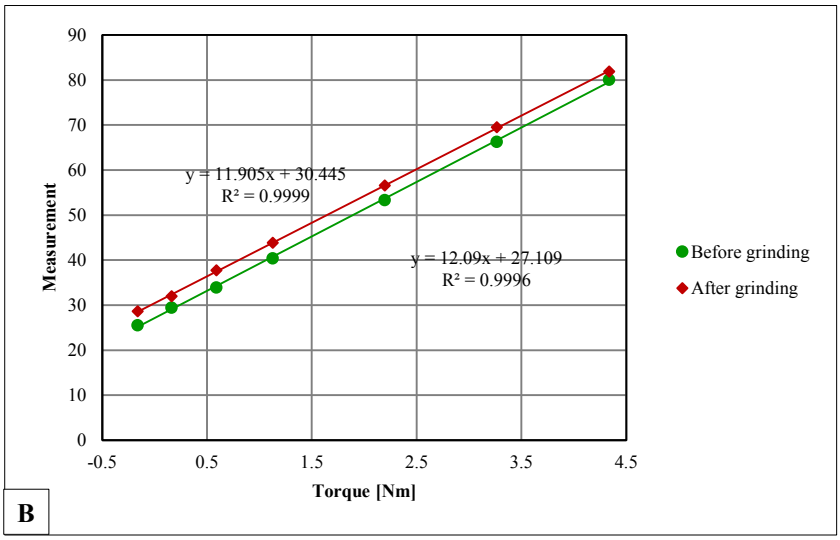

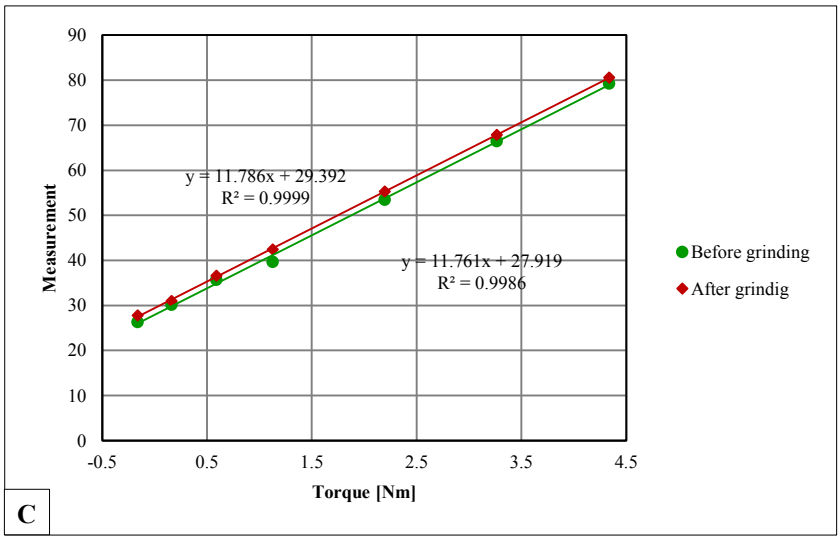

Appendix 7. The set up for the open comminution sequence with a laboratory rod mill and ball mill (without pre-screening) used for comminution tests to characterize the high-SiO_2 ore type at the laboratory of the Institute of Mineral Processing, Montanuniversitaet Leoben.

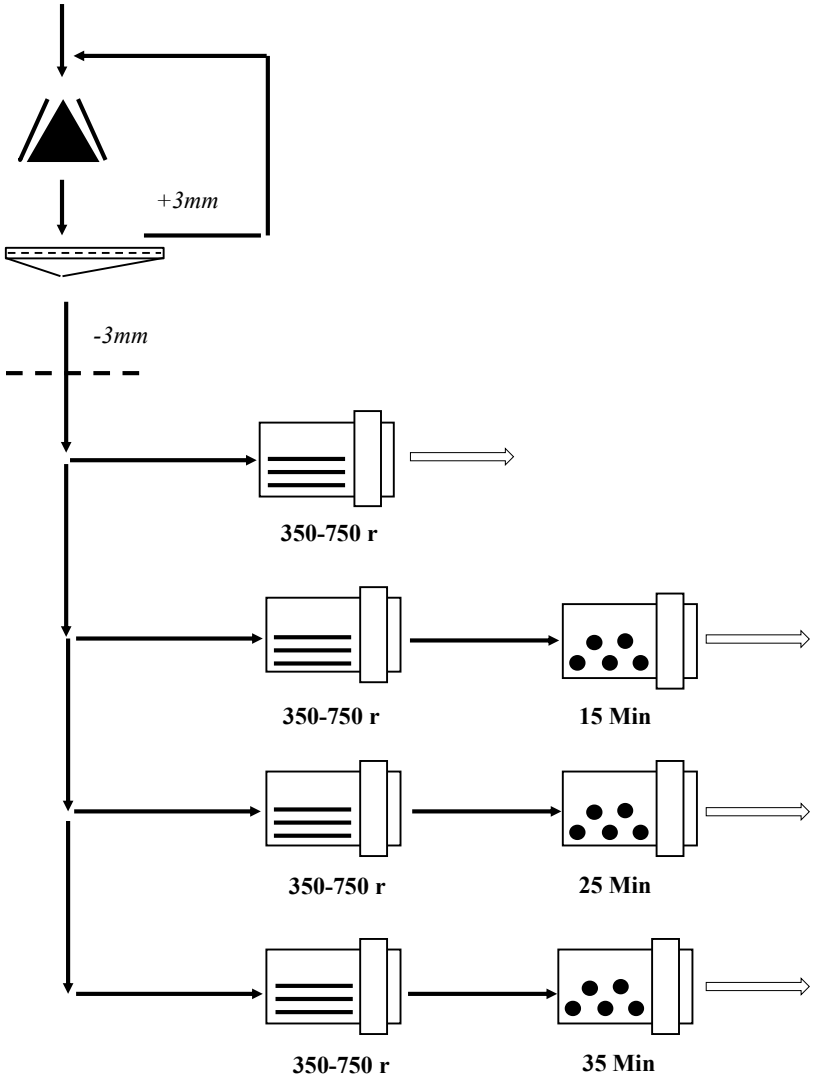

Appendix 8. Calibration data for the laboratory ball mill used for the comminution tests in an open comminution circuit with several comminution times (15, 25 and 35 minutes) at the laboratory at the Institute of Mineral Processing. The technical data for the mill is displayed in Table 2.

	Comm. stage	**Time** [min]	**U** (revol.)	**Feed** [g]	**Bulk solids [gcm^{-3}]**	**Idle moment** [Nm]	**Gross torque moment** [Nm]	**Net torques moment** [Nm]	**Net torques moment (mean)** [Nm]
6252	1	15	957	1416.6	2.995	0.184	3.915	3.732	3.693
	2	25	1596	1416.5		0.184	3.874	3.691	
	3	35	2232	1416.1		0.184	3.842	3.658	
6351	1	15	957	1395.5	2.950	0.204	3.739	3.535	3.475
	2	25	1596	1395.2		0.163	3.619	3.457	
	3	35	2232	1395.0		0.163	3.596	3.434	
6363	1	15	957	1456.7	3.080	0.178	3.721	3.543	3.509
	2	25	1596	1456.6		0.178	3.680	3.501	
	3	35	2232	1456.7		0.178	3.661	3.482	
6367	1	15	957	1490.0	3.150	0.188	3.915	3.728	3.689
	2	25	1596	1489.9		0.188	3.874	3.687	
	3	35	2232	1490.1		0.188	3.842	3.654	
6370	1	15	957	1338.6	2.830	0.154	3.687	3.533	3.526
	2	25	1596	1338.6		0.154	3.683	3.529	
	3	35	2232	1338.5		0.154	3.670	3.515	
6387	1	15	957	1504.0	3.180	0.295	3.954	3.659	3.610
	2	25	1596	1504.1		0.200	3.803	3.603	
	3	35	2232	1504.5		0.200	3.767	3.567	

Appendix 9.The comminution set up (a jaw crusher, a cone crusher with screening, a laboratory tumbling mill with steel rods and steel balls as grinding media) used for the comminution tests at LKAB's mineral processing laboratory in Malmberget in relation to the "Silica in the Mine" project (Drugge 2009).

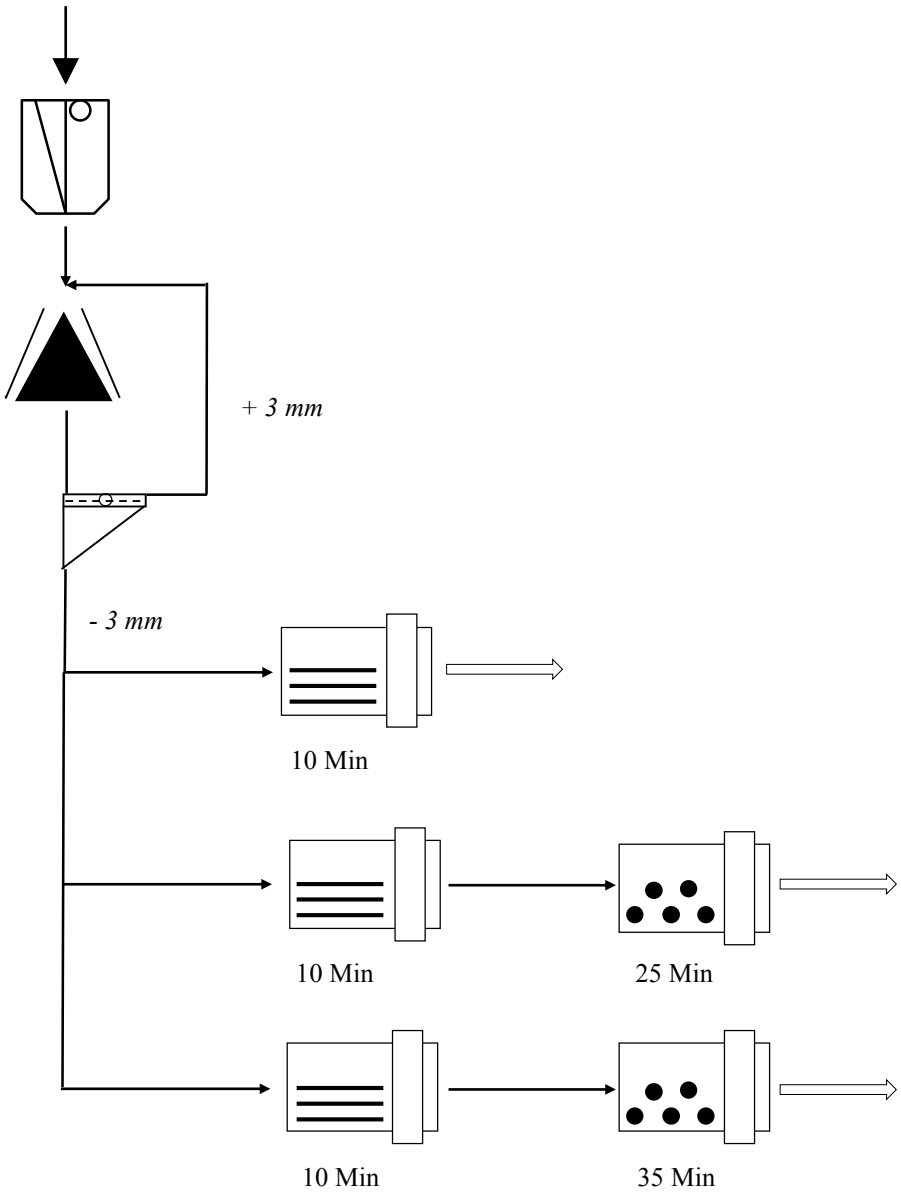

Appendix 10. Data for the Davis magnetic tube tests related to the comparative mineral processing test carried out at the laboratory of the Institute of Mineral Processing. Further, the data is used for the construction of the Henry-Reinhardt charts.

6382 (B1)		**100/40 µm** [g]	**Ferquency** [s^{-1}]	wt. %	**< 0.04 µm** [g]	**Ferquency** [s^{-1}]	wt. %
Amperage / Feed		60.41			60.13		
0.12 A	Magnetics	2.17	1.43	3.64	1.69	1.29	2.84
0.18 A	Magnetics	30.58	1.39	51.24	33.18	1.34	55.82
0.225 A	Magnetics	26.04	1.45	43.63	21.08	1.48	35.46
1.78 A	Magnetics	0.05	1.50	0.08	0.35	1.46	0.59
1.78 A	Waste	0.84	--	1.41	3.14	--	5.28
	Σ	59.68			59.44		
	Loss [%]	1.21			1.15		

6365 (B2)		**100/40 µm** [g]	**Ferquency** [s^{-1}]	wt. %	**< 0.04 µm** [g]	**Ferquency** [s^{-1}]	wt. %
Amperage / Feed		54.10			54.74		
0.12 A	Magnetics	2.20	1.35	4.11	1.55	1.28	2.88
0.18 A	Magnetics	39.18	1.43	73.11	39.2	1.37	72.86
0.225 A	Magnetics	8.48	1.47	15.82	3.81	1.45	7.08
1.78 A	Magnetics	0.06	1.30	0.11	0.22	1.47	0.41
1.78 A	Waste	3.67		6.85	9.02		16.77
	Σ	53.59			53.8		
	Loss [%]	0.94			1.72		

6354 (D)		**100/40 µm** [g]	**Ferquency** [s^{-1}]	wt. %	**< 0.04 µm** [g]	**Ferquency** [s^{-1}]	wt. %
Amperage/ Feed		30.45			30.61		
0.12 A	Magnetics	2.72	1.40	8.76	0.82	1.39	2.76
0.18 A	Magnetics	21.59	1.49	69.51	18.92	1.45	63.68
0.225 A	Magnetics	2.64	1.36	8.50	4.51	1.49	15.18
1.78 A	Magnetics	1.78	1.45	5.73	0.26	1.51	0.88
	Waste	2.33		7.50	5.20		17.50
	Σ	31.06		100.00	29.71		100.00
	Loss [%]	-2.00			2.94		

Appendix 11. The output data for the Davis magnetic tube tests related to the mineral processing tests for characterization of the high-SiO_2 ore type carried out at the laboratory of the Institute of Mineral Processing, Montanuniversitaet Leoben (0.1, 0.2, 1.8 = concentrate, magnetics; >1.8 = waste).

6252 80/63 µm			
I_E	**Mass**	**Mass**	**SiO_2**
A	g	%	%
0.1	0.969	2.55	0.91
0.2	18.5416	48.89	0.74
1.8	16.8887	44.53	0.70
>1.8	1.5268	4.03	24.39
	37.9261	100.00	1.68

6252 63/40 µm		
Mass	**Mass**	**SiO_2**
g	%	%
0.5751	1.07	0.57
16.6309	30.92	0.52
24.5754	45.69	0.42
12.0114	22.33	20.62
53.7928	100.01	4.96

6252 <40 µm		
Mass	**Mass**	**SiO_2**
g	%	%
0.6846	1.65	0.57
18.5288	44.79	0.34
17.1319	41.41	0.26
5.0219	12.14	27.81
41.3672	99.99	3.65

6351 80/63 µm			
I_E	**Mass**	**Mass**	**SiO_2**
A	g	%	%
0.1	1.7845	4.28	0.73
0.2	21.1247	50.64	0.62
1.8	16.8509	40.40	0.59
>1.8	1.9514	4.68	55.62
	41.7115	100.00	3.19

6351 63/40 µm		
Mass	**Mass**	**SiO_2**
g	%	%
0.664	1.66	0.70
20.3359	50.91	0.55
16.5705	41.48	0.49
2.3742	5.94	56.48
39.9446	99.99	3.86

6351 <40 µm		
Mass	**Mass**	**SiO_2**
g	%	%
0.8053	2.06	0.61
23.1034	59.22	0.45
7.8655	20.16	0.40
7.2418	18.56	38.94
39.016	100.00	7.59

6370 80/63 µm			
I_E	**Mass**	**Mass**	**SiO_2**
A	g	%	%
0,1	1.6601	4.11	0.65
0,2	18.352	45.42	0.66
1,8	14.819	36.67	0.65
>1,8	5.5779	13.80	31.66
	40.409	100.00	4.94

6370 63/40 µm		
Mass	**Mass**	**SiO_2**
g	%	%
0.8906	2.14	0.48
19.3825	46.67	0.48
14.6623	35.30	0.46
6.5998	15.89	28.67
41.5352	100.00	4.95

6370 <40 µm		
Mass	**Mass**	**SiO_2**
g	%	%
0.663	1.57	0.34
18.1429	43.10	0.35
10.9942	26.12	0.21
12.2989	29.21	18.57
42.099	100.00	5.64

6370 80/63 µm			
I_E	**Mass**	**Mass**	**SiO_2**
A	g	%	%
0,1	1.6601	4.11	0.65
0,2	18.352	45.42	0.66
1,8	14.819	36.67	0.65
>1,8	5.5779	13.80	31.66
	40.409	100.00	4.94

6370 63/40 µm		
Mass	**Mass**	**SiO_2**
g	%	%
0.8906	2.14	0.48
19.3825	46.67	0.48
14.6623	35.30	0.46
6.5998	15.89	28.67
41.5352	100.00	4.95

6370 <40 µm		
Mass	**Mass**	**SiO_2**
g	%	%
0.663	1.57	0.34
18.1429	43.10	0.35
10.9942	26.12	0.21
12.2989	29.21	18.57
42.099	100.00	5.64

Appendix 12. Results of the chemical analysis of the magnetic and non-magnetic fractions after Davis magnetic tube tests related to the comparative mineral processing tests carried out at laboratory of the Institute of the Mineral Processing. Used methods XRF (Labtium method *179X*) and IPC-OES (Labtium method *720p*).

Sample	Laboratory Sample ID	Fraction [mm]	Description	Fe [%]	P [%]	SiO_2 [%]	Al_2O_3 [%]	CaO [%]	MgO [%]	MnO [%]	TiO_2 [%]	V_2O_5 [%]	K_2O [%]	Na_2O [%]	S [%]
6382	L10069022	0.1/0.04	Davis Tube 0.12 A (magnetics)	57.70	<0.050	0.87	0.15	<0.014	0.13	0.07	0.40	0.22	<0.06	–	<0.02
(B1)	L10069023	0.1/0.04	Davis Tube 0.18 A (magnetics)	69.18	0.0130	0.30	0.06	0.13	0.14	0.08	0.36	0.05	0.02	<0.027	0.01
	L10069024	0.1/0.04	Davis Tube 0.225 A (magnetics)	69.25	0.0120	0.27	0.05	0.10	0.11	0.07	0.35	0.05	0.02	<0.027	0.01
	---	0.1/0.04	Davis Tube 1.78 A (magnetics)	*Too less material*											
	L10069025	0.1/0.04	Davis Tube 1.78 A non-magnetics	4.26	0.171	29.31	4.01	29.24	8.41	0.88	2.77	0.03	0.33	–	0.39
	L10069026	<0.04	Davis Tube 0.12 A (magnetics)	58.00	<0.050	0.53	0.17	0.05	0.11	0.07	0.35	0.21	<0.06		0.04
	L10069027	<0.04	Davis Tube 0.18 A (magnetics)	69.32	0.007	0.26	0.05	0.10	0.12	0.07	0.31	0.05	0.01	<0.027	0.01
	L10069028	<0.04	Davis Tube 0.225 A (magnetics)	69.11	0.010	0.34	0.06	0.19	0.15	0.08	0.36	0.05	0.01	<0.027	0.01
	L10069029	<0.04	Davis Tube 1.78 A (magnetics)	51.20	0.069	0.88	0.07*	6.47*	0.29	0.14	0.89	0.19	0.08*	–	0.02
	L10069030	<0.04	Davis Tube 1.78 A (non-magnetics)	6.69	0.226	26.31	4.06	22.66	10.26	1.51	9.11	0.05	0.68	–	0.38
6365	L10069068	0.1/0.04	Davis Tube 0.12 A (magnetics)	57.50	<0.050	1.11	0.23	0.26	0.23	0.06	0.27	0.22	<0.06	–	0.0675
(B2)	L10069069	0.1/0.04	Davis Tube 0.18 A (magnetics)	68.41	0.010	0.88	0.12	0.51	0.30	0.06	0.23	0.05	0.04	<0.027	0.0104
	L10069070	0.1/0.04	Davis Tube 0.225 A (magnetics)	67.71	0.010	1.27	0.16	0.81	0.48	0.07	0.26	0.05	0.05	<0.027	0.0477
	---	0.1/0.04	Davis Tube 1.78 A (magnetics)	*Too less material*											
	L10069071	0.1/0.04	Davis Tube 1.78 A (non-magnetics)	4.82	0.050	37.87	2.31	27.00	10.41	0.52	0.59	0.02	–	–	0.686
	L10069072	<0.04	Davis Tube 0.12 A (magnetics)	57.60	<0.050	0.93	0.20	0.11	0.18	0.06	0.21	0.22	<0.06	–	0.0217
	L10069073	<0.04	Davis Tube 0.18 A (magnetics)	69.04	<0.014	0.51	0.09	0.33	0.17	0.06	0.19	0.05	0.03	<0.027	0.0118
	L10069074	<0.04	Davis Tube 0.225 A (magnetics)	58.80	<0.050	1.07	0.17	0.26	0.19	0.07	0.29	0.22	<0.06	–	<0.02
	L10069075	<0.04	Davis Tube 1.78 A (magnetics)	47.70	<0.050	2.93	0.23*	8.92*	0.64	0.14	0.88	0.19	0.33*	–	0.0415
	L10069076	<0.04	Davis Tube 1.78 A (non-magnetics)	4.76	0.070	26.70	2.93	30.40	10.20	0.64	2.66	0.01	1.12	0.214	0.441

*=Calculated values by Labtium Oy because of the contamination in distilled water during the analysis.

Ore type	Laboratory Sample ID	Fraction [mm]	Description	Fe [%]	P [%]	SiO_2 [%]	Al_2O_3 [%]	CaO [%]	MgO [%]	MnO [%]	TiO_2 [%]	V_2O_5 [%]	K_2O [%]	Na_2O [%]	S [%]
6354	L10069045	0.1/0.04	Davis Tube 0.12 A (magnetics)	56.70	0.050	1.73	0.17	1.76	0.54	0.13	0.17	0.23	<0.06		<0.02
(D3)	L10069046	0.1/0.04	Davis Tube 0.18 A (magnetics)	65.47	0.660	1.47	0.11	2.03	0.82	0.13	0.15	0.05	0.03	<0.027	0.01
	L10069047	0.1/0.04	Davis Tube 0.225 A (magnetics)	53.70	<0.050	3.06	0.18	3.20	0.93	0.14	0.17	0.21	<0.06	–	<0.02
	L10069048	0.1/0.04	Davis Tube 1.78 A (magnetics)	8.54	2.600	28.67	0.93*	25.86*	11.46	0.29	0.26	0.04	0.29*	–	0.04
	L10069049	0.1/0.04	Davis Tube 1.78 A (non-magnetics)	3.13	3.130	11.08	1.46	33.02	10.23	0.34	0.19	0.02	<0.06	–	0.12
	L10069050	<0.04	Davis Tube 0.12 A (magnetics)	58.00	<0.050	1.01	0.15	0.88	0.25	0.12	0.12	0.23	<0.06	–	<0.02
	L10069077	<0.04	Davis Tube 0.18 A (magnetics)	68.27	0.220	0.54	0.05	0.68	0.30	0.12	0.11	0.05	0.02	<0.027	0.01
	L10069051	<0.04	Davis Tube 0.225 A (magnetics)	57.60	<0.050	1.28	0.21	0.84	0.31	0.12	0.14	0.23	<0.06	–	<0.02
	L10069052	<0.04	Davis Tube 1.78 A (magnetics)	48.20	<0.050	7.87	0.23*	14.44*	2.54	0.16	0.24	0.16	0.52*	–	0.03
	L10069053	<0.04	Davis Tube 1.78A (non-magnetics)	2.60	1.550	11.53	1.36	32.04	10.40	0.31	0.54	0.02	<0.06	–	0.10

*=Calculated values by Labtium Oy because of the contamination in distilled water during the analysis.

Appendix 13. Chemical assays on 11 elements for the feed and after comminution for 10 minutes in the laboratory rod mill and 35 minutes in the laboratory ball mill related to the characterization of ore type B2 at the laboratory of the Institute of Mineral Processing, Montanuniversitaet Leoben. Assays were carried out by XRF at LKABs chemical laboratory, Kiruna.

Sample Nr	Methode	Sieve fraction	Fe %	P %	SiO2 %	K_2O %	Al_2O_3 %	CaO %	MgO %	MnO %	1TiO2 %	V_2O_5 %	Na_2O %
6252.01	As received	> 1.0 mm	66.14	0.344	2.99	0.035	0.28	2.00	1.46	0.10	0.74	0.212	<0.070
6252.02	As received	1.0/0.5 mm	66.37	0.317	2.88	0.033	0.26	1.93	1.41	0.10	0.74	0.217	<0.070
6252.03	As received	0.5/0.315 mm	65.06	0.339	3.40	0.037	0.31	2.24	1.68	0.10	0.75	0.211	<0.070
6252.04	As received	0.315/0.1 mm	64.40	0.38	3.74	0.041	0.33	2.51	1.83	0.10	0.78	0.212	<0.070
6252.05	As received	0.1/0.04 mm	64.74	0.585	3.07	0.042	0.29	2.85	1.47	0.09	0.58	0.208	<0.070
6252.06	As received	< 0.04 mm	61.92	0.629	4.92	0.056	0.43	3.50	2.41	0.10	0.81	0.207	<0.070
6252.22	Ball mill. 35 min	>80 µm	67.50	0.183	2.52	0.048	0.33	1.18	1.34	0.10	0.58	0.218	<0.070
6252.23	Ball mill. 35 min	80/63 µm	68.65	0.238	1.60	0.018	0.14	1.26	0.75	0.10	0.52	0.223	<0.070
6252.24	Ball mill. 35 min	63/40 µm	68.12	0.325	1.75	0.022	0.15	1.60	0.81	0.09	0.49	0.224	<0.070
6252.25	Ball mill. 35 min	<40 µm	63.33	0.464	4.24	0.046	0.39	2.93	2.06	0.10	0.86	0.208	<0.070
6351.01	As received	> 1.0 mm	61.26	0.026	8.09	0.285	1.31	1.77	2.34	0.13	1.17	0.19	<0.070
6351.02	As received	1.0/0.5 mm	62.54	0.019	6.95	0.179	0.94	2.18	1.87	0.14	1.10	0.189	<0.070
6351.03	As received	0.5/0.315 mm	62.51	0.021	6.83	0.172	0.94	2.26	1.95	0.14	1.11	0.189	<0.070
6351.04	As received	0.315/0.1 mm	65.75	0.02	4.33	0.132	0.67	1.39	1.41	0.11	0.84	0.205	<0.070
6351.05	As received	0.1/0.04 mm	61.37	0.052	6.92	0.224	1.00	2.40	2.67	0.15	1.54	0.185	<0.070
6351.06	As received	< 0.04 mm	67.17	0.025	3.40	0.144	0.56	0.97	1.14	0.09	0.62	0.203	<0.070
6351.22	Ball mill. 35 min	>80 µm	67.25	0.013	3.71	0.187	0.73	0.52	1.11	0.09	0.50	0.198	<0.070
6351.23	Ball mill. 35 min	80/63 µm	68.17	0.013	3.27	0.102	0.39	0.58	0.66	0.08	0.48	0.206	<0.070
6351.24	Ball mill. 35 min	63/40 µm	67.58	0.016	3.81	0.105	0.42	0.74	0.69	0.08	0.54	0.207	<0.070
6351.25	Ball mill. 35 min	<40 µm	60.59	0.033	7.93	0.198	1.11	2.71	2.47	0.16	1.42	0.191	<0.070
6363.01	As received	> 1.0 mm	64.44	0.012	5.97	0.281	0.58	1.39	1.64	0.11	0.76	0.193	<0.070
6363.02	As received	1.0/0.5 mm	62.94	0.020	7.30	0.306	0.73	1.66	1.94	0.11	0.76	0.185	<0.070
6363.03	As received	0.5/0.315 mm	64.13	0.018	6.21	0.280	0.66	1.45	1.72	0.12	0.72	0.189	<0.070
6363.04	As received	0.315/0.1 mm	67.12	0.016	3.68	0.221	0.44	0.90	1.12	0.11	0.55	0.204	<0.070
6363.05	As received	0.1/0.04 mm	67.67	0.014	3.22	0.226	0.42	0.79	1.03	0.10	0.48	0.204	<0.070
6363.06	As received	< 0.04 mm	62.57	0.020	6.69	0.452	0.87	1.85	1.90	0.14	1.40	0.194	<0.070
6363.22	Ball mill. 35 min	>80 µm	68.27	0.014	2.97	0.186	0.36	0.55	0.94	0.10	0.32	0.204	<0.070
6363.23	Ball mill. 35 min	80/63 µm	68.91	0.013	2.56	0.117	0.25	0.53	0.70	0.09	0.30	0.202	<0.070
6363.24	Ball mill. 35 min	63/40 µm	67.97	0.014	3.34	0.148	0.32	0.71	0.90	0.09	0.35	0.196	<0.070
6363.25	Ball mill. 35 min	<40 µm	60.95	0.023	8.32	0.457	0.94	2.17	2.33	0.14	1.19	0.187	<0.070

Sample Nr	Methode	Sieve fractions	Fe %	P %	SiO_2 %	K_2O %	Al_2O_3 %	CaO %	MgO %	MnO %	TiO_2 %	V_2O_5 %	Na_2O %
6367.01	As received	> 1.0 mm	68.54	0.017	1.79	0.136	0.33	0.88	0.82	0.15	0.95	0.210	<0.070
6367.02	As received	1.0/0.5 mm	67.38	0.014	2.44	0.171	0.47	1.38	1.08	0.16	0.95	0.205	<0.070
6367.03	As received	0.5/0.315 mm	66.95	0.017	2.72	0.194	0.53	1.50	1.24	0.16	0.91	0.202	<0.070
6367.04	As received	0.315/0.1 mm	67.87	0.018	2.16	0.177	0.41	1.23	1.05	0.15	0.80	0.209	<0.070
6367.05	As received	0.1/0.04 mm	67.83	0.016	2.26	0.185	0.39	1.19	1.11	0.15	0.75	0.210	<0.070
6367.06	As received	< 0.04 mm	64.60	0.028	3.71	0.284	0.62	1.86	1.67	0.26	1.52	0.206	<0.070
6367.22	Ball mill. 35 min	>80 µm	69.41	0.013	1.32	0.131	0.38	0.39	0.64	0.10	0.61	0.211	<0.070
6367.23	Ball mill. 35 min	80/63 µm	69.91	0.012	1.10	0.080	0.24	0.57	0.46	0.11	0.60	0.212	<0.070
6367.24	Ball mill. 35 min	63/40 µm	69.02	0.011	1.55	0.105	0.32	0.83	0.65	0.12	0.66	0.210	<0.070
6367.25	Ball mill. 35 min	<40 µm	64.10	0.019	4.00	0.262	0.69	2.26	1.78	0.26	1.47	0.200	<0.070
6370.01	As received	> 1.0 mm	59.95	0.584	6.01	0.475	1.16	6.44	0.96	0.21	0.41	0.159	<0.070
6370.02	As received	1.0/0.5 mm	61.01	0.56	5.11	0.376	0.96	6.42	0.82	0.20	0.37	0.15	<0.070
6370.03	As received	0.5/0.315 mm	60.25	0.523	5.25	0.371	0.99	7.32	0.87	0.23	0.36	0.154	<0.070
6370.04	As received	0.315/0.1 mm	60.30	0.666	4.92	0.414	0.98	7.20	0.94	0.21	0.33	0.158	<0.070
6370.05	As received	0.1/0.04 mm	60.52	1.009	4.43	0.416	0.88	6.80	0.91	0.18	0.30	0.162	<0.070
6370.06	As received	< 0.04 mm	57.82	1.072	4.97	0.462	1.06	9.18	1.08	0.26	0.50	0.141	<0.070
6370.22	Ball mill. 35 min	>80 µm	64.21	0.332	4.91	0.430	0.98	2.80	0.85	0.11	0.27	0.176	<0.070
6370.23	Ball mill. 35 min	80/63 µm	63.57	0.506	4.96	0.325	0.75	3.81	0.62	0.12	0.25	0.167	<0.070
6370.24	Ball mill. 35 min	63/40 µm	62.74	0.635	5.09	0.305	0.75	4.54	0.60	0.13	0.28	0.168	<0.070
6370.25	Ball mill. 35 min	<40 µm	55.64	0.896	6.45	0.517	1.36	10.55	1.21	0.32	0.51	0.142	<0.070
6387.01	As received	> 1.0 mm	66.45	0.005	3.64	0.06	0.32	1.22	1.63	0.13	0.97	0.208	<0.070
6387.02	As received	1.0/0.5 mm	65.76	0.007	4.13	0.065	0.34	1.39	1.87	0.14	0.97	0.207	<0.070
6387.03	As received	0.5/0.315 mm	65.74	0.006	4.16	0.068	0.35	1.38	1.88	0.14	0.97	0.205	<0.070
6387.04	As received	0.315/0.1 mm	65.36	0.008	4.44	0.08	0.39	1.51	1.99	0.13	0.93	0.204	<0.070
6387.05	As received	0.1/0.04 mm	66.41	0.008	3.75	0.083	0.35	1.30	1.69	0.12	0.72	0.207	<0.070
6387.06	As received	< 0.04 mm	66.11	0.012	3.80	0.097	0.40	1.39	1.74	0.13	0.87	0.207	<0.070
6387.22	Ball mill. 35 min	>80 µm	66.31	0.006	4.08	0.097	0.36	1.01	1.81	0.12	0.68	0.206	<0.070
6387.23	Ball mill. 35 min	80/63 µm	67.46	0.005	3.23	0.048	0.23	0.93	1.37	0.12	0.63	0.209	<0.070
6387.24	Ball mill. 35 min	63/40 µm	68.13	0.005	2.71	0.045	0.20	0.84	1.17	0.11	0.58	0.210	<0.070
6387.25	Ball mill. 35 min	<40 µm	64.41	0.008	4.92	0.084	0.46	1.75	2.25	0.15	1.16	0.204	<0.070

Appendix 14. Chemical assays on 11 essential elements after DT tests for characterization of ore type B2 carried out by ICP-OES at the chemical laboratory Labtium Oy in Rovaniemi, Finland) after the Davis magnetic tube test (MP= magnetic product; W = waste, non-magnetics) at the laboratory of the Institute of Mineral Processing in Leoben.

Sample Nr	Mass (g)	Description	Fe %	P %	Al_2O_3 %	SiO_2 %	CaO %	MgO %	MnO %	TiO_2 %	V_2O_5 %	K_2O %	Na_2O %	S %	P_2O_5 %
6252-1	0.969	35 min; 80/63 µm; 0.1 A; MP	69.60	0.08	0.02	0.91	0.55	0.31	0.10	0.52	0.23	<0.05	x	0.03	0.18
6252-2	18.542	35 min; 80/63 µm; 0.2 A; MP	69.10	0.08	<0.01	0.74	0.53	0.31	0.10	0.51	0.23	<0.05	x	0.03	0.17
6252-3	16.889	35 min; 80/63 µm; 1.8 A; MP	70.10	0.09	<0.01	0.70	0.60	0.30	0.10	0.52	0.24	<0.05	x	0.02	0.19
6252-4	1.527	35 min; 80/63 µm; 1.8 A; W	9.19	2.66	1.95	24.39	26.44	11.66	0.15	1.43	0.06	0.25	x	0.08	5.81
6252-5	0.575	35 min; 63/40 µm; 0.1 A; MP	69.10	0.08	<0.01	0.57	0.45	0.21	0.09	0.43	0.23	<0.05	x	<0.02	0.17
6252-6	16.631	35 min; 63/40 µm; 0.2 A; MP	69.10	0.09	<0.01	0.52	0.63	0.22	0.09	0.44	0.23	<0.05	x	<0.02	0.19
6252-7	24.575	35 min; 63/40 µm; 1.8 A; MP	70.60	0.08	<0.01	0.42	0.46	0.15	0.09	0.43	0.24	<0.05	x	0.05	0.17
6252-8	12.011	35 min; 63/40 µm; 1.8 A; W	6.42	2.28	1.56	20.62	30.64	1036	0.15	1.82	0.05	0.21	x	0.05	4.98
6252-9	0.685	35 min; < 40 µm; 0.1 A; MP	68.40	<0.05	<0.01	0.57	0.67	0.24	0.09	0.32	0.23	<0.05	x	0.03	<0.05
6252-10	18.529	35 min; < 40 µm; 0.2 A; MP	72.90	<0.05	<0.01	0.34	0.29	0.14	0.09	0.36	0.24	<0.05	x	0.03	<0.05
6252-11	17.132	35 min; < 40 µm; 1.8 A; MP	70.40	<0.05	<0.01	0.26	0.31	0.12	0.09	0.35	0.23	<0.05	x	<0.02	<0.05
6252-12	5.022	35 min; < 40 µm; 1.8 A; W	4.08	0.69	2.38	27.81	23.22	13.68	0.19	3.99	0.06	0.23	x	0.15	1.51
6351-1	1.785	35 min; 80/63 µm; 0.1 A; MP	72.90	<0.05	<0.01	0.73	0.22	0.18	0.06	0.42	0.23	<0.05	x	<0.02	<0.05
6351-2	21.125	35 min; 80/63 µm; 0.2 A; MP	70.90	<0.05	<0.01	0.62	0.19	0.13	0.06	0.40	0.22	<0.05	x	<0.02	<0.05
6351-3	16.851	35 min; 80/63 µm; 1.8 A; MP	72.60	<0.05	<0.01	0.59	0.18	0.10	0.06	0.41	0.22	<0.05	x	0.02	<0.05
6351-4	1.951	35 min; 80/63 µm; 1.8 A; W	5.35	0.13	5.86	55.62	8.45	8.21	0.34	2.25	0.03	1.41	x	0.05	0.29
6351-5	0.664	35 min; 63/40 µm; 0.1 A; MP	72.40	<0.05	0.03	0.70	0.23	0.14	0.06	0.40	0.22	<0.05	x	0.04	<0.05
6351-6	20.336	35 min; 63/40 µm; 0.2 A; MP	70.70	<0.05	<0.01	0.55	0.19	0.13	0.06	0.38	0.22	<0.05	x	<0.02	<0.05
6351-7	16.571	35 min; 63/40 µm; 1.8 A; MP	72.70	<0.05	0.04	0.49	0.20	0.09	0.06	0.38	0.22	<0.05	x	0.03	<0.05
6351-8	2.374	35 min; 63/40 µm; 1.8 A; W	5.01	0.16	5.33	56.48	9.81	7.64	0.37	2.95	0.04	1.26	x	0.16	0.35
6351-9	0.805	35 min; < 40 µm; 0.1 A; MP	72.50	<0.05	0.02	0.61	0.25	0.20	0.06	0.34	0.22	<0.05	x	<0.02	<0.05
6351-10	23.103	35 min; < 40 µm; 0.2 A; MP	72.30	<0.05	<0.01	0.45	0.21	0.12	0.06	0.37	0.22	<0.05	x	0.02	<0.05
6351-11	7.866	35 min; < 40 µm; 1.8 A; MP	72.70	<0.05	<0.01	0.40	0.15	0.07	0.06	0.35	0.22	<0.05	x	0.04	<0.05
6351-12	7.242	35 min; < 40 µm; 1.8 A; W	5.84	0.14	5.39	38.94	13.85	11.61	0.55	5.70	0.06	0.84	x	0.04	0.30

Sample Nr	Mass (g)	Description	Fe %	P %	Al_2O_3 %	SiO_2 %	CaO %	MgO %	MnO %	TiO_2 %	V_2O_5 %	K_2O %	Na_2O %	S %	P_2O_5 %
6370-1	1.660	35 min; 80/63 µm; 0.1 A; MP	69.20	<0.05	0.02	0.65	0.41	0.07	0.06	0.23	0.19	<0.05	x	0.05	<0.05
6370-2	18.352	35 min; 80/63 µm; 0.2 A; MP	72.10	<0.05	0.03	0.66	0.43	0.07	0.06	0.23	0.20	<0.05	x	0.02	<0.05
6370-3	14.819	35 min; 80/63 µm; 1.8 A; MP	72.60	<0.05	<0.01	0.65	0.42	0.05	0.06	0.24	0.20	<0.05	x	0.04	<0.05
6370-4	5.578	35 min; 80/63 µm; 1.8 A; W	3.99	1.14	4.67	31.66	25.88	3.63	0.49	0.35	0.02	1.78	x	1.03	2.49
6370-5	0.891	35 min; 63/40 µm; 0.1 A; MP	72.40	<0.05	<0.01	0.48	0.35	0.09	0.06	0.23	0.20	<0.05	x	0.02	<0.05
6370-6	19.383	35 min; 63/40 µm; 0.2 A; MP	72.00	<0.05	<0.01	0.48	0.32	0.06	0.06	0.23	0.20	<0.05	x	0.04	<0.05
6370-7	14.662	35 min; 63/40 µm; 1.8 A; MP	71.60	0.07	<0.01	0.46	0.47	0.05	0.06	0.23	0.20	<0.05	x	<0.02	0.15
6370-8	6.600	35 min; 63/40 µm; 1.8 A; W	3.65	1.17	4.31	28.67	28.26	3.45	0.52	0.53	0.02	1.48	x	0.74	2.56
6370-9	0.663	35 min; < 40 µm; 0.1 A; MP	72.90	<0.05	<0.01	0.34	0.48	0.08	0.06	0.20	0.20	<0.05	x	<0.02	<0.05
6370-10	18.143	35 min; < 40 µm; 0.2 A; MP	73.80	<0.05	0.02	0.35	0.40	0.06	0.06	0.22	0.21	<0.05	x	<0.02	<0.05
6370-11	10.994	35 min; < 40 µm; 1.8 A; MP	73.90	<0.05	<0.01	0.21	0.19	0.05	0.05	0.21	0.20	<0.05	x	<0.02	<0.05
6370-12	12.299	35 min; < 40 µm; 1.8 A; W	3.61	0.52	4.18	18.57	32.46	3.63	0.84	1.09	0.02	1.28	x	0.48	1.14
6387-1	0.258	35 min; 80/63 µm; 0.1 A; MP	72.00	<0.05	0.05	1.76	0.51	0.64	0.11	0.63	0.23	<0.05	x	<0.02	<0.05
6387-2	19.589	35 min; 80/63 µm; 0.2 A; MP	70.30	<0.05	0.04	1.52	0.44	0.59	0.11	0.61	0.22	<0.05	x	<0.02	<0.05
6387-3	20.289	35 min; 80/63 µm; 1.8 A; MP	71.40	<0.05	0.06	1.65	0.51	0.61	0.11	0.63	0.23	<0.05	x	0.04	<0.05
6387-4	1.467	35 min; 80/63 µm; 1.8 A; W	9.40	<0.05	2.55	41.07	12.40	17.74	0.31	1.37	0.05	0.57	x	0.17	<0.05
6387-5	0.310	35 min; 63/40 µm; 0.1 A; MP	69.50	<0.05	<0.01	0.98	0.32	0.37	0.10	0.52	0.22	<0.05	x	<0.02	<0.05
6387-6	19.238	35 min; 63/40 µm; 0.2 A; MP	72.10	<0.05	0.06	1.02	0.33	0.37	0.10	0.54	0.23	<0.05	x	0.03	<0.05
6387-7	20.136	35 min; 63/40 µm; 1.8 A; MP	72.90	<0.05	0.06	0.93	0.38	0.35	0.10	0.54	0.23	<0.05	x	0.04	<0.05
6387-8	1.561	35 min; 63/40 µm; 1.8 A; W	7.52	<0.05	2.38	42.79	13.26	17.24	0.34	1.85	0.05	0.46	x	0.13	<0.05
6387-9	0.822	35 min; < 40 µm; 0.1 A; MP	72.30	<0.05	0.04	0.55	0.25	0.24	0.10	0.45	0.22	<0.05	x	<0.02	<0.05
6387-10	19.733	35 min; < 40 µm; 0.2 A; MP	70.00	<0.05	0.02	0.50	0.20	0.23	0.10	0.45	0.22	<0.05	x	0.02	<0.05
6387-11	18.862	35 min; < 40 µm; 1.8 A; MP	69.40	<0.05	<0.01	0.43	0.22	0.18	0.10	0.44	0.22	<0.05	x	0.06	<0.05
6387-12	4.140	35 min; < 40 µm; 1.8 A; W	5.96	<0.05	3.42	38.94	14.55	17.08	0.48	6.11	0.08	0.45	x	0.05	<0.05

Appendix 15. Numeric data of the screen analysis after each grinding stage (the laboratory rod mill and the laboratory ball mill) at the laboratory at the Institute of Mineral Processing, Montanuniversitaet Leoben. The mean density for samples is estimated from *Equation*: $\bar{x} \rightarrow \frac{\sum m_i}{\rho} = \sum \frac{m_i}{\rho_i}$

Sample **6382** (B1) - Screen analysis after 3 cycles in the rod mill						
Fraction size	**Sieve fractions**		**Retained**	**Passed**	**Density (ρ)**	**Volume specific mass**
[mm]	Mass [g]	wt [%]	[%]	[%]	[g/cm^2]	[1/ρ]
> 0.5	0	0	0	100.00	-	-
0.5 / 0.315	75.65	36.18	36.18	63.82	5.07	0.1972
0.315 / 0.1	92.38	44.18	80.35	19.65	5.07	0.1973
0.1 / 0.04	30.33	14.50	94.85	5.15	5.31	0.1882
< 0.04	10.76	5.15	100.00	0.00	4.95	0.2019
Σ	209.12	100.00	-	-	$\bar{x}$ = 5.10	$\bar{x}$ = 0.1961

Sample **6365** (B2) - Screen analysis after cycles 3 + 4 in the rod mil						
Fraction size	**Sieve fractions**		**Retained**	**Passed**	**Density (ρ)**	**Volume specific mass**
[mm]	Mass [g]	wt [%]	[%]	[%]	[g/cm^2]	[1/ρ]
> 0.5	0	0	0	100	-	-
0.5 / 0.315	209.03	27.78	27.78	72.22	4.77	0.2096
0.315 / 0.1	291.45	38.73	66.51	33.49	4.86	0.2057
0.1 / 0.04	175.99	23.39	89.89	10.11	4.95	0.2022
< 0.04	76.06	10.11	100.00	0.00	4.58	0.2183
Σ	752.53	100.00	-	-	$\bar{x}$ = 4.83	$\bar{x}$ = 0.2071

Sample **6354** (D3) - Screen analysis after cycles 4 + 5 in the rod mill						
Fraction size	**Sieve fractions**		**Retained**	**Passed**	**Density (ρ)**	**Volume specific mass**
[mm]	Mass [g]	wt [%]	[%]	[%]	[g/cm^2]	[1/ρ]
>0.5	0	0	0	100.00	-	-
0.5 / 0.315	253.81	32.82	32.82	67.18	4.84	0.2068
0.315 / 0.1	260.48	33.68	66.50	33.50	4.89	0.2046
0.1 / 0.04	142.99	18.49	84.99	15.01	4.50	0.2222
< 0.04	116.05	15.01	100.00	0.00	4.57	0.2187
Σ	773.33	100.00	-	-	$\bar{x}$ = 4.75	$\bar{x}$ = 0.2104

Sample **6382** (B1) - Screen analysis after cycles 3 + 4 in the ball mill						
Fraction size	**Sieve fractions**		**Retained**	**Passed**	**Density (ρ)**	**Volume specific mass**
[mm]	Mass [g]	wt [%]	[%]	[%]	[g/cm^2]	[1/ρ]
> 0.1	0	0	0	100	-	-
0.1 / 0.04	464.00	69.01	69.01	30.99	5.11	0.1957
< 0.04	208.37	30.99	100.00	0.00	4.99	0.2004
Σ	672.37	100.00	-	-	$\bar{x}$ = 5.07	$\bar{x}$ = 0.1972

Sample **6365** (B2) - Screen analysis after cycles 3+4 in the ball mill						
Fraction size	**Sieve fractions**		**Retained**	**Passed**	**Density (ρ)**	**Volume specific mass**
[mm]	Mass [g]	wt [%]	[%]	[%]	[g/cm^2]	[1/ρ]
> 0.1	0	0	0	100.00	-	-
0.1 / 0.04	432.88	71.26	28.74	28.74	4.84	0.2066
< 0.04	174.57	28.74	100.00	0.00	4.70	0.2128
Σ	607.45	100.00	-	-	$\bar{x}$ = 4.80	$\bar{x}$ = 0.2084

Sample **6354** (D3) - Screen analysis after cycles 3+4 in the ball mill (Leoben)						
Fraction size	**Sieve fractions**		**Retained**	**Passed**	**Density (ρ)**	**Volume specific mass**
[mm]	Mass [g]	wt [%]	[%]	[%]	[g/cm^2]	[1/ρ]
> 0.1	0	0	0	100	-	-
0.1 / 0.04	370.11	61.67	61.67	38.33	4.71	0.2123
< 0.04	230.00	38.33	100.00	0.00	4.62	0.2165
Σ	600.11	100.00	-	-	$\bar{x}$ = 4.68	$\bar{x}$ = 0.2139

Results of the air jet screening displayed as amount of the finest material (< 0.04 mm) in the particle size class 0.1 / 0.04 mm carried out at the laboratory of the Institute of Mineral Processing

Amount of particles < 0.04 mm **Sample**		**Before air jet screening** (0.1 / 0.04 mm)	**After air jet screening** (0.1 / 0.04 mm)	**wt . %**
6382 (B1)	100% < 3.15 mm	14.84	14.63	1.42
	100% < 0.5 mm	15.64	15.33	1.98
	100% < 0.1 mm	15.56	15.13	2.76
6365 (B2)	100% < 3.15 mm	15.77	15.08	4.38
	100% < 0.5 mm	15.64	15.33	1.98
	100% < 0.1 mm	15.06	14.76	1.99
6354 (D3)	100% < 3.15 mm	16.37	15.11	7.70
	100% < 0.5 mm	15.73	14.84	5.66
	100% < 0.1 mm	15.24	15.08	1.05

Appendix 16. Numeric data of the particle size distribution (screen analysis) for characterization of ore type B2 after each grinding stage at the laboratory of the Institute of Mineral Processing, Montanuniversitaet Leoben.

Sample 6252 (B2) **Sample 6351** (B2)

Particle size distribution after 550 rounds in the laboratory rod mill

Fraction size [µm]	**Sieve fractions**		**Retained**	**Passed**	**Sieve fractions**		**Retained**	**Passed**
	wt [g]	wt [%]	[%]	[%]	wt [g]	wt [%]	[%]	[%]
> 250	44.04	14.52	14.52	85.48	5.71	0.49	0.49	99.51
250/160	152.91	13.46	27.98	72.02	72.35	6.24	6.73	93.27
160/125	91.57	6.53	34.51	65.49	91.68	7.91	14.64	85.36
125/80	171.17	14.99	49.49	50.51	287.83	24.83	39.48	60.52
80/63	110.42	8.87	58.36	41.64	163.78	14.13	53.61	46.39
63/40	209.54	13.10	71.47	28.53	185.29	15.99	69.60	30.40
<40	363.24	28.53	100.00	0	352.40	30.40	100.00	0
Σ	1142.89	100.00	-	-	1159.04	100.00	-	-

Particle size distribution after 15 minutes in the laboratory ball mill

Fraction size [µm]	**Sieve fractions**		**Retained**	**Passed**	**Sieve fractions**		**Retained**	**Passed**
	wt [g]	wt [%]	[%]	[%]	wt [g]	wt [%]	[%]	[%]
> 80	96.36	19.29	19.29	80.71	105.94	21.06	21.06	78.94
80/63	47.95	9.60	28.89	71.11	69.82	13.88	34.93	65.07
63/40	115.49	23.12	52.00	48.00	111.15	22.09	57.03	42.97
<40	239.79	48.00	100.00	0	216.2	42.97	100.00	0
Σ	499.59	100.00	-	-	503.11	100.00	-	-

Particle size distribution after 25 minutes in the laboratory ball mill

Fraction size [µm]	**Sieve fractions**		**Retained**	**Passed**	**Sieve fractions**		**Retained**	**Passed**
	wt [g]	wt [%]	[%]	[%]	wt [g]	wt [%]	[%]	[%]
> 80	51.3	10.46	10.46	89.54	71.87	13.65	13.65	86.35
80/63	61.3	12.50	22.95	77.05	85.73	16.29	29.94	70.06
63/40	102.21	20.84	43.79	56.21	132.71	25.21	55.15	44.85
<40	275.74	56.21	100.00	0	236.09	44.85	100.00	0
Σ	490.55	100.00	-	-	526.4	100.00	-	-

Particle size distribution after 55 minutes in the laboratory ball mill

Fraction size [µm]	**Sieve fractions**		**Retained**	**Passed**	**Sieve fractions**		**Retained**	**Passed**
	wt [g]	wt [%]	[%]	[%]	wt [g]	wt [%]	[%]	[%]
> 80	29.78	6.01	6.01	93.99	58.1	10.59	10.59	89.41
80/63	48.73	9.84	15.86	84.14	80.49	14.67	25.26	74.74
63/40	92.78	18.74	34.60	65.40	104.14	18.98	44.25	55.75
<40	323.81	65.40	100.00	0	305.84	55.75	100.00	0
Σ	495.1	100.00	-	-	548.57	100.00	-	-

Sample 6363 (B2) **Sample 6367** (B2)

Particle size distribution after 550 rounds in the laboratory rod mill

Fraction size [µm]	Sieve fractions		Retained	Passed	Sieve fractions		Retained	Passed
	wt [g]	wt [%]	[%]	[%]	wt [g]	wt [%]	[%]	[%]
> 250	8.51	0.75	0.75	99.25	93.35	7.45	7.45	92.55
250/160	107.66	9.54	10.29	89.71	220.88	17.62	25.07	74.93
160/125	127.12	11.26	21.55	78.45	130.67	10.43	35.50	64.50
125/80	273.71	24.25	45.80	54.20	304.52	24.30	59.80	40.20
80/63	182.08	16.13	61.94	38.06	127.48	10.17	69.97	30.03
63/40	149.86	13.28	75.21	24.79	146.36	11.68	81.65	18.35
<40	279.76	24.79	100.00	0	229.99	18.35	100.00	0
Σ	1128.7	100.00	-	-	1253.25	100.00	-	-

Particle size distribution after 15 minutes in the laboratory ball mill

Fraction size [µm]	Sieve fractions		Retained	Passed	Sieve fractions		Retained	Passed
	wt [g]	wt [%]	[%]	[%]	wt [g]	wt [%]	[%]	[%]
> 80	104.57	31.28	31.28	68.72	206.48	39.75	39.75	60.25
80/63	47.12	14.09	45.37	54.63	78.86	15.18	54.93	45.07
63/40	64.89	19.41	64.78	35.22	94.36	18.17	73.10	26.90
<40	117.77	35.22	100.00	0	139.72	26.90	100.00	0
Σ	334.35	100.00	-	-	519.42	100.00	-	-

Particle size distribution after 25 minutes in the laboratory ball mill

Fraction size [µm]	Sieve fractions		Retained	Passed	Sieve fractions		Retained	Passed
	wt [g]	wt [%]	[%]	[%]	wt [g]	wt [%]	[%]	[%]
> 80	79.57	22.93	22.93	77.07	156.73	30.21	30.21	69.79
80/63	56.29	16.22	39.14	60.86	74.11	14.28	44.49	55.51
63/40	68.22	19.66	58.80	41.20	98.62	19.01	63.50	36.50
<40	143	41.20	100.00	0	189.35	36.50	100.00	0
Σ	347.08	100.00	-	-	518.81	100.00	-	-

Particle size distribution after 35 minutes in the laboratory ball mill

Fraction size [µm]	Sieve fractions		Retained	Passed	Sieve fractions		Retained	Passed
	wt [g]	wt [%]	[%]	[%]	wt [g]	wt [%]	[%]	[%]
> 80	85.19	16.61	16.61	83.39	110.44	22.08	22.08	77.92
80/63	84.87	16.55	33.16	66.84	89.82	17.96	40.04	59.96
63/40	112.98	22.03	55.19	44.81	116.9	23.37	63.42	36.58
<40	229.8	44.81	100.00	0	182.96	36.58	100.00	0
Σ	512.84	100.00		-	500.12	100.00	-	-

Sample 6370 (B2) **Sample 6387** (B2)

Particle size distribution after 550 rounds in the laboratory rod mill

Fraction size [μm]	Sieve fractions		Retained	Passed	Sieve fractions		Retained	Passed
	wt [g]	wt [%]	[%]	[%]	wt [g]	wt [%]	[%]	[%]
> 250	56.98	5.77	5.77	94.23	171.57	12.59	12.59	87.41
250/160	129.47	13.12	18.90	81.10	183.9	13.49	26.08	73.92
160/125	98.25	9.96	28.85	71.15	98.85	7.25	33.34	66.66
125/80	174.72	17.71	46.56	53.44	183.86	13.49	46.83	53.17
80/63	50.15	5.08	51.64	48.36	153.15	11.24	58.06	41.94
63/40	238.60	24.18	75.82	24.18	130.38	9.57	67.63	32.37
<40	238.59	24.18	100.00	0	441.17	32.37	100.00	0
Σ	986.76	100.00	-	-	1362.88	100.00	-	-

Particle size distribution after 15 minutes in the laboratory ball mill

Fraction size [μm]	Sieve fractions		Retained	Passed	Sieve fractions		Retained	Passed
	wt [g]	wt [%]	[%]	[%]	wt [g]	wt [%]	[%]	[%]
> 80	143.41	29.18	29.18	70.82	126.02	21.95	21.95	78.05
80/63	60.51	12.31	41.49	58.51	62.62	10.91	32.85	67.15
63/40	92.18	18.76	60.25	39.75	105.56	18.38	51.24	48.76
<40	195.39	39.75	100.00	0	280	48.76	100.00	0
Σ	491.49	100.00	-	-	574.2	100.00	-	-

Particle size distribution after 25 minutes in the laboratory ball mill

Fraction size [μm]	Sieve fractions		Retained	Passed	Sieve fractions		Retained	Passed
	wt [g]	wt [%]	[%]	[%]	wt [g]	wt [%]	[%]	[%]
> 80	106.23	21.77	21.77	78.23	58.53	12.75	12.75	87.25
80/63	88.37	18.11	39.88	60.12	49.71	10.82	23.57	76.43
63/40	73.12	14.98	54.86	45.14	83.58	18.20	41.77	58.23
<40	220.29	45.14	100.00	0	267.4	58.23	100.00	0
Σ	488.01	100.00	-	-	459.22	100.00	-	-

Particle size distribution after 35 minutes in the laboratory ball mill

Fraction size [μm]	Sieve fractions		Retained	Passed	Sieve fractions		Retained	Passed
	wt [g]	wt [%]	[%]	[%]	wt [g]	wt [%]	[%]	[%]
> 80	87.59	17.88	17.88	82.12	27.22	5.99	5.99	94.01
80/63	62.61	12.78	30.66	69.34	49.15	10.81	16.80	83.20
63/40	100.41	20.50	51.15	48.85	96.33	21.20	38.00	62.00
<40	239.31	48.85	100.00	0	281.79	62.00	100.00	0
Σ	489.92	100.00	-	-	454.49	100.00	-	-

Appendix 17. Estimation of net torque (ΔM_D), net energy consumption (ΔE), power draw (N) and mass specific energy consumption (Δe) for samples 6382 (B1), 6365 (B2) and 6354 (D3) based on data from the comminution tests with the laboratory ball mill at the laboratory of the Institute of Mineral Processing.

Sample 6382 (B1)

MILL RUN	REVOLUTIONS		TIME	RECORDER			NET TORQUE	NET ENERGY CONSUMPTION		POWER	MASS SPECIFIC ENERGY		MASS OF FINES
	U	ΣU	t	Paper feed	Integration units IE	IE/t	ΔM_D	ΔE		ΔN	Δe		
	[ ]	[ ]	[s]	[mm/s]	[ ]	[s^{-1}]	[Nm]	Δ [kJ]	Σ [kJ]	[W]	Δ [J/g]	Σ [J/g]	[g]
Empty	-	-	306.0	1	5700	18.63	-	-	-	-	-	-	-
Loaded (1)	495	495	449.0	1	31715	70.63	3.46	10.77	10.77	23.98	39.36	39.36	273.6
Loaded (2)	615	1110	580.0	1	41441	71.45	3.52	13.59	24.53	23.43	41.56	80.92	327.0
Loaded (3)	643	1753	610.0	1	43526	71.35	3.51	14.18	38.67	23.25	42.39	123.31	334.6
Loaded (4)	664	2417	631.6	1	45410	71.90	3.55	14.80	53.88	23.43	43.39	166.70	341.1
Empty	-	-	231.1	-	4680	20.25	-	-	-	-	-	-	-

Sample 6365 (B2)

MILL RUN	REVOLUTIONS		TIME	RECORDER			NET TORQUE	NET ENERGY CONSUMPTION		POWER	MASS SPECIFIC ENERGY		MASS OF FINES
	U	ΣU	t	Paper feed	Integration units IE	IE/t	ΔM_D	ΔE		ΔN	Δe		
	[ ]	[ ]	[s]	[mm/s]	[ ]	[s^{-1}]	[Nm]	Δ [kJ]	Σ [kJ]	[W]	Δ [J/g]	Σ [J/g]	[g]
Empty	-	-	294.0	1	5313	18.07	-	-	-	-	-	-	-
Loaded (1)	161	161	150.5	1	10835	71.99	3.61	3.66	3.66	24.30	12.89	12.89	283.6
Loaded (2)	191	352	178.5	1	13058	73.15	3.69	4.43	8.17	24.82	19.18	32.07	231.0
Loaded (3)	367	719	344.5	1	25010	72.60	3.65	8.43	16.51	24.46	28.32	60.39	297.6
Loaded (4)	410	1129	388.5	1	28025	72.14	3.62	9.34	25.71	24.03	29.56	89.96	315.8
Empty	-	-	315.0	-	5588	17.74	-	-	-	-	-	-	-

Sample 6354 (D3)

MILL RUN	REVOLUTIONS		TIME	RECORDER			NET TORQUE	NET ENERGY CONSUMPTION		POWER	MASS SPECIFIC ENERGY		MASS OF FINES
	U	ΣU	t	Paper feed	Integration units IE	IE/t	ΔM_D	ΔE		ΔN	Δe		
	[ ]	[ ]	[s]	[mm/s]	[ ]	[s^{-1}]	[Nm]	Δ [kJ]	Σ [kJ]	[W]	Δ [J/g]	Σ [J/g]	[g]
Empty	-	-	315.0	1	5588	17.74	-	-	-	-	-	-	-
Loaded (1)	300	300	281.0	1	19898	70.81	3.58	6.76	6.76	24.04	21.17	21.17	319.1
Loaded (2)	330	630	312.3	1	22425	71.81	3.65	7.57	14.45	24.24	24.60	45.77	307.8
Loaded (3)	340	970	325.6	1	23705	72.80	3.72	7.95	22.67	24.40	26.09	71.86	304.6
Loaded (4)	350	1320	331.5	1	24085	72.65	3.71	8.16	30.76	24.61	27.25	99.11	299.3
Empty	-	-	315.1	-	5795	18.39	-	-	-	-	-	-	-

Appendix 18. The complete data for energy register for two comminution steps of samples 6382 (B1), 6365 (B2) and 6354 (D3) based on the grinding tests carried out with the laboratory rod mill and the laboratory ball mill at the laboratory of the Institute of Mineral Processing.

Specific energy consumption 6382 (B1)			**< 3.15 mm**	**< 0.5 mm**	**< 0.1mm**
$\mathbf{C_p}$		-	-	1.2	1
$\mathbf{M_k}$	[kg]	-	-	7.802	-
g	[m/s^2]	-	-	9.81	-
D	[m]	-	-	0.154	-
$\mathbf{U/M_F}$	[1/kg]	-	-	231	-
Δe'	[J/kg]	-	-	3273	42891
	[J/g]	-	-	3.27	42.89
	[kWh/t]	-	-	0.91	11.91
Mass (passing)	[%]	-	-	72.18	37.06
Mass (retaining)	[%]	-	-	27.82	62.94
Δe	[kWh/t]	-	-	0.25	7.50
	[J/g]	-	0	0.91	26.99
Δa	[cm^2/g]	-	302	341	766
		-	-	(4-1)	(7-4)
R	[cm^2/J]	-	-	374	28
ΣΔe	[J/g]	-	0	0.91	27.91
ΣΔa	[cm^2/g]	-	302	341	766
ΣΔe	[J/g]	0	19.35	20.26	47.25
$\mathbf{D_a}$	[cm^2/g]	0	302	341	766

Specific energy consumption 6365 (B2)			**< 3.15 mm**	**< 0.5 mm**	**< 0.1mm**
$\mathbf{C_p}$		-	-	1.2	1
$\mathbf{M_k}$	[kg]	-	-	7.802	-
g	[m/s^2]	-	-	9.81	-
D	[m]	-	-	0.154	-
$\mathbf{U/M_F}$	[1/kg]	-	-	208	-
Δe'	[J/kg]	-	-	2949	28941
	[J/g]	-	-	2.95	28.94
	[kWh/t]	-	-	0.82	8.04
Mass (passing)	[%]	-	-	50.31	41.73
Mass (retaining)	[%]	-	-	49.69	58.27
Δe	[kWh/t]	-	-	0.41	4.68
	[J/g]	-	0	1.47	16.86
Δa	[cm^2/g]	-	139	250	596
		-	-	(4-1)	(7-4)
R	[cm^2/J]	-	-	171	35
ΣΔe	[J/g]	-	0	1.47	18.33
ΣΔa	[cm^2/g]	-	139	250	596
ΣΔe	[J/g]	0	7.59	9.06	25.94

Specific energy consumption 6354 (D3)			**< 3.15 mm**	**< 0.5 mm**	**< 0.1mm**
$\mathbf{C_p}$		-	-	1.2	1
$\mathbf{M_k}$	[kg]	-	-	7.802	-
g	[m/s^2]	-	-	9.81	-
D	[m]	-	-	0.154	-
$\mathbf{U/M_F}$	[1/kg]	-	-	514	-
Δe'	[J/kg]	-	-	7267	26670
	[J/g]	-	-	7.27	26.67
	[kWh/t]	-	-	2.02	7.41
Mass (passing)	[%]	-	-	38.45	40.44
Mass (retaining)	[%]	-	-	61.55	59.56
Δe	[kWh/t]	-	-	1.24	4.41
	[J/g]	-	0	4.47	15.88
Δa	[cm^2/g]	-	192	403	826
		-	-	(4-1)	(7-4)
R	[cm^2/J]	-	-	90	52
ΣΔe	[J/g]	-	0	4.47	20.36
ΣΔa	[cm^2/g]	-	192	403	826
ΣΔe	[J/g]	0	7.51	11.98	27.87
$\mathbf{D_a}$	[cm^2/g]	0	192	403	826

Appendix 19. Chemical composition of the minerals used for this study based on the Electron Probe Micro-Analysis (EMPA) carried out by Nordstrand (2012) and Aupers (2014). Density from www.webmineral.com; www.mindat.org.

Mineral	Elements								Density [g/cm^3]
Actinolite	0.77 % Al	8.23 % Ca	5.24 % Fe	0.24 % H	0.38 % K	12.02 % Mg	0.18 % Mn	0.73 % Na	3.04
	42.67 % O	25.11 % Si	0.09 % Ti	0.01 % V					
Albite	10.37 % Al	0.14 % Ca	8.61 % Na	48.76 % O	31.99 % Si				2.62
Allanite	7.63 % Al	7.43 % Ca	10.96 % Ce	0.32 % F	5.06 % La	0.65 % Mg	0.43 % Mn	3.53 % Nd	3.75
	34.53 % O	0.05 % P	1.42 % Pr	14.77 % Si	0.22 % Ti	0.10 % V	0.16 % Y		
Anhydrite	29.35 % Ca	0.03 % Fe	44.62 % O	21.78 % S	0.26 % Sr				2.30
Apatite	38.48 % Ca	3.42 % F	36.87 % O	18.65 % P					3.15
Barite	68.33 % Ba	16.16 % O	15.51 % S						4.48
Calcite	0.12 % Al	12.48 % C	37.03 % Ca	0.37 % F	0.35 % Mg	0.88 % Mn	48.73 % O	0.04 % Sr	2.71
Chalcopyrite	34.63 % Cu	30.43 % Fe	34.94 % S						4.18
Chlorite	9.79 % Al	0.02 % Ca	11.34 % Fe	0.01 % K	14.21 % Mg	0.35 % Mn	43.99 % O	13.36 % Si	2.65
	0.02 % Ti								
Dolomite/Ankerite	12.55 % C	20.62 % Ca	5.51 % Fe	9.70 % Mg	1.28 % Mn	50.16 % O			2.84
Gypsum	23.28 % Ca	2.34 % H	55.75 % O	18.62 % S					2.3
Hematite	72.01 % Fe	20.79 % O	0.07 % Ti	0.14 % V					5.15
Ilmenite	29.02 % Fe	9.07 % Mn	31.36 % O	30.55 % Ti					4.72
K-Feldspar	9.69 % Al	14.05 % K	45.99 % O	30.27 % Si					2.55
Magnetite	72.01 % Fe	20.79 % O	0.07 % Ti	0.14 % V					5.15
Monazite	29.65 % Ce	15.29 % La	9.52 % Nd	28.09 % O	14.08 % P	2.32 % Pr			5.15
Phlogopite	6.05 % Al	0.06 % Cl	2.01 % F	5.72 % Fe	0.24 % H	8.30 % K	14.05 % Mg	0.07 % Mn	2.8
	42.65 % O	19.75 % Si	0.65 % Ti						
Pyrite	46.55 % Fe	53.45 % S							5.01
Quartz	53.26 % O	46.74 % Si							2.62
Rutile	1.05 % Fe	39.81 % O	59.14 % Ti						4.25
Talc	0.02 % Cl	1.03 % F	3.34 % Fe	0.53 % H	17.12 % Mg	49.16 % O	28.69 % Si		2.75
Thorite	0.30 % Ba	0.83 % Ca	3.46 % Ce	0.27 % F	0.52 % Fe	1.09 % La	1.17 % Nd	16.98 % O	3.48
	0.66 % Pr	9.57 % Si	55.5 % Th	3.26 % U	0.11 % V	0.13 % W	0.28 % Y		
Titanite	0.40 % Al	20.08 % Ca	0.18 % F	1.03 % Fe	40.23 % O	14.26 % Si	22.78 % Ti		5.35
Zircon	34.91 % O	15.32 % Si	49.77 % Zr						4.65

Appendix 20. Distribution (wt.% in sample) of silicates and quartz in samples 6252, 6351, 6363, 6367, 6370 and 6387 (particle size classes >80 µm, 80/63 µm, 63/40 µm and <40 µm) after crushing and comminution in the laboratory rod mill (10 minutes) and in the laboratory ball mill (35 minutes) at the laboratory of the Institute of Mineral Processing.

MINERAL	6252					6351				
	>80 [µm]	80/63 [µm]	63/40 [µm]	<40 [µm]	Comb. [µm]	>80 [µm]	80/63 [µm]	63/40 [µm]	<40 [µm]	Comb. [µm]
Actinolite	0.121	0.118	0.120	1.289	1.647	0.045	0.079	0.048	0.466	0.637
Albite	0.000	0.002	0.002	0.000	0.004	0.007	0.029	0.015	0.051	0.101
Allanite	0.000	0.000	0.000	0.000	0.000	0.000	0.000	0.000	0.000	0.000
Chlorite	0.024	0.009	0.010	0.031	0.074	0.101	0.072	0.044	0.122	0.340
K-Feldspar	0.000	0.000	0.000	0.000	0.000	0.001	0.009	0.003	0.015	0.028
Phlogopite	0.026	0.013	0.023	1.580	1.641	0.084	0.109	0.077	1.454	1.724
Quartz	0.002	0.005	0.012	0.264	0.282	0.062	0.288	0.200	1.677	2.226
Talc	0.003	0.003	0.001	0.021	0.028	0.007	0.008	0.004	0.101	0.119
Thorite	0.000	0.000	0.000	0.000	0.000	0.000	0.000	0.000	0.001	0.002
Titanite	0.014	0.024	0.039	0.050	0.128	0.018	0.072	0.064	0.297	0.452
Zircon	0.000	0.000	0.000	0.000	0.000	0.000	0.000	0.000	0.000	0.000
Σ	0.190	0.173	0.207	3.233	3.804	0.326	0.666	0.454	4.183	5.629

MINERAL	6363					6367				
	>80 [µm]	80/63 [µm]	63/40 [µm]	<40 [µm]	Comb. [µm]	>80 [µm]	80/63 [µm]	63/40 [µm]	<40 [µm]	Comb. [µm]
Actinolite	0.253	0.250	0.418	0.918	1.840	0.007	0.024	0.030	0.113	0.173
Albite	0.022	0.025	0.021	0.101	0.168	0.028	0.029	0.043	0.032	0.132
Allanite	0.000	0.000	0.000	0.000	0.000	0.001	0.000	0.000	0.000	0.001
Chlorite	0.020	0.005	0.007	0.002	0.034	0.082	0.019	0.015	0.091	0.207
K-Feldspar	0.000	0.000	0.000	0.000	0.001	0.000	0.000	0.001	0.001	0.002
Phlogopite	0.196	0.112	0.159	1.539	2.006	0.243	0.097	0.107	0.634	1.081
Quartz	0.041	0.059	0.092	0.585	0.777	0.022	0.027	0.048	0.138	0.236
Talc	0.000	0.001	0.001	0.005	0.007	0.004	0.006	0.006	0.043	0.060
Thorite	0.000	0.000	0.000	0.004	0.004	0.000	0.000	0.000	0.000	0.000
Titanite	0.033	0.039	0.067	0.136	0.275	0.014	0.015	0.045	0.035	0.109
Zircon	0.000	0.000	0.000	0.000	0.000	0.000	0.000	0.000	0.000	0.000
Σ	0.565	0.492	0.764	3.289	5.111	0.401	0.216	0.296	1.087	2.000

MINERAL	6370					6387				
	>80 [µm]	80/63 [µm]	63/40 [µm]	<40 [µm]	Comb. [µm]	>80 [µm]	80/63 [µm]	63/40 [µm]	<40 [µm]	Comb. [µm]
Actinolite	0.000	0.000	0.000	0.000	0.001	0.214	0.284	0.287	1.822	2.606
Albite	0.127	0.058	0.112	0.256	0.552	0.001	0.002	0.000	0.016	0.019
Allanite	0.007	0.003	0.009	0.000	0.019	0.000	0.000	0.000	0.000	0.000
Chlorite	0.100	0.012	0.038	0.045	0.195	0.010	0.006	0.010	0.028	0.053
K-Feldspar	0.028	0.012	0.026	0.080	0.146	0.000	0.000	0.000	0.000	0.000
Phlogopite	0.798	0.143	0.461	1.830	3.232	0.046	0.035	0.037	0.911	1.029
Quartz	0.533	0.199	0.704	1.778	3.213	0.003	0.007	0.012	0.247	0.268
Talc	0.000	0.000	0.000	0.000	0.000	0.005	0.003	0.003	0.010	0.022
Thorite	0.000	0.000	0.000	0.000	0.001	0.000	0.000	0.000	0.000	0.000
Titanite	0.000	0.000	0.004	0.029	0.034	0.016	0.029	0.062	0.167	0.273
Zircon	0.000	0.000	0.000	0.000	0.000	0.000	0.001	0.000	0.000	0.001
Σ	1.594	0.427	1.354	4.017	7.392	0.295	0.367	0.410	3.199	4.271

Appendix 21. Elemental deportment of silicon (Si) in essential silicates given as total mass and normalized to 100 % for the four finest particle size classes after comminution in a laboratory rod mill (10 minutes) and in a laboratory ball mill (35 minutes). Allanite, zircon and thorite are grouped under Others.

6252 Ball mill

Elemental Deportment (Si)	MASS					MASS % IN FRACTION				
Size fraction	> 80 µm	80/63 µm	63/40 µm	< 40 µm	Comb.	> 80 µm	80/63 µm	63/40 µm	< 40 µm	Comb.
Actinolite	0.1502	0.1468	0.1488	1.6409	2.0867	77.21	80.23	72.32	81.05	80.02
Albite	0.0004	0.0024	0.0037	0.0000	0.0065	0.22	1.33	1.78	0.00	0.25
Chlorite	0.0162	0.0059	0.0066	0.0208	0.0496	8.33	3.24	3.20	1.03	1.90
K-Feldspar	0.0001	0.0000	0.0000	0.0000	0.0001	0.03	0.02	0.00	0.00	0.00
Other	0.0000	0.0001	0.0001	0.0000	0.0002	0.01	0.04	0.07	0.00	0.01
Phlogopite	0.0133	0.0047	0.0110	0.2971	0.3260	6.82	2.55	5.32	14.68	12.50
Quartz	0.0003	0.0018	0.0057	0.0000	0.0078	0.16	0.96	2.77	0.00	0.30
Talc	0.0038	0.0041	0.0019	0.0299	0.0397	1.96	2.22	0.93	1.48	1.52
Titanite	0.0102	0.0171	0.0279	0.0358	0.0910	5.24	9.37	13.55	1.77	3.49
Σ	0.1944	0.1829	0.2056	2.0246	2.6076	99.98	99.96	99.95	100.00	99.99

6351 Ball mill

Elemental Deportment (Si)	MASS					MASS % IN FRACTION				
Size fraction	> 80 µm	80/63 µm	63/40 µm	< 40 µm	Comb.	> 80 µm	80/63 µm	63/40 µm	< 40 µm	Comb.
Actinolite	0.0618	0.1086	0.0656	0.6547	0.8908	15.14	9.88	8.97	12.41	11.85
Albite	0.0119	0.0517	0.0255	0.0910	0.1801	2.91	4.71	3.49	1.72	2.40
Chlorite	0.0750	0.0529	0.0327	0.0922	0.2529	18.37	4.82	4.47	1.75	3.36
K-Feldspar	0.0021	0.0148	0.0048	0.0259	0.0477	0.52	1.35	0.66	0.49	0.63
Other	0.0000	0.0002	0.0001	0.0006	0.0009	0.01	0.02	0.01	0.01	0.01
Phlogopite	0.0887	0.1116	0.0792	0.8720	1.1515	21.73	10.15	10.82	16.53	15.32
Quartz	0.1432	0.6904	0.4673	3.1405	4.4413	35.09	62.81	63.85	59.52	59.09
Talc	0.0107	0.0120	0.0062	0.1617	0.1906	2.63	1.09	0.84	3.06	2.54
Titanite	0.0144	0.0566	0.0502	0.2375	0.3588	3.54	5.15	6.86	4.50	4.77
Σ	0.4079	1.0989	0.7316	5.2761	7.5144	99.94	99.97	99.96	99.99	99.98

6363 Ball mill

Elemental Deportment (Si)	MASS					MASS % IN FRACTION				
Size fraction	> 80 µm	80/63 µm	63/40 µm	< 40 µm	Comb.	> 80 µm	80/63 µm	63/40 µm	< 40 µm	Comb.
Actinolite	0.3264	0.3226	0.5385	1.1964	2.3840	48.25	51.63	55.90	35.65	42.41
Albite	0.0363	0.0411	0.0339	0.1670	0.2784	5.37	6.58	3.52	4.98	4.95
Chlorite	0.0138	0.0035	0.0047	0.0014	0.0234	2.04	0.56	0.49	0.04	0.42
K-Feldspar	0.0001	0.0005	0.0000	0.0008	0.0014	0.01	0.09	0.00	0.02	0.02
Other	0.0001	0.0000	0.0000	0.0020	0.0021	0.01	0.00	0.00	0.06	0.04
Phlogopite	0.1980	0.1130	0.1596	1.4363	1.9069	29.26	18.08	16.57	42.80	33.93
Quartz	0.0775	0.1142	0.1762	0.4423	0.8102	11.46	18.27	18.29	13.18	14.41
Talc	0.0002	0.0008	0.0008	0.0080	0.0098	0.03	0.13	0.08	0.24	0.17
Titanite	0.0238	0.0288	0.0492	0.1005	0.2023	3.52	4.61	5.11	2.99	3.60
Σ	0.6761	0.6246	0.9630	3.3547	5.6185	99.94	99.95	99.96	99.97	99.96

6363 Ball mill

Elemental Deportment (Si)	MASS					MASS % IN FRACTION				
Size fraction	**> 80 µm**	**80/63 µm**	**63/40 µm**	**< 40 µm**	**Comb.**	**> 80 µm**	**80/63 µm**	**63/40 µm**	**< 40 µm**	**Comb.**
Actinolite	0.0087	0.0296	0.0381	0.1426	0.2190	2.18	12.28	11.71	16.70	12.04
Albite	0.0449	0.0460	0.0697	0.0514	0.2119	11.28	19.09	21.40	6.01	11.65
Chlorite	0.0548	0.0129	0.0100	0.0614	0.1392	13.77	5.37	3.06	7.19	7.65
K-Feldspar	0.0002	0.0005	0.0010	0.0010	0.0027	0.04	0.21	0.32	0.12	0.15
Other	0.0005	0.0000	0.0000	0.0000	0.0006	0.13	0.02	0.01	0.00	0.03
Phlogopite	0.2375	0.0905	0.0976	0.4707	0.8963	59.64	37.55	29.99	55.12	49.29
Quartz	0.0343	0.0426	0.0670	0.0385	0.1824	8.62	17.69	20.57	4.51	10.03
Talc	0.0061	0.0079	0.0091	0.0626	0.0857	1.54	3.28	2.80	7.33	4.71
Titanite	0.0102	0.0106	0.0322	0.0252	0.0781	2.55	4.40	9.88	2.95	4.30
Σ	0.3972	0.2407	0.3247	0.8534	1.8160	99.75	99.89	99.75	99.94	99.86

6370 Ball mill

Elemental Deportment (Si)	MASS					MASS % IN FRACTION				
Size fraction	**> 80 µm**	**80/63 µm**	**63/40 µm**	**< 40 µm**	**Comb.**	**> 80 µm**	**80/63 µm**	**63/40 µm**	**< 40 µm**	**Comb.**
Actinolite	0.0006	0.0001	0.0005	0.0000	0.0012	0.03	0.01	0.02	0.00	0.01
Albite	0.1994	0.0904	0.1757	0.4057	0.8713	8.98	13.45	7.95	7.79	8.45
Chlorite	0.0667	0.0081	0.0253	0.0307	0.1309	3.00	1.21	1.15	0.59	1.27
K-Feldspar	0.0416	0.0183	0.0391	0.1195	0.2185	1.87	2.72	1.77	2.29	2.12
Other	0.0055	0.0020	0.0065	0.0002	0.0142	0.25	0.29	0.29	0.00	0.14
Phlogopite	0.7712	0.1380	0.4438	1.6617	3.0148	34.73	20.53	20.09	31.91	29.24
Quartz	1.1340	0.4141	1.5135	2.9678	6.0293	51.06	61.59	68.50	56.99	58.48
Talc	0.0003	0.0000	0.0000	0.0000	0.0004	0.02	0.00	0.00	0.00	0.00
Titanite	0.0001	0.0001	0.0029	0.0206	0.0237	0.00	0.01	0.13	0.40	0.23
Σ	2.2194	0.6712	2.2073	5.2062	10.3041	99.94	99.83	99.91	99.97	99.94

6387 Ball mill

Elemental Deportment (Si)	MASS					MASS % IN FRACTION				
Size fraction	**> 80 µm**	**80/63 µm**	**63/40 µm**	**< 40 µm**	**Comb.**	**> 80 µm**	**80/63 µm**	**63/40 µm**	**< 40 µm**	**Comb.**
Actinolite	0.2447	0.3240	0.3276	2.1081	3.0045	81.55	85.58	81.58	82.47	82.62
Albite	0.0019	0.0034	0.0000	0.0229	0.0282	0.62	0.91	0.00	0.90	0.78
Chlorite	0.0060	0.0038	0.0059	0.0170	0.0328	2.01	1.01	1.47	0.67	0.90
K-Feldspar	0.0001	0.0000	0.0000	0.0000	0.0001	0.02	0.00	0.00	0.00	0.00
Other	0.0000	0.0009	0.0000	0.0000	0.0009	0.00	0.24	0.00	0.00	0.03
Phlogopite	0.0301	0.0214	0.0218	0.2711	0.3444	10.03	5.65	5.43	10.61	9.47
Quartz	0.0002	0.0021	0.0016	0.0137	0.0177	0.08	0.56	0.40	0.54	0.49
Talc	0.0069	0.0043	0.0042	0.0133	0.0287	2.31	1.13	1.06	0.52	0.79
Titanite	0.0101	0.0186	0.0403	0.1095	0.1784	3.36	4.91	10.02	4.28	4.91
Σ	0.2999	0.3786	0.4015	2.5557	3.6357	99.98	99.98	99.97	99.98	99.98

Appendix 22. Intergrowth (mineral association) of Fe Oxide (in practice entirely magnetite) and gangue minerals in different particle size classes after crushing and comminution in a laboratory rod mill (10 minutes) and in a laboratory ball mill (35 minutes) at the laboratory at the Institute of Mineral Processing.

	6252				**6351**			
Mineral associations	**> 80 µm**	**80/63 µm**	**63/40 µm**	**< 40 µm**	**> 80 µm**	**80/63 µm**	**63/40 µm**	**< 40 µm**
Fe Oxide liberated	96.89	98.00	98.23	92.21	97.49	97.21	97.86	91.57
Fe Oxide / Silicates (binary)	2.37	1.20	1.09	1.25	2.03	2.15	1.37	2.94
Fe Oxide / Carbonates (binary)	0.14	0.05	0.07	0.27	0.15	0.15	0.07	0.11
Fe Oxide / Phosphates (binary)	0.30	0.35	0.20	0.65	0.00	0.04	0.05	0.14
Fe Oxide / Carbonates / Silicates (ternary)	0.02	0.01	0.00	0.01	0.01	0.02	0.03	0.07
Fe Oxide / Carbonates / Phosphates (ternary)	0.00	0.00	0.00	0.01	0.00	0.00	0.00	0.00
Fe Oxide / Carbonates / Phosphates / Silicates (ternary)	0.04	0.00	0.00	0.01	0.00	0.00	0.01	0.01
Other	0.23	0.38	0.40	5.58	0.31	0.43	0.60	5.15
Σ	100.00	100.00	100.00	100.00	100.00	100.00	100.00	100.00

	6363				**6367**			
Mineral associations	**> 80 µm**	**80/63 µm**	**63/40 µm**	**< 40 µm**	**> 80 µm**	**80/63 µm**	**63/40 µm**	**< 40 µm**
Fe Oxide liberated	98.10	98.10	97.46	92.31	98.43	97.85	97.96	93.33
Fe Oxide / Silicates (binary)	1.74	1.65	2.05	3.90	0.91	1.19	0.74	1.49
Fe Oxide / Carbonates (binary)	0.01	0.01	0.00	0.06	0.16	0.12	0.11	0.36
Fe Oxide / Phosphates (binary)	0.01	0.00	0.00	0.17	0.02	0.03	0.02	0.08
Fe Oxide / Carbonates / Silicates (ternary)	0.01	0.00	0.00	0.12	0.01	0.05	0.04	0.07
Fe Oxide / Carbonates / Phosphates (ternary)	0.00	0.00	0.00	0.00	0.00	0.00	0.00	0.00
Fe Oxide / Carbonates / Phosphates / Silicates (ternary)	0.00	0.00	0.01	0.00	0.00	0.00	0.00	0.10
Other	0.14	0.24	0.49	3.45	0.47	0.76	1.14	4.57
Σ	100.00	100.00	100.00	100.00	100.00	100.00	100.00	100.00

	6370				**6387**			
Mineral associations	**> 80 µm**	**80/63 µm**	**63/40 µm**	**< 40 µm**	**> 80 µm**	**80/63 µm**	**63/40 µm**	**< 40 µm**
Fe Oxide liberated	95.66	97.92	96.67	81.59	96.27	96.66	97.60	86.29
Fe Oxide / Silicates (binary)	2.60	0.86	1.40	0.57	3.38	2.72	1.64	1.14
Fe Oxide / Carbonates (binary)	0.74	0.43	0.59	0.78	0.01	0.07	0.04	0.02
Fe Oxide / Phosphates (binary)	0.17	0.18	0.22	0.43	0.01	0.02	0.01	0.03
Fe Oxide / Carbonates / Silicates (ternary)	0.09	0.03	0.03	0.01	0.04	0.04	0.01	0.01
Fe Oxide / Carbonates / Phosphates (ternary)	0.06	0.03	0.00	0.00	0.00	0.00	0.01	0.00
Fe Oxide / Carbonates / Phosphates / Silicates (ternary)	0.07	0.03	0.05	0.00	0.01	0.00	0.00	0.00
Other	0.61	0.52	1.02	16.62	0.29	0.48	0.69	12.51
Σ	100.00	100.00	100.00	100.00	100.00	100.00	100.00	100.00

Appendix 23. Intergrowth (mineral associations) of Fe Oxide (in practice entirely magnetite) and silicates (inclusive quartz) in different particle size classes after crushing and comminution in a laboratory rod mill (10 minutes) and in a laboratory ball mill (35 minutes) at the laboratory of the Institute of Mineral Processing.

	6252				6351			
Mineral association	**> 80 µm**	**80/63 µm**	**63/40 µm**	**< 40 µm**	**> 80 µm**	**80/63 µm**	**63/40 µm**	**< 40 µm**
Fe Oxide liberated	96.89	98.00	98.23	92.21	97.49	97.21	97.86	91.57
Fe Oxide - Actinolite (binary)	0.68	0.27	0.20	0.20	0.06	0.05	0.04	0.14
Fe Oxide - Phlogopite (binary)	0.20	0.13	0.20	0.49	0.54	0.52	0.51	0.98
Fe Oxide - Chlorite (binary)	0.52	0.14	0.12	0.35	0.77	0.54	0.23	0.94
Fe Oxide - Talc (binary)	0.02	0.09	0.00	0.00	0.04	0.03	0.00	0.00
Fe Oxide - Titanite (binary)	0.26	0.35	0.38	0.00	0.24	0.47	0.22	0.23
Fe Oxide - Albite (binary)	0.00	0.00	0.00	0.00	0.01	0.00	0.00	0.00
Fe Oxide - Quartz (binary)	0.01	0.01	0.00	0.08	0.15	0.20	0.07	0.20
Other	1.41	1.02	0.87	6.68	0.69	0.97	1.06	5.94
Σ	100.00	100.00	100.00	100.00	100.00	100.00	100.00	100.00

	6363				6367			
Mineral association	**> 80 µm**	**80/63 µm**	**63/40 µm**	**< 40 µm**	**> 80 µm**	**80/63 µm**	**63/40 µm**	**< 40 µm**
Fe Oxide liberated	98.10	98.10	97.46	92.31	98.43	97.85	97.96	93.33
Fe Oxide - Actinolite (binary)	0.15	0.11	0.15	1.24	0.00	0.01	0.02	0.15
Fe Oxide - Phlogopite (binary)	1.02	1.09	1.28	2.17	0.48	0.71	0.35	0.68
Fe Oxide - Chlorite (binary)	0.08	0.02	0.01	0.02	0.17	0.11	0.07	0.27
Fe Oxide - Talc (binary)	0.00	0.00	0.00	0.00	0.02	0.02	0.00	0.07
Fe Oxide - Titanite (binary)	0.30	0.26	0.46	0.00	0.13	0.19	0.22	0.11
Fe Oxide - Albite (binary)	0.01	0.01	0.01	0.00	0.05	0.01	0.00	0.00
Fe Oxide - Quartz (binary)	0.02	0.02	0.02	0.23	0.02	0.01	0.01	0.05
Other	0.31	0.39	0.62	4.03	0.71	1.09	1.38	5.33
Σ	100.00	100.00	100.00	100.00	100.00	100.00	100.00	100.00

	6370				6387			
Mineral association	**> 80 µm**	**80/63 µm**	**63/40 µm**	**< 40 µm**	**> 80 µm**	**80/63 µm**	**63/40 µm**	**< 40 µm**
Fe Oxide liberated	95.66	97.92	96.67	81.59	96.27	96.66	97.60	86.29
Fe Oxide - Actinolite (binary)	0.00	0.00	0.00	0.00	1.50	1.02	0.41	0.27
Fe Oxide - Phlogopite (binary)	1.41	0.33	0.93	0.10	0.64	0.60	0.44	0.26
Fe Oxide - Chlorite (binary)	0.32	0.04	0.14	0.25	0.28	0.13	0.08	0.08
Fe Oxide - Talc (binary)	0.00	0.00	0.00	0.00	0.00	0.00	0.00	0.00
Fe Oxide - Titanite (binary)	0.00	0.00	0.00	0.00	0.44	0.53	0.44	0.09
Fe Oxide - Albite (binary)	0.00	0.05	0.00	0.00	0.00	0.00	0.00	0.00
Fe Oxide - Quartz (binary)	0.56	0.34	0.19	0.18	0.00	0.02	0.00	0.02
Other	2.05	1.32	2.08	17.88	0.87	1.04	1.02	13.00
Σ	100.00	100.00	100.00	100.00	100.00	100.00	100.00	100.00

Appendix 24. Henry-Reinhardt charts of the fraction 80/63 µm; Samples 6252 (B2-a), 6351 (B2-b), 6370 (B2-b) and 6387 (B2-a) after the comminution in a laboratory rod mill (10 minutes) and in a laboratory ball mill (35 minutes) and the Davis magnetic tube test carried out at the laboratory of the Institute of Mineral Processing. Basic intergrowth curve of magnetics = red, cumulative curve for magnetics = blue, cumulative curve for non-magnetics = green.

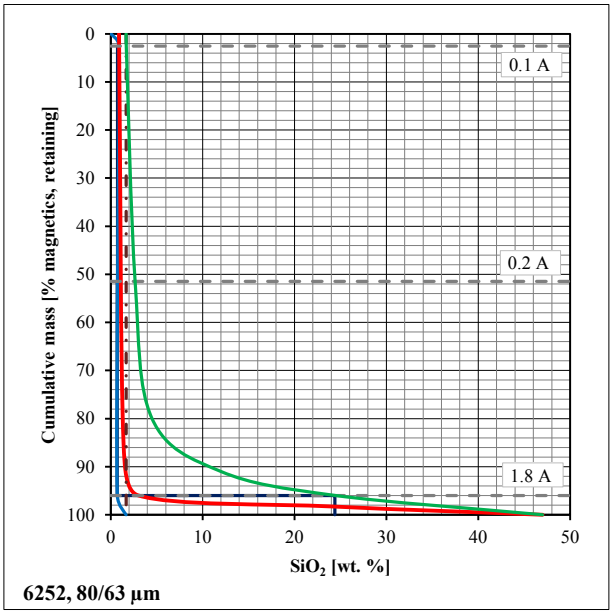

6252, 80/63 µm

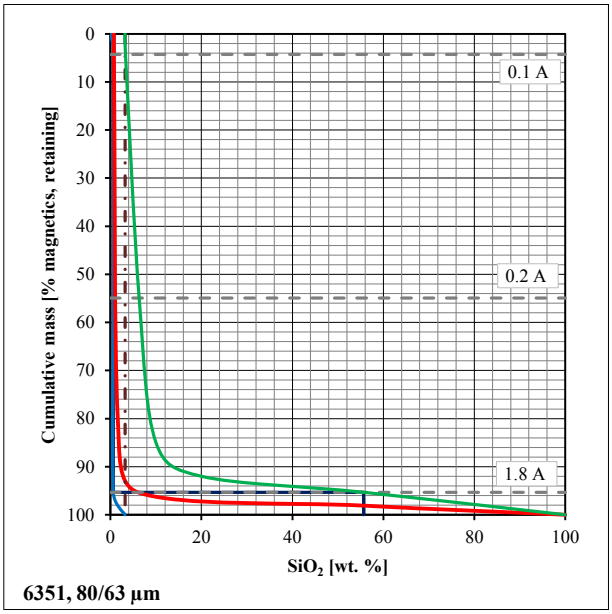

6351, 80/63 µm

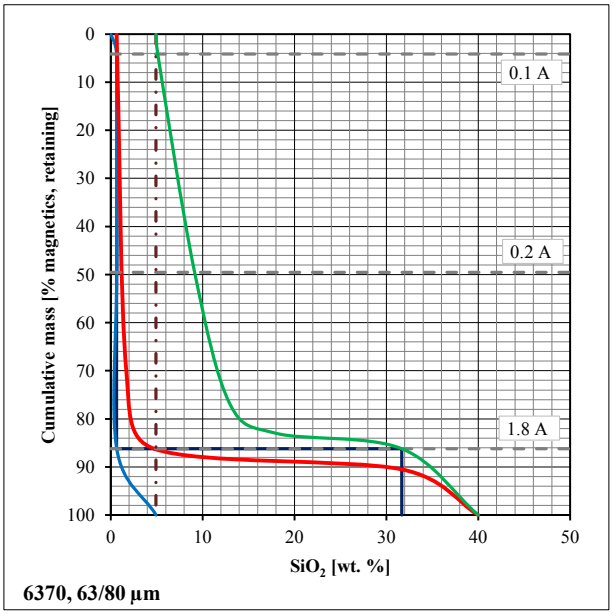

6370, 63/80 µm

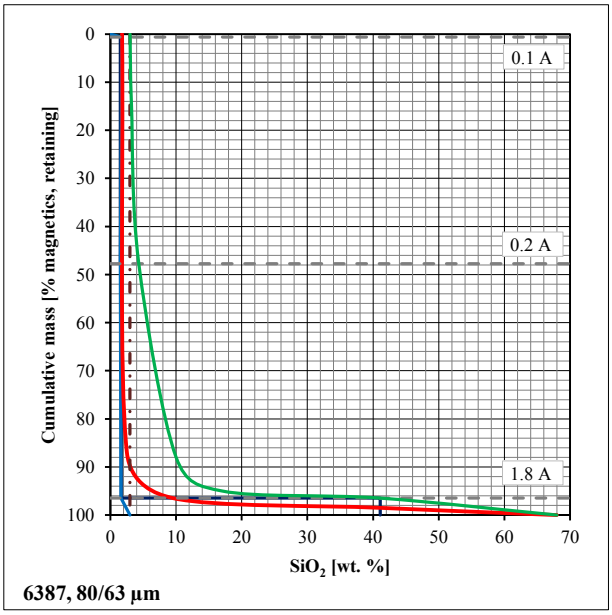

6387, 80/63 µm

Appendix 25. Liberation of Fe Oxide (magnetite); 100–90 % liberated, 90–60 % high grade middling, 60–30 % low grade middlings, 30–0 % locked presented as wt.% in fraction.

	6252 Subtype **B2-a**					**6351** Subtype **B2-b**				
	Fraction					**Fraction**				
	> 80 µm	**80/63 µm**	**63/40 µm**	**< 40 µm**	**Comb.**	**> 80 µm**	**80/63 µm**	**63/40 µm**	**< 40 µm**	**Comb.**
100%	0.10	0.15	0.97	23.59	15.43	0.33	1.16	3.68	19.48	11.59
< 100%	96.79	97.85	97.26	68.38	78.66	97.16	96.05	94.15	72.05	82.66
<= 90%	2.19	1.58	1.48	6.56	4.81	1.87	2.05	1.62	6.06	4.14
<= 60%	0.47	0.27	0.17	0.82	0.62	0.18	0.32	0.31	1.54	0.97
<= 30%	0.44	0.16	0.12	0.65	0.49	0.46	0.42	0.24	0.87	0.63
0%	0.00	0.00	0.00	0.00	0.00	0.00	0.00	0.00	0.00	0.00
Σ	100.00	100.00	100.00	100.00	100.00	100.00	100.00	100.00	100.00	100.00

	6363 Subtype **B2-a**					**6367** Subtype **B2-b**				
	Fraction					**Fraction**				
	> 80 µm	**80/63 µm**	**63/40 µm**	**< 40 µm**	**Comb.**	**> 80 µm**	**80/63 µm**	**63/40 µm**	**< 40 µm**	**Comb.**
100%	0.03	0.07	1.02	21.16	9.51	0.14	0.25	2.26	11.99	4.94
< 100%	98.07	98.01	96.42	70.86	85.77	98.29	97.60	95.69	81.20	91.38
<= 90%	1.65	1.75	2.30	6.25	3.83	1.27	1.97	1.68	5.27	2.94
<= 60%	0.05	0.03	0.08	1.09	0.51	0.12	0.06	0.21	0.96	0.43
<= 30%	0.20	0.13	0.19	0.64	0.38	0.17	0.12	0.16	0.58	0.31
0%	0.00	0.00	0.00	0.00	0.00	0.00	0.00	0.00	0.00	0.00
Σ	100.00	100.00	100.00	100.00	100.00	100.00	100.00	100.00	100.00	100.00

	6370 Subtype **B2-b**					**6387** Subtype **B2-a**				
	Fraction					**Fraction**				
	> 80 µm	**80/63 µm**	**63/40 µm**	**< 40 µm**	**Comb.**	**> 80 µm**	**80/63 µm**	**63/40 µm**	**< 40 µm**	**Comb.**
100%	0.00	0.05	0.36	2.40	1.20	0.03	0.02	0.41	3.72	2.38
< 100%	95.66	97.88	96.29	79.03	88.38	96.24	96.64	97.18	82.38	87.95
<= 90%	3.06	1.61	2.69	13.71	7.73	2.27	2.60	2.00	11.14	7.71
<= 60%	0.43	0.20	0.25	3.37	1.72	0.83	0.33	0.20	1.99	1.35
<= 30%	0.84	0.27	0.40	1.49	0.97	0.63	0.40	0.20	0.78	0.60
0%	0.00	0.00	0.00	0.00	0.00	0.00	0.00	0.00	0.00	0.00
Σ	100.00	100.00	100.00	100.00	100.00	100.00	100.00	100.00	100.00	100.00

Additional APPENDIX 1 for Figure 18. Results of the screen analyses and the specific density determined with He-Gas Pycnometer (AccuPyc 1330) of samples 6382, 6365 and 6354 after crushing (As received) at LKAB's mineral processing laboratory in Malmberget. The mean density for a sample is estimated from *Equation*

$$\bar{x} \rightarrow \frac{\sum m_i}{\rho} = \sum \frac{m_i}{\rho_i}$$

Sample **6382 (**B1) - Screen analysis after crushing *(-3 mm*) at LKAB's mineral processing laboratory						
Fraction size	**Sieve fractions**		**Retained**	**Passed**	**Density (ρ)**	**Volume specific mass**
[mm]	Mass [g]	wt [%]	[%]	[%]	[g/cm^2]	[1/ρ]
>3.15	0.06	0.01	0.01	99.99	-	-
3.15 / 1.0	184.69	18.72	18.72	81.28	5.06	0.1975
1.0 / 0.5	89.77	9.10	27.82	72.18	5.03	0.1986
0.5 / 0.315	78.24	7.93	35.75	64.25	5.06	0.1977
0.315 / 0.1	322.26	32.66	68.40	31.60	5.10	0.1961
0.1 / 0.04	189.65	19.22	87.62	12.38	5.12	0.1955
< 0.04	122.15	12.38	100.00	0.00	4.95	0.2019
Σ	986.82	100.00	-	-	$\bar{x}$ = 5.07	$\bar{x}$ = 0.1973

Sample **6365** (B2) - Screen analysis after crushing *(-3 mm*) at LKAB's mineral processing laboratory						
Fraction size	**Sieve fractions**		**Retained**	**Passed**	**Density (ρ)**	**Volume specific mass**
[mm]	Mass [g]	wt [%]	[%]	[%]	[g/cm^2]	[1/ρ]
>3.15	0.38	0.04	0.04	99.96	-	-
3.15 / 1.0	387.50	36.14	36.18	63.82	4.85	0.2063
1.0 / 0.5	144.83	13.51	49.68	50.32	4.80	0.2081
0.5 / 0.315	64.61	6.03	55.71	44.29	4.94	0.2025
0.315 / 0.1	205.70	19.18	74.89	25.11	4.88	0.2050
0.1 / 0.04	195.24	18.21	93.10	6.90	4.90	0.2040
< 0.04	73.94	6.90	100.00	0.00	4.53	0.2205
Σ	1072.20	100.00	-	-	$\bar{x}$ = 4.84	$\bar{x}$ = 0.2066

Sample **6354** (D3) - Screen analysis after crushing *(-3 mm*) at LKAB's mineral processing laboratory						
Fraction size	**Sieve fractions**		**Retained**	**Passed**	**Density (ρ)**	**Volume specific mass**
[mm]	Mass [g]	wt [%]	[%]	[%]	[g/cm^2]	[1/ρ]
>3.15	3.76	0.36	0.36	99.64	-	-
3.15 / 1.0	490.73	46.61	46.91	53.09	4.71	0.2121
1.0 / 0.5	155.03	14.72	61.62	38.38	4.68	0.2138
0.5 / 0.315	69.50	6.60	73.82	26.18	4.66	0.2145
0.315 / 0.1	125.89	11.96	80.41	19.59	4.39	0.2279
0.1 / 0.04	117.69	11.18	92.56	7.44	4.28	0.2338
< 0.04	90.26	8.57	100.00	0.00	4.38	0.2283
Σ	1052.86	100.00	-	-	$\bar{x}$ = 4.52	$\bar{x}$ = 0.2213

Additional APPENDIX 2 for Figure 18. The data of the screening analysis after every grinding step (10 minutes in rod mil, 25 minutes and 35 minutes in ball) at LKAB's Mineral Processing Laboratory in Malmberget.

Sample 6382 (B1)

	Rod mill (10 minutes)		**Ball mill** (25 minutes)		**Ball mill** (35 minutes)	
Particle size [mm]	**Retained** [%]	**Passed** [%]	**Retained** [%]	**Passed** [%]	**Retained** [%]	**Passed** [%]
0.355 / 0.25	0	100	0	100	0	100
0.25 / 0.18	0	100	0	100	0	100
0.18 / 0.125	2.8	97.2	0	100	0	100
0.125 / 0.09	23.5	76.5	0.1	99.9	0	100
0.09 / 0.063	46.8	53.2	2.9	97.1	0.7	99.3
0.063 /0 .045	63.6	36.4	19.4	80.6	11.1	88.9
< 0.045	72.7	27.3	36.3	63.7	25.7	74.3
Σ	100.00	0	100.00	0	100.00	0.00

Sample 6365 (B2)

	Rod mill (10 minutes)		**Ball mill** (25 minutes)		**Ball mill** (35 minutes)	
Particle size [mm]	**Retained** [%]	**Passed** [%]	**Retained** [%]	**Passed** [%]	**Retained** [%]	**Passed** [%]
0.25 / 0.18	0	100	0	100	0	100
0.18 / 0.125	0.3	99.7	0	100	0	100
0.125 / 0.09	9.4	90.6	0	100	0	100
0.09 / 0.063	33.7	66.3	1.7	98.3	0.4	99.6
0.063 /0 .045	56.5	43.5	15.1	84.9	9.4	90.6
< 0.045	68.3	31.7	32.2	67.8	23.8	76.2
Σ	100.00	0	100.00	0	100.00	0.00

Sample 6354 (D3)

	Rod mill (10 minutes)		**Ball mill** (25 minutes)		**Ball mill** (35 minutes)	
Particle size	**Retained**	**Passed**	**Retained**	**Passed**	**Retained**	**Passed**
[mm]	[%]	[%]	[%]	[%]	[%]	[%]
2.8 / 2.0	0	100	0	100	0	100
2.0 / 1.4	0.1	99.9	0.1	99.9	0	100
1.4 / 1.0	0.3	99.7	0.2	99.8	0	100
1.0 / 0.71	0.4	99.6	0.2	99.8	0	100
0.71 / 0.5	0.5	99.5	0.2	99.8	0	100
0.5 / 0.355	2.2	97.8	0.2	99.8	0	100
0.355 / 0.25	8.4	91.6	0.2	99.8	0	100
0.25 / 0.18	18.9	81.1	0.3	99.7	0	100
0.18 / 0.125	28.2	71.8	0.3	99.7	0.1	99.9
0.125 / 0.09	37.9	62.1	0.4	99.6	0.3	99.7
0.09 / 0.063	47.4	52.6	1.6	98.4	0.6	99.4
0.063 /0 .045	57.4	42.6	11.0	89.0	5.8	94.2
< 0.045	64.5	35.5	24.2	75.8	15.9	84.1
Σ	100.00	0	100.00	0	100.00	0.00

Additional APPENDIX 3 for Figure 21. Particle size distribution of the feed material for the mineral processing tests after crushing (– 3mm) at LKAB's mineral processing laboratory in Malmberget.

Sample **6252** (B2) – particle size distribution after crushing *(*-3 mm).

Fraction size [mm]	**Sieve fractions** wt [g]	wt [%]	**Retained** [%]	**Passed** [%]
>1.0	507.26	32.33	32.33	67.67
1.0 / 0.5	382.4	24.37	56.70	43.30
0.5 / 0.315	136.12	8.68	65.38	34.62
0.315 / 0.1	214.63	13.68	79.06	20.94
0.1 / 0.04	164.51	10.48	89.54	10.46
< 0.04	164.1	10.46	100.00	0.00
Σ	1569.02	100	-	-

Sample **6351** (B2) - particle size distribution after crushing (-3 mm).

Fraction size [mm]	**Sieve fractions** wt [g]	wt [%]	**Retained** [%]	**Passed** [%]
>1.0	475.37	33.95	33.95	66.05
1.0 / 0.5	151.12	10.79	44.75	55.25
0.5 / 0.315	79.46	5.68	50.42	49.58
0.315 / 0.1	268.59	19.18	69.61	30.39
0.1 / 0.04	268.41	19.17	88.78	11.22
< 0.04	157.07	11.22	100.00	0.00
Σ	1400.02	100.00	-	-

Sample **6363** (B2) - particle size distribution after crushing (-3 mm).

Fraction size [mm]	**Sieve fractions** wt [g]	wt [%]	**Retained** [%]	**Passed** [%]
>1.0	213.31	17.51	17.51	82.49
1.0 / 0.5	160.7	13.19	30.69	69.31
0.5 / 0.315	109.87	9.02	39.71	60.29
0.315 / 0.1	381.74	31.33	71.04	28.96
0.1 / 0.04	250.72	20.58	91.62	8.38
< 0.04	102.16	8.38	100.00	0.00
Σ	1218.5	100.00	-	-

Sample **6367** (B2) - particle size distribution after crushing (-3 mm).

Fraction size [mm]	**Sieve fractions** wt [g]	wt [%]	**Retained** [%]	**Passed** [%]
>1.0	635.11	46.08	46.08	53.92
1.0 / 0.5	170.6	12.38	58.45	41.55
0.5 / 0.315	84.98	6.17	64.62	35.38
0.315 / 0.1	205.34	14.90	79.51	20.49
0.1 / 0.04	177.87	12.90	92.42	7.58
< 0.04	104.5	7.58	100.00	0.00
Σ	1378.4	100.00	-	-

Sample **6370** (B2) - particle size distribution after crushing (-3 mm).

Fraction size [mm]	**Sieve fractions**		**Retained**	**Passed**
	wt [g]	wt [%]	[%]	[%]
>1.0	413.46	37.04	37.04	62.96
1.0 / 0.5	149	13.35	50.39	49.61
0.5 / 0.315	88.78	7.95	58.35	41.65
0.315 / 0.1	241.42	21.63	79.98	20.02
0.1 / 0.04	156.73	14.04	94.02	5.98
< 0.04	66.78	5.98	100.00	0.00
Σ	1116.17	100.00	-	-

Sample **6387** (B2) - particle size distribution after crushing ***(-3 mm*)**.

Fraction size [mm]	**Sieve fractions**		**Retained**	**Passed**
	wt [g]	wt [%]	[%]	[%]
>1.0	589.09	45.66	45.66	54.34
1.0 / 0.5	205.36	15.92	61.58	38.42
0.5 / 0.315	94.56	7.33	68.91	31.09
0.315 / 0.1	156.01	12.09	81.00	19.00
0.1 / 0.04	62.67	4.86	85.86	14.14
< 0.04	182.43	14.14	100.00	0.00
Σ	1290.12	100.00	-	-

Additional APPENDIX 4 for Figure 31. The data of the determination on magnetite content with Satmagan carried at the laboratory of the Institute of the Mineral Processing.

6382 (B1) As received	**Magnetite content**			
Fraction [mm]	**Mass** [%]	**Mass** [%]	**Mass** [%]	**Mass ($\bar{x}$)** [%]
0.5 / 0.315				97.45 *
0.315 / 0.1				99.56 *
0.1 / 0.04				99.23 *
< 0.04				91.4 *

6382 (B1) Rod mill / cycle 3+4	**Magnetite content**			
Fraction [mm]	**Mass** [%]	**Mass** [%]	**Mass** [%]	**Mass ($\bar{x}$)** [%]
0.5 / 0.315				96.45 *
0.315 / 0.1				97.11 *
0.1 / 0.04				87.13 *
< 0.04				93.85 *

6382 (B1) Ball mill		**Magnetite content**			
Fraction [mm]	**Davis Magnetic Tube**	**Mass** [%]	**Mass** [%[	**Mass** [%]	**Mass ($\bar{x}$)** [%]
0.1 / 0.04	0.12 A / magnetics	> 100	- -	- -	100.00
0.1 / 0.04	0.18 A / magnetics	> 100	- -	- -	100.00
0.1 / 0.04	0.225 A / magnetics	> 100	- -	- -	100.00
0.1 / 0.04	1.78 A / magnetics	> 100	- -	- -	100.00
0.1 / 0.04	1.78 A / non-magnetics	0.915	0.944	0.972	0.94
< 0.04	0.12 A / magnetics	98.49	98.65	98.46	98.53
< 0.04	0.18 A / magnetics	99.82	99.55	> 100	> 100
< 0.04	0.225 A / magnetics	99.99	98.84	> 100	> 100
< 0.04	1.78 A / magnetics	- -	- -	- -	> 100 *
< 0.04	1.78 A / non-magnetics	1.422	1.453	1.456	1.444

6365 (B2) As received	**Magnetite content**			
Fraction [mm]	**Mass** [%]	**Mass** [%]	**Mass** [%]	**Mass ($\bar{x}$)** [%]
0.5/0.315	88.27	91.45	88.95	89.65
0.315/0.1	96.21	94.51	95.08	95.27
0.1/0.04	95.50	95.42	94.62	95.18
< 0.04	86.78	87.41	87.08	87.09

6365 (B2) Rod mill / cycle 4 + 5	**Magnetite content**			
Fraction [mm]	**Mass** [%]	**Mass** [%]	**Mass** [%]	**Mass ($\bar{x}$)** [%]
0.5/0.315	88.95	87.89	88.12	88.32
0.315/0.1	92.75	90.61	91.69	91.68
0.1/0.04	94.20	93.62	94.38	94.07
< 0.04	81.95	82.36	81.82	82.04

6365 (B2) Ball mill	**Magnetite content**				
Fraction [mm]	**Davis Magnetic Tube**	**Mass** [%]	**Mass** [%]	**Mass** [%]	**Mass ($\bar{x}$)** [%]
0.1 / 0.04	0.12 A / magnetics	> 100	- -	- -	> 100
0.1 / 0.04	0.18 A / magnetics	> 100	- -	- -	> 100
0.1 / 0.04	0.225 A / magnetics	> 100	- -	- -	> 100
0.1 / 0.04	1.78 A / magnetics				> 100 *
0.1 / 0.04	1.78 A / non-magnetics	0.915	0.944	0.972	0.944
< 0.04	0.1 A / magnetics	> 100	> 100	> 100	> 100
< 0.04	0.18 A / magnetics	> 100	> 100	> 100	> 100
< 0.04	0.225 A / magnetics	99.92	99.97	> 100	> 100
< 0.04	1.78 A / magnetics				> 100 *
< 0.04	1.78 A / non-magnetics	0.863	0.733	0.736	0.777

6354 (D3) As received	**Magnetite content**			
Fraction [mm]	**Mass** [%]	**Mass** [%]	**Mass** [%]	**Mass ($\bar{x}$)** [%]
0.5 / 0.315	84.56	85.00	84.17	84.58
0.315 / 0.1	82.15	80.53	81.62	81.43
0.1 / 0.04	67.13	67.39	67.70	67.41
< 0.04	69.65	70.14	70.00	69.93

6354 (D3) Rod mill / cycle 3	**Magnetite content**			
Fraction [mm]	**Mass** [%]	**Mass** [%]	**Mass** [%]	**Mass ($\bar{x}$)** [%]
0.5 / 0.315	90.45	91.20	91.50	91.05
0.315 / 0.1	88.92	88.77	88.73	88.81
0.1 / 0.04	75.23	75.90	75.37	75.50
< 0.04	74.73	75.08	74.90	74.90

6354 (D3) Ball mill	**Magnetite content**				
Fraction [mm]	**Davis Magnetic Tube**	**Mass** [%]	**Mass** [%]	**Mass** [%]	**Mass ($\bar{x}$)** [%]
0.1 / 0.04	0.12 A / magnetics	98.90	98.89	98.45	98.75
0.1 / 0.04	0.18 A / magnetics	96.68	96.71	96.63	96.67
0.1 / 0.04	0.225 A / magnetics	91.01	91.39	91.15	91.18
0.1 / 0.04	1.78 A / non-magnetics				> 100 *
0.1 / 0.04	1.78 A / non-magnetics	1.677	1.567	1.559	1.601
< 0.04	0.1 A / magnetics	96.85	96.80	96.51	96.72
< 0.04	0.18 A / magnetics	> 100			> 100
< 0.04	0.225 A / magnetics	99.17	99.40	99.59	99.39
< 0.04	1.78 A / magnetics				90 *
< 0.04	1.78 A / non-magnetics	0.962	0.983	1.035	0.993

Additional APPENDIX 5 for Figure 31. Particle size distribution for selected samples representing the high-SiO_2 ore type B2 after comminution tests at LKAB's mineral processing laboratory. 10 Min corresponds a comminution time of 10 minutes in the laboratory rod mill, 25 Min corresponds a comminution time of 10 minutes in the laboratory rod mill and 25 minutes in the laboratory ball mill, and 35 Min corresponds a comminution time of 10 minutes in the laboratory rod mill and 35 minutes in the laboratory ball mill.

Fraction	**Sample 6252**			**Sample 6351**			**Sample 6363**		
[mm]	**10 Min**	**25 Min**	**35 Min**	**10 Min**	**25 Min**	**35 Min**	**10 Min**	**25 Min**	**35 Min**
0.5 / 0.355	100	100	100	100	100	100	100	100	100
0.355 /0.25	100	100	100	100	100	100	100	100	100
0.25 / 0.18	100	100	100	99.8	100	100	100	100	100
0.18 / 0.125	99.8	100	100	96	99.8	100	99.5	100	100
0.125 / 0.09	92.3	99.8	100	80.3	99.8	99.9	86.8	99.9	100
0.09 / 0.063	70.9	98.6	99.6	64.8	99.6	99	62.9	98	99.4
0.063 / 0.045	46	88.2	92.6	50.1	94.8	89.7	39	80.5	91.1
< 0.045	34.4	71.5	80.2	38.5	82.1	74.3	27.5	64.1	74

Fraction	**Sample 6367**			**Sample 6370**			**Sample 6387**		
[mm]	**10 Min**	**25 Min**	**35 Min**	**10 Min**	**25 Min**	**35 Min**	**10 Min**	**25 Min**	**35 Min**
0.5 / 0.355	100	100	100	100	100	100	100	100	100
0.355 /0.25	100	100	100	99.9	100	100	99.2	100	100
0.25 / 0.18	99.9	100	100	98.9	100	100	92.3	100	100
0.18 / 0.125	97.3	99.9	100	86.5	100	100	78.6	100	100
0.125 / 0.09	78.2	99.8	99.9	64.1	99.8	99.9	66.2	99.9	100
0.09 / 0.063	57.2	97.4	99.1	46.6	96.4	99	55.5	98.8	99.7
0.063 / 0.045	36.6	84.7	90.5	30.4	75.5	87.5	44.2	89	93.8
< 0.045	27	67	76.3	22.3	60.7	72	35.9	75.3	82.3

Additional APPENDIX 6 for Figures 38, 39, and 40. Numeric data of the particle size distribution (wet screen analysis) and P_{80} value for every grinding stage at LKAB's mineral processing laboratory for samples presented in Figures 38, 39, and 40. By method, 10 corresponds comminution in 10 minutes in the rod mill, 10+25 and 10+35 corresponds comminution in 10 minutes in the rod mill and 25 minutes in the ball mill respectively 35 minutes.

Sample	Ore type	Method	< 2.8 mm	< 2 mm	< 1.4 mm	< 1 mm	< 710 µm	< 500 µm	< 355 µm	< 250 µm	< 180 µm	< 125 µm	< 90 µm	< 63 µm	< 45 µm	P_{80}
6255	B1	10	100	100	100	100	100	100	100	99.9	97.6	79.9	61.9	44.8	34.5	125
		10+25	100	100	100	100	100	100	100	100	100	99.6	98.4	89.0	72.7	52
		10+35	100	100	100	100	100	100	100	100	100	99.9	99.5	93.7	80.7	44
6365	B1	10	100	100	100	100	100	100	100	99.8	91.5	68.1	47.3	31.9	22.9	151
		10+25	100	100	100	100	100	100	100	100	100	99.9	96.5	79.9	62.2	63
		10+35	100	100	100	100	100	100	100	100	100	99.9	99.1	87.4	70.0	55
6384	B1	10	100	100	100	100	100	100	100	99.9	96.2	80.0	60.8	42.3	30.6	125
		10+25	100	100	100	100	100	100	100	100	100	99.9	97.1	79.3	62.4	64
		10+35	100	100	100	100	100	100	100	100	100	100	99.4	90.2	72.6	52
6386	B1	10	100	100	100	100	100	100	99.9	99.5	90.2	68.8	52.2	38.4	29.6	151
		10+25	100	100	100	100	100	100	100	100	100	99.9	96.5	81.9	66.0	60
		10+35	100	100	100	100	100	100	100	100	100	100	99.0	88.6	75.1	51
6397	B1	10	100	100	100	100	100	100	99.8	96.7	83.0	68.0	53.2	38.9	29.2	168
		10+25	100	100	100	100	100	100	100	100	99.9	99.8	96.9	82.9	65.5	60
		10+35	100	100	100	100	100	100	100	100	100	99.9	99.2	90.6	75.6	50
6440	B1	10	100	100	100	100	100	100	99.9	99.6	94.1	76.2	57.1	40.4	30.2	135
		10+25	100	100	100	100	100	100	100	100	100	99.9	99.5	96.2	77.8	47
		10+35	100	100	100	100	100	100	100	100	100	100	99.8	97.4	87.3	35
6359	B2	10	100	100	100	100	100	100	100	99.9	96.2	80.4	62.4	45.2	34.0	124
		10+25	100	100	100	100	100	100	100	100	100	99.9	98.6	87.0	71.4	54
		10+35	100	100	100	100	100	100	100	100	100	99.9	99.5	92.9	78.8	46
6361	B2	10	100	100	100	100	100	100	100	100	99.6	93.7	74.3	51.7	38.3	99
		10+25	100	100	100	100	100	100	100	99.9	99.9	99.9	99.0	88.9	73.4	52
		10+35	100	100	100	100	100	100	100	100	99.9	99.9	99.6	93.8	80.8	44
6385	B2	10	100	100	100	100	100	99.4	93.2	78.5	66.1	54.5	44.5	34.5	28.0	259
		10+25	100	100	100	100	100	100	100	100	100	99.8	96.4	80.8	65.6	62
		10+35	100	100	100	100	100	100	100	100	99.9	99.9	98.9	88.8	75.2	51

Sample	Ore type	Method	< 2.8 mm	< 2 mm	< 1.4 mm	< 1 mm	< 710 µm	< 500 µm	< 355 µm	< 250 µm	< 180 µm	< 125 µm	< 90 µm	< 63 µm	< 45 µm	P_{80}
6396	B2	10	100	100	100	100	100	100	100	99.2	90.2	70.5	53.7	37.6	27.4	149
		10+25	100	100	100	100	100	100	100	100	100	99.8	97.2	82.3	64.4	60
		10+35	100	100	100	100	100	100	100	100	100	99.8	99.0	90.4	74.4	51
6400	B2	10	100	100	100	100	100	100	100	99	85.8	65.6	49.9	36.6	28.5	162
		10+25	100	100	100	100	100	100	100	100	100	99.8	98.2	88.5	72.6	53
		10+35	100	100	100	100	100	100	100	100	100	99.9	98.4	90.7	72.1	52
6412	B2	10	100	99.9	99.9	99.8	99.8	98.7	91.8	77.4	63.6	50.6	39.2	29.8	21.6	267
		10+25	100	99.9	99.9	99.9	99.9	99.8	99.8	99.7	99.6	99.4	96.8	83.5	65.6	59
		10+35	100	100	100	100	100	100	99.9	99.9	99.9	99.8	99.3	93.7	79.1	46
6254	D3	10	100	100	100	100	100	100	100	100	99.6	83.7	58.0	35.4	23.2	119
		10+25	100	100	100	100	100	100	100	100	100	99.9	98.2	82.8	62.9	60
		10+35	100	100	100	100	100	100	100	100	100	99.7	99.3	91.3	74.9	50
6351	D3	10	100	100	100	100	100	100	100	100	99.9	94.9	76.2	52.9	38.5	96
		10+25	100	100	100	100	100	100	100	100	100	99.9	99.2	90.4	75.8	50
		10+35	100	100	100	100	100	100	100	100	100	100	99.9	95.7	82.3	42
6369	D1	10	100	100	100	100	100	100	100	100	99.8	93.2	69.6	46.7	33.9	104
		10+25	100	100	100	100	100	100	100	100	100	99.9	98.0	84.0	66.8	58
		10+35	100	100	100	100	100	100	100	100	100	100	99.4	91.4	77.2	48
6440	D3	10	100	100	100	100	100	100	100	100	99.6	93.1	76.2	59.3	42.3	97
		10+25	100	100	100	100	100	100	100	100	100	100	99.9	97.1	86.5	37
		10+35	100	100	100	100	100	100	100	100	100	100	99.9	99.8	92.2	26
8028	D5	10	100	100	100	100	100	100	100	100	97.6	80.3	59.0	40.9	30.5	124
		10+25	100	100	100	100	100	100	100	100	100	100	97.8	83.4	66.8	59
		10+35	100	100	100	100	100	100	100	100	100	100	99.5	91.0	76.6	49
8030	D3	10	100	100	100	100	100	100	99.9	94.3	67.6	44.2	29.6	19.7	14.7	210
		10+25	100	100	100	100	100	100	100	100	99.9	99.5	90.0	66.6	49.4	77
		10+35	100	100	100	100	100	100	100	100	100	99.9	97.3	80.2	63.4	63

Additional APPENDIX 7 for Figure 41. Particle size distribution below 125 µm was determined by Malver Mastersizer 2000, volume specific surface area (s_v) was determined by Svensson's method and specific gravity (density) was determined by He-gas Pycnometer (AccuPyc 1330) at LKAB's mineral processing laboratory.

Sample	Ore type	Method	< 125 µm	< 45 µm	< 20 µm	Specific surface area [cm^{-1}]	Specific surface area [cm^2/g]	Density [g/cm^3]
6255	B1	10	80.4	39.1	17.6	3161	656	4.82
		10+25	98.8	67.2	33.2	6628	1378	4.81
		10+35	100	76.3	39.9	8002	1664	4.81
6365	B1	10	69	28.7	12.1	2165	440	4.92
		10+25	98.2	59.4	27.6	5906	1205	4.90
		10+35	99.5	65.6	31.1	6828	1388	4.92
6384	B1	10	67.2	26.4	12	2416	516	4.68
		10+25	98.4	60.5	27.9	6018	1275	4.72
		10+35	99	66.9	32.8	7209	1524	4.73
6386	B1	10	58.5	24.7	11.7	2887	580	4.98
		10+25	97.4	61	28.7	6023	1212	4.97
		10+35	98.6	67.8	33.3	7070	1423	4.97
6397	B1	10	61.7	27.2	12.1	2950	602	4.90
		10+25	97.3	59.9	27.3	6383	1300	4.91
		10+35	98.7	67.3	32.1	7215	1472	4.90
6409	B1	10	73.5	33.1	14.3	2687	556	4.83
		10+25	91.3	52.5	23.5	4821	992	4.86
		10+35	98.2	65.2	31.2	7194	1486	4.84
6440	B1	10	70.3	28.6	13	2810	565	4.97
		10+25	100	71	34.2	7436	1496	4.97
		10+35	100	79.7	41.4	8461	1702	4.97

Sample	Ore type	Method	< 125 µm	< 45 µm	< 20 µm	Specific surface area [cm^{-1}]	Specific surface area [cm^2/g]	Density [g/cm^3]
6359	B2	10	81.2	39.3	16.5	3196	662	4.83
		10+25	98.3	62.5	28.4	6580	1365	4.82
		10+35	99.7	72.4	35.3	7349	1525	4.82
6361	B2	10	85.7	37.2	14.6	3588	759	4.73
		10+25	98.4	63.6	28.8	6330	1347	4.70
		10+35	98.8	68.2	32	7541	1601	4.71
6385	B2	10	40.1	18.2	8.1	2632	539	4.88
		10+25	97.3	61.9	29.4	5928	1210	4.90
		10+35	97.9	67.5	32.8	7130	1452	4.91
6396	B2	10	65.1	27.8	12.9	2660	554	4.80
		10+25	97.6	60.3	27.7	6540	1365	4.79
		10+35	98.5	66.7	31.8	7279	1516	4.80
6400	B2	10	60.2	26	12.2	2810	600	4.68
		10+25	97.8	64.4	31.1	7123	1525	4.67
		10+35	98.1	66.7	33.4	7366	1577	4.67
6412	B2	10	41.1	17.3	8.4	2204	443	4.97
		10+25	97.5	61.2	29	6598	1330	4.96
		10+35	99.8	71.4	35.5	7861	1585	4.96

Sample	Ore type	Method	< 125 µm	< 45 µm	< 20 µm	Specific surface area [cm^{-1}]	Specific surface area [cm^2/g]	Density [g/cm^3]
6359	B2	10	81.2	39.3	16.5	3196	662	4.83
		10+25	98.3	62.5	28.4	6580	1365	4.82
		10+35	99.7	72.4	35.3	7349	1525	4.82
6361	B2	10	85.7	37.2	14.6	3588	759	4.73
		10+25	98.4	63.6	28.8	6330	1347	4.70
		10+35	98.8	68.2	32	7541	1601	4.71
6385	B2	10	40.1	18.2	8.1	2632	539	4.88
		10+25	97.3	61.9	29.4	5928	1210	4.90
		10+35	97.9	67.5	32.8	7130	1452	4.91
6396	B2	10	65.1	27.8	12.9	2660	554	4.80
		10+25	97.6	60.3	27.7	6540	1365	4.79
		10+35	98.5	66.7	31.8	7279	1516	4.80
6400	B2	10	60.2	26	12.2	2810	600	4.68
		10+25	97.8	64.4	31.1	7123	1525	4.67
		10+35	98.1	66.7	33.4	7366	1577	4.67
6412	B2	10	41.1	17.3	8.4	2204	443	4.97
		10+25	97.5	61.2	29	6598	1330	4.96
		10+35	99.8	71.4	35.5	7861	1585	4.96